Doctoral Dissertation

in the discipline:

Materials Engineering

Production and analysis of nanomaterials properties for applications in supercapacitors

Author: **Muhammad Danish Ali** M.Phil.

Supervisor: Prof. SUT **Anna Starczewska**, Ph.D., D.Sc.,

Co-supervisor: **Marcin Jesionek**, Ph.D.

Institute of Physics, Centre for Science and Education

Silesian University of Technology

September 2026

Dedication

To My Parents

Mr. and Mrs. Anayat Ullah

Author Declaration

I declare that the doctoral dissertation entitled “Production and analysis of nanomaterials properties for applications in supercapacitors” is consistent with the doctoral dissertation prepared and submitted as part of the education at the doctoral school run by the Silesian University of Technology.

Muhammad Danish Ali

Institute of Physics, Centre for Science and Education

Silesian University of Technology

Use of Artificial Intelligence (AI) Tools

The author acknowledges the use of the free version of **Grammarly** and **Microsoft 365 Copilot** to enhance the linguistic quality of this dissertation, including grammar, punctuation, sentence structure, and overall readability. The license for **Microsoft 365 Copilot** used during editing was provided by the **Silesian University of Technology, Poland**.

No AI tools were employed to generate research content, develop scientific methodologies, interpret data, or formulate conclusions. The author retains full responsibility and accountability for the integrity, accuracy, and originality of the entire work.

Muhammad Danish Ali

Institute of Physics, Centre for Science and Education

Silesian University of Technology

Acknowledgements

I would like to express my sincere gratitude to all those who supported me throughout my doctoral studies and contributed to the completion of this dissertation.

First and foremost, I am deeply grateful to my supervisor, **Dr hab. Anna Starczewska, Prof. PŚ,** for her continuous guidance, scientific support, valuable advice, and encouragement throughout my PhD journey. I also sincerely thank my co-supervisor, **Dr Marcin Jesionek**, for his support, constructive discussions, and assistance during my research.

I would like to express my appreciation to **Prof. dr hab. inż. Marian Nowak**, former Head of the Department, and to **Dr hab. Andrzej Grabowski, Prof. PŚ; Dr hab. Mirosława Kępińska, Prof. PŚ; Dr hab. inż. Krystian Mistewicz; Dr inż. Piotr Duka; Dr inż. Piotr Szperlich; and Dr inż. Bartłomiej Toroń, Paweł Solecki,** and **Dr. Tushar Kanti Das** for their scientific support, cooperation, and for creating a supportive research environment.

I am particularly grateful to **Dr Tushar Kanti Das** from the Centre for Science and Education, Silesian University of Technology, for their support and collaboration in interdisciplinary research activities.

I sincerely thank **Prof. Ahmad Azmin Mohamad** of **Universiti Sains Malaysia** for hosting and supporting me during my international research internship. I am also grateful to **Uzair Naeem** and Dr **MD Anwar Ali Anshari** for their assistance, cooperation, and valuable scientific discussions during my stay.

My sincere appreciation is extended to **Prof. An Hardy** and the researchers at **Hasselt University** for their hospitality, scientific guidance, and support during my research training in the field of supercapacitor electrode materials.

I sincerely thank **Dr hab. inż. Przemysław Ledwoń** of **Silesian University of Technology** for his invaluable support and guidance during the electrochemical testing. I am also grateful to **Ammara Aslam** for their assistance, cooperation, and valuable scientific discussions during my stay.

I also acknowledge the valuable academic opportunities provided through the **EURECA-PRO** and the **SGroup** Blended Intensive Programme at the **University of Valladolid**, **Spain**. I am especially thankful to **María del Mar Fernández Sainz** for her support and contribution to these international academic activities.

I gratefully acknowledge the Rector of the Silesian University of Technology, **Prof. Marek Pawełczyk**, for supporting an academic environment that promotes multidisciplinary research, international cooperation, and the professional development of doctoral students.

I also sincerely thank the **International Mobility Office** and the **Joint Doctoral School of the Silesian University of Technology**, particularly **Dr Danuta Stasiowska** and **Dr Patrycja Hąbek**, for their

administrative and organizational support. I gratefully acknowledge the financial support provided through the **Excellence Initiative – Research University programme, NAWA, Erasmus+, EURECA-PRO,** and **the Young Scientist Research Grant**, which enabled my research development and international scientific activities.

I sincerely thank **Aneela Anayat, Muhammad Usman, Fatima Usman, Anam Anayat, Areej Tabassum, Horia Fatima, Muhammad Yahya, and Muhammad Zamman** for their unwavering support and encouragement throughout my studies.

Finally, I wish to express my deepest gratitude to **my wife, Ammara Aslam,** for her unwavering support, patience, understanding, and encouragement throughout this journey. I am equally thankful to **my family and friends** for their continuous support, motivation, and belief in me.

Abstract

The development of electrode materials with high charge-storage capability, electrical response, and stable electrochemical performance remains an important requirement for advanced supercapacitor systems. In this work, graphene oxide-antimony sulfoiodide (GO-SbSI) binary composites and graphene oxide-antimony sulfoiodide-manganese dioxide (GO-SbSI-MnO_2, GSM) ternary composites were prepared at different concentrations to investigate the relationship between material composition, structural properties, electrical response, and electrochemical charge-storage behavior. GO was prepared using the Hummers method, SbSI nanowires were synthesized through a sonochemical route, and MnO_2 nanostructures were prepared by a hydrothermal method. The binary and ternary composites were subsequently produced using controlled sonochemical and combined hydrothermal-sonochemical procedures.

The prepared materials were investigated using X-ray diffraction (XRD), scanning and field-emission scanning electron microscopy, energy-dispersive X-ray spectroscopy (EDS), transmission electron microscopy, X-ray photoelectron spectroscopy (XPS), Fourier-transform infrared spectroscopy (FTIR), UV-Vis spectroscopy, complex impedance spectroscopy, and standard electrochemical techniques. The structural and morphological investigations showed the coexistence of GO sheets and SbSI nanowires in the binary composites, while the GSM materials contained contributions from GO, SbSI, and MnO_2, with morphology and structural response changing according to composition. The XRD results showed the characteristic crystalline reflections associated with SbSI and α-MnO_2, while XPS, EDS, and FTIR measurements supported the presence of the expected constituent elements and chemical environments, specifically verifying the active functional groups and oxidation states. The optical and frequency-dependent electrical measurements further showed that changes in composition influenced the absorption response, polarization, impedance, dielectric behavior, and AC electrical response of the prepared materials.

Electrochemical properties were evaluated through cyclic voltammetry, galvanostatic charge-discharge, and electrochemical impedance spectroscopy, alongside cycling stability and charge-storage kinetic analyses. At a scan rate of 5 mV/s, GO and SbSI exhibited specific capacitances of 57.60 F/g and 52.82 F/g, respectively. The GO-SbSI (30:70 wt.%) composite reached the highest CV-derived specific capacitance of 320 F/g, outperforming the base materials. The GCD measurements showed a different compositional dependence, demonstrating that the optimum response depended on the applied measurement conditions rather than increasing continuously with SbSI concentration, owing to synergistic effects and structural trade-offs between electronic conductivity and active surface area.

A stronger compositional effect was observed in the GSM ternary series. The optimized ternary composition, labeled as GSM 1:80:20, produced the largest CV response and reached a specific capacitance of 1200 F/g at 5 mV/s under the three-electrode testing conditions. The same electrode

retained approximately 80% of its initial capacitance after 3000 charge-discharge cycles and exhibited a comparatively favorable impedance response among the investigated GSM compositions. These results identified GSM 1:80:20 as the most effective ternary composition within the investigated concentration range.

Selected GO-SbSI 30/70 and GSM 1:80:20 materials were further evaluated in two-electrode coin-cell configurations. The GSM 1:80:20 coin cell delivered a CV-derived specific capacitance of 400 F/g at 5 mV/s, decreasing to 77.86 F/g at 100 mV/s, while its coulombic efficiency remained approximately 89- 91% during most of the 3000-cycle test before decreasing toward the end of cycling. The coin-cell impedance and kinetic analyses indicated a substantial diffusion-related contribution to charge storage.

These findings demonstrate that the electrochemical and electrical behavior of GO-SbSI and GO-SbSI-MnO_2 materials is strongly composition-dependent, and that controlled incorporation of SbSI and MnO_2 into the GO-based system can substantially modify the charge-storage performance. Among the investigated materials, GSM 1:80:20 provided the strongest overall electrochemical response and showed its ability to operate in an assembled two-electrode supercapacitor configuration.

Keywords: Supercapacitor, Graphene oxide; SbSI nanowires; MnO_2 nanostructures; GO-SbSI binary composites; GO-SbSI-MnO_2 ternary composites; Supercapacitor electrodes; Electrochemical energy storage; Coin-cell devices.

Abstrakt

Opracowanie materiałów elektrodowych charakteryzujących się dużą zdolnością do magazynowania ładunku, korzystnymi właściwościami elektrycznymi oraz stabilnymi parametrami elektrochemicznymi pozostaje istotnym wymogiem w rozwoju zaawansowanych układów superkondensatorowych. W niniejszej pracy przygotowano dwuskładnikowe kompozyty tlenku grafenu i jodosiarczku antymonu (GO-SbSI) oraz trójskładnikowe kompozyty tlenku grafenu, jodosiarczku antymonu i dwutlenku manganu (GO-SbSI-MnO_2, GSM) o różnych stężeniach w celu zbadania zależności pomiędzy składem materiału, jego właściwościami strukturalnymi i elektrycznymi oraz elektrochemicznymi właściwościami magazynowania ładunku. GO otrzymano metodą Hummersa, nanodruty SbSI zsyntetyzowano metodą sonochemiczną, natomiast nanostruktury MnO_2 otrzymano metodą hydrotermalną. Następnie kompozyty dwu- i trójskładnikowe wytworzono z zastosowaniem odpowiednio kontrolowanej metody sonochemicznej oraz połączonych metod hydrotermalnej i sonochemicznej.

Otrzymane materiały scharakteryzowano za pomocą dyfrakcji rentgenowskiej (XRD), skaningowej mikroskopii elektronowej, skaningowej mikroskopii elektronowej z emisją polową, spektroskopii rentgenowskiej z dyspersją energii (EDS), transmisyjnej mikroskopii elektronowej, rentgenowskiej spektroskopii fotoelektronów (XPS), spektroskopii w podczerwieni (FTIR), spektroskopii UV-Vis spektroskopii impedancyjnej oraz standardowych metod elektrochemicznych. Badania strukturalne i morfologiczne wykazały współistnienie płatków GO i nanodrutów SbSI w kompozytach dwuskładnikowych, natomiast materiały GSM zawierały składniki pochodzące od GO, SbSI i MnO_2, a ich morfologia i właściwości strukturalne zmieniały się w zależności od składu. Wyniki badań XRD wykazały charakterystyczne piki dyfrakcyjne pochodzące od faz krystalicznych SbSI i α-MnO_2, natomiast pomiary XPS, EDS i FTIR potwierdziły obecność oczekiwanych pierwiastków składowych oraz odpowiadających im stanów chemicznych, w szczególności potwierdzając obecność aktywnych grup funkcyjnych i określonych stopni utlenienia. Pomiary właściwości optycznych oraz elektrycznych wykazały ponadto, że zmiany składu wpływały na charakterystykę absorpcji, polaryzację, impedancję, właściwości dielektryczne oraz odpowiedź elektryczną w zmiennym polu elektrycznym.

Właściwości elektrochemiczne wyznaczono za pomocą woltamperometrii cyklicznej, galwanostatycznego ładowania i rozładowania oraz elektrochemicznej spektroskopii impedancyjnej, a także na podstawie badań stabilności cyklicznej i analizy kinetyki magazynowania ładunku. Przy szybkości skanowania wynoszącej 5 mV/s GO i SbSI wykazywały pojemności właściwe odpowiednio 57,60 F/g i 52,82 F/g. Kompozyt GO-SbSI (30:70% wag.) osiągnął najwyższą pojemność właściwą wyznaczoną na podstawie pomiarów CV, wynoszącą 320 F/g, przewyższając pod tym względem wartości dla materiałów wyjściowych. Pomiary GCD wykazały odmienną zależność od składu, wskazując, że optymalna odpowiedź zależała od zastosowanych warunków pomiarowych, a nie

wzrastała w sposób ciągły wraz ze zwiększaniem zawartości SbSI. Wynikało to z efektów synergistycznych oraz kompromisu pomiędzy przewodnictwem elektrycznym a dostępną powierzchnią aktywną, wynikającego ze zmian strukturalnych.

Wyraźniejszy wpływ składu zaobserwowano w przypadku trójskładnikowej serii GSM. Zoptymalizowany skład trójskładnikowy, oznaczony jako GSM 1:80:20, wykazywał największą odpowiedź w pomiarach CV i osiągnął pojemność właściwą 1200 F/g przy szybkości skanowania 5 mV/s w układzie trójelektrodowym. Ta sama elektroda zachowała około 80% swojej początkowej pojemności po 3000 cyklach ładowania i rozładowania oraz wykazywała stosunkowo korzystne właściwości impedancyjne na tle pozostałych badanych kompozytów GSM. Wyniki te wskazują, że GSM 1:80:20 był najefektywniejszym składem trójskładnikowym w badanym zakresie stężeń.

Wybrane materiały GO-SbSI 30/70 oraz GSM 1:80:20 poddano dalszym badaniom w dwuelektrodowych ogniwach typu coin cell. Ogniwo GSM 1:80:20 osiągnęło pojemność właściwą wyznaczoną na podstawie pomiarów CV wynoszącą 400 F/g przy szybkości skanowania 5 mV/s, która zmniejszyła się do 77,86 F/g przy 100 mV/s. Jednocześnie jego sprawność kulombowska utrzymywała się na poziomie około 89-91% przez większość testu obejmującego 3000 cykli, po czym uległa obniżeniu pod koniec badania cyklicznego. Analiza impedancyjna i kinetyczna ogniwa typu coin cell wskazała na znaczący udział procesów związanych z dyfuzją w magazynowaniu ładunku.

Uzyskane wyniki wskazują, że właściwości elektrochemiczne i elektryczne materiałów GO-SbSI oraz GO-SbSI-MnO_2 są silnie zależne oed ich składu oraz że kontrolowane wprowadzanie SbSI i MnO_2 do układu opartego na GO może w istotny sposób modyfikować właściwości magazynowania ładunku. Spośród badanych materiałów GSM 1:80:20 wykazywał najlepszą ogólną odpowiedź elektrochemiczną oraz zdolność do pracy w skonstruowanym dwuelektrodowym układzie superkondensatora.

Słowa kluczowe: superkondensator, tlenek grafenu; nanodruty SbSI; nanostruktury MnO_2; dwuskładnikowe kompozyty GO-SbSI; trójskładnikowe kompozyty GO-SbSI-MnO_2; elektrody superkondensatorów; elektrochemiczne magazynowanie energii; ogniwa typu coin cell.

Contents

Abstract ix

Abstrakt xi

LIST OF FIGURES xvii

LIST OF TABLES xxi

LIST OF SYMBOLS xxiii

LIST OF ACRONYMS xxvii

Chapter 1 1

INTRODUCTION 1

1.1 Principle Information of Supercapacitors 4

1.2 Types of Supercapacitors 6

a. Electric double-layer capacitors (EDLCs) 6

b. Pseudo-supercapacitors (PSCs) 6

c. Hybrid supercapacitors (HSCs) 6

1.2.1 Electric Double-Layer Capacitors 6

1.2.2 Pseudo-supercapacitors 9

1.2.3 Hybrid Supercapacitors 12

1.3 Components of Supercapacitors 15

1.3.1 Electrode Materials 16

1.3.2 Electrolytes 18

1.3.3 Separator 19

1.3.4 Current Collectors 20

1.3.5 Sealants 20

1.4 Motivation of the Work 21

Chapter 2 23

AIM AND OBJECTIVES 23

2.1 Aims 24

2.2 Research Objectives 25

Chapter 3 27

SYNTHESIS TECHNIQUES 27

3.1 Materials 27

3.2 Synthesis Methodology 28

3.2.1 Synthesis of Graphene Oxide 28
3.2.2 Preparation of Antimony Sulfoiodide 29
3.2.3 Preparation of Manganese Dioxide 30
3.2.4 Preparation of GO-SbSI Binary Composites 30
3.2.5 Preparation of GO-SbSI-MnO_2 Ternary Composite 32
3.2.6 Conditions 34
3.3 Sample Preparation for Characterization Testing 35
3.3.1 Fourier-Transform Infrared (FTIR) Spectroscopy 35
3.3.2 Ultraviolet-Visible (UV-Vis) Spectroscopy 35
3.3.3 Scanning Electron Microscopy (SEM) 36
3.3.4 Impedance Spectroscopy 37
3.3.5 Electrochemical measurement 37
Chapter 4 41
MORPHOLOGY AND STRUCTURAL STUDY 41
4.1 Morphology and EDS Analysis 41
4.1.1 SEM of GO 41
4.1.2 SEM of SbSI 42
4.1.3 SEM of GO-SbSI Composites 43
4.1.4 Nanowire Length Distribution of SbSI and GO-SbSI Composites 45
4.1.5 FESEM of GSM composites 46
4.1.6 Nanowire Length Distribution of GSM Composites 49
4.2 Transmission electron microscopy (TEM) 51
4.2.1 TEM of GO 52
4.2.2 TEM of SbSI 52
4.2.3 TEM of GO-SbSI Composites: 54
4.2.4 TEM of GSM 1:20:80 and GSM 1:80:20 55
4.3 X-ray Diffractometry 58
4.3.1 XRD of GO 59
4.3.2 XRD of SbSI 60
4.3.3 XRD of GO-SbSI Composites 60
4.3.4 XRD of GSM Composites 63
4.4 X-ray Photoelectron Spectroscopy 66
4.4.1 GO-SbSI composites 66
4.4.2 GSM composites 70
Chapter 5 77
OPTICAL STUDY 77

5.1.1 UV-Vis of GO 78
5.1.2 UV-Vis of SbSI 79
5.1.3 UV-Vis of GO-SbSI Composite 80
5.1.4 UV-Vis of GSM Composites 81
5.2 Fourier Transform Infrared Spectroscopy (FTIR) 85
5.2.1 FTIR of GO 85
5.2.2 FTIR of SbSI 86
5.2.3 FTIR of GO-SbSI Composites 87
5.2.4 FTIR of GSM Composites 89
Chapter 6 93
IMPEDANCE SPECTROSCOPY 93
6.1 GO, SbSI and GO-SbSI Composites 93
6.1.1 Complex Impedance and Nyquist Plot Analysis 93
6.1.2 Real and Imaginary Permittivity, Tangent Losses, and AC Conductivity 98
6.2 GSM composites 105
6.2.1 Complex Impedance and Nyquist Plot Analysis 105
6.2.2 Real and Imaginary Permittivity, Tangent Losses, and AC Conductivity 110
Chapter 7 117
ELECTROCHEMICAL STUDY 117
7.1 GO, SbSI, and GO-SbSI composites 118
7.1.1 Cyclic voltammetry of GO 118
7.1.2 Cyclic voltammetry of SbSI 119
7.1.3 Cyclic voltammetry of GO-SbSI composites 119
7.1.4 GCD testing of GO 124
7.1.5 GCD testing of SbSI 125
7.1.6 GCD testing of GO-SbSI Composites 126
7.1.7 Electrochemical Impedance Spectroscopy 130
7.1.8 Charge-storage kinetics 131
7.2 GSM Composites 134
7.2.1 Cyclic voltammetry 134
7.2.2 GCD testing 139
7.2.3 Electrochemical Impedance Spectroscopy 143
7.2.4 Charge-storage Kinetics 145
Chapter 8 147
DEVICE STUDY 147

8.1 Electrochemical testing of GO-SbSI coin cell 149
8.1.1 Cyclic Voltammetry 149
8.1.2 GCD testing 151
8.1.3 Electrochemical Impedance Spectroscopy 153
8.1.4 Charge-storage kinetics 154
8.2 Electrochemical testing of GSM coin cell 155
8.2.1 Cyclic Voltammetry 155
8.2.2 GCD testing 156
8.2.3 Electrochemical Impedance Spectroscopy 158
8.2.4 Charge-storage kinetics 159
Chapter 9 161
CONCLUSION 161
References 165

LIST OF FIGURES

Figure 1.1 Ragone plot representing the power density and energy density of energy storage devices, including capacitors, supercapacitors, rechargeable batteries, and fuel cells. 2
Figure 1.2 Number of publications from 1998 to 2025 on the topic of supercapacitors based on the Scopus database [33]. 3
Figure 1.3 Schematic illustration of a supercapacitor working. (Step 1) represents the charging mode of an SC, (Step 2) represents the fully charged mode of a SC, and (Step 3) represents the discharging mode of a SC. 4
Figure 1.4 (a) Schematic illustration of the internal structure of an EDLC [48]. (b) energy storage mechanism of EDLC, (c) current-potential characteristic of EDLC, and (d) charging-discharging behavior of an EDLC. 7
Figure 1.5 Schematic illustration of a pseudo-supercapacitor. [48]. 9
Figure 1.6 Schematic and electrochemical performance of a redox pseudocapacitor: (a) structural configuration and surface adsorption mechanism, (b) characteristic cyclic voltammetry (CV) profile for a MnO_2 system, and (c) typical GCD behavior. 11
Figure 1.7 Schematic and electrochemical performance of an intercalation pseudo- supercapacitor: (a) structural configuration and ion insertion mechanism, (b) CV profile for a Nb2O5 system, and (c) typical GCD behavior. 12
Figure 1.8 Schematic mechanism diagram of an asymmetric supercapacitor, highlighting the rapid surface charge kinetics (pseudocapacitive activity) at the anode and bulk ion dynamics (electrosorption of guest ions) at the cathode [48]. 13
Figure 1.9 Schematic representation and electrochemical characteristics of a BHSC: (a) the bulk faradaic energy storage mechanism, (b) CV profile, and (c) typical GCD profile. 15
Figure 3.1 Schematic representation of the chemical synthesis route for preparing Graphene Oxide. 28
Figure 3.2 Schematic illustration of the step-by-step synthetic procedure for preparing antimony sulfoiodide nanowires. 29
Figure 3.3 Schematic representation of the hydrothermal synthesis pathway for the preparation of MnO_2 NWs. 30
Figure 3.4 Schematic representation of (a) the ultrasonic dispersion of GO in ethanol and (b) the subsequent in situ sonochemical synthesis of the GO-SbSI nanowire nanocomposites. 31
Figure 3.5 Schematic presentation of the synthesis methodology for the GSM ternary nanocomposites, showing (a) the independent dispersion processes of GO and MnO_2 NWs in separate ethanol volumes, and (b) the subsequent in-situ interfacial coupling of the components within the SbSI precursor matrix. 33
Figure 3.6 (a) Photograph of the fabricated pellet, and (b) the pellet mounted in the FTIR PerkinElmer Spectrum One spectrometer for FTIR characterization. 35
Figure 3.7 (a) The cuvette with material dissolved in ethanol. (b) The cuvette placed in the Cary 50 Conc UV-Vis spectrometer. 36
Figure 3.8 The process of sample preparation for SEM. (a) The sample dissolution in ethanol, (b) by the drop-casting method, the coated material on silicon chips. 36
Figure 3.9 Visual presentation of the working electrode fabrication process: (a) grinding and homogenization of a SbSI paste with an agate mortar and pestle, (b) a fully homogenized GO-SbSI composite slurry variant coating the mortar walls, (c) a nickel foam current collector coated with the SbSI slurry, and (d) a nickel foam current collector coated with the GO-SbSI composite slurry variant, both showing a defined 1.0cm2 active area and an exposed metallic section for electrical testing contact. 38
Figure 4.1 SEM surface morphology of Graphene Oxide flake, highlighting the folded edges and flat basal planes indicative of successful liquid-phase chemical exfoliation. 42
Figure 4.2 SEM micrograph showcasing the morphology and structural distribution of the synthesized SbSI nanostructures. 42
Figure 4.3 The SEM micrographs showing the surface morphology of GO-SbSI composites; a) GO-SbSI 70/30, b) GO-SbSI 60/40, c) GO-SbSI 50/50, d) GO-SbSI 40/60, e) GO-SbSI 30/70, illustrating the integration of the components. 43

Figure 4.4 Nanowire size distribution histograms with corresponding Gaussian fits for a) GO-SbSI 70/30, b) GO-SbSI 60/40, c) GO-SbSI 50/50, GO-SbSI 40/60, GO-SbSI 30/70, and SbSI. 45
Figure 4.5 Scanning electron microscopy micrographs displaying the surface morphology and interlocking structure of the hybrid GSM nanocomposites; a) GSM 1:20:80, b) GSM 1:30:70, c) GSM 1:40:60, d) GSM 1:50:50, e) GSM 1:60:40, f) GSM 1:70:30, and g) GSM 1:80:20. 48
Figure 4.6 The calculated nanowire size distribution of prepared sample; a) GAM 1: 20:80, b) GSM 1:30:70, c) GSM 1:40:60, d) GSM 1:50:50, e) GSM 1:60:40, f) GSM 1:70:30, and g) GSM 1:80:20. 50
Figure 4.7 TEM micrographs revealing the morphology of synthesized graphene oxide sheets at two different regions (a and b). 52
Figure 4.8 Electron diffraction and structural characterization of the chalcohalide phase: (a) TEM micrograph of individual SbSI nanowires showing a needle-like morphology with fine surface decorations, (b) HRTEM lattice image of a single nanowire core, and (c) magnified view of the atomic fringes showing a resolved d-spacing of 0.671(15) nm matching the (110) crystallographic plane. TEM of GO-SbSI Composites: 53
Figure 4.9 TEM micrographs showing the morphological growth across the developed GO-SbSI binary composite series at a uniform 0.5 μm scale: (a) GO-SbSI 70/30, (b) GO-SbSI 60/40, (c) GO-SbSI 50/50, (d) GO-SbSI 40/60, and (e) GO-SbSI 30/70. 55
Figure 4.1 TEM and HRTEM micrographs of the GSM composite with a ratio of 1:20:80: (a) TEM image of the composite, (b) HRTEM image of the crystal lattice of a nanowire, and (c) magnified lattice fringes with the measured interplanar spacing d = 0.634(24) nm. 56
Figure 4.11 TEM and HRTEM micrographs of the GSM 1:80:20 composite: (a) TEM image of the composite, (b) HRTEM image of the selected area, and (c) magnified region marked in yellow box with the measured interplanar spacing d=0.516(14) nm. 57
Figure 4.12 XRD pattern of GO in the range of 10-60°. 59
Figure 4.13 XRD Spectra of SbSI with JCPDS card # 88-0988. 60
Figure 4.14 XRD spectra of the GO, SbSI, and GO-SbSI composites. 61
Figure 4.15 XRD peak variations due to interfacial coupling in GO, SbSI, and GO-SbSI composites. 63
Figure 4.16 XRD patterns of GMS composites (1:20:80 -1:80:20). Peaks correspond to α-MnO_2, SbSI, and GO phases in composites. 65
Figure 4.17 XPS spectra of GO-SbSI 70/30: (a) survey scan and elemental peaks of (b) C 1s, (c) O 1s-Sb 3d, (d) S 2p, and (e) I 3d. 68
Figure 4.18 XPS spectra of GO-SbSI 30:70: (a) survey scan and elemental peaks of (b) C 1s, (c) O 1s-Sb 3d, (d) S 2p, and (e) I 3d. 70
Figure 4.19 High-resolution XPS spectra of GSM 1:20:80: (a) survey spectrum, (b) Mn 2p, (c) O 1s, (d) C 1s, (e) Sb 3d, (f) S 2p, and (g) I 3d. 72
Figure 4.20 High-resolution XPS spectra of GSM 1:80:20: (a) survey spectrum, (b) Mn 2p, (c) O 1s, (d) C 1s, I Sb 3d, (f) I $3d_{5/2}$, and (g) S 2p1. 74
Figure 5.1 UV-Vis absorption spectrum of the GO showing characteristic electronic transitions in the ultraviolet and visible wavelength regions. 78
Figure 5.2 UV-Vis absorption spectrum of the SbSI showing characteristic electronic transitions in the ultraviolet and visible wavelength regions. 79
Figure 5.3 (a) The UV region spectra of GO, various ratios of GO-SbSI 70/30, - 30/70, and SbSI against absorbance. (b) The visible region spectra of GO, various ratios of GO-SbSI 70/30, - 30/70, and SbSI against absorbance. 80
Figure 5.4 Optical absorption spectra demonstrating the high-energy ultraviolet absorption features alongside a distinct visible-region shoulder, highlighting the electronic band structure modifications of the material (GSM composites). 83
Figure 5.5 FTIR spectra of GO. 86
Figure 5.6 FTIR spectrum of SbSI. 87
Figure 5.7 FTIR transmission spectra of GO, SbSI nanowires, and their corresponding GO-SbSI composites (70/30, 60/40, 50/50, 40/60, and 30/70). The highlighted vertical bars indicate characteristic functional groups and vibrational modes tracking interfacial coupling. 88

Figure 5.8 FTIR spectra of GSM 1:20:80-GSM 1:80:20. Characteristic Mn-O, Sb-S, Sb-I, and GO functional groups are observed, with intensity changes reflecting compositional tuning. 90
Figure 6.1 (a) Frequency dependence of the real part of complex impedance Z' for GO, SbSI, and the GO-SbSI binary composites with varying compositional ratios; (b) Dependance of Z' on the SbSI content for a frequency of 100 Hz. 96
Figure 6.2 Imaginary part of impedance as a function of frequency for GO, SbSI and GO-SbSI composites (70/30, 60/40, 50/50, 40/60, and 30/70). 96
Figure 6.3 Nyquist plots (Z′ vs. Z″) for GO, SbSI, and GO-SbSI composites as (70/30, 60/40, 50/50, 40/60, and 30/70). 97
Figure 6.4 (a) Frequency dependence of the real part of permittivity ε' as a function of frequency for GO, SbSI, and various GO/SbSI composites as (70/30, 60/40, 50/50, 40/60, and 30/70) composites; (b) Dependance of ε' on the SbSI content for a frequency of 100 Hz. 99
Figure 6.5 Variations of the imaginary part of permittivity versus frequency for GO, SbSI, and GO-SbSI composites (70/30, 60/40, 50/50, 40/60, and 30/70). 101
Figure 6.6 Frequency dependence of the tangent loss (tan δ) for GO, SbSI, and their various GO-SbSI composites. 103
Figure 6.7 Frequency dependence of AC electrical conductivity of GO, SbSI, GO-SbSI 70/30, GO-SbSI 60/40, GO-SbSI 50/50, GO-SbSI 40/60, and GO-SbSI 30/70. 104
Figure 6.8 Frequency dependence of the real part of impedance Z' as a function of frequency for GSM composites with various component ratios (1:20:80, 1:30:70, 1:40:60, 1:50:50, 1:60:40, 1:70:30, and 1:80:20); (b) Variation of real part of impedance (Z′) with concentration of SbSI in GSM ternary composites at 0.1 kHz. 105
Figure 6.9 Imaginary part of impedance as a function of frequency for GSM composites (1:20:80, 1:30:70, 1:40:60, 1:50:50, 1:60:40, 1:70:30, and 1:80:20). 107
Figure 6.10 Nyquist plots (Z′ vs. Z″) for GSM composites as (1:20:80, 1:30:70, 1:40:60, 1:50:50, 1:60:40, 1:70:30, and 1:80:20). 109
Figure 6.11 Frequency dependence of the real part of permittivity e as a function of frequency for GSM ternary composites (1:20:80, 1:30:70, 1:40:60, 1:50:50, 1:60:40, 1:70:30, and 1:80:20); (b) Variation of the real part of permittivity (ε′) with concentration of SbSI in GSM ternary composites at 0.1 kHz. 110
Figure 6.12 Variations of the imaginary part of permittivity (ε″) versus frequency for GSM ternary composites (1:20:80, 1:30:70, 1:40:60, 1:50:50, 1:60:40, 1:70:30, and 1:80:20). 112
Figure 6.13 Frequency dependence of the tangent loss (tan δ) for GSM ternary composites (1:20:80, 1:30:70, 1:40:60, 1:50:50, 1:60:40, 1:70:30, and 1:80:20). 114
Figure 6.14 Frequency dependence of AC electrical conductivity of GSM ternary composites (1:20:80, 1:30:70, 1:40:60, 1:50:50, 1:60:40, 1:70:30, and 1:80:20). 115
Figure 7.1 Experimental setup of the electrochemical cell employed for electrochemical characterization testing, comprising an Hg/HgO reference electrode (yellow), a platinum-wire counter electrode (red), and a working electrode (white). 117
Figure 7.2 CV curves of the GO electrode recorded at scan rates ranging from 5 to 100 mV/s. 118
Figure 7.3 CV curves of the SbSI electrode recorded at scan rates ranging from 5 to 100 mV/s. 119
Figure 7.4 Cyclic voltammetry curves of GO-SbSI composites with varying weight ratios. Comparative CV profiles recorded at different scan rates for (a) GO-SbSI 70:30, (b) GO-SbSI 60:40, (c) GO-SbSI 50:50, (d) GO-SbSI 40:60, and (e) GO-SbSI 30:70. (f) CV curves comparison at 100 mV/s among GO, SbSI, and GO-SbSI composites. 121
Figure 7.5 CV-derived specific capacitance of GO, SbSI, and GO-SbSI composite electrodes at 5 mV/s. 124
Figure 7.6 GCD curves of the GO electrode recorded at current densities ranging from 0.5 to 2.5 A/g. 125
Figure 7.7 GCD curves of the SbSI electrode recorded at current densities ranging from 0.5 to 2.5 A/g. 125
Figure 7.8 GCD curves of (a) GO-SbSI 70/30, (b) GO-SbSI 60/40, (c) GO-SbSI 50/50, (d) GO-SbSI 40/60, and (e) GO-SbSI 30/70 recorded at current densities ranging from 0.5 to 2.5 A/g. 127
Figure 7.9 Energy density and power density of GO, SbSI, and GO-SbSI electrodes at 2.5 A/g. 129
Figure 7.1 Capacitance retention of the GO-SbSI 70/30 electrode over 3000 GCD cycles. 130
Figure 7.11 Nyquist plots of (a) GO, (b) SbSI, (c) GO-SbSI 70/30, (d) GO-SbSI 60/40, (e) GO-SbSI 50/50, (f) GO-SbSI 40/60, and (g) GO-SbSI 30/70 electrodes. 131

Figure 7.12 Charge-storage kinetic analysis of the GO-SbSI composite electrodes. Dunn-method separation of surface-controlled and diffusion-controlled current contributions for (a) measured and calculated CV curve of GO-SbSI 70/30; (b) measured and calculated CV curve of GO-SbSI 30/70; (c) Estimated surface-controlled and diffusion-controlled contributions at different scan rates; (d) Cathodic peak-current density plotted against (v1/2), for V= 0.1V; the line represents the best linear fitting; (e)log (i)-log (v) plot used to determine a b-value of 0.732. 133
Figure 7.13 CV curves of (a) GSM 1:20:80, (b) GSM 1:30:70, (c) GSM 1:40:60, (d) GSM 1:50:50, (e) GSM 1:60:40, and (f) GSM 1:70:30 recorded at scan rates ranging from 5 to 100 mV/s. 135
Figure 7.14 CV curves of GSM 1:80:20 recorded at scan rates ranging from 5 to 100 mV/s. 136
Figure 7.15 CV-derived specific capacitance of the GSM electrodes at mV/s. 138
Figure 7.16 GCD curves of GSM composites (a) GSM 1:20:80, (b) GSM 1:30:70, (c) GSM 1:40:60, (d) GSM 1:50:50, (e) GSM 1:60:40, and (f) GSM 1:70:30 recorded at current densities ranging from 0.5 to 2.5 A/g. 139
Figure 7.17 GCD curves of GSM 1:80:20 recorded at current densities ranging from 0.5 to 2.5 A/g. 140
Figure 7.18 ED and PD of the GSM electrodes at 2.5 A/g. 142
Figure 7.19 Capacitance retention of GSM 1:80:20 over 3000 GCD cycles. 143
Figure 7.20 Nyquist plots of GSM 1:20:80, GSM 1:30:70, GSM 1:40:60, GSM 1:50:50, GSM 1:60:40, GSM 1:70:30, and GSM 1:80:20 electrodes. 144
Figure 7.21 Charge-storage kinetic analysis of the GSM electrodes. Dunn-method separation of surface-controlled and diffusion-controlled current contributions for (a) GSM 1:20:80 and (b) GSM 1:80:20; (c) log(i)-log(v) plot for b-value determination (b=0.7). (d) Estimated surface-controlled and diffusion-controlled contributions at different scan rates. (e, f) Peak-current density plotted against v1/2; for V = 0.1 V. 145
Figure 7.22 The degradation of the electrode tested after testing. 146
Figure 8.1 Exploded view of the coin cell consisting of a top cover (positive current collector), wave spring, spacer, composite positive electrode, Grade 392 quantitative cellulose filter-paper separator, carbon-based negative electrode, and bottom case (negative current collector). 148
Figure 8.2 Photograph of the assembled coin cell. 149
Figure 8.3 CV curves of the GO-SbSI 30/70 coin cell recorded at scan rates ranging from 5 to 100 mV/s. 150
Figure 8.4 GCD curves of the GO-SbSI 30/70 coin cell recorded at applied currents ranging from 1 to 20 mA. 151
Figure 8.5 Coulombic efficiency of the GO-SbSI 30/70 coin cell over 3000 charge-discharge cycles. 153
Figure 8.6 Nyquist plot of GO-SbSI 30/70 coin cell. 154
Figure 8.7 Charge-storage kinetic analysis of the GO-SbSI 30/70 coin cell: Dunn-method separation of surface-controlled and diffusion-controlled current contributions for (a) measured and calculated CV curve of GO-SbSI 70/30 coin cell, (b)log(i)-log(v) plot used to determine the b-value of 0.6 (c) peak-current dependence on v1/2with the corresponding linear fits, and (d) estimated surface-controlled and diffusion-controlled contributions at different scan rates. 155
Figure 8.8 CV curves of the GSM 1:80:20 coin cell recorded at different scan rates. 156
Figure 8.9 GCD curves of the GSM 1:80:20 coin cell recorded at applied current densities ranging from 1 to 25 A/g. 157
Figure 8.10 Coulombic efficiency of the GSM 1:80:20 coin cell over 3000 charge-discharge cycles. 158
Figure 8.11 Nyquist plots Z" versus Z' of (a) the GO-SbSI 30/70 coin cell and (b) the GSM 1:80:20 coin cell. 159
Figure 8.12 Charge-storage kinetic analysis of the GSM 1:80:20 coin cell: (a) estimated surface-controlled and diffusion-controlled current contributions at a selected scan rate; (b) log (i)-log(v) plot used to determine b-value of 0.49; (c) cathodic peak-current dependence on v1/2 with the corresponding linear fit; and (d) estimated surface-controlled and diffusion-controlled contributions at different scan rates. 160

LIST OF TABLES

Table 1-1	A comparison between all types of SC and their various parameters.	6
Table 1-2	Electrochemical performance parameters of various carbon-based, transition metal oxide, and composite electrode materials used in supercapacitors.	17
Table 3-1	The materials used during the synthesis process.	28
Table 3-2	Prepared samples along with the weight percentage of individual components.	31
Table 3-3	Prepared samples of GO-SbSI-MnO_2 composites along with the weight percentage of individual components.	34
Table 3-4	Thickness and area of the prepared pellets of GO, SbSI, GO-SbSI composites and GMS composites.	37
Table 4-1	Gaussian fitting parameters of SbSI nanowire length distributions and EDS-derived elemental compositions and normalized Sb:S:I shares of GO-SbSI composites and SbSI.	46
Table 4-2	Gaussian fitting parameters of SbSI nanowire length distributions and EDS-derived elemental compositions of GO/SbSI/MnO_2 composites.	51
Table 5-1	An overview of the UV-Vis peak position for all GSM sample composites and the proposed optical transition mechanisms.	84
Table 5-2	The peaks of GO-SbSI 70/30, GO-SbSI 60/40, GO-SbSI 50/50, GO-SbSI 40/60, and GO-SbSI 30/70 are presented in the table with their bonding group ranges.	89
Table 5-3	Summary of the peak positions of FTIR, the allocation of functional groups, and the origin of the underlying materials in the GSM composite series.	91
Table 6-1	Extracted fmax and τ values of GO, SbSI and GO-SbSI composites under varying weight percentage compositions.	96
Table 6-2	Observed Z'' peak frequencies and corresponding impedance relaxation times of the GSM composite with different compositional ratios.	108
Table 7-1	Electrode mass, scan rate, integrated CV area, specific capacitance, energy density, and power density of GO, SbSI, and GO-SbSI composite electrodes.	122
Table 7-2	Specific capacitance, energy density, and power density of GO, SbSI, and GO-SbSI composite electrodes calculated from GCD measurements at different current densities.	128
Table 7-3	Electrode mass, scan rate, integrated CV area, specific capacitance, energy density, and power density of the GSM electrodes.	136
Table 7-4	Electrode mass, current density, discharge time, specific capacitance, energy density, and power density of the GSM electrodes calculated from GCD measurements.	141
Table 8-1	Scan rate, electrode mass, integrated CV area, specific capacitance, energy density, and power density of the GO-SbSI 30/70 coin cell.	150
Table 8-2	Current density, discharge time, specific capacitance, energy density, and power density of the GO-SbSI 30/70 coin cell calculated from GCD measurements.	152
Table 8-3	Scan rate, electrode mass, integrated CV area, specific capacitance, energy density, and power density of the GSM 1:80:20 coin cell.	156
Table 8-4	Current density, discharge time, specific capacitance, energy density, and power density of the GSM 1:80:20 coin cell calculated from GCD measurements.	158

LIST OF SYMBOLS

Electrochemical and energy storage symbols

Symbol	Meaning / Definition	Unit / Remarks
A	Electrode or sample surface area.	m^2 or cm^2, context dependent
a	Power-law proportionality constant in $I = av^b$.	Context-dependent
b	Power-law exponent used to assess charge-storage kinetics.	Dimensionless
C	Capacitance.	F
C_s	Specific capacitance.	F/g
C_{dl}	Total electric double-layer capacitance.	F
C_H	Helmholtz-layer capacitance.	F
C_{diff}	Diffuse-layer capacitance.	F
C'	Real part of the complex capacitance.	F
C''	Imaginary part of the complex capacitance.	F
E	Electrode/electrochemical potential.	V
E^0	Reference or standard electrode potential in the Nernst expression.	V
E_D	Energy density, denoted ED in tables and text.	Wh/kg
E_S	Specific-energy term appearing in Equation 1.3 of the thesis.	Wh/kg
F	Faraday constant.	C/mol
I	Electrical current; also used as peak/current term in the power-law relation.	A
i	Measured electrochemical current.	A
$i(V)$	Current measured at a selected potential V in the Dunn analysis.	A
k_1	Dunn-method constant associated with the surface-controlled current contribution.	Units depend on the form of the fitted equation
k_2	Dunn-method constant associated with the diffusion-controlled current contribution.	Units depend on the form of the fitted equation
m	Mass of active/deposited electrode material.	g or kg

n *(Nernst)*	Number of participating electrons in the Nernst-type expression.	Dimensionless
P_D	Power density, denoted PD in tables and text.	W/kg
Q	Charge/reaction term used in the Nernst expression; the thesis relates Q to stored charge.	Context-dependent
R	Universal gas constant.	J mol^{-1} K^{-1}
R_{ESR}	Equivalent series resistance of the device.	Ω
R_{ct}	Charge-transfer resistance at the electrode/electrolyte interface.	Ω
R^2	Coefficient of determination used for fitting/kinetic analysis.	Dimensionless
t	Time.	s
t_D	Discharge time.	s
T	Absolute temperature.	K
v	Cyclic-voltammetry scan rate.	mV/s or V/s
$v^{1/2}$	Square root of scan rate, used in diffusion/peak-current analysis.	$(V/s)^{1/2}$ or corresponding scan-rate unit
V	Voltage/potential; also the potential window where specified.	V
V_{max}	Maximum operating voltage.	V
X	Fractional surface coverage of ions on the active-material surface.	Dimensionless
z	Charge/electron-number term used in Equation 1.6.	Dimensionless
ΔV^+	Positive-electrode potential range.	V
ΔV^-	Negative-electrode potential range.	V
ΔV	Total cell operating-voltage window.	V

Crystallographic and structural symbols

d (XRD/HRTEM)	Interplanar spacing between adjacent crystal planes/lattice fringes.	nm or Å
D	Apparent crystallite/coherent diffraction-domain size calculated using the Scherrer relation.	nm
(hkl)	Miller indices identifying crystallographic planes.	Dimensionless
Kα	Characteristic K-alpha X-ray radiation line (e.g., Cu Kα or Al Kα).	Radiation designation

n (Bragg)	Diffraction order in Bragg's law.	Dimensionless
2θ	Measured diffraction angle in an XRD pattern.	degree (°)
θ	Bragg angle.	degree (°) or rad
λ	X-ray wavelength.	Å or nm
β	Full width at half maximum (FWHM) used in the Scherrer equation.	rad
α	Alpha-phase designation, used for α-MnO_2.	Phase notation

Impedance, dielectric and relaxation symbols

M'	Real part of the electric modulus.	Dimensionless
M''	Imaginary part of the electric modulus.	Dimensionless
Z'	Real part of complex impedance.	Ω
Z''	Imaginary part of complex impedance.	Ω
ε_0	Permittivity of free space (vacuum permittivity).	F/m
ε_r	Relative permittivity of the electrolyte in the Helmholtz model.	Dimensionless
ε'	Real part of relative permittivity (dielectric constant).	Dimensionless
ε''	Imaginary part of relative permittivity (dielectric loss).	Dimensionless
$tan\ \delta$	Dielectric loss tangent.	Dimensionless
Δ	Dielectric loss angle used in tan δ.	rad or dimensionless angle notation
Σ	Electrical conductivity.	S/m; S/cm is also reported in the GSM discussion
σ_{ac}	AC electrical conductivity.	S/m or S/cm, according to the plotted dataset
T	Electrical/dielectric relaxation time.	s, ms, or μs
F	Frequency of the applied alternating field.	Hz
f_{max}	Frequency at the maximum of the relaxation response.	Hz
Ω	Angular frequency, defined as ω = 2πf.	rad/s
Π	Mathematical constant pi in angular-frequency and relaxation equations.	Dimensionless

Optical, statistical and general scientific notation

$\pi \rightarrow \pi^*$	Electronic transition from a bonding π orbital to an antibonding π* orbital.	Optical-transition notation

$n \rightarrow \pi^*$	Electronic transition from a non-bonding orbital to an antibonding π* orbital.	Optical-transition notation
π^*	Antibonding pi orbital.	Orbital notation
sp^2	sp^2 hybridization state of carbon.	Hybridization notation
sp^3	sp^3 hybridization state of carbon.	Hybridization notation
Mn^{3+}/Mn^{4+}	Manganese oxidation states referred to in the optical/electrical discussion.	Oxidation-state notation
μ	Micro prefix, 10^{-6}; used in μm and μs.	SI prefix
Ω	Ohm, unit of electrical resistance/impedance.	SI derived unit
$\mathring{A}$	Angstrom, 10^{-10} m; used for X-ray wavelength/interplanar distance notation.	Length unit
∘	Degree symbol used for diffraction angles, temperatures, and phase angles.	Angle/temperature notation
±	Plus-minus symbol used to express uncertainty or variation.	Mathematical notation
≈	Approximately equal to.	Mathematical notation
≤	Less than or equal to.	Mathematical notation
×	Multiplication sign; also used in scientific notation.	Mathematical notation
%	Percent.	Dimensionless percentage
at.%	Atomic percent used in EDS/elemental-composition tables.	Composition notation
wt.%	Weight percent used for composite compositions.	Composition notation
ln	Natural logarithm used in the Nernst-type equations.	Mathematical operator
sin	Sine function used in Bragg's law.	Mathematical operator
cos	Cosine function used in the Scherrer equation.	Mathematical operator
tan	Tangent function used in dielectric-loss notation.	Mathematical operator

LIST OF ACRONYMS

AC	Activated carbon
ACN	Acetonitrile
ASC	Asymmetric supercapacitor
BHSC	Battery-type hybrid supercapacitor
CIS	Complex impedance spectroscopy
CNT	Carbon nanotube
CP	Conducting polymer
Cs	Specific capacitance
CV	Cyclic voltammetry
E_D	Energy density
EDLC	Electric double-layer capacitor
EDS	Energy-dispersive X-ray spectroscopy
EIS	Electrochemical impedance spectroscopy
EMIM	1-Ethyl-3-methylimidazolium
EMRG	Energy Materials Research Group
ESR	Equivalent series resistance
FESEM	Field-emission scanning electron microscopy
FTIR	Fourier-transform infrared spectroscopy
FWHM	Full width at half maximum
GCD	Galvanostatic charge-discharge
GO	Graphene oxide
GO-SbSI	Graphene oxide-SbSI binary composite
GSM	GO-SbSI-MnO_2
HRTEM	High-resolution transmission electron microscopy
HSC	Hybrid supercapacitor
JCPDS	Joint Committee on Powder Diffraction Standards
LiTFSI	Lithium bis(trifluoromethanesulfonyl)imide
MOF	Metal-organic framework
MOx	Metal oxide(s)
NMP	N-methyl-2-pyrrolidone
NW / NWs	Nanowire / nanowires
PAA	Polyacrylic acid
PANI	Polyaniline
P_D	Power density

PE	Polyethylene
PEO	Polyethylene oxide
PP	Polypropylene
PPy	Polypyrrole
PSC	Pseudo-supercapacitor
PTFE	Polytetrafluoroethylene
PTh	Polythiophene
PVA	Polyvinyl alcohol
PVB	Polyvinyl butyral
PVC	Polyvinyl chloride
PVDF	Polyvinylidene fluoride
rGO	Reduced graphene oxide
SC / SCs	Supercapacitor/supercapacitors
SEM	Scanning electron microscopy
SSC	Symmetric hybrid supercapacitor
$TBAPF_6$	Tetrabutylammonium hexafluorophosphate
$TEABF_4$	Tetraethylammonium tetrafluoroborate
TEM	Transmission electron microscopy
TFSI	Bis(trifluoromethanesulfonyl)imide
TMO	Transition-metal oxide
UHV	Ultra-high vacuum
UPD	Underpotential deposition
UV-Vis	Ultraviolet-visible spectroscopy
XPS	X-ray photoelectron spectroscopy
XRD	X-ray diffraction

Chapter 1

INTRODUCTION

Modern technological development is strongly connected with electrical energy resources. The increasing energy demand is mainly related to two categories of systems: personal electronic devices such as multimedia devices [1], automotive [2], laptops [3], and computers [4], as well as industrial systems. This growing demand can be supported through renewable energy resources. To date, renewable energy systems [5] mainly include wind turbines [6], geothermal installations [7], biofuel-derived energy [8], hydroelectric power [9], photovoltaic solar modules [10], and wave-based generators [11]. These systems play an important role in electricity generation. However, their performance is strongly affected by geographical and environmental conditions. For example, wind and solar systems depend on weather conditions, hydroelectric systems are affected by landscape and water availability, and wave-based systems can be influenced by changes in coastal regions caused by human activities. Because of these limitations, renewable energy sources cannot always provide stable and continuous electricity generation. Therefore, modern energy systems require efficient energy storage technologies that can reduce fluctuations and provide reliable energy output over extended durations.

Generally, electricity storage technologies are divided into four major categories: electrochemical [12], chemical [13], mechanical [14], and purely electrical systems [15]. Electrochemical energy storage systems such as lithium-ion batteries, supercapacitors, and lead-acid batteries operate through charge accumulation and charge transfer processes. During these processes, the system stores or releases electrical energy by converting it into chemical energy and vice versa. Chemical energy storage systems, such as hydrogen storage, biofuels, and fossil fuels, store energy in the form of chemical bonding energy. Mechanical systems, such as electric generators and water dams, operate using kinetic and potential energy. In contrast, electrical systems store energy directly through dielectric, magnetic, or superconducting fields.

Each energy storage device possesses unique operational properties that determine its practical applications. Two important parameters are power density P_D and energy density E_D. Power density describes how fast a material can charge or discharge, while energy density describes how much energy can be stored or delivered from the material. The relationship between these two parameters is commonly represented through a Ragone plot [16] presented in Figure 1.1.

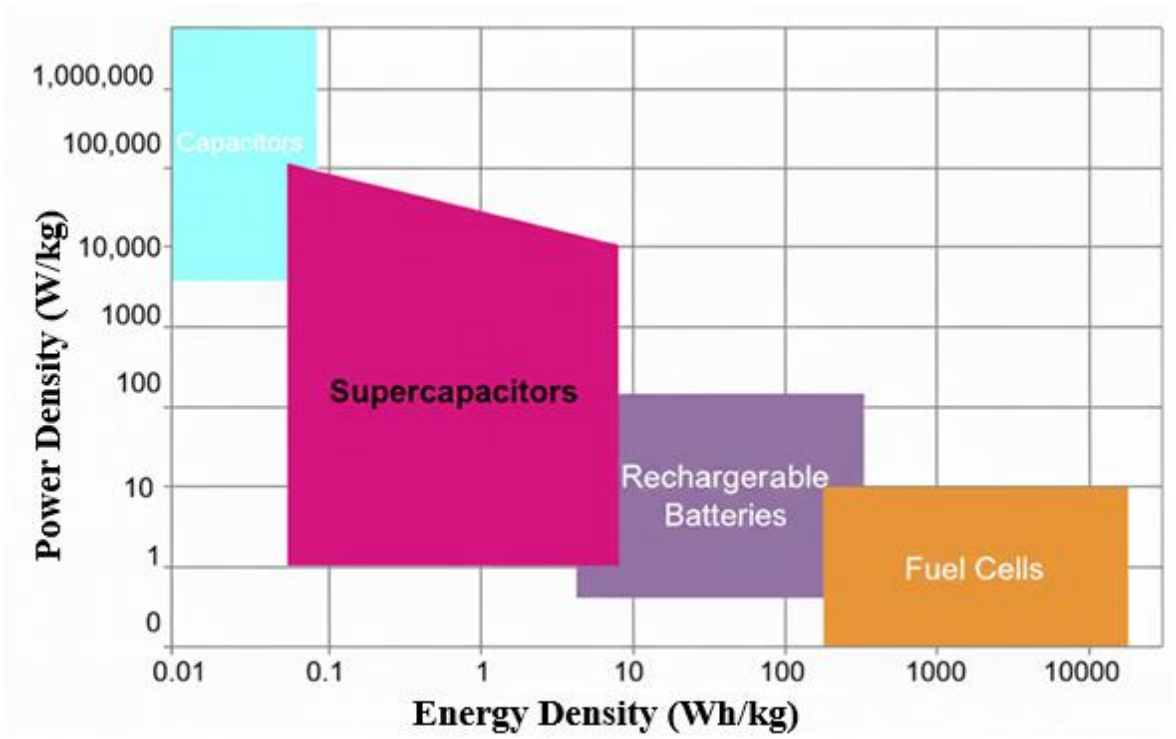


Figure 1.1: Ragone plot representing the power density and energy density of energy storage devices, including capacitors, supercapacitors, rechargeable batteries, and fuel cells.

This plot is widely used to compare the electrochemical performance of different energy storage devices, including capacitors, supercapacitors (SCs), batteries, and fuel cells. The plot demonstrates that capacitors possess very high power density but low E_D. Their power density ranges from 500 to 10^6 W/kg, while their energy density ranges from 0.01 to 0.1 Wh/kg. Supercapacitors can deliver power density in the range of 1 to 10^5 W/kg and energy density between 0.08 and 10 Wh/kg. The high power density of SCs indicates their fast charging and discharging capability, which can occur within seconds or minutes. Batteries can deliver power density between 0.5 and 100 W/kg and energy density between 5 and 150 Wh/kg. Their charging and discharging processes generally require minutes to hours. Therefore, batteries are more suitable for long-term energy storage applications, whereas SCs are more suitable for applications requiring rapid charge and discharge performance. Fuel cells exhibit power density in the range of 0-5 W/kg and energy density between 130 and 12000 Wh/kg.

Rechargeable lithium-ion batteries have dominated the energy storage market for nearly two decades and are widely used in portable electronic devices [17] and electric mobility applications [18]. Although these batteries provide relatively high energy density and are suitable for long-distance energy supply [19], their electrode materials still face limitations related to specific power, rapid charge-discharge capability, and cycle life [20, 21]. Fuel cells are also theoretically capable of

supplying energy and power for vehicle electrification, but their practical applications are limited by low efficiency, high cost, and operational complexity [22, 23].

Capacitors are widely used to filter signal noise and stabilize voltage in electronic power supplies. In comparison, supercapacitors (SCs) can bridge the gap between conventional dielectric capacitors and rechargeable batteries because they provide high power density together with moderate energy density. In batteries, energy storage mainly depends on bulk chemical charge-transfer reactions, whereas SCs store energy through electrostatic charge accumulation or fast reversible faradaic reactions at the electrode-electrolyte interface [24]. Due to these charge-storage mechanisms, SCs show rapid charging and discharging, long cycle life, good cyclic stability, and the ability to meet sudden power requirements during vehicle start-up. Therefore, they are useful for backup power supplies [25, 26], load-leveling systems [27], regenerative braking systems [28, 29], and electronic devices [30, 31]. SCs are also used in rail and tram systems, where SC modules combined with traction motors or combustion engines can improve braking efficiency and stabilize power delivery under changing track conditions [32]. This arrangement can reduce fuel consumption, decrease the load on the primary power source, and control sudden power peaks during rail transport. Because of these advantages and their important role in modern energy-storage systems, research interest in SCs has increased considerably during the last decade, as shown in Figure 1.2.

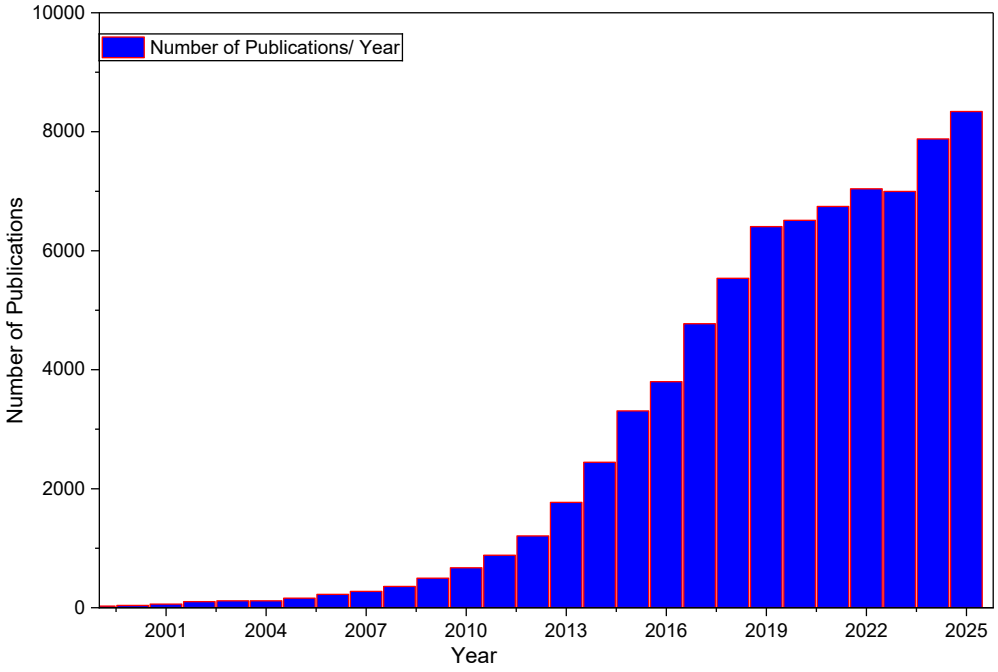


Figure 1.2: Number of publications from 1998 to 2025 on the topic of supercapacitors based on the Scopus database [33].

1.1 Principle Information of Supercapacitors

Supercapacitors, also known as ultracapacitors, are energy storage devices capable of delivering high power density and moderate energy density compared with conventional capacitors. The term “supercapacitor” was first introduced in a General Electric patent in 1957 [34], and later SOHIO Corporation patented the device during the 1960s and 1970s [35, 36]. After this development, several manufacturers such as ECOND (Russia), NEC, and Panasonic (Japan) contributed to the advancement of SC technology. Later, during the 1990s, Maxwell developed an SC with a power density of 20 kW/kg under the Department of Energy ultracapacitor program [37]. Similarly, the European company Batscap (now Blue Solutions) also developed devices with comparable performance. Nowadays, many companies, including Maxwell, JM Energy, Blue Solutions, Yunasko, Nesscap, and Ioxus, are involved in the production of SC devices.

The schematic illustration of an SC is presented in Figure 1.3. A typical SC consists of two electrodes, a separator, and an electrolyte. The separator acts as a membrane that allows ions to pass through while preventing direct electrical contact between the electrodes. In the SC system, the electrolyte connects both electrodes through ion movement across the separator.

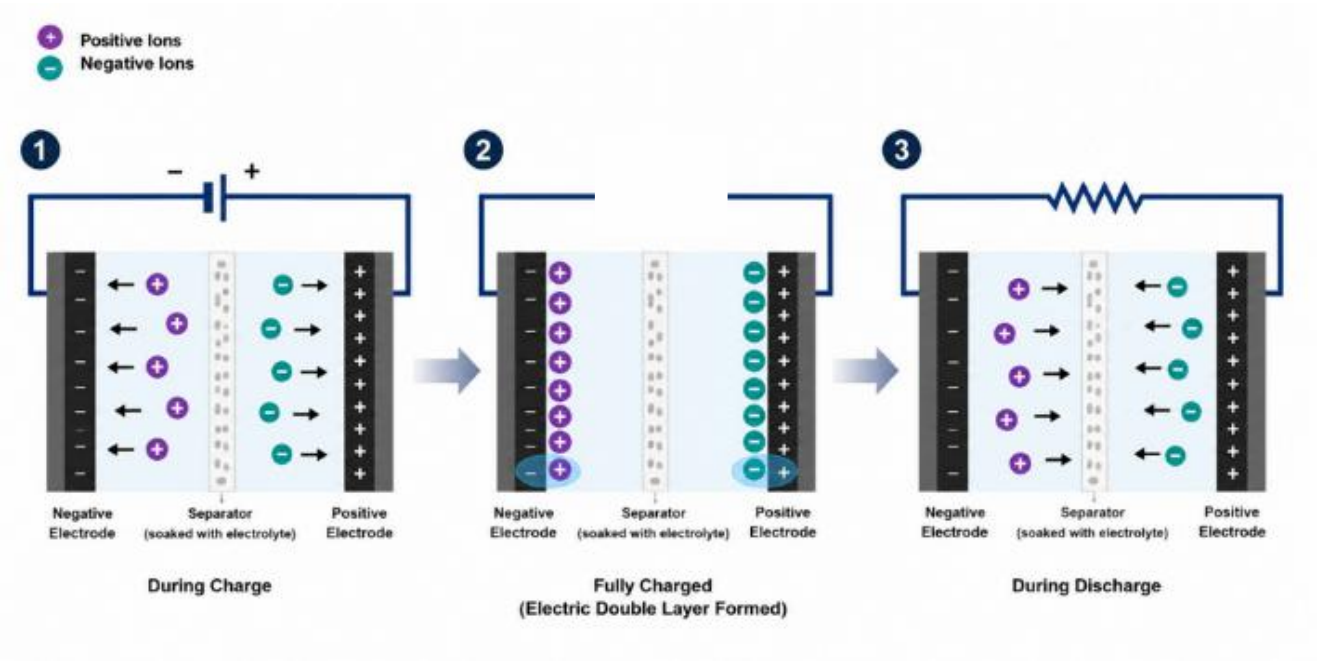


Figure 1.3: Schematic illustration of a supercapacitor working. (Step 1) represents the charging mode of an SC, (Step 2) represents the fully charged mode of an SC, and (Step 3) represents the discharging mode of an SC.

When a potential is applied during the charging process (Step 1 in Figure 1.3), negatively charged electrolyte ions move toward the positively charged electrode, while positively charged ions

move toward the negatively charged electrode. As these ions gather at the opposite electrodes (Step 2 in Figure 1.3), an electric double layer is formed at the electrode-electrolyte interface to balance the surface charge, putting the SC into charging mode. During discharge (Step 3 in Figure 1.3), ion detachment is observed as ions are displaced from the electrodes and move back toward the separator to move freely.

In addition to electrostatic charge accumulation, some ions may also participate in fast reversible faradaic reactions depending on the electrode material, contributing pseudo-capacitance to the total device capacitance. When metal oxides function as the negative electrode, a faradaic reduction reaction takes place during charging, where the active material accepts electrons and shifts to lower valence states. To balance this transfer, charge storage can proceed through multiple mechanisms; predominantly, a cation from the electrolyte chemisorbs on the electrode surface, which facilitates a rapid charging-discharging process and balances the redox state.

For a typical supercapacitor, the energy density and power density mainly depend on capacitance, operating voltage, and internal resistance. The capacitance per unit mass is called specific capacitance. C_S and can be expressed as [38]:

$$\boldsymbol{C_S = \frac{I \int V dt}{2\, m V^2}} \qquad \textit{(1-1)}$$

where: I is the current flow through the electrodes, V is the potential window, t is the time, and m is the mass of the deposited electrode. The potential window V shows the range of applied voltage over which the electrode can operate. The energy density E_D and maximum power density P_D of the SC can be expressed as [38, 39]:

$$\boldsymbol{E_D = \frac{1}{2\times 3.6} C_S V^2} \qquad \textit{(1-2)}$$

and

$$\boldsymbol{P_D = \frac{{V_{max}}^2}{R_{ESR}} = \frac{E_S \times 3.6}{t_D}} \qquad \textit{(1-3)}$$

where V_{max} is the maximum operating voltage, R_{ESR} - the equivalent series resistance of the device, and t_D - the discharge time. The constant multiplier of 3.6 is incorporated into these equations as a unit conversion factor to express the energy density in standard Watt-hours per kilogram (Wh/kg) rather than Joules per gram (J/g). These relationships indicate that the electrochemical performance of SCs mainly depends on three key parameters: high specific capacitance, wide operating voltage window, and low internal resistance. Therefore, the design of high-performance SCs mainly focuses on developing high-capacitance electrode materials, wider operating voltage electrolytes, and low-

resistance device configurations. To achieve these goals, several strategies are commonly used, including construction of porous structures, defect engineering, hybrid material fabrication, and the exploration of new electrode materials.

Generally, SC electrodes are fabricated using materials selected for their distinct charge-storage mechanisms and structural properties, such as high-surface-area carbon [40] and porous carbon-derived materials [41], pseudocapacitive transition metal oxides [42], and redox-active conductive polymers [43, 44] that facilitate faradaic charge transfer. The electrochemical performance of SCs is also strongly influenced by the electrolyte because its ions participate directly in the charge storage process.

1.2 Types of Supercapacitors

Supercapacitors (SCs) are mainly divided into three major categories:

a. **Electric double-layer capacitors (EDLCs)**

b. **Pseudo-supercapacitors (PSCs)**

c. **Hybrid supercapacitors (HSCs)**

A comparative summary of different SC types, including their energy density, power density, cyclic stability, and applications, is presented in Table 1.1.

Table 1-1: A comparison between all types of SC and their various parameters.

SC Type	Active Materials	C_s $(\frac{F}{g})$	P_D (W/kg)	E_D (Wh/kg)	Cycling Stability (%)	Applications
EDLC	Carbon and its derivatives	11.25-174 [45]	1000-10000 [46]	2-10 [47]	92-100 [45]	High power application (regenerative braking)
PS	MO_x CP	60-1280 [45]	50-4000 [47]	15-60 [47]	67-98 [45]	Portable electronics, Renewable energy System
HSC	Mixed (PC, MO_x, and CP)	258-2377 [45]	250-Higher values [47]	15-250 [47]	75-99 [45]	Diverse applications (balance b/w E_D and P_D)

1.2.1 Electric Double-Layer Capacitors

Figure 1.4a presents the construction of the EDLC supercapacitor connected to an external power system. The device consists of two porous electrodes, current collectors, an electrolyte, and a separator. During charging, the external power-supply unit transfers electrons from the positive electrode to the negative electrode through the external circuit. As a result, cations and anions in the electrolyte move towards the oppositely charged electrode surfaces and form electrical double layers.

The separator prevents direct electrical contact and short-circuiting between the electrodes, while allowing electrolyte ions to pass through. During discharging, the ions move away from the electrode surfaces, and the stored electrons flow through the external circuit to supply electrical energy to the connected load or grid. In an EDLC, represented by a nanocarbon electrode, electrolyte ions accumulate electrostatically at the electrode surface without bulk intercalation into the material or chemical reactions (Figure 1.4 b). In Figure 1.4b, the geometric shapes distinguish between the different types of ionic species present in the electrolyte solution. The green diamonds represent the counter-ions (specifically anions, given the positive charge on the electrode surface) that aggregate near the interface to form the compact Helmholtz and diffuse layers. Meanwhile, the orange circles represent the co-ions (cations) which are electrostatically repelled by the positively charged electrode and remain randomly dispersed throughout the bulk electrolyte. This rapid and reversible surface adsorption produces a nearly rectangular CV curve (Figure 1.4 c) and an approximately symmetrical triangular galvanostatic charge-discharge (GCD) profile (Figure 1.4 d). Therefore, EDLC behavior is distinguished by non-faradaic charge storage, rapid charge-discharge capability, and minimal changes in the electrode structure.

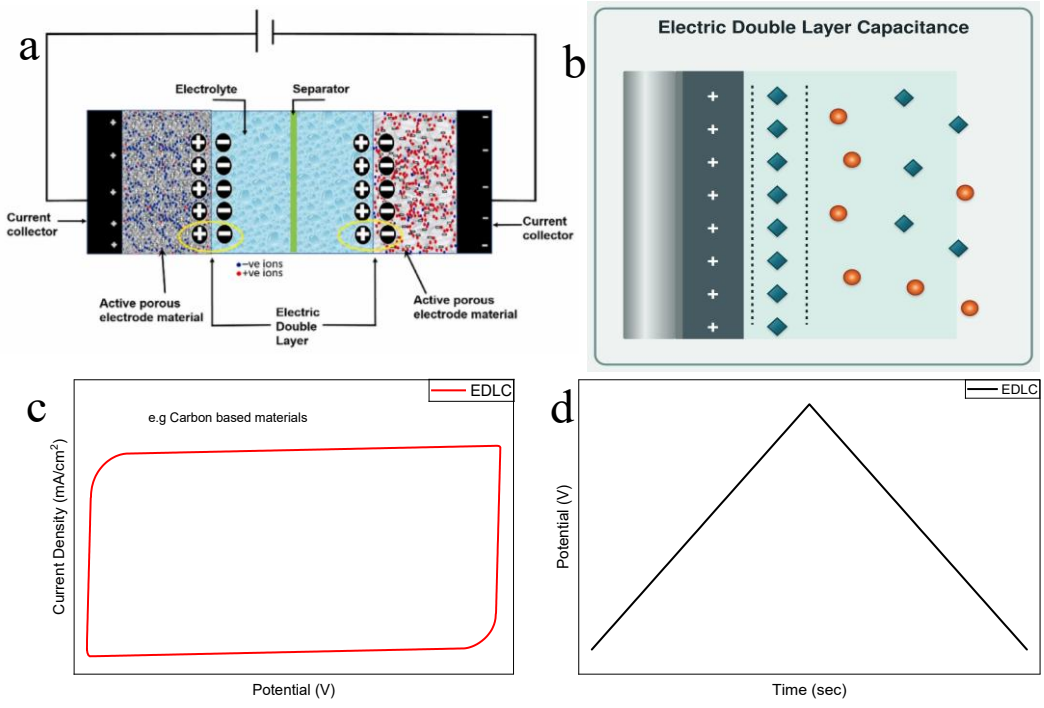


Figure 1.4: (a) Schematic illustration of the internal structure of an EDLC [48]. (b) energy storage mechanism of EDLC, (c) current-potential characteristic of EDLC, and (d) charging-discharging behavior of an EDLC.

Since charge storage in EDLCs mainly occurs at the interface, the capacitance directly depends on the active surface area of the electrode [49]. Therefore, materials with high surface area and good

electrical conductivity, such as carbon materials and their derivatives (carbon nanotubes (CNTs)) [50], activated carbon [51], and graphene [52], are widely used as electrodes in EDLCs.

The Helmholtz model, proposed in 1853 [53, 54], serves as the foundational framework to explain the arrangement of charges at the electrode-electrolyte interface. While subsequent models have refined this theory to account for ion diffusion and thermal agitation, the Helmholtz model remains a simplified conceptual model that introduces the basic parallel-plate mechanics of charge separation, though it fails to account for dynamic factors like ion mobility and potential distribution within the electrolyte. According to this model, opposite charges accumulate at the interface and remain separated by a very small atomic-scale distance, similar to the behavior of a parallel-plate capacitor. The model assumes that oppositely charged ions form a rigid layer near the electrode surface to neutralize the electrode charge. The capacitance of the system can be expressed as:

$$\boldsymbol{C = \frac{\varepsilon_0 \varepsilon_r A}{d}} \qquad \textit{(1-4)}$$

where A represents the electrode surface area, d is the separation distance between charges, ε_0 is the permittivity of vacuum, and εr is the relative permittivity of the electrolyte.

The Gouy-Chapman model [55] provides a more detailed explanation of the electric double layer. According to this model, oppositely charged ions are not rigidly attached to the electrode surface. Instead, the ions are distributed within the surrounding electrolyte and remain in continuous motion. This model describes a diffuse layer of ions in continuous motion, resulting in EDLC capacitance that varies with voltage and concentration [55]. Compared with the Helmholtz model, the Gouy-Chapman model provides a more realistic interpretation of the double-layer structure and a more accurate estimate of double-layer thickness [56].

Later, Stern [57] further improved this theory by considering the finite size of ions. He explained that ions cannot approach the electrode surface indefinitely because of their physical dimensions. The Stern model combines the concepts of both the Helmholtz and Gouy-Chapman models. Specifically, the Stern model divides the interface into two main regions: a compact layer (also called the Stern layer) and a diffuse layer. The compact layer sits directly adjacent to the electrode surface and is bounded by the inner Helmholtz plane (comprising specifically adsorbed desolvated ions) and the outer Helmholtz plane (comprising solvated ions at their closest distance of approach). Beyond this compact boundary lies the diffuse layer, where ions are distributed according to thermal motion and electrostatic forces as proposed in the Gouy-Chapman model [56]. While the Helmholtz model completely neglects thermal motion and the Gouy-Chapman model treats ions as point charges-leading to an unphysical overestimation of capacitance at high voltages-the Stern model resolves these limitations by accounting for the physical size of the ions. Mathematically, this alters the capacitance

formula by treating the total double-layer capacitance (C_{dl}) as a series combination of the compact Helmholtz layer capacitance (C_H) and the diffuse layer capacitance (C_{diff}):

$$\frac{1}{C_{dl}} = \frac{1}{C_H} + \frac{1}{C_{diff}} \qquad (1\text{-}5)$$

Consequently, this reciprocal relationship ensures that the total capacitance is constrained by the smaller value of the two layers, correcting the overestimation flaw of the point-charge assumption. Because of this correction, the Gouy-Chapman-Stern framework serves as the primary theoretical baseline for understanding interfacial capacitance, although modern experimental characterization often requires advanced modifications to account for pore geometry, ion-solvent interactions, and non-ideal capacitive behaviors.

1.2.2 **Pseudo-supercapacitors**

PSCs store energy through faradaic reactions occurring at the electrode-electrolyte interface and within the near-surface bulk of the material via intercalation. These reactions involve the transfer of electrons between the electrode material and electrolyte through reversible oxidation and reduction processes. When an external potential is applied, the mobile ions already present inside the electrolyte migrate toward the oppositely charged electrodes. Upon reaching the interface, these ions undergo fast redox reactions with the active materials-such as transition metal oxides, chalcogenides, or conducting polymers- to enable charge transfer.

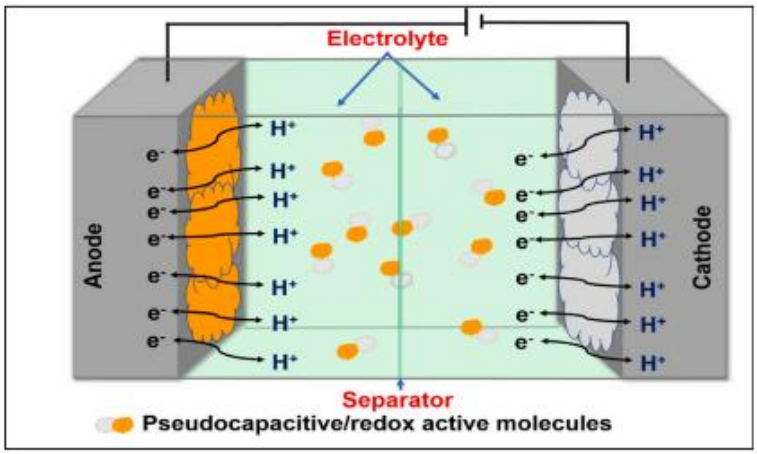


***Figure 1.5: Schematic illustration of a pseudo-supercapacitor**. [48].*

Figure 1.5 shows the working mechanism of a PSC, where electrochemically active materials are used at both electrodes. The orange and white coatings represent pseudocapacitive materials, such as conducting polymers or transition metal oxides, while the dots represent redox-active molecules. During charging, electrolyte cations (such as H^+, Li^+, or Na^+ migrate based on electrode polarity; as shown in the diagram, ions desorb from the anode (left) and move into the electrolyte, while ions in

the electrolyte move toward and insert into the cathode surface (right). Meanwhile, electrons pass through the external circuit. The charge is stored through fast and reversible oxidation-reduction reactions between these electrolyte ions and the active electrode materials. These reactions occur either through surface ion adsorption with faradaic electron transfer or through the fast insertion (intercalation) of ions into the surface and near-surface regions of the electrodes. During discharge, these reactions take place in the reverse direction: ions return to their initial states, and electrons flow backward through the external circuit to power a load.

Three primary mechanisms contribute to pseudocapacitance:

a. ***Underpotential deposition (UPD):*** This mechanism occurs [58] when metal cations deposit onto a foreign, distinct metal substrate; in this mechanism, electrochemical adsorption occurs at a potential higher than the Nernst redox potential, resulting in the formation of a monolayer of metal ions on a different metal surface.

b. ***Redox pseudocapacitance:*** This process (Figure 1.6a) occurs [59] when electrolyte ions interact directly with the surface or near-surface regions of transition metal oxides or conducting polymers; in this process, reversible electrochemical reactions occur near the electrode surface, where ions are adsorbed, and charge transfer takes place.

c. ***Intercalation pseudocapacitance:*** This mechanism (Figure 1.7a) occurs [59] when electrolyte ions penetrate beyond the outer surface into the internal tunnels or layers of a bulk host structure; this mechanism involves the insertion of ions into layered redox-active materials without causing phase transformation, while maintaining rapid charge-transfer kinetics.

These mechanisms involve reversible ion adsorption or ion intercalation into active material. As a result, a direct relationship exists between stored charge Q and electrode potential E. This relationship is commonly explained using the Nernst equation [60]:

$$\boldsymbol{E = E^0 - \frac{RT}{zF} ln(Q)} \qquad \textit{(1-6)}$$

and in the form of electrode charge.

$$\boldsymbol{E \approx E^0 - \frac{RT}{nF} ln\left(\frac{X}{1-X}\right)} \qquad \textit{(1-7)}$$

where E^0 represents the standard electrode potential, R is the universal gas constant (R=8.314 J mol^{-1} K^{-1}), T is the absolute temperature in Kelvin, n represents the number of participating electrons, F is the Faraday constant (approximated as F=96485.3321 C mol^{-1} for standard calculations), and X represents the fractional surface coverage of ions on the active material surface.

The electrochemical behavior of a surface redox pseudocapacitor is illustrated through the CV response in Fig. 1.6b. It involves rapid and reversible faradaic reactions at or near the electrode surface. To illustrate this concept, a manganese dioxide MnO_2 electrode operating in a sodium-based electrolyte serves as a classic model system. In this illustrated system, Na^+ ions undergo rapid surface adsorption and desorption at the interface while electrons are transferred through changes in the oxidation state of Mn between the Mn^{4+} and Mn^{3+} states.

For surface redox pseudocapacitive materials, the CV curve (Figure 1.6 b) retains a broad, nearly rectangular form, although some deviation appears because of the redox contribution. The corresponding GCD profile (Figure 1.6 c) is also nonlinear compared with the strictly triangular EDLC curve, reflecting the voltage-dependent nature of the faradaic charge-storage process.

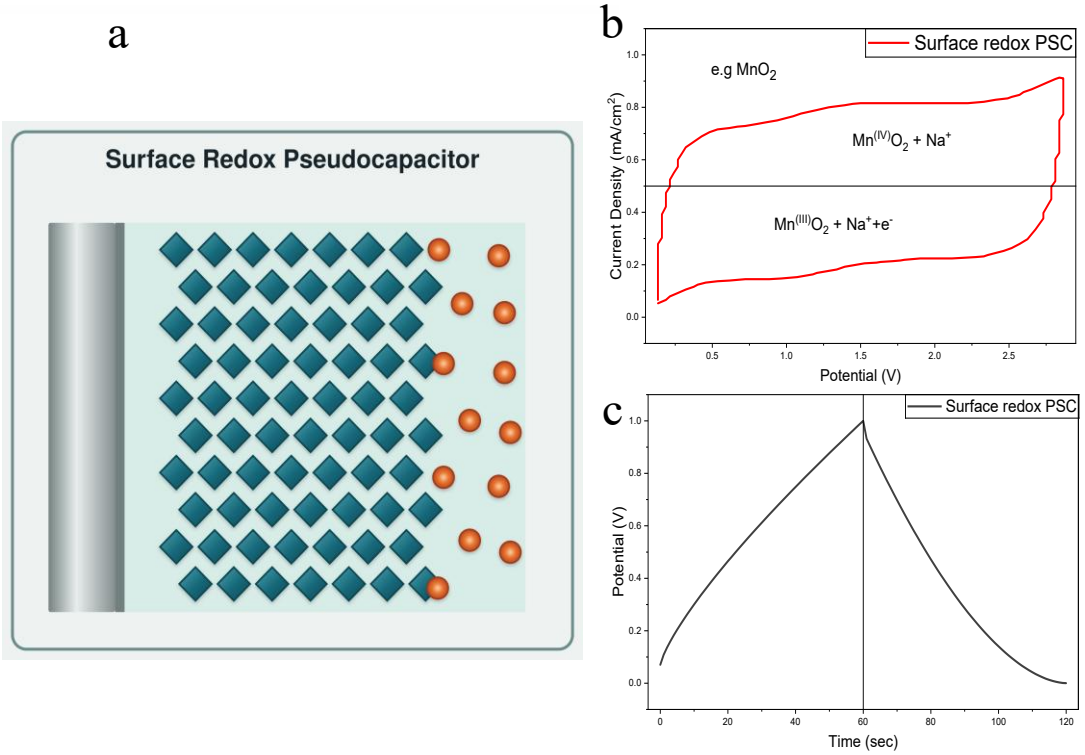


Figure 1.6: Schematic and electrochemical performance of a redox pseudocapacitor: (a) structural configuration and surface adsorption mechanism, (b) characteristic cyclic voltammetry (CV) profile for a MnO_2 system, and (c) typical GCD behavior.

Intercalation pseudocapacitance occurs when guest ions rapidly enter and leave suitable sites within the electrode structure without producing a major phase transformation. As shown schematically in Figure 1.7a, working electrolyte cations (such as Li^+ or Na^+) insert directly into the bulk channels of the host crystal lattice. This specific mechanism is electrochemically illustrated using a representative lithium-ion/niobium pentoxide (Nb_2O_5) model system in Figure 1.7b, where Li^+ ions are inserted into

the lattice structure during reduction and extracted during oxidation. This continuous process produces a broad, featureless CV signature (Figure 1.7b) and a non-linear, sloped GCD profile (Figure 1.7c) due to the wide distribution of available ion-insertion sites and operating potentials.

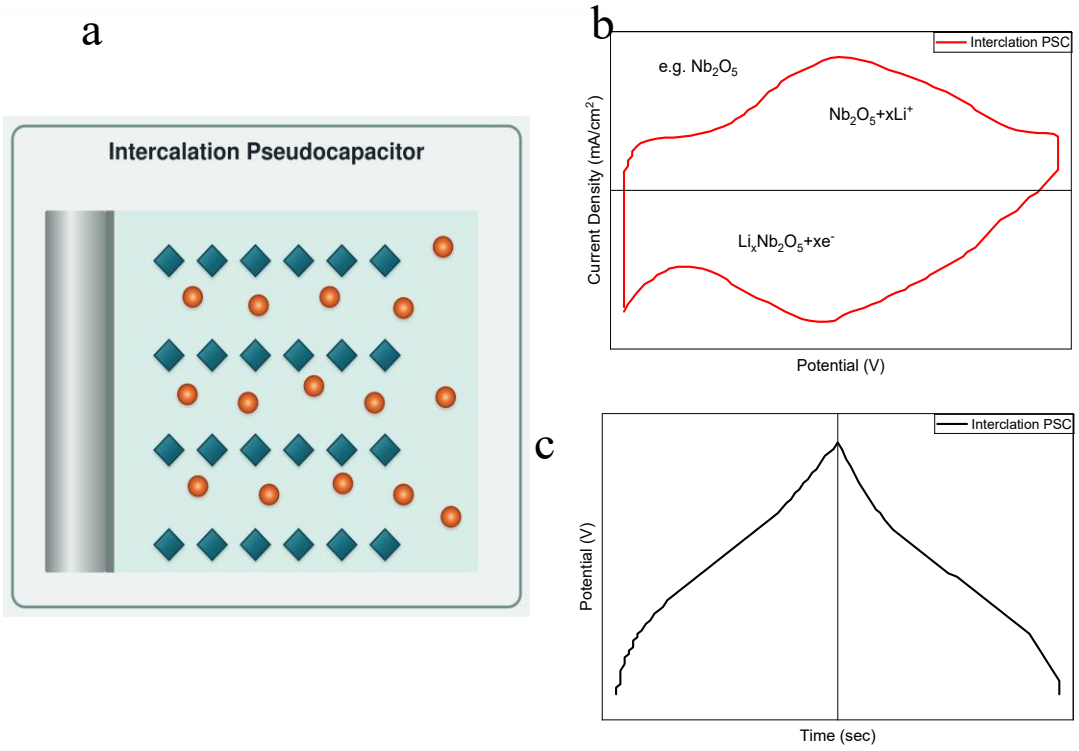


Figure 1.7: Schematic and electrochemical performance of an intercalation pseudo-supercapacitor: (a) structural configuration and ion insertion mechanism, (b) CV profile for a Nb_2O_5 system, and (c) typical GCD behavior.

1.2.3 Hybrid Supercapacitors

Hybrid supercapacitors (HSCs) combine different charge storage mechanisms in a single device to overcome the energy density limitations of EDLCs and PSCs while maintaining power performance.

HSCs are generally divided into three categories [59]:

i. Asymmetric hybrid supercapacitors (ASCs)
ii. Symmetric hybrid supercapacitors (SSCs)
iii. Battery-type hybrid supercapacitors (BHSCs)

1.2.3.1 Asymmetric Hybrid Supercapacitors

Figure 1.8 shows the configuration and working mechanism of an asymmetric hybrid supercapacitor. It consists of two different electrodes separated by an ion-permeable separator and placed in an electrolyte. One electrode stores charge mainly through the adsorption of electrolyte ions, while the other electrode stores additional charge through fast and reversible surface or near-surface faradaic reactions. During charging, electrons move through the external circuit, and electrolyte ions pass through the separator towards the corresponding electrode surfaces to maintain charge neutrality. The adsorption-based electrode provides rapid charging and high-power capability, while the pseudocapacitive electrode increases the amount of stored energy. During discharging, these processes take place in the reverse direction, and the stored electrons flow through the external circuit. The combination of these two distinct charge-storage mechanisms within this asymmetric configuration provides a suitable balance between energy density and power density.

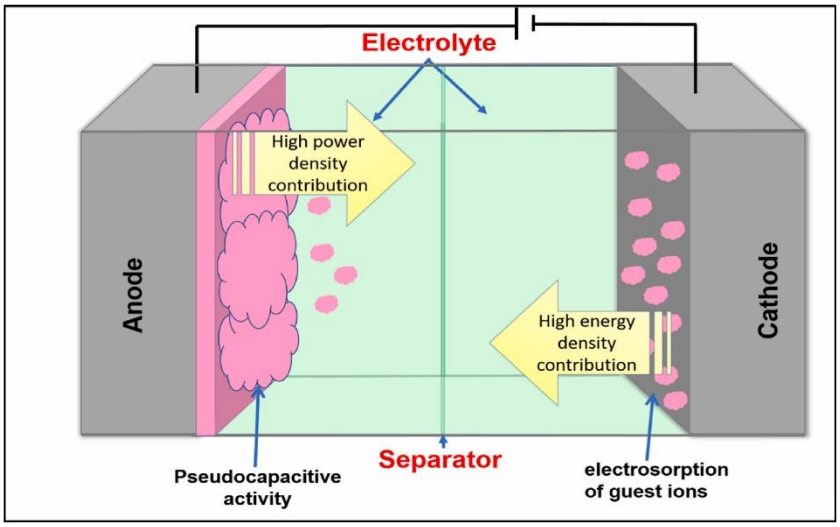


Figure 1.8: Schematic mechanism diagram of an asymmetric supercapacitor, highlighting the rapid surface charge kinetics (pseudocapacitive activity) at the anode and bulk ion dynamics (electrosorption of guest ions) at the cathode *[48].*

The fundamental operational mechanism of ASCs, a key subclass within hybrid configurations, relies on pairing two distinct electrode materials to maximize electrochemical performance. As highlighted in recent advancements in supercapacitor architectures, this design mitigates the energy density limitations of symmetric systems by combining materials with disparate charge-storage mechanisms to optimize both power output and capacitance [61].

By combining an EDLC-type electrode (typically carbon-based) with a pseudocapacitive electrode, an ASC effectively extends the operational voltage window while balancing kinetic rates. The complementary working potential ranges of the negative electrode (ΔV-) and the positive electrode (ΔV_+) sum together to significantly widen the total cell operating voltage window ($\Delta V = \Delta V- + \Delta V_+$),

which directly yields a simultaneous enhancement in the energy density of the device. As a specific example, an ASC configuration utilizing MnO_2 nanorods successfully achieved an energy density of 17 Wh/kg while operating stably at a 1.8 V potential window [62].

For the stable operation of ASCs, proper charge balancing between the electrodes is very important. In addition, electrolyte compatibility, electrode material selection, and mass loading strongly influence the electrochemical performance of the device. Optimized ASCs can provide good cyclic stability and improved capacitance retention at 23000 cycles with 100% retention [62].

1.2.3.2 Symmetric Hybrid Supercapacitors

A symmetric hybrid supercapacitor is prepared by using two identical composite electrodes as the positive and negative electrodes. It stores charge through both ion adsorption and reversible redox reactions. The addition of electrochemically active materials, such as transition-metal oxides or conducting polymers, into the carbon structure increases the C_S and energy density of the device.

The use of identical electrodes also makes the fabrication and assembly process comparatively simple. The carbon material provides rapid charge movement and high-power density, while the active material provides additional charge storage through pseudocapacitive reactions. Therefore, symmetric hybrid supercapacitors can provide higher energy storage than conventional EDLCs while maintaining good power performance. However, the addition of redox-active materials may increase the internal resistance and reduce the cycling stability compared with pure carbon-based EDLCs [63].

SSCs exhibit highly reversible charging-discharging behavior, excellent cyclic stability, and long operational lifetime. Electrochemically, this ideal capacitive behavior is characterized by highly rectangular, symmetric CV curves and linear, perfectly triangular GCD profiles. However, the operating potential window is limited because of the identical electrode materials and electrolyte properties, resulting in a lower energy density range of 3-6 Wh/kg [63].

1.2.3.3 Battery-Type Hybrid Supercapacitors

Battery-type hybrid supercapacitors (BHSCs) integrate two distinct charge-storage behaviors, specifically, a capacitive or pseudocapacitive process at one electrode and a diffusion-controlled, faradaic process at the battery-type counter electrode into a single device layout to optimize both energy and power performance. Battery-type materials utilize a deep, bulk-dependent faradaic reaction mechanism conceptually illustrated in Figure 1.9a, where electrochemically active ions insert directly into the bulk interior of the host crystal lattice rather than remaining restricted to the surface. This difference in kinetic behavior is clearly visible in the electrochemical profiles. In the cyclic voltammetry (CV) response shown in Figure 1.9b, the material exhibits sharp, well-separated oxidation and reduction peaks. For example, using a nickel oxide (NiO) electrode in an alkaline electrolyte, these peaks correspond directly to the reversible phase transformation governed by the surface/bulk reaction:

$$NiO + OH^- \leftrightarrow NiOOH + e^- \quad (1\text{-}8)$$

Consequently, the corresponding galvanostatic charge-discharge profile (Figure 1.9c) displays distinct, flat voltage plateaus during both the charge and discharge stages of the electrochemical cycle, which is a classic signature of a diffusion-controlled phase transformation common to battery-type materials.

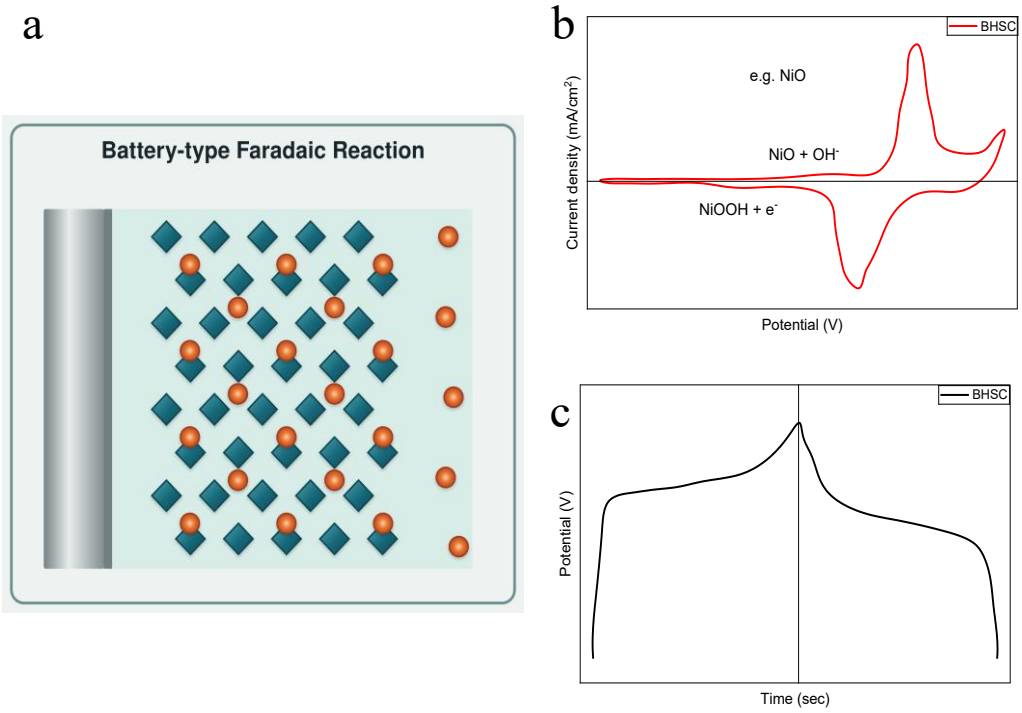


Figure 1.9: Schematic representation and electrochemical characteristics of a BHSC: (a) the bulk faradaic energy storage mechanism, (b) CV profile, and (c) typical GCD profile.

Consequently, BHSCs can provide an energy density close to that of conventional batteries while still maintaining relatively fast charge-discharge kinetics. However, the deep phase transformations and structural degradation that occur during continuous cycling can significantly reduce the long-term cyclic stability of these hybrid systems.

1.3 Components of Supercapacitors

Achieving high energy and power performance in both pseudocapacitors and hybrid systems depends heavily on the synergy between the device components. Consequently, the following sections comprehensively examine the selection criteria, intrinsic properties, and structural advancements of these essential components, specifically focusing on electrode materials, electrolytes, separators, current collectors, and sealants.

1.3.1 Electrode Materials

Electrode materials directly influence the charge-storage mechanism, capacitance, energy density, power density, and cycling stability of supercapacitors [64]. Their performance depends on electrochemical activity, porosity, surface area, and electrical conductivity [65].

Carbon materials, such as activated carbon [51], carbon nanotubes [50], and graphene oxide [52], are widely used due to their high surface area and electrical conductivity [41]. In EDLCs, charge is stored exclusively through the physical adsorption of electrolyte ions. This ion movement depends heavily on pore architecture: macropores facilitate bulk ion transport, mesopores enable smooth diffusion, and micropores provide the high surface area needed for storage. Therefore, a balanced pore network is required to avoid transport restriction while maintaining high charge density. [66].

Transition-metal oxides such as MnO_2 [67], RuO_2 [68], and Fe_2O_3 [69], transition-metal dichalcogenides like MoS_2 [70], and conductive polymers such as polyaniline (PANI) [71], polypyrrole (PPy) [72], and polythiophene (PTh) [73] etc. provide charge storage through reversible faradaic reactions. Their redox activity can increase capacitance and energy density, but repeated cycling may cause structural degradation. Their electrochemical stability also depends strongly on the electrolyte. Combining these materials with conductive carbon structures can reduce these limitations because the carbon framework serves as a mechanically resilient, high-surface-area backbone that buffers the severe volumetric expansion and contraction experienced by pseudocapacitive materials during cycling, while simultaneously providing a continuous electrical pathway that compensates for their low intrinsic electronic conductivity.

The composite electrodes include such materials as carbon-carbon, carbon/transition-metal oxide, carbon/MOF, carbon/conductive-polymer, and multicomponent structures. Some of them are presented in Table 1.2. In these materials, the carbon component facilitates electrical conduction and ion transport, while the other components provide additional electrochemically active sites. Table 1.2 compares the electrochemical performance parameters of devices using these composite electrodes, including electrolyte, cell voltage, E_D, P_D, cycling stability, and specific capacitance (Cs). Most of the reported electrodes contain graphene oxide (GO) or reduced graphene oxide (rGO) combined with transition-metal oxides, metal-organic frameworks (MOFs), MOF-derived structures, conductive polymers, or porous carbon materials [74-80]. MOF-based materials generally exhibit high capacitance and energy density, whereas carbon-rich electrodes can provide high power density because of their favorable conductivity and ion mobility [79, 81, 82]. In addition to graphene-based materials, other emerging carbon allotropes with mixed Sp and Sp^2 hybridized networks have also attracted attention because of their tunable electronic properties and potential applications in energy storage [83].

Table 1-2: Electrochemical performance parameters of various carbon-based, transition metal oxide, and composite electrode materials used in supercapacitors.

Electrode Material	Electrolyte	Cell Voltage (V)	E_D (Wh/kg)	P_D (W/kg)	Cycling Stability (%/cycles)	Cs (F/g)	References
rGO (pure)	2 M KOH	1	-	-	-	114	[75]
rGO	AEI-TFSI	2	61	940	-	250	[76]
MnO_2	2M NaCl	1			65%/800	130	[67]
MnO_2	1M Na_2SO_4	0.8	-	-	-	123	[67]
SbSI	1M NaOH	6			91.4%/3000	259	[84]
SbSI	1M $TEABF_4$	6				161	[84]
GO-MnO_2	6M KOH	1	-	-	84.1%/1000	211	[85]
gC_3N_4/SbSI	1M H_2SO_4	1	-	-	96%/1000	212	[86]
MoS_2-rGO composite	1 M H_2SO_4	1.5	23	370	-	361	[74]
Flexible PANI/rGO	1 M H_2SO_4	0.8	24.45	368	-	299	[77]
AC on rGO surface	1 M Na_2SO_4	1.6	11.9	469.24	-	541	[78]
Porous carbon/GO composite	EMI-TFSI	2.5	32.8	57,000	-	155	[41]
MO-MOF/GO	1 M H_2SO_4	-	55	400	87.5%/6000	617	[79]
Graphene and Ni-doped porous carbon	6 M KOH	-	18	475	90%/10,000	245	[80]
MOF/4, 4‘-Biphenyl dicarboxylic acid	1 M H_2SO_4	-	48.1	1064.7	92%/5000	250.6 mAh/g	[87]
Ni-MOF/rGO	1 M KOH	-	37.8	227	59%/500	758	[88]
Cu-MOF/G	6 M KOH	-	34.5	1350	93.8%/1000	482	[89]
Ni-MOF/GO	6 M KOH	-	39.43	34.29	93.5%/1000	1017	[90]
Ni-MOF/rGO (hydrothermal)	6 M KOH	-	16.5	250	82.4%/5000	630	[91]
Co-MOF/GO	6 M KOH	-	8.1	850	78.8%/1000	549.9	[92]
Zn-MOF/rGO	3 M KOH	-	7.1	400	87%/5000	82.5	[93]
Zeolitic Imidazolate Frameworks /GO	6 M KOH	-	12.7	447	96.6%/10,000	225	[94]

Ce-MOF/GO	3 M KOH + 0.2 M $K_3Fe(CN)_6$	-	111	449.7	85%/5000	2221.2	[95]
Hierarchically Porous Cu-MOF /rGO	1 M Na_2SO_4	-	57.2	4380	83.3%/4000	366.6	[96]
MnO_2-CQDs- Graphene Aerogel composite	-	-	38.2	20	-	721	[97]
Fe_2O_3-MOF/GO	1 M H_2SO_4	-	79.2	405	96.3%/5000	869.2	[81]
Ni/Co-MOF-rGO	6 M KOH	-	72.8	42.5	91.6%/6000	860	[82]
CuOx@mC@PANI@rGO	1 M H_2SO_4	-	-	-	70%/500	534.5	[98]

1.3.2 **Electrolytes**

Electrolytes act as ionic conductors, enabling charge transfer between the electrodes. In SCs, the electrolyte directly affects power density, energy density, cyclic stability, operating potential window, and capacitance [99]. The charging and discharging behavior of SCs depends on the movement of electrolyte ions through the pores of the electrode material. Therefore, the selection of a suitable electrolyte is an important step in evaluating electrode performance. The electrolyte ion size should also be compatible with the pore structure of the electrode material [100]. In addition, electrolyte selection plays an important role in the energy storage mechanism. Electrolytes with wider operating potential windows can further improve the energy density of SCs.

Several electrolyte properties, such as electrochemical stability [101], permittivity behavior [102], ionic size [103], and viscosity [104], strongly influence the electrochemical behavior of SCs [105]. For effective ion adsorption and transportation, the electrolyte ion size should be compatible with the pore size of the electrode material. A mismatch between these dimensions can increase equivalent series resistance and severely limit the accessible double-layer capacitance [106].

Based on literature reviews detailing the historical evolution and current material configurations of energy storage systems, electrolytes are broadly classified into four categories: organic electrolytes [107], ionic liquids [108], aqueous electrolytes [109], and solid-state electrolytes [110].

Organic electrolytes are composed of conductive salts, such as $TEABF_4$, dissolved in organic solvents such as acetonitrile (ACN) [111]. These electrolytes provide a wide potential window of about 2.5-3.0 V, which contributes to higher energy density. However, they usually exhibit lower ionic conductivity (54.2 mS/cm for 1.6 M concentration in the case of $TEABF_4$/ACN) and higher cost. Other

examples are tetrabutylammonium hexafluorophosphate ($TBAPF_6$) in acetone [112] and lithium hexafluorophosphate in ACN [113].

Ionic liquid electrolytes are salts that remain in liquid form at or near room temperature and are completely composed of cations and anions. These electrolytes exhibit high thermal stability, negligible vapor pressure, and wide operating voltage windows, making them suitable for advanced SC applications. Common examples include [EMIM][BF_4] (1-ethyl-3- methylimidazolium tetrafluoroborate) [114] and ionic liquid electrolytes containing LiTFSI [115]. However, their high viscosity limits ionic conductivity [104].

Aqueous electrolytes are widely used in supercapacitors because of their high ionic conductivity, low resistance, low cost, and comparatively safe handling. However, their operating voltage is normally limited by the decomposition of water, whose theoretical stability window is approximately 1.23 V [116]. Literature reports demonstrate that the maximum achievable cell voltage also depends on the electrode materials, electrolyte concentration, pH, and testing conditions. Highly concentrated water-in-salt electrolytes can suppress water activity and extend the electrochemical stability window, with some reported systems approaching 3.0 V [116]. However, this value is not universal and must be confirmed experimentally for each electrode-electrolyte system. Common examples of aqueous electrolytes include H_2SO_4 [74], KOH [88], and KCl [117].

Solid-state electrolytes are solid or gel-type ion-conducting materials that eliminate liquid leakage and improve the safety and flexibility of electrochemical devices. These electrolytes are widely used in flexible and wearable SCs because they provide mechanical stability together with ionic transport. Common examples include [PVA/H_2SO_4] poly(vinyl alcohol)/ sulfuric acid gel electrolyte [118], PEO/LiCl (Poly(ethylene oxide)/lithium chloride) solid polymer electrolyte [119], and Li_2S-P_2S_5 inorganic solid electrolytes [120].

1.3.3 Separator

A separator is a thin, semi-permeable membrane placed between the two electrodes of an SC. It allows electrolyte ions to move between the electrodes while preventing electrical short circuits. The porosity and structure of the separator can influence the energy density, mechanical strength, and ionic conductivity of the device [121].

Separators in energy storage devices are generally classified into various types based on their structural and material characteristics, with the main categories being microporous film, nonwoven gel polymer separators, and solid polymer separators [122]. Microporous film separators typically have pore sizes exceeding 5-10 nm, frequently ranging from 30 to 100 nm in commercial membranes [122], and are widely used in acidic and organic electrolyte systems due to their suitability for ambient and low-temperature operations below 100 ^oC. In contrast, nonwoven separators are fabricated from overlapping fiber networks with larger pore volumes. Examples of materials used for these nonwoven

mats include glass [123], polyvinyl chloride (PVC) [124], polyester [124], polytetrafluoroethylene (PTFE) [124], cotton, and polyolefins [124]. Nonwoven separators prepared from PVDF, PTFE, cellulose fibers, and PVC [124] are also commonly utilized because of their excellent chemical stability in alkaline environments.

Also, crosslinked hydrogels or porous thermoplastic membranes are commonly used as separators. These separators are fabricated using materials such as synthetic rubber (solid type) [125], PVDF (gel type) [126], polyethylene (PE) (microporous) [127], polyacrylic acid (PAA) (gel type) [128], and polypropylene (PP) (microporous) [129]. These materials are preferred because of their low cost, easy processing, flexibility, chemical stability, and good mechanical properties. PP is widely used due to its high electrochemical stability; however, pristine PP suffers from poor electrolyte wettability due to its nonpolar surface energy [130, 131].

1.3.4 Current Collectors

The current collector acts as a conductive pathway between the electrode material and the external circuit. Poor electrical conductivity at the electrode interface can increase internal resistance and reduce the storage efficiency of the device. Therefore, good electrical contact and the use of conductive additives are important for efficient charge transport.

Current collectors are commonly fabricated from thin metal films such as aluminum [132] and copper [133]. because of their high electrical conductivity. In addition, polymeric binders such as Nafion [134], PVB [135], PTFE [135], and PVDF [134] are added to electrode pastes together with conductive carbon additives such as Super P [136] and acetylene black [137]. These binders improve the mechanical stability of the electrode materials during long-term cycling tests and enhance adhesion between the electrode material and the current collector [138]. However, excessive use of polymeric binders can increase internal resistance and reduce the power output of the device [138].

1.3.5 Sealants

The long-term stability of SCs strongly depends on proper sealing of the device. During long-term operation, electrode degradation may occur because of surface oxidation triggered by ambient oxygen exposure, packaging defects, and gas evolution caused by electrolyte decomposition activated by trace moisture contaminants. The severity of these effects depends on the type of solvent and electrolyte ions used in the system, which dictate the device's intrinsic electrochemical window.

An effective sealing system prevents moisture and gases from entering the SC cell, thereby preserving high shunt resistance between the electrodes by preventing conductive internal leakage pathways. High shunt current can increase self-discharge and reduce the overall efficiency of the device. Poor sealing may also result in short circuits and device degradation. Therefore, sealants must

provide good electrical insulation, puncture resistance, and mechanical protection while maintaining low device weight for safe operation.

1.4 Motivation of the Work

The current literature on high-performance SC electrodes focuses extensively on composite architectures pairing a carbonaceous matrix with transition metal oxides. Carbon-based materials, such as GO, provide the necessary surface area and electrical conductivity to maintain cyclic stability, while pseudocapacitive components, such as manganese dioxide, provide high specific capacitance through fast surface redox reactions. Although such binary composites are heavily investigated, their performance limits are often constrained by slow ion diffusion at high charge-discharge rates [139].

To overcome these diffusion limitations, contemporary materials research explores multi-component architectures that couple materials with complementary physical and electrochemical properties [140]. In these new material trends, metal chalcohalides attract significant attention for their unique combination of mechanical anisotropy, semiconducting properties, and strong internal electronic polarization [140]. Specifically, SbSI is a unique quasi-one-dimensional ferroelectric semiconductor characterized by a high permittivity and a spontaneous internal dielectric moment. While SbSI is used in optoelectronics [141, 142], its application in electrochemical energy storage systems remains highly limited [84]. Recent explorations have successfully integrated SbSI into carbon matrices, demonstrating promising charge storage capabilities [86].

However, a clear research gap exists regarding the electrochemical synergy and chemical stability of multi-component systems that simultaneously incorporate chalcohalides and transition metal oxides into carbon frameworks. Although a previous study has examined them individually, the potential to utilize the spontaneous ferroelectric polarization of SbSI to modify charge storage kinetics remains largely unexplored [84]. The combination of chalcohalide, MnO_2, and carbon-based components provides a multi-component structure in which the individual materials can contribute different electrical, interfacial, and electrochemical properties. Therefore, this work systematically investigates the influence of this multi-component framework on charge-storage behavior and evaluates the stability of the chalcohalide-containing composites under different electrochemical conditions.

Chapter 2

AIM AND OBJECTIVES

The development of high-capacity, high-voltage, and structurally stable electrode materials is still a major challenge in the research of supercapacitors [64]. While standard high-surface-area carbon materials are commercially available, the primary material challenge involves synthesizing specialized architectures that simultaneously maximize electrochemically accessible surface area and electrical conductivity without escalating internal charge-transfer resistance or accelerating structural degradation at extended operating voltages [143].

Within the exploration of alternative high-performance electrode configurations, metal chalcohalides have emerged as an intriguing class of compounds due to their strong internal electronic polarization and active charge-storage sites. Among these materials, SbSI is a distinctive quasi-one-dimensional ferroelectric semiconductor with a high permittivity and spontaneous internal polarization. Although SbSI has demonstrated potential for charge-storage applications, its use as an individual supercapacitor electrode is limited by its low intrinsic electrical conductivity and relatively small accessible surface area.

To systematically address these specific constraints and unlock the electrochemical potential of the chalcohalide phase, this research investigates the integration of supportive and synergetic material matrices. GO was selected as a primary structural template to provide a high-surface-area carbonaceous framework capable of anchoring the SbSI nanostructures, thereby improving both structural integrity and electrical transport pathways. GO contains two-dimensional sheets and oxygen-based functional groups that can improve the wettability of electrolytes and provide chemically active anchoring sites for other active materials. However, these functional groups disrupt the sp^2 carbon network and reduce the intrinsic conductivity of pristine sheets. GO therefore functions primarily as a supportive framework and a surface-active substrate, rather than a highly conductive component [144].

To further enhance the faradaic charge-storage capacity of the system, Manganese dioxide (MnO_2) is widely studied as a pseudocapacitive electrode material because of its high theoretical specific capacity [145], natural abundance, and relatively low toxicity. It stores charge through a rapid and reversible Faradaic reaction that occurs on the surface and near the surface. However, its low intrinsic conductivity limits the movement of electrons and reduces the use of its active material [143]. Therefore, MnO_2 is usually combined with the carbon-supported chalcohalide network to improve charge transfer and reduce electrode resistance [146].

When GO, SbSI, and MnO_2 are combined at a suitable concentration, the blend of their respective properties is expected to optimize the accessibility of the ions, the transfer of loads, and the total specific capacity. Lower equivalent series resistance (ESR) supports rapid energy supply and

high-power density, while increased capacity and an appropriate operating voltage improve energy density. However, these improvements in electronic performance depend largely on the distribution and concentration of each component; electrical measurements indicate that at low loading levels, the semiconducting nature of the SbSI nanowires dominates the electrical behavior, creating resistive interfaces that restrict charge transport until the conductive networks cross a critical structural percolation threshold [147], a behavior derived from the sequential incorporation of the GO matrix and the secondary MnO_2 phase to tune the properties of the baseline SbSI phase [84].

2.1 Aims

The main aim of this study is to systematically evaluate how structural variations, compositional ratios, and interfacial coupling within these specific multi-component networks influence the resulting electrochemical charge-storage behavior of the SbSI phase. For this purpose, GO, SbSI, and MnO_2 were selected for the preparation of binary and ternary composite materials. The GO-SbSI binary composites were prepared by changing the relative concentrations of GO and SbSI to isolate the baseline interactions between the carbon scaffold and the chalcohalide, while the GSM ternary composites were produced by maintaining a fixed GO content and changing the concentrations of SbSI and MnO_2. This approach ensures that the structural and capacitive trends are thoroughly mapped across a controlled concentration series, rather than drawing generalized conclusions from a single isolated composition.

The second aim was to analyze the properties of the individual materials and their binary and ternary composites using the available experimental techniques. Their crystalline structure, morphology, elemental composition, chemical bonding, optical behavior, and permittivity response were examined to build a clear baseline tracking how composition alters the physical matrix. Electrochemical measurements were then performed to determine their specific capacitance, charge-discharge behavior, rate response, charge-transfer resistance, and capacitive phase behavior derived via EIS and cycling stability. The results obtained for different concentrations were compared under the same testing conditions to determine how changes in composition affected the measured properties of the materials. This comparison was also used to identify the optimum composition showing the most suitable overall electrochemical performance within the investigated series.

The final aim was to evaluate the prepared materials beyond the standard three-electrode testing system by subsequently investigating their performance within a two-electrode coin-cell configuration. For this purpose, the compositional boundaries of the concentration series-specifically the initial baseline framework and the terminal composition-were selected for full-cell assembly. This strategic choice was made to evaluate the extreme limits of the concentration range, providing a high-contrast benchmark to observe how maximum variations in component loading influence the performance parameters when scaled up into a practical device. Their electrochemical responses were compared to

determine how the change in material concentration affected the performance of the complete cells. In this way, the study connected the fundamental structural synthesis and properties analysis of the chalcohalide-based nanomaterials with their practical electrochemical behavior in an assembled device configuration.

2.2 Research Objectives

The main objective of this research was to prepare and investigate GO-SbSI binary and GO-SbSI-MnO_2 ternary composites with different concentrations for their possible application as supercapacitor electrode materials. To achieve these objectives, the following specific research tasks were established:

i. To synthesize graphene oxide from graphite using an established chemical oxidation method.
ii. To synthesize SbSI nanostructures via a standard sonochemical method.
iii. To synthesize MnO_2 architectures using a conventional hydrothermal method.
iv. To develop and optimize a novel, in-situ sonochemical synthesis approach specifically designed in this work to assemble the GO-SbSI binary composites across a controlled series of concentrations.
v. To design and implement a new multi-step in-situ preparation route combining sequential hydrothermal and sonochemical techniques, uniquely developed in this work to systematically vary the relative concentrations of SbSI and MnO_2 within the GSM ternary composites.
vi. To characterize the crystalline structure, phase purity, and general structural parameters of the prepared binary and ternary materials using X-ray diffraction (XRD).
vii. To examine the surface morphology, elemental distribution, and electronic states of the composites using scanning electron microscopy (SEM), transmission electron microscopy (TEM), and X-ray photoelectron spectroscopy (XPS).
viii. To analyze the functional groups, interfacial chemical interactions, and optical absorption behavior through Fourier-transform infrared (FTIR) and UV-Vis spectroscopy.
ix. To investigate the frequency-dependent electrical properties, permittivity behavior, and bulk conductivity profiles of the prepared materials using complex impedance spectroscopy (CIS).
x. To evaluate the electrochemical performance of the fabricated electrodes in a three-electrode system using cyclic voltammetry (CV), galvanostatic charge-discharge

(GCD), and electrochemical impedance spectroscopy (EIS), supplemented by charge-storage kinetic and ion diffusion calculations.

xi. To evaluate the optimized electrode materials within a practical two-electrode coin-cell supercapacitor configuration, directly contrasting the device-level performance parameters with the three-electrode analytical data.

Chapter 3

SYNTHESIS TECHNIQUES

In this study, a systematic multi-step synthesis strategy was implemented to independently prepare the constituent material phases before sequentially assembling them into binary and ternary composite architectures. Rather than initiating the experimental workflow directly with the complex multi-component system, GO, SbSI, and MnO_2 were first synthesized as individual building blocks to establish clear baseline structural characteristics. The modified Hummers method was chosen for the initial preparation of graphene oxide because the chemical exfoliation process efficiently introduces oxygen-containing functional groups that facilitate stable aqueous dispersion and provide dense attachment sites for secondary materials. A standalone sonochemical approach was used to obtain pure SbSI nanostructures, while the hydrothermal method was selected for the synthesis of the manganese dioxide phase because the localized high-temperature and high-pressure conditions in a closed vessel significantly enhance the crystallinity, stability, and controlled one-dimensional growth of MnO_2 nanowires [148].

Following the preparation of these base building blocks, the novel GO-SbSI binary composites were successfully synthesized by implementing an in-situ sonochemical precipitation technique. This progressive workflow ultimately culminated in the fabrication of the GSM ternary nanocomposites using a customized sequential hydrothermal and in-situ sonochemical strategy. This specific combination of synthesis methods was selected to strategically optimize the structural features of each distinct component. The final in-situ sonochemical technique was utilized to incorporate the SbSI nanostructures directly onto the pre-formed GO and MnO_2 network. Ultrasonic irradiation was chosen because acoustic cavitation creates high localized energy zones that promote uniform nucleation of the chalcohalide, minimize the aggregation of individual nanoparticles, and secure a strong mechanical and electronic interconnect between the three distinct material phases.

3.1 Materials

Materials used during the synthesis process are presented in Table 3.1. The tables also include the molecular weights, purities, and manufacturers.

Table 3-1: The materials used during the synthesis process.

Material Name	Molecular Weight or purity	Purchased from
Graphite		B&K Multi-Industry Company
Potassium permanganate	M = 158.04 g/mol; 99.0%	WAR-CHEM Sp. z o.o. (Poland)
Sodium nitrate	84.99 g/mol	WAR-CHEM Sp. z o.o. (Poland)
Hydro sulphuric acid	99%	
Hydrogen peroxide	30%	POCH S.A. (Poland)
Manganese sulphate	169.02 g/mol	WAR-CHEM Sp. z o.o. (Poland)
Sodium hydroxide	39.99 g/mol	
Sulfur	99.5%	POCH S.A. (Poland)
Antimony	99%	
Iodine		POCH S.A. (Poland)
Ethanol	M = 46.07 g/mol; 99.8%	WAR-CHEM Sp. z o.o. (Poland)

3.2 Synthesis Methodology

3.2.1 Synthesis of Graphene Oxide

The synthesis of GO was done using Hummers' method [149]. The complete process of GO synthesis is illustrated in Figure 3.1. 120 mL of hydro-sulfuric acid (H_2SO_4) was taken in a beaker and placed in an ice bath; in addition to this, 3 g of graphite was added to the H_2SO_4, gradually 3g of sodium nitrate ($NaNO_3$) was added to the mixture, and after 30 min, 9 g of potassium permanganate ($KMnO_4$) was slowly added to the mixture. After this, the mixture was stirred for 2 hours. After 2 hours, the bath was removed and stirred again for 1 hour. After completion of 3 hours of stirring, the mixture was placed again in the ice bath, and 100 mL of distilled water was added. The temperature was maintained at 98 ° C. After 30 min, hydrogen peroxide (H_2O_2) was added to the mixture. After 30 min, the mixture was transferred to the 1L flask, and the pH was maintained around 7 by the washing method. Finally, the mixture was filtered through filter paper and dried at 60 C.

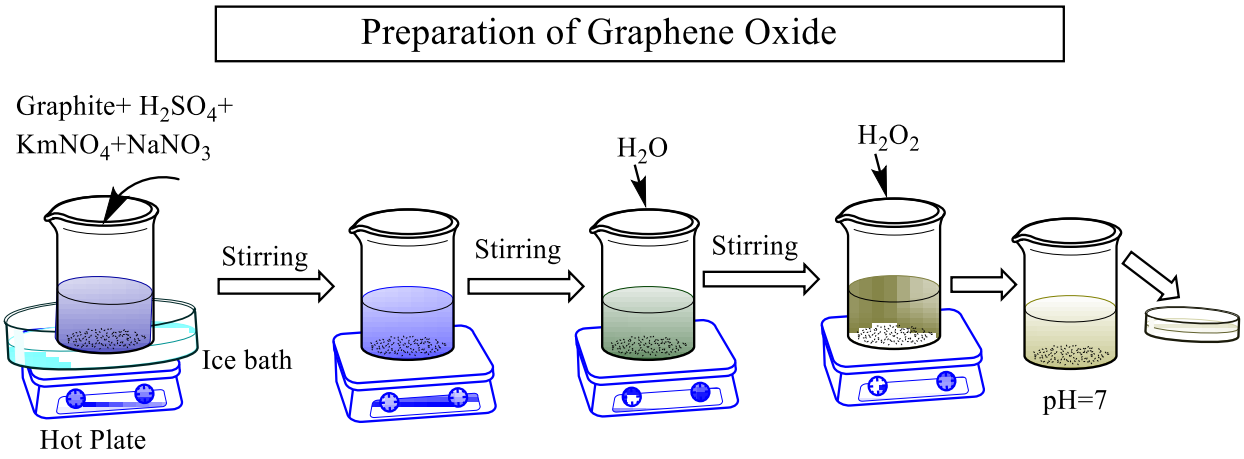


Figure 3.1: Schematic representation of the chemical synthesis route for preparing Graphene Oxide.

3.2.2 Preparation of Antimony Sulfoiodide

The SbSI nanowires (NW) were synthesized using a modified version of Nowak's method [150]. High-purity elemental powders of antimony (Sb) (0.92g), sulfur (S) (0.24g), and iodine (I) (0.95) were combined in a stoichiometric molar ratio of 1:1:1, ensuring proper stabilization of the chalcohalide phase. The measured powders were dispersed in ethanol, which acted as both a solvent and a medium to promote homogeneous mixing (Figure 3.2). The vessel was tightly closed after the addition of solvent and measured quantities.

The precursor suspension was treated with ultrasonic treatment on a bath sonicator for 3 hours. This ultrasonication provided intense acoustic cavitation and localized heating, promoting the dissolution of iodine, breaking down Sb and S agglomerates, and accelerating the nucleation of SbSI nuclei through enhanced collisions of reactive species. During the sonication process, the initially dark suspension gradually transformed into a bright orange color, indicative of the formation of SbSI nanostructures.

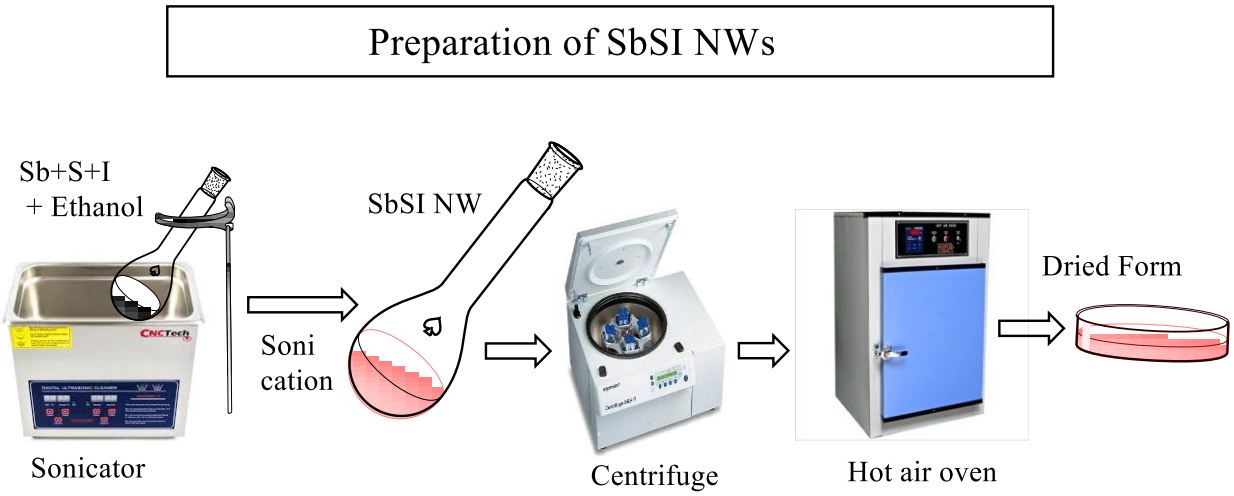


Figure 3.2: Schematic illustration of the step-by-step synthetic procedure for preparing antimony sulfoiodide nanowires.

After the reaction, a distinct orange precipitate made up of SbSI NWs was observed, settling at the bottom of the beaker, indicating the successful formation of the SbSI material phase. The NWs were carefully decanted and washed repeatedly with ethanol to remove residual by-products, such as unreacted iodine, sulfates, and any soluble impurities. The ethanol washing also helped prevent agglomeration and preserved the one-dimensional morphology of the nanowires.

The purified SbSI NWs were then transferred to clean Petri dishes and dried at a controlled temperature, typically between 60 and 80 ° C, to evaporate any residual solvent while avoiding thermal decomposition of the product. This drying step yielded the final solid SbSI product.

3.2.3 Preparation of Manganese Dioxide

In the preparation of MnO_2 nanowires, the hydrothermal process was used to synthesize the material [151]. In this process, the 60 mL aqueous solution of potassium permanganate ($KmNO_4$) (1.43g) was slowly added to the 40 ml aqueous solution of $NaNO_3$ (0.67g) by 2 ml/min, were selected to establish an optimized stoichiometric molar ratio required for the complete chemical reduction of Mn^{4+} and the mixture was stirred for 1 hour (Figure 3.3). After 1 hour, when $KMnO_4$ was completely dissolved in $NaNO_3$, the mixture was transferred to a Teflon vessel, and the hydrothermal vessel was tightly closed. The hydrothermal vessel was placed in the hot oven for 14 hours at 180 ºC. After the hydrothermal treatment, the mixture was transferred to the flask for cleaning. The mixture was washed with distilled water several times and dried at 80 C.

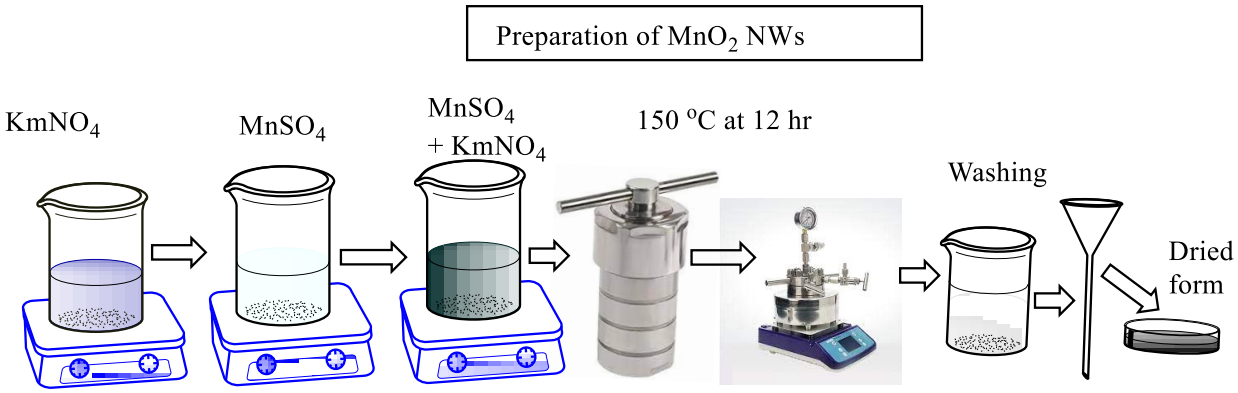


Figure 3.3: Schematic representation of the hydrothermal synthesis pathway for the preparation of MnO_2 NWs.

3.2.4 Preparation of GO-SbSI Binary Composites

The in situ sonochemical method used to achieve interfacial coupling between the SbSI nanowires and the GO matrix was developed as part of this work. The reaction parameters were systematically optimized across a series of various experimental trials to overcome initial synthesis challenges, such as the formation of unwanted Sb_2S_3 secondary phases and poor adhesion of the chalcohalide onto the carbon sheets. Early trials conducted at lower temperatures 40 ºC to 55 ºC or with short sonication times (under 40 minutes) resulted in incomplete precursor conversion and uneven nanoparticle distribution. Furthermore, high initial concentrations of the iodine precursor led to volatile losses and non-stoichiometric phase composition. Through these sequential iterations, it was determined that maintaining a stable temperature window of 70 ºC and a continuous ultrasonic irradiation period of 3 hours provided the necessary energy to secure complete reaction conversion and a uniform, structurally stable binary layout without phase segregation. Typical procedures include dissolving soluble Sb, S, and I precursors in ethanol and subjecting them to ultrasonic irradiation. After 50 minutes of initial sonication, the GO dispersion (Figure 3.4a) was introduced into the pre-treatment mixture at 40 mg (Figure 3.4b), and the mixture was sonicated at 70 ºC for 3 hours to drive the growth

of quasi-1D SbSI nanowires onto the surface of the 2D GO sheets. During this process, a clear color change from orange to light green, and finally to green, was observed, indicating the sequence of reactions. The final powder exhibited a different green tone depending on the mass ratio of the components. The compositional series of these GO-SbSI binary composites is summarized in Table 3.2.

The concentration percentages and the corresponding mass ratios used during the synthesis process are presented in Table 3.2. For the GO-SbSI binary compounds, the materials were prepared across various weight percentages (from 70/30 to 30/70). To maintain a consistent total batch size during synthesis, the mixtures were scaled to a fixed basis of 21 total mass parts, where the relative parts of GO and SbSI were adjusted to precisely match each target percentage configuration as detailed in Table 3.2.

Table 3-2: Prepared samples along with the weight percentage of individual components.

Material	Concentration of GO (%)	Concentration of SbSI (%)
GO	100	0
GO-SbSI 70/30	70	30
GO-SbSI 60/40	60	40
GO-SbSI 50/50	50	50
GO-SbSI 40/60	40	60
GO-SbSI 30/70	30	70
SbSI	0	100

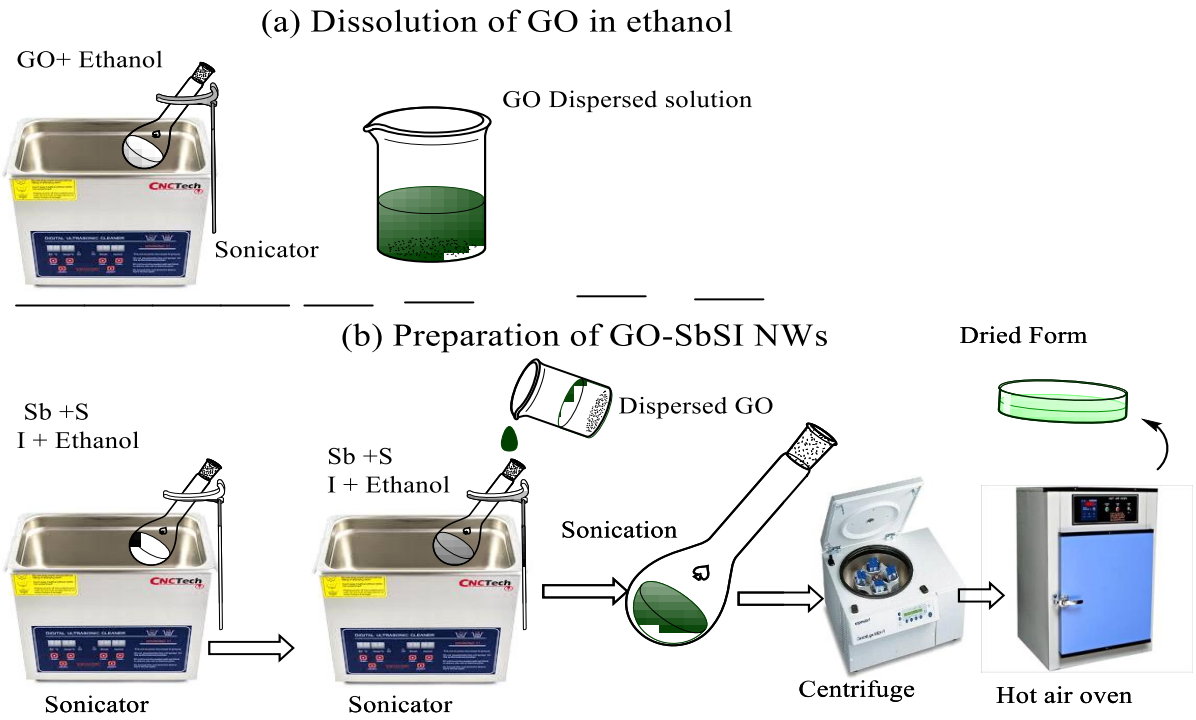


Figure 3.4: Schematic representation of (a) the ultrasonic dispersion of GO in ethanol and (b) the subsequent in situ sonochemical synthesis of the GO-SbSI nanowire nanocomposites.

3.2.5 Preparation of GO-SbSI-MnO_2 Ternary Composite

In this study, a multi-step in situ sonochemical method was developed to prepare the GSM ternary composites. The integration of the third phase required a separate optimization matrix consisting of various distinct experimental trials to prevent the agglomeration of MnO_2 nanowires and ensure uniform multi-component interfacial coupling. Initial attempts to combine all components simultaneously resulted in severe phase separation, where the SbSI nucleated independently rather than bonding with the MnO_2 and GO frameworks. Trials exploring high MnO_2-to-GO mass ratios (exceeding 85 wt.%) experienced dense mass crowding that disrupted the acoustic cavitation paths, leading to localized thermal hot spots and partial structural collapse of the oxide phase. By adjusting the sequence of component introduction-suspending the MnO_2 and GO in separate beakers prior to their controlled introduction into the chalcohalide matrix-and strictly maintaining the optimal cavitation parameters established in the binary trials, the structural and electrochemical requirements for the ternary framework were successfully achieved. Typically, a predetermined amount of GO is first homogeneously dispersed in ethanol under continuous ultrasonication (Figure 3.5a), giving a stable and exfoliated suspension. At the same time, pre-synthetic MnO_2 nanowires were suspended in separate ethanol volumes (Figure 3.5a) and subjected to intense ultrasonic radiation to ensure a uniform distribution of the 1D oxide phase. The suspension of the dispersed MnO_2 nanowires was then carefully combined with the GO dispersion under continuous agitation.

After this precursor mixture phase, the same in-situ sonochemical assembly step was used for binary composites to integrate the third stage. The precursors of Sb, S, and I stoichiometry were introduced into the reaction flask containing ethanol to form the SbSI precursor mixture (Figure 3.5b). The separate GO and MnO_2 dispersions were then systematically introduced into this chalcohalide matrix. The entire system was subjected to three hours of ultrasonic radiation at 70 ^{o}C, using high-level acoustic cavitation energy to direct the nucleation and interfacial coupling of a single-disc chalcohalide SbSI nanowire to the surface of a 2D GO sheet and a single-disc MnO_2 network. During this processing period, the slurry exhibits a color change from orange to light green, and finally to dark green or light brown, which marks the successful completion of the multi-component coupling reaction. The resulting three-layer composite powders show different green shades depending on the configured mass ratios, which are systematically summarized in Table 3.3.

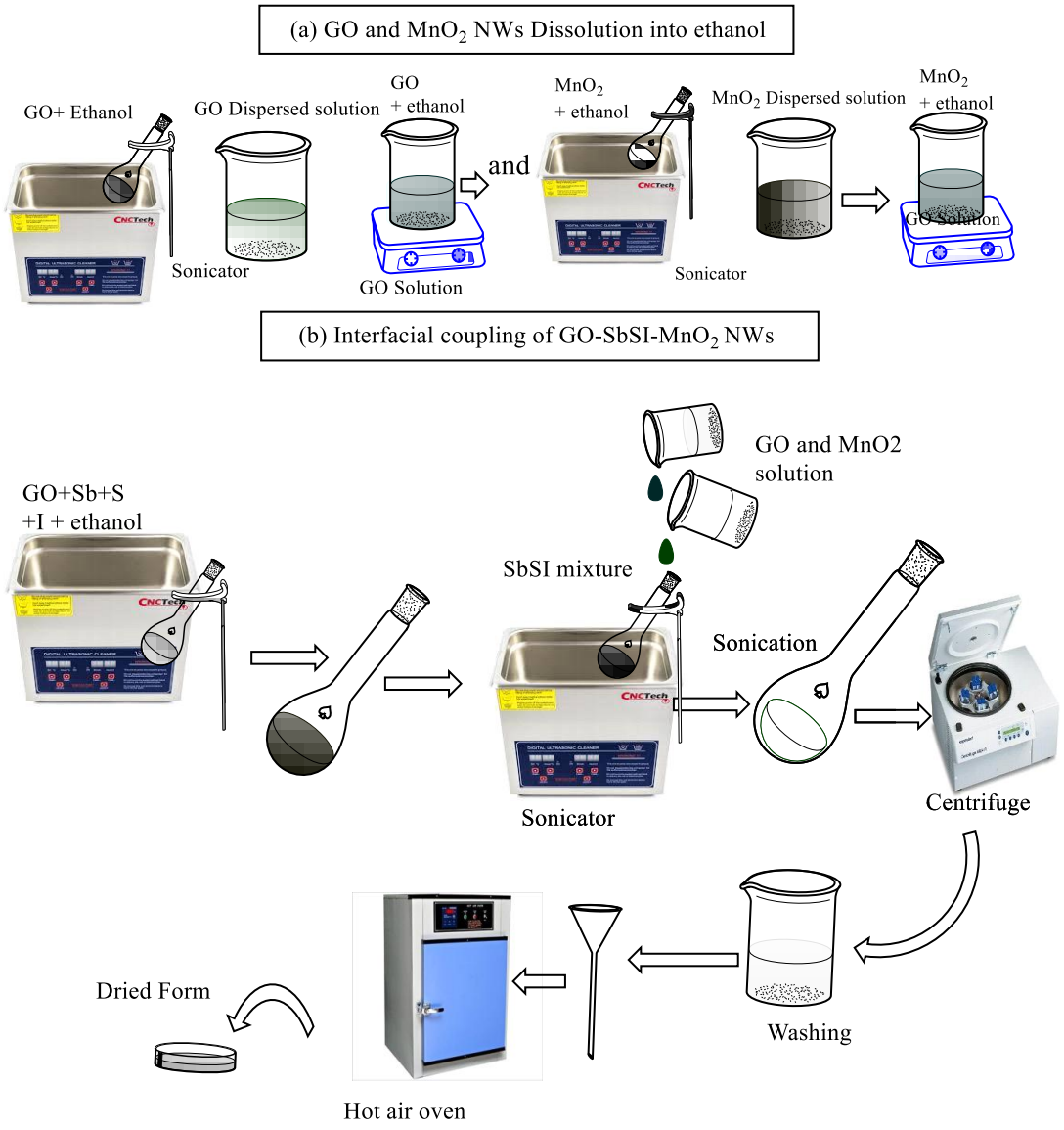


Figure 3.5: Schematic presentation of the synthesis methodology for the GSM ternary composites, showing (a) the independent dispersion processes of GO and MnO_2 NWs in separate ethanol volumes, and (b) the subsequent in-situ interfacial coupling of the components within the SbSI precursor matrix.

For the GSM compounds, the composites were synthesized in a proportional ratio of 45 and in a total proportional ratio of 45 parts and in various concentrations, as described in Table 3.3.

Table 3-3: Prepared samples of GO-SbSI-MnO_2 composites along with the weight percentage of individual components.

Material	Concentration of GO (%)	Concentration of SbSI (%)	Concentration of MnO_2 (%)
GSM 1:20:80	Fixed 40 mg	20	80
GSM 1:30:70	Fixed 40 mg	30	70
GSM 1:40:60	Fixed 40 mg	40	60
GSM 1:50:50	Fixed 40 mg	50	50
GSM 1:60:40	Fixed 40 mg	60	40
GSM 1:70:30	Fixed 40 mg	70	30
GSM 1:80:20	Fixed 40 mg	80	20

3.2.6 Conditions

The optimization of the in-situ sonochemical synthesis route established a narrow window of critical experimental parameters required to successfully yield phase-pure GO-SbSI and GSM composites. The precise operational boundaries determined through the experimental trials are detailed below:

a. **Vessel Sealing and Atmosphere:** The sonochemical reactions were conducted in a hermetically sealed glass reactor vessel under ambient air atmosphere. Sealing the container is strictly mandatory to prevent the rapid volatilization and evaporation of the ethanol solvent at elevated processing temperatures, which would otherwise alter the precursor concentration and prematurely terminate the nucleation process.

b. **Temperature Stability Window:** The reaction temperature must be rigidly maintained at 70 °C with an acceptable tolerance window of only +2 °C. Thermal variations exceeding this range disrupt the kinetic balance; temperatures below 65 °C severely reduce the precursor conversion rate, while temperatures approaching the boiling point of ethanol, 75 °C generate excessive solvent vapor pressure that dampens the acoustic cavitation intensity.

c. **Stoichiometric Control:** To prevent the formation of highly stable amorphous or crystalline secondary impurities-such as antimony trisulfide Sb_2S_3 or unreacted elemental iodine-the initial atomic ratio of the Sb, S, and I precursors must be fixed at a strict 1:1:1 stoichiometry. Deviations in this mass balance alter the local supersaturation levels, halting the highly directional, c-axis growth required to form the characteristic quasi-1D SbSI nanowires.

d. **Reaction Duration Boundaries:** The continuous ultrasonic irradiation period is constrained to a window of 180 $\pm$ 10 minutes. Restricting the processing duration to less than 160 minutes leaves a substantial fraction of unreacted precursors in the slurry, as confirmed by low yields. Conversely, extending the sonication period beyond 210 minutes induces severe acoustic erosion and Ostwald ripening, which compromises the interfacial mechanical anchoring between the SbSI phase, the 1D MnO_2 networks, and the 2D GO sheets.

3.3 Sample Preparation for Characterization Testing

3.3.1 Fourier-Transform Infrared (FTIR) Spectroscopy

For FTIR analysis, the samples were prepared using the standard KBr pellet technique [152]. In this procedure, the composite powder and spectroscopic-grade KBr were thoroughly mixed in a 1:10 weight ratio to ensure a uniform distribution of the material within the KBr matrix. The homogeneous powder mixture was then transferred to a pellet die (Figure 3.6a) and compressed under hydraulic pressure to produce transparent solid discs possessing adequate mechanical strength for subsequent optical transmission testing.

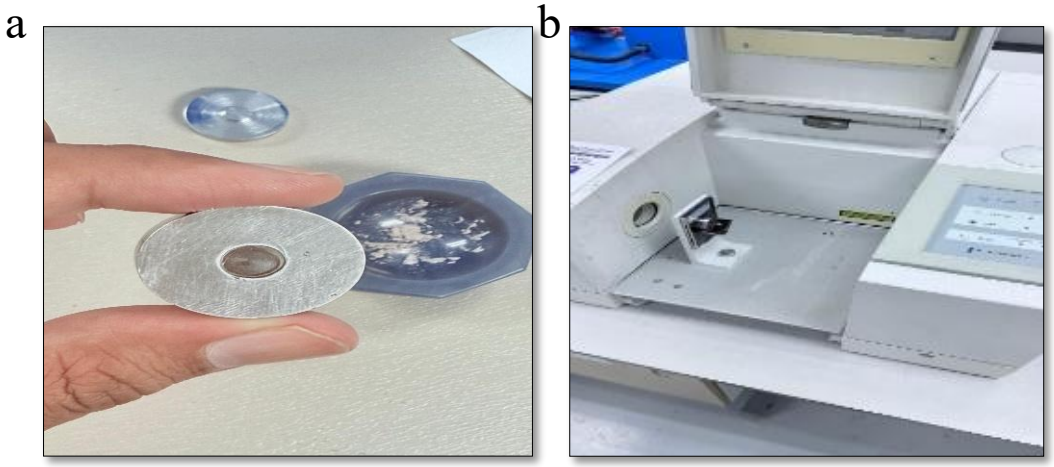


Figure 3.6: (a) Photograph of the fabricated pellet, and (b) the pellet mounted in the FTIR PerkinElmer Spectrum One spectrometer for FTIR characterization.

3.3.2 Ultraviolet-Visible (UV-Vis) Spectroscopy

The UV-Vis spectroscopy analysis was carried out using an ethanol and distilled water mixture in a 20:80 volume ratio as the solvent. The solvent mixture was first sonicated for approximately 20 min to obtain a homogeneous solution. Subsequently, 0.1 mg of the testing material was added to the solution and further sonicated for 30 min to ensure uniform dispersion of the sample. The prepared suspension was then transferred to a quartz cuvette and placed in the Cary 50 Conc UV-Vis spectrometer for analysis, as shown in the experimental setup in Figure 3. Specifically, Figure 3.7a displays the quartz cuvette filled with the prepared composite suspension, while Figure 3.7b illustrates the sample compartment of the spectrometer.

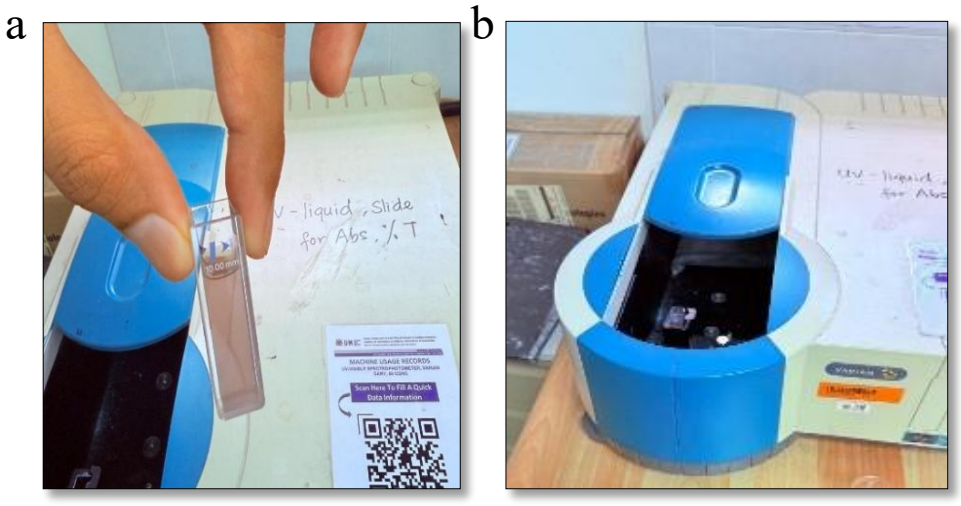


Figure 3.7: (a) The cuvette with material dissolved in ethanol. (b) The cuvette placed in the Cary 50 Conc UV-Vis spectrometer.

3.3.3 Scanning Electron Microscopy (SEM)

Two methods were used to measure the morphology: Scanning Electron Microscopy (SEM) and Field Emission Scanning Electron Microscopy (FESEM). For the SEM results, 10 µg of the prepared sample was added to ethanol and sonicated. After that, a few drops of the obtained solution were dropped onto a silicon chip and dried in a vacuum chamber. Figure 3.8b shows the sample coating on the silicon substrate; to obtain better images, a thin layer of gold was additionally sputtered onto the samples.

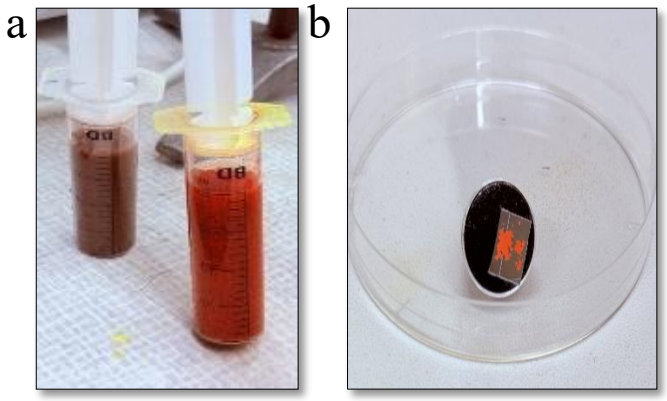


Figure 3.8: The process of sample preparation for SEM. (a) The sample dissolution in ethanol, (b) by the drop-casting method, the coated material on silicon chips.

3.3.4 Impedance Spectroscopy

In order to measure impedance spectroscopy, the prepared composite powder is converted to a solid pellet to evaluate its electrical behavior. In typical methods, a specific mass of synthesized powder is loaded into a hardened steel strip matrix. The forming unit was controlled by a hydraulic press to compress the loose powder into a thick cylindrical pellet with flat, parallel faces and mechanical stability.

To ensure optimal electrical contact during impedance measurement, the sputter coating system deposited a thin gold layer (Au) on the upper and lower surfaces of the compressed pellet. The double-sided gold coating acts as a highly conductive contact interface and minimizes the contact resistance between the sample surface and the testing electrode during frequency-dependent electrical testing.

The pellet thickness and area were measured and are presented in Table 3.4.

Table 3-4: Thickness and area of the prepared pellets of GO, SbSI, GO-SbSI composites and GMS composites.

Sample	Thickness (10^{-3} m)	Area (10^{-4} m^2)
GO	1.414 (15)	3.584 (48)
GO-SbSI 70/30	1.328 (84)	3.556 (26)
GO-SbSI 60/40	1.292 (15)	3.545 (47)
GO-SbSI 50/50	1.278 (19)	3.541 (60)
GO-SbSI 40/60	1.338 (18)	3.560 (56)
GO-SbSI 30/70	1.134 (55)	3.496 (17)
SbSI	1.302 (13)	3.548 (41)
GSM 1:20:80	1.782 (12)	3.699 (28)
GSM 1:30:70	1.832 (22)	3.715 (52)
GSM 1:40:60	1.845 (63)	3.719 (24)
GSM 1:50:50	1.720 (29)	3.682 (48)
GSM 1:60:40	1.867 (15)	3.726 (46)
GSM 1:70:30	1.623 (18)	3.649 (54)
GSM 1:80:20	1.582 (14)	3.636 (38)

3.3.5 Electrochemical measurement

To perform electrochemical measurements, a working electrode was fabricated from the material under investigation. The slurry for the working electrode was prepared using a total mass of 20 mg at a ratio of 80:15:5 wt.% for the active composite material, polyvinylidene fluoride (PVDF) binder, and carbon black conductive additive, respectively. The precise quantity of each component was calculated by defining a target total dry batch mass, allocating the respective weight fractions

according to this 80:15:5 ratio, and weighing the raw powders on an analytical balance before transferring them into an agate mortar. The mixture was thoroughly ground and homogenized with the gradual addition of a few drops of N-methyl-2-pyrrolidone (NMP) solvent to achieve a smooth, viscous paste. This slurry preparation stage is visually demonstrated in Figure 3.10 for two representative composite variants within the sample series: panel (a) depicts the grinding of a brown-tinted composite paste, while panel (b) shows the completed homogenization of a black-tinted slurry variant.

Pre-cleaned nickel foam current collectors with total dimensions of 1.5 cm × 1 cm were utilized, and a defined 1.0 × 1.0 cm^2 active area was coated with the prepared slurry using the doctor-blade coating method. As illustrated in the photographs in Figures 3.10c and 3.10d, the resulting working electrodes feature a uniform, flat composite layer covering the designated 1cm2 active zone-showing the brown-tinted and black-tinted material variants, respectively-while leaving the remaining top section of the silver metallic foam uncoated to serve as the electrical contact for testing. After this coating step, the fabricated electrodes were dried at 50 ºC in an oven to remove the residual NMP solvent before electrochemical measurements.

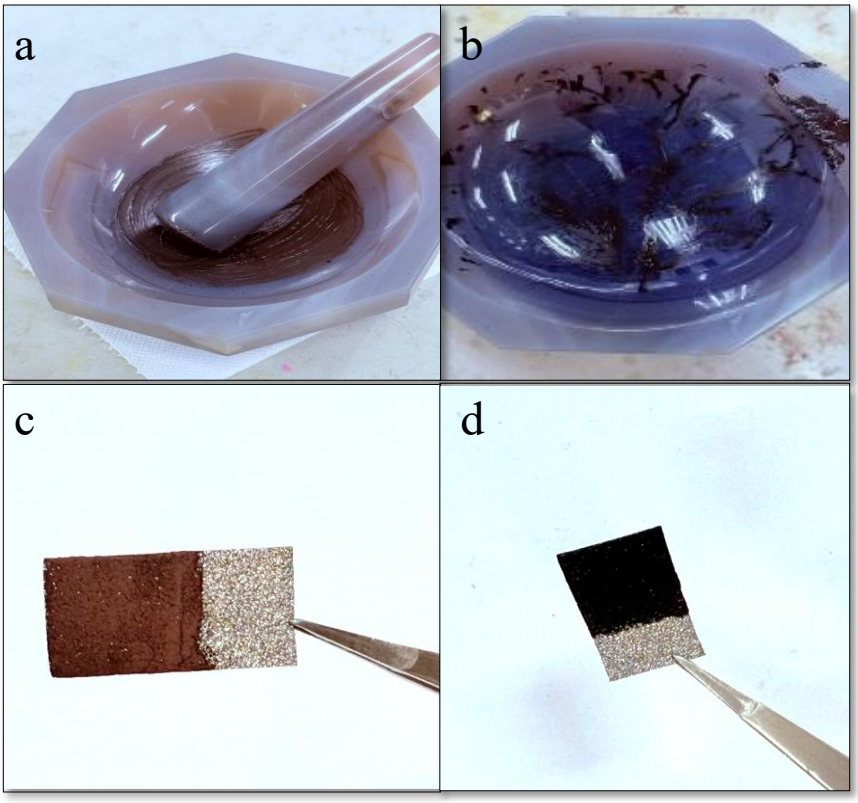


Figure 3.9: Visual presentation of the working electrode fabrication process: (a) grinding and homogenization of a SbSI paste with an agate mortar and pestle, (b) a fully homogenized GO-SbSI composite slurry variant coating the mortar walls, (c) a nickel foam current collector coated with the SbSI slurry, and (d) a nickel foam current collector coated with the GO-SbSI composite slurry variant, both showing a defined 1.0cm^2 active area and an exposed metallic section for electrical testing contact.

The mass of the active material loaded onto the working electrode was determined by the mass difference method. The bare electrode substrate was first cleaned and weighed using an analytical balance. The as-prepared slurry was then coated onto the electrode and dried, after which the electrode was weighed again. The mass loading of the active material was calculated from the difference between the final and initial weights. The values of mass are presented in Chapters 7 and 8.

Chapter 4

MORPHOLOGY AND STRUCTURAL STUDY

In order to confirm that the desired GO, SbSI, and GO-SbSI composites were successfully obtained through the synthesis processes described in Chapter 3, a series of morphological and structural studies were carried out. Scanning electron microscopy (SEM) and field-emission scanning electron microscopy (FESEM) were employed to examine the surface morphology, microstructure, and dimensions of the synthesized materials, while energy-dispersive X-ray spectroscopy (EDS) was used to verify their elemental composition and confirm the incorporation of the expected constituent elements. X-ray diffraction (XRD) analysis was performed to identify the crystalline phases present and evaluate phase purity, thereby verifying the formation of the intended crystal structure. Finally, X-ray photoelectron spectroscopy (XPS) was carried out to investigate the surface chemical composition and oxidation states of the elements, providing further confirmation of the chemical nature of the synthesized compounds and composites.

4.1 Morphology and EDS Analysis

To obtain higher-resolution images of the synthesized samples, the synthesized materials were examined using a Phenom ProX Desktop scanning electron microscope (model 800-07334) at the Institute of Physics, Centre for Science and Education, Silesian University of Technology, Katowice, Poland. The samples with gold coating supported on silicon chips were secured to aluminum stubs using conductive carbon tape and analyzed under high-vacuum conditions at room temperature using an accelerating voltage of 15 kV.

FESEM was carried out using a FEI Verios 460L XHR-FESEM, used with the permission of the School of Materials and Mineral Resources Engineering, Universiti Sains Malaysia. The samples were sputter-coated with a thin conductive layer of platinum before analysis to prevent charging effects, and images were recorded at room temperature under an accelerating voltage of, e.g., 15 kV at various magnifications. The resulting images were used to evaluate the size, shape, surface texture, distribution, and agglomeration of the nanowires and composite components.

4.1.1 SEM of GO

The SEM image of the GO is presented in Figure 4.1. The micrograph of GO reveals an exfoliated sheet assembly with localized multi-layer folding exhibiting the characteristic two-dimensional (2D) lamellar morphology of GO. The sheet displays a thin, flake-like surface morphology under the electron beam, with pronounced wrinkling, folding, and crumpling along its periphery. These surface deformations arise from the intrinsic flexibility of the exfoliated GO layers and from the presence of oxygen-containing functional groups (hydroxyl, epoxide, and carboxyl groups) introduced during the oxidation of graphite, which disrupt the planarity of the sp^2 carbon lattice. The edges of the

sheet are irregular and folded over themselves in places, a feature commonly observed in GO due to the restacking and curling tendency of individual layers upon drying. Similar GO sheet morphologies have been reported in the literature [153-155].

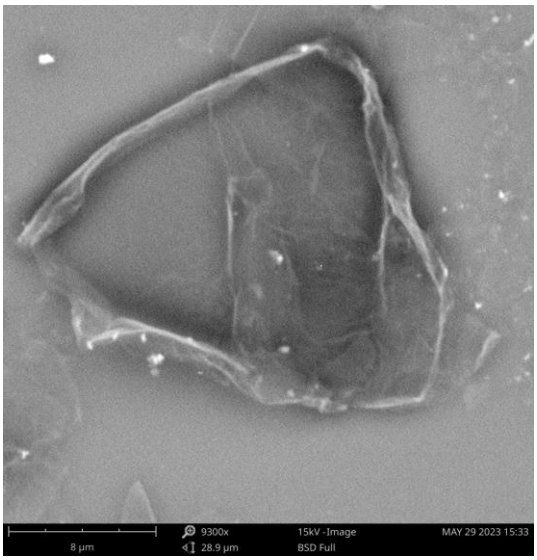


Figure 4.1: SEM surface morphology of Graphene Oxide flake, highlighting the folded edges and flat basal planes indicative of successful liquid-phase chemical exfoliation.

4.1.2 SEM of SbSI

The SEM image of the SbSI is presented in Figure 4.1b.

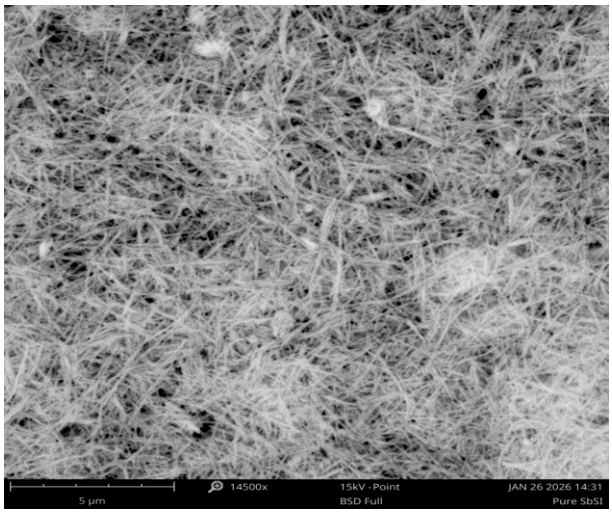


Figure 4.2: SEM micrograph showcasing the morphology and structural distribution of the synthesized SbSI nanostructures.

The micrograph of SbSI shows a highly uniform and densely packed network of long, thin, needle-like (whisker-shaped) crystallites randomly oriented and entangled across the entire field of view. The whiskers appear relatively uniform in width and are distributed homogeneously, forming a

continuous fibrous network. This morphology is consistent with the known one-dimensional, needle-like crystal habit of SbSI, which arises from its chain-like crystal structure and anisotropic growth behavior along the c-axis. Almost the same morphology of SbSI nanowires is observed in the literature [156-158].

4.1.3 SEM of GO-SbSI Composites

The morphology of GO-SbSI composites with different composites is presented in Figure 4.3 (a-e).

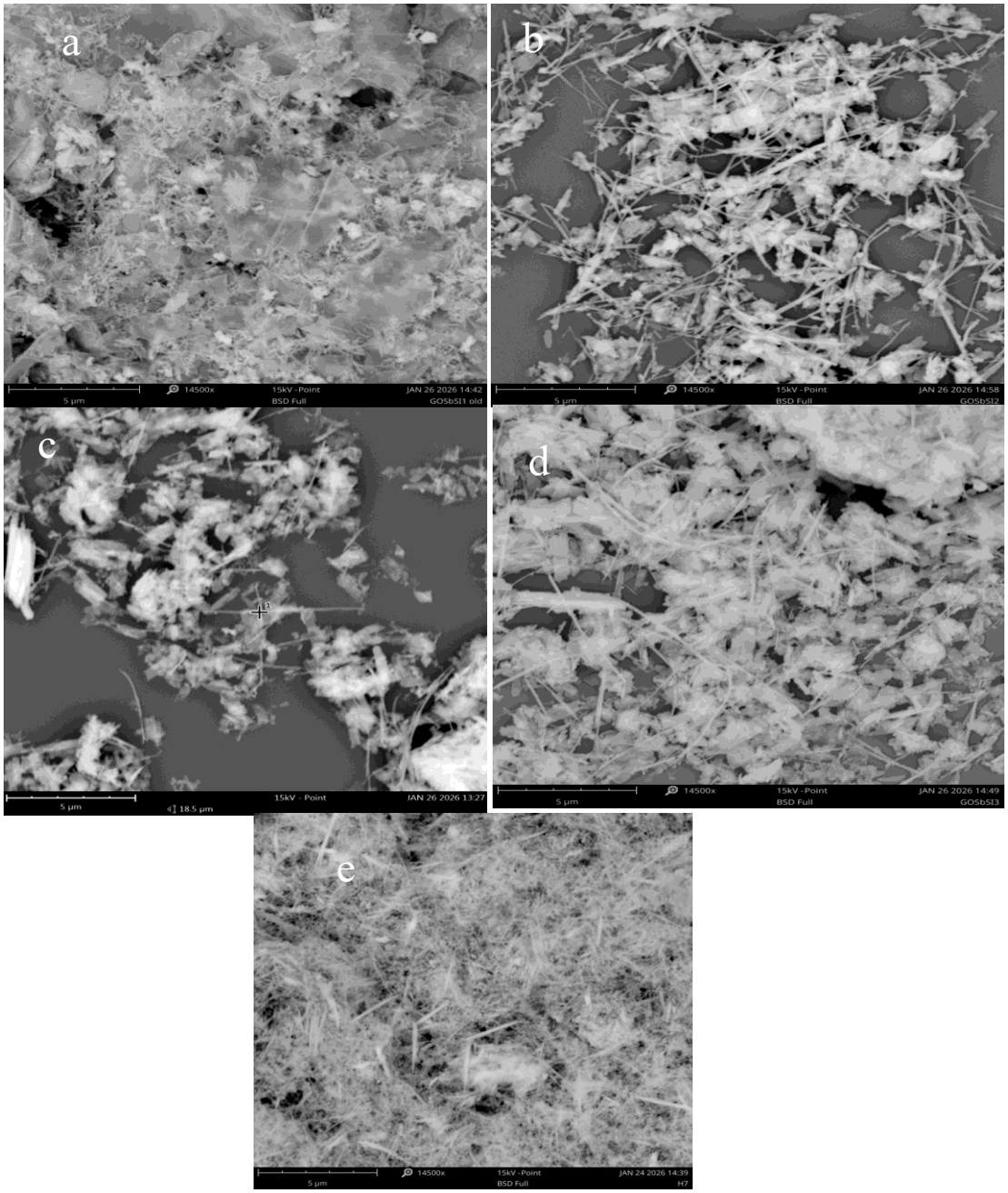


Figure 4.3: The SEM micrographs showing the surface morphology of GO-SbSI composites; a) GO-SbSI 70/30, b) GO-SbSI 60/40, c) GO-SbSI 50/50, d) GO-SbSI 40/60, e) GO-SbSI 30/70, illustrating the integration of the components.

The micrograph shows a heterogeneous surface in which residual flake-like GO fragments coexist with a comparatively sparse distribution of fine, elongated, needle-like structures corresponding to SbSI. The GO component still appears as the dominant matrix phase, forming irregular plate-like fragments and folded sheet remnants, while the SbSI phase is distributed as thin wires interspersed between and over these fragments.

With an increase in SbSI content to 40 wt.%, the density of the wire structures increases perceptibly compared to Figure 4.3b. The image shows a denser network of thin, rod-shaped SbSI crystallites randomly oriented across the sample, dispersed with smaller and more fragmented GO platelets than were observed at the 70:30 ratio. The GO sheets no longer appear as large continuous flakes, but rather as broken, plate-like clusters partially embedded within the growing SbSI network. This suggests that as the relative proportion of SbSI increases, the one-dimensional whisker growth becomes the predominant morphological feature, leading to a highly interconnected crystal network that encapsulates and anchors the fragmented GO flakes.

At an equal weight ratio of GO and SbSI (50/50), the micrograph shows a further densification of the fibrous network, with needle-like SbSI structures now forming a more interconnected mesh across the imaged area in Figure 4.3c. Larger, brighter clusters of plate-like material remain visible, which likely correspond to residual GO aggregates or regions of denser SbSI nucleation. Compared to Figures 4.3a and b, the flat flake surfaces are mostly covered, replaced by a dense network of shorter, more crowded growths. This shows that the material morphology shifts dominantly toward a wire-like structure as the growth of the one-dimensional chalcohalide phase becomes more extensive, progressively covering and intercalating within the underlying GO framework.

As the SbSI content is increased further to 60 wt.% (60/40), the micrograph (Figure 4.3d) shows a markedly denser and more compact arrangement of needle-like features. The needle-like SbSI crystallites are shorter and more densely packed, and the platelet fragments appear smaller and more numerous, giving the surface a granular, high-density texture rather than the more open, sparsely distributed morphology seen at lower SbSI loadings. This progressive densification is consistent with increased nucleation density of the SbSI phase as its relative concentration in the precursor mixture rises.

At the 30/70 ratio (Figure 4.1e), the morphology is dominated almost entirely by elongated, needle-like growth, with only minor and scattered evidence of residual plate-like GO fragments. The image shows a fibrous, mat-like texture in which individual SbSI crystallites overlap and interweave extensively, forming a network that closely resembles the morphology of SbSI (Figure 2), though with a somewhat coarser and less uniform fiber distribution. The reduction in GO content to 30 wt.% is reflected in the near-disappearance of the sheet-like features that were prominent at the higher GO ratios.

Overall, the binary composition series reveals a clear structural transition from a matrix dominated by large, flat two-dimensional GO sheets with isolated chalcohalide needles at low loading levels, to a highly dense, interwoven network of quasi-one-dimensional SbSI nanowires that progressively coats, breaks up, and encapsulates the carbon framework as the chalcohalide concentration increases.

4.1.4 Nanowire Length Distribution of SbSI and GO-SbSI Composites

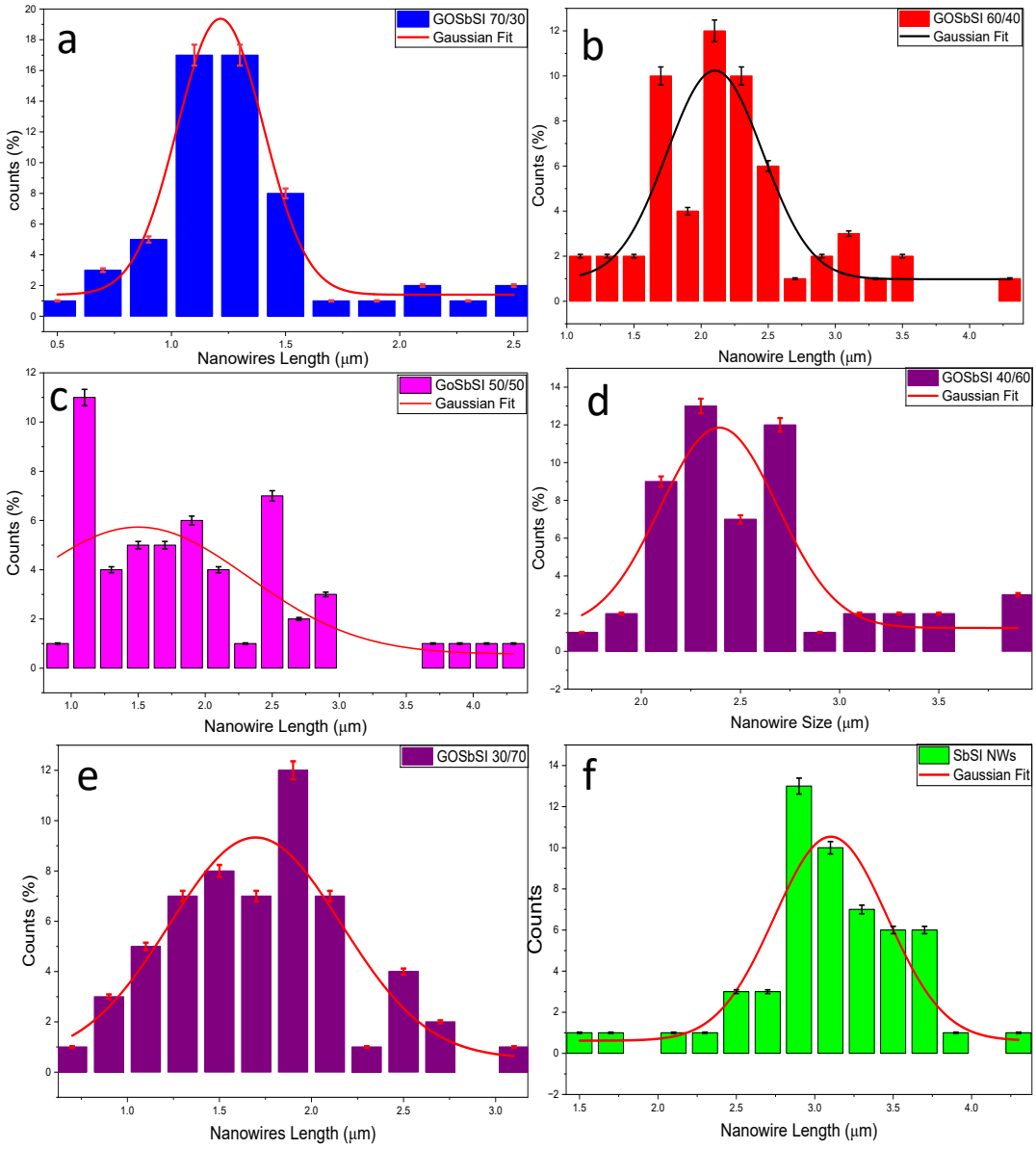


Figure 4.4: Nanowire size distribution histograms with corresponding Gaussian fits for a) GO-SbSI 70/30, b) GO-SbSI 60/40, c) GO-SbSI 50/50, GO-SbSI 40/60, GO-SbSI 30/70, and SbSI.

To quantify the effect of GO content on the dimensional characteristics of the SbSI nanowires within the composites, histograms of nanowire length distribution were constructed from SEM image analysis and fitted with Gaussian functions, as presented in Figure 4.4(a-f). The dimensions of the

nanostructures were quantified using ImageJ software directly from the high-magnification SEM micrographs. The software calibration was established against the internal scale bar of each micrograph to ensure accurate pixel-to-micrometer conversion. To ensure statistical validity, approximately 60-70 distinct, non-overlapping SbSI nanowires were randomly selected and measured across multiple fields of view for each composite ratio. The length of each nanowire was determined by measuring its full longitudinal span from tip to tip along its long axis. The compiled measurements were then plotted to generate the size distribution profiles used to calculate the average length distribution.

The statistical parameters extracted from the Gaussian fitting of the nanowire length distribution histograms alongside the corresponding chemical compositions determined by EDS are comprehensively summarized in Table 4.1. The statistical data reveal that the concentration ratio strongly influences the growth kinetics and final size uniformity of the chalcohalide phase. In the absence of a carbon template, pure SbSI displays the largest average length (3.103(54) μm) with a clean single-peak profile. The introduction of the GO framework generally limits the maximum growth along the c-axis, forcing a shift toward shorter average nanowire lengths. However, this dimensional suppression is non-linear. At intermediate loading ratios (such as the 50/50 and 60/40 balances), the distribution profiles broaden significantly and show lower R^2 values, which stems from localized mass crowding and competitive nucleation at active sites on the carbon planes. In contrast, at the extreme boundaries of the series (70/30 and 30/70 ratios), the systems stabilize into highly homogeneous, uniform single-peak size regimes with narrow widths and high R^2 values exceeding 0.95, demonstrating that well-defined composition limits are mandatory to secure size uniformity.

Table 4-1: Gaussian fitting parameters of SbSI nanowire length distributions and EDS-derived elemental compositions and normalized Sb:S:I shares of GO-SbSI composites and SbSI.

Sample composition (GO/SbSI, wt.%)	Mean nanowire length, μ (μm)	Goodness of fit (R^2)	Oxygen, O (at. %)	Antimony, Sb (at. %)	Iodine, I (at. %)	Sulfur, S (at. %)	Normalized SbSI share (Sb:S:I, at. %)
70/30	1.214(10)	0.98	43.38	12.08	6.22	2.42	58:11:30
60/40	2.103(65)	0.91	54.31	8.92	2.16	3.25	62:22:15
50/50	1.50(33)	0.78	44.68	5.19	1.14	4.2	49:39:10
40/60	2.392(66)	0.93	50.45	11.6	4.55	7.17	49:30:19
30/70	1.696(71)	0.95	46.42	12.2	4.52	8.9	47:34:17
SbSI	3.103(54)	0.97	-----	28.14	17.87	14.32	46: 23:29

4.1.5 FESEM of GSM composites

Across the entire GSM ternary series, the micrographs reveal a common architectural framework characterized by an interwoven network of 1D nanowires and needle-like crystallites integrated with the underlying carbon matrix, uniformly accompanied by nanoscale particulate

decorations. At the lowest SbSI to MnO_2 ratio (GSM 1:20:80), the micrograph reveals a dense, highly aligned network of long, thin, needle-like nanowires uniformly distributed across the entire field of view in Figure 4.5a. The wires appear relatively straight and slender, with a narrow diameter and a rough, granular surface texture arising from a fine coating of small, discrete nanoparticles decorating their length. This granular decoration, combined with the exceptionally high areal density of thin fibers, is consistent with MnO_2 being the dominant phase at this composition, as these specific high-aspect-ratio fiber dimensions directly match the structural signatures established for the pristine hydrothermally synthesized MnO_2 nanowires detailed in Chapter 3. The wires are densely packed and randomly oriented, forming a compact, felt-like network with minimal open porosity. Also, it is worth noting that similar dot-like features were observed in all GSM samples, with their abundance increasing in proportion to the SbSI ratio, suggesting a direct correlation between these particulate features and the chalcohalide phase.

As the SbSI proportion increases relative to MnO_2 (1:30:70), the micrograph (Figure 4.5b) shows a somewhat less densely packed arrangement of rod-like structures, several of which appear noticeably brighter, thicker, and more faceted than the surrounding thinner wires. Radially clustered aggregates are visible near the center of the image, where multiple wires appear to emanate from a common nucleation point. The coexistence of two distinguishable morphologies-thinner, more numerous fibers and thicker, brighter rods-suggests the early emergence of a second nanowire population as the SbSI content increases from the previous composites.

At this intermediate composite (1:40:60), the network consists of moderately long, needle-shaped wires oriented in multiple directions, forming a loosely interwoven mesh in Figure 4.5c. The wire surfaces continue to display a fine granular texture, and the overall wire diameter appears slightly larger and more variable than in Figure 4.5a, reflecting the growing contribution of the SbSI phase alongside the still-substantial MnO_2 content. The density of the network remains high, though slightly more open spacing between wire bundles is visible compared to the lower SbSI-content samples.

At equal proportions of SbSI and MnO_2 (1:50:50), the micrograph shows a coarser (Figure 4.5d), more heterogeneous network composed of both thin, granular wires and considerably thicker, smoother rod-like structures with more well-defined facets and larger diameters. One particularly prominent, elongated rod spans much of the image, its smoother surface and larger cross-section contrasting sharply with the finer, more textured wires surrounding it. This coexistence of two clearly distinguishable morphological populations-fine, dotted wires versus thick, smooth rods-becomes most apparent at this near-equal composition.

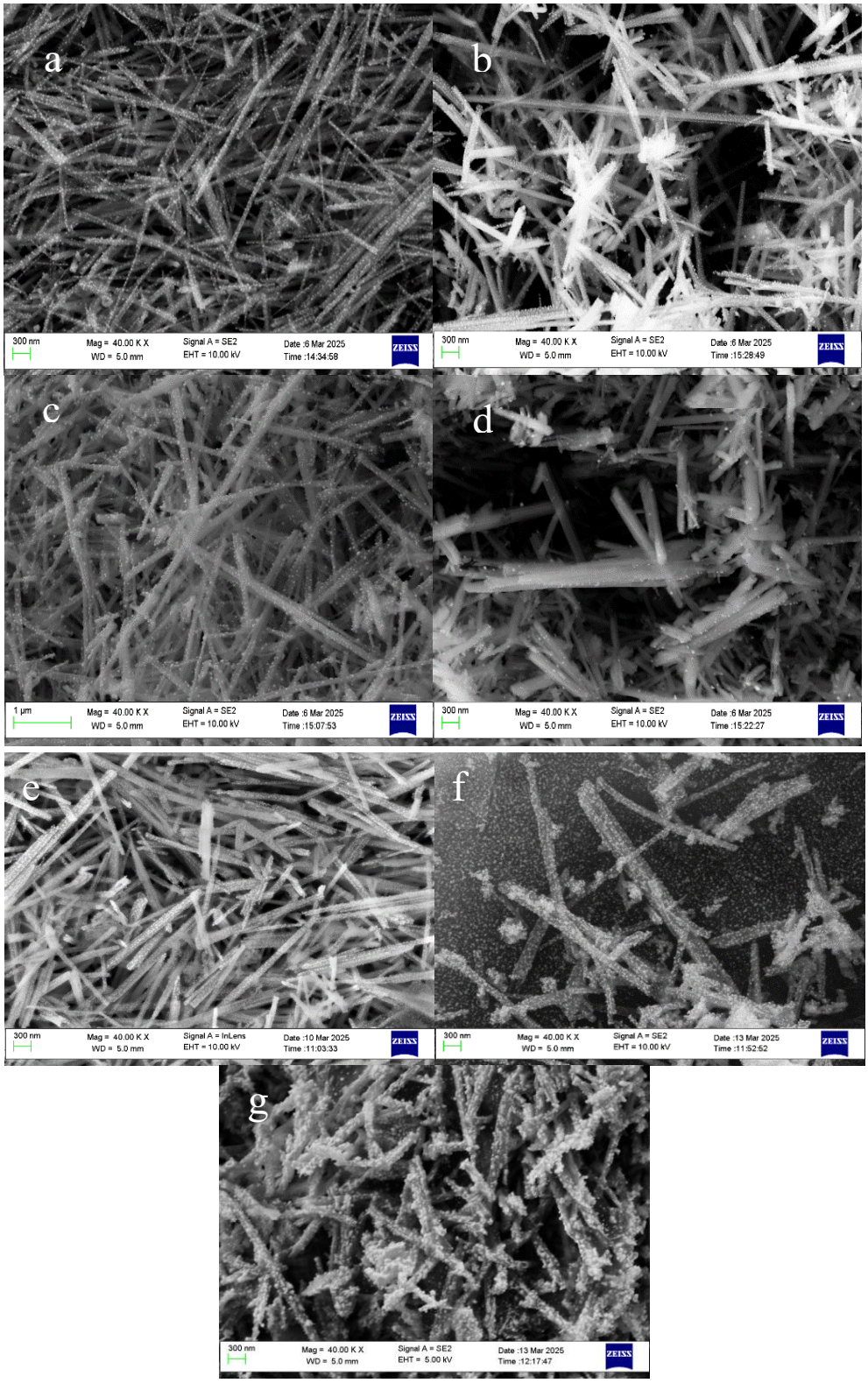


Figure 4.5: Scanning electron microscopy micrographs displaying the surface morphology and interlocking structure of the hybrid GSM nanocomposites; a) GSM 1:20:80, b) GSM 1:30:70, c) GSM 1:40:60, d) GSM 1:50:50, e) GSM 1:60:40, f) GSM 1:70:30, and g) GSM 1:80:20.

In GSM 1:60:40, with SbSI now present in a larger proportion than MnO_2, the micrograph in Figure 4.5e shows an increased density of longer, thicker, and more clearly faceted rod-like structures with smoother surfaces, interspersed with a smaller number of thinner, granular fibers. The overall texture of the network shifts toward larger, more elongated crystallites, consistent with SbSI nanowire growth becoming increasingly dominant as its relative concentration rises. The wires remain densely entangled, though the increased average wire thickness gives the network a coarser overall appearance than at lower SbSI ratios.

In GSM 1:70:30, At this composition, the Figure 4.5f shows a markedly sparser, more open network in which thick, smooth-surfaced rods with well-defined facets are the clearly dominant feature, with only a light dusting of small nanoparticles visible on the substrate and along portions of the rod surfaces. The wires are noticeably longer and thicker than in the MnO_2-rich composites, and the reduced areal density suggests fewer nucleation sites overall, consistent with the diminished MnO_2 content limiting the population of fine secondary crystallites.

At the highest SbSI-to-MnO_2 ratio (1:80:20), Figure 4.5g shows a dense, coral-like or branched network of relatively thick, rough-surfaced wires, many of which appear to radiate outward from common junction points in a dendritic or bush-like arrangement. The wire surfaces are covered with a continuous fine granular coating, giving them a rugged, textured appearance distinct from the smoother rods seen at intermediate SbSI ratios. This branched, high-density morphology, combined with the dominant SbSI content nominally expected at this composition, indicates a more complex, interconnected growth pattern at the highest SbSI loading examined.

4.1.6 Nanowire Length Distribution of GSM Composites

To quantify the influence of the SbSI-to-MnO2 ratio on the dimensional characteristics of the nanowires within the GSM ternary composites, length distribution histograms were constructed from SEM image analysis and fitted with Gaussian functions, as shown in Figure 4.6(a-g). The length measurements were extracted using ImageJ software by calibrating the pixel density against the internal micrometer scale bar of each micrograph. For each ternary ratio, a representative pool of approximately 60 distinct, non-overlapping nanowires was randomly selected across multiple fields of view. The length of each structure was registered by manually tracing a linear vector from tip to tip along its longitudinal axis. Due to the dense packing and the frequent alignment of individual nanowires into tight bundles, the physical thickness of the fibers could not be resolved with sufficient statistical accuracy from the FESEM images; consequently, this statistical geometric characterization focuses exclusively on the continuous length profiles.

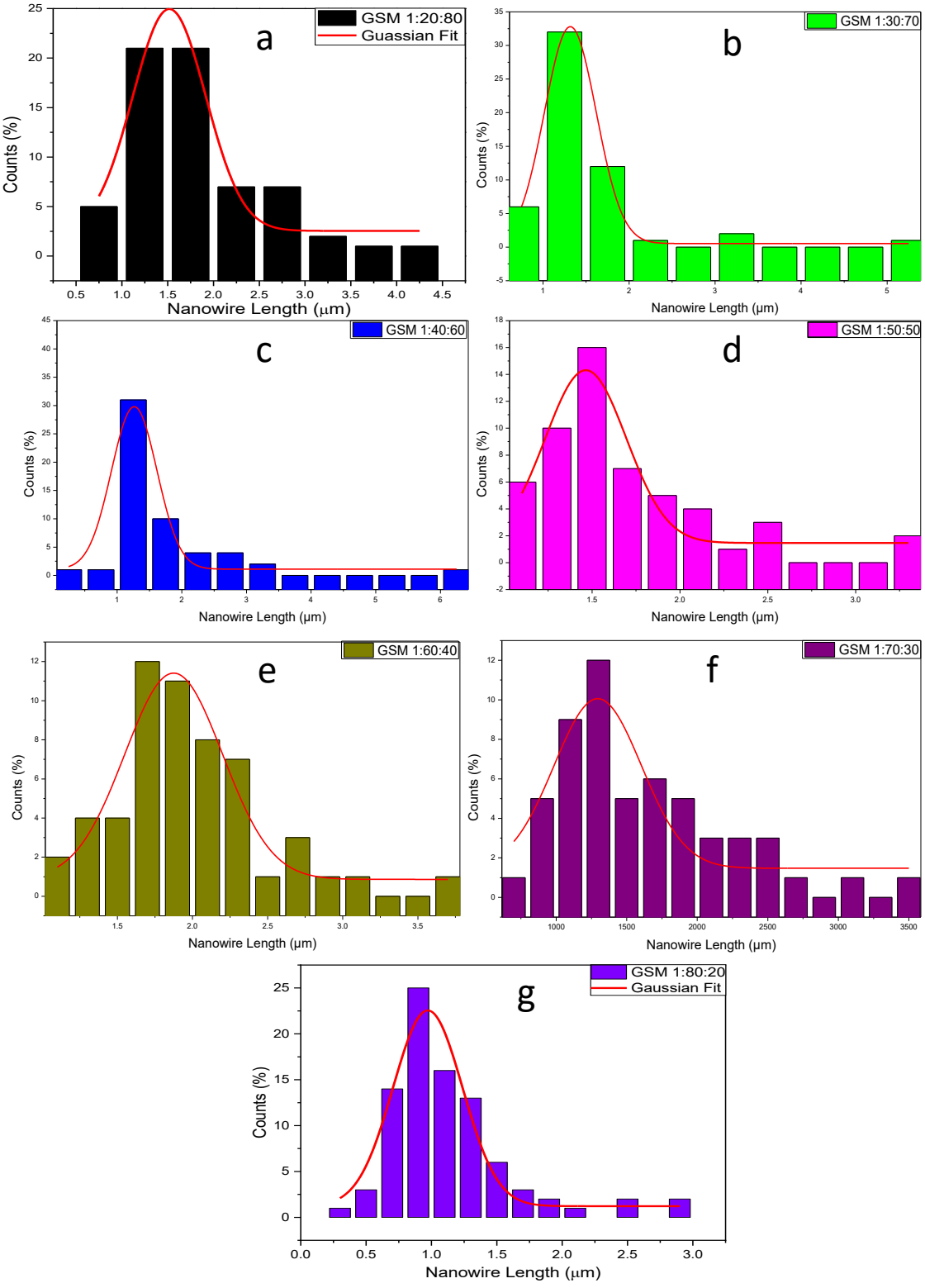


Figure 4.6:The calculated nanowire size distribution of prepared sample; a) GAM 1: 20:80, b) GSM 1:30:70, c) GSM 1:40:60, d) GSM 1:50:50, e) GSM 1:60:40, f) GSM 1:70:30, and g) GSM 1:80:20.

The statistical parameters extracted from the Gaussian fitting of the nanowire length distribution histograms alongside the corresponding chemical compositions determined by EDS are

comprehensively summarized in Table 4.2. The morphological dimensions and elemental compositions highlight a profound divergence from ideal chalcohalide stoichiometry alongside a non-linear structural evolution. Across all ternary mixtures, the normalized atomic ratios reveal a heavily antimony-rich and severely iodine-deficient composition. This non-stoichiometry aligns with literature regarding sonochemically processed chalcohalide composites, where high-energy acoustic cavitation leads to localized thermal micro-zones that induce volatile escape of iodine species and favor the precipitation of unreacted antimony clusters over a balanced crystalline lattice. The raw oxygen concentration displays a complex, non-linear downward trend, dropping from a maximum of 53.29 at. % in the oxide-heavy matrices to a baseline of roughly 33.02 at. % in the chalcohalide-heavy samples, reflecting the changing volumetric shares of the highly oxygenated MnO_2 and GO templates. Geometrically, the average nanowire length decreases non-linearly as the SbSI share rises, culminating in the smallest dimensions (0.97(3) μm) at the 1:80:20 ratio. This dimensional contraction matches uniform single-peak size distribution histograms with high R^2 values exceeding 0.95 at the series boundaries, whereas intermediate loading levels (such as the 1:50:50 sample) exhibit poor multi-peak profiles and lower R^2 values due to severe competitive mass-crowding between the growing chalcohalide phases and the surrounding oxide networks.

Table 4-2: Gaussian fitting parameters of SbSI nanowire length distributions and EDS-derived elemental compositions of GO/SbSI/MnO_2 composites.

Sample designation	Mean nanowire length, μ (μm)	Goodness of fit (R^2)	Oxygen, O (at.%)	Antimony, Sb (at.%)	Sulfur, S (at.%)	Iodine, I (at.%)	Normalized SbSI share (Sb:S:I, at.%)
GSM 1:20:80	1.52(5)	0.94	51.54	1.39	1.64	0.07	44:52:3
GSM 1:30:70	1.317(12)	0.93	49.94	3.66	2.23	0.57	56:34:8
GSM 1:40:60	1.26(6)	0.95	53.29	4.04	1.85	0.51	63:28:7
GSM 1:50:50	1.46(3)	0.82	10.22	8.93	1.51	1.68	73:12:13
GSM 1:60:40	1.87(3)	0.91	43	6.4	3.43	1.63	55:29:14
GSM 1:70:30	1.294(55)	0.88	33.46	8.98	7.83	3.68	43:38:17
GSM 1:80:20	0.97(3)	0.96	33.02	16.2	6.96	3.72	60:25:13

4.2 Transmission electron microscopy (TEM)

Transmission electron microscopy is an analytical technique that is used to study the internal structure and morphology of materials at very high magnification with nanometer and even atomic-scale resolution.

TEM of GO, SbSI, and the GO-SbSI binary composites was examined using a JEOL JEM 3010 high-resolution transmission electron microscope (HRTEM) operating at 300 kV, located at the Faculty of Science and Technology, University of Silesia (Chorzów, Poland). Conversely, the structural

analysis of the GSM ternary nanocomposites was performed using an FEI TECNAI G2 20 S-TWIN field emission transmission electron microscope operating at 200 kV, supported by the School of Materials and Mineral Resources Engineering, Universiti Sains Malaysia (Penang, Malaysia).

4.2.1 TEM of GO

TEM images showing the morphology of the GO sheets at two magnifications are presented in Figure 4.7. Figure 4.7a shows a low-magnification view of a single, electron-transparent GO flake with an irregular, folded polygonal outline and characteristic surface wrinkles. Darker contrast in the central region indicates localized restacking or multilayer folding, within which several straight, high-contrast filamentous structures are embedded, suggesting entanglement with elongated nanostructures. Figure 4.7b shows a higher-magnification view of a more densely crumpled graphene oxide aggregate, in which a bundle of dark, twisted fibrous strands is clearly intertwined with the folded sheet, while the surrounding translucent regions retain the same fine wrinkle texture seen in Figure 4.7a. Together, the images illustrate the thin, flexible, wrinkled nature of the graphene oxide sheets and their intimate physical entanglement with the embedded filamentous nanostructures.

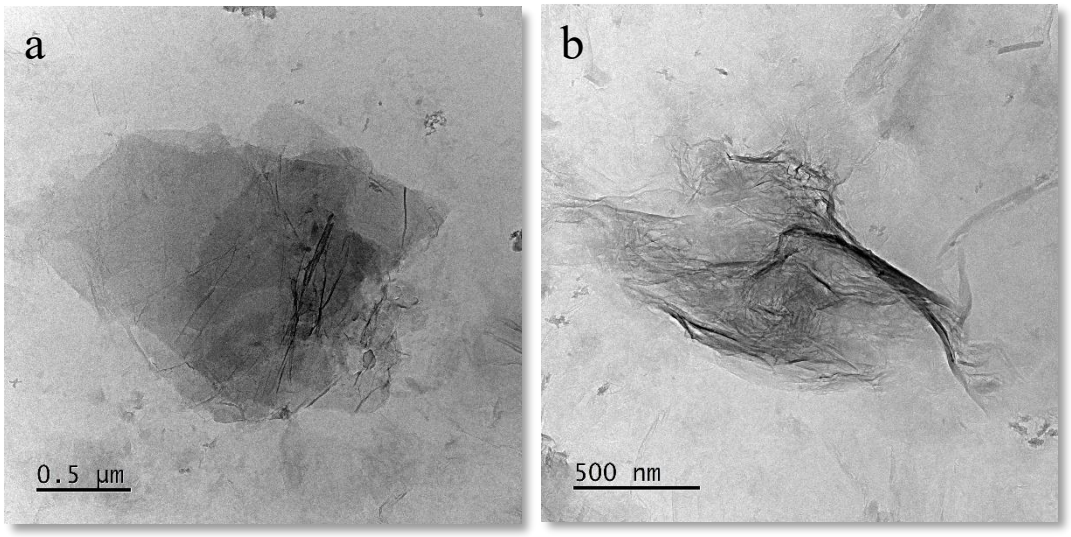


Figure 4.7: TEM micrographs revealing the morphology of synthesized graphene oxide sheets at two different regions (a and b).

4.2.2 TEM of SbSI

TEM micrographs characterize the morphology, thickness, and crystal structure of the synthesized SbSI nanostructures at progressive magnifications. Figure 4.8a presents a primary magnification view of individual SbSI nanowires displaying a straight, needle-like morphology. These 1D structures exhibit a relatively uniform thickness ranging from 40 to 80 nm along their length. Small dot-like nanoscale features are uniformly distributed along the nanowire surfaces, creating a rough, decorated surface texture [159]. This surface topology is consistent with the EDS results, which show

a higher-than-expected Sb content and a lower S content relative to the theoretical stoichiometry of SbSI, suggesting the formation of an antimony-enriched surface phase along the crystalline core boundaries.

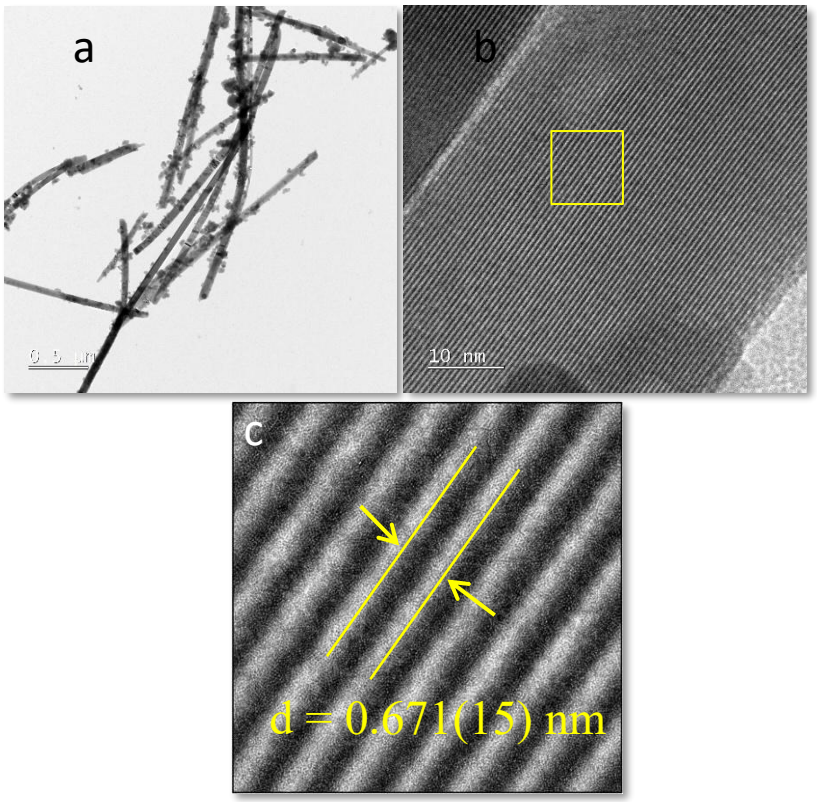


Figure 4.8: Electron diffraction and structural characterization of the chalcohalide phase: (a) TEM micrograph of individual SbSI nanowires showing a needle-like morphology with fine surface decorations, (b) HRTEM lattice image of a single nanowire core, and (c) magnified view of the atomic fringes showing a resolved d-spacing of 0.671(15) nm matching the (110) crystallographic plane.

Figure 4.8b shows a high-resolution TEM image of a single nanowire, revealing well-defined, continuous lattice fringes running parallel to the nanowire's long axis, confirming its single-crystalline nature; the yellow box marks the region magnified in Figure 4.8c. This magnified view of the localized lattice matrix (Figure 4.8c) displays clearly resolved, parallel atomic planes with an interplanar d-spacing of 0.671(36) nm, as directly quantified via ImageJ software. This value is in exceptional agreement with the reported spacing of approximately 0.6517 nm along the c-axis growth direction, matching the established values derived from the standard orthorhombic lattice parameters of SbSI [160]. This close correlation provides definitive proof, indexing the observed atomic fringes to the (001) crystallographic plane of orthorhombic SbSI, confirming the highly ordered, single-crystalline structural integrity of the sonochemically grown nanowires, which maintain a general longitudinal length of approximately 2.5 μm.

4.2.3 TEM of GO-SbSI Composites:

The morphology of the GO-SbSI composites was investigated by TEM (Figure 4.9). The micrographs show that the GO:SbSI ratio strongly influences the size, shape, and spatial distribution of the SbSI nanostructures, as well as the appearance of the GO support. In all images, two types of features can be distinguished: light, thin, and semi-transparent areas, attributed to GO sheets, and dark, high-contrast needle- or rod-like objects, attributed to SbSI. The higher contrast of SbSI results from the higher electron density of the heavy elements (Sb, I) compared with the carbon-based GO.

In the sample with the highest GO content (70/30, Figure 4.9a), the micrograph is dominated by a large, thin GO sheet extending over most of the TEM image. The sheet has wrinkled and folded regions, which are typical of few-layer GO. Numerous needle-like SbSI nanowires of different lengths lie on the surface of the sheet and along its edges. This indicates that in a GO-rich composite, the sheets act as a large support on which the SbSI nanostructures are dispersed.

When the SbSI content increases to 40% (60/40, Figure 4.9b), the morphology of the image changes. Long, straight or slightly curved SbSI nanowires and their bundles cross the field of view and often overlap. Thin GO fragments and small flakes are attached to the surface of the nanowires or adjacent to them, and only a limited area of free GO sheet is visible. Individual nanowires are considerably longer than the rods observed in the 70/30 sample, and the nanowires form partly interconnected, network-like arrangements.

In the 50/50 composite (Figure 4.9c), a thick, elongated, and slightly curved SbSI nanowire dominates the image. Its surface is rough and covered with small, dark particles, which gives the nanowire a decorated appearance. Noted, fragmented GO flakes with irregular edges are visible in the surrounding area of the wire and partially in contact with it. A similar morphology is observed for the 40/60 sample (Figure 4.9d), where a thick nanowire or nanowire bundle with alternating darker and lighter segments is in contact with GO sheet fragments. In both samples, the GO is present mainly as small, thin fragments rather than extended sheets, and the SbSI is the main structural component.

In the sample with the highest SbSI content (30/70, Figure 4.9e), the composite is composed of dense agglomerates of SbSI nanowires and dark flakes. These agglomerates are surrounded by a fragmented, web-like GO network with thin filaments extending outward. Compared with the samples containing less SbSI, the nanostructures are shorter and more clustered, and they are no longer distributed evenly over the GO.

Overall, the TEM observations show a gradual change in morphology with the GO:SbSI ratio. At high GO content, SbSI nanowires are dispersed over large GO sheets. At intermediate ratios (60/40 to 40/60), the SbSI nanowires become larger and dominate the structure, while the GO is reduced to small flakes attached to them. At the highest SbSI loading, the nanostructures tend to agglomerate, which may limit the effective contact between the two phases.

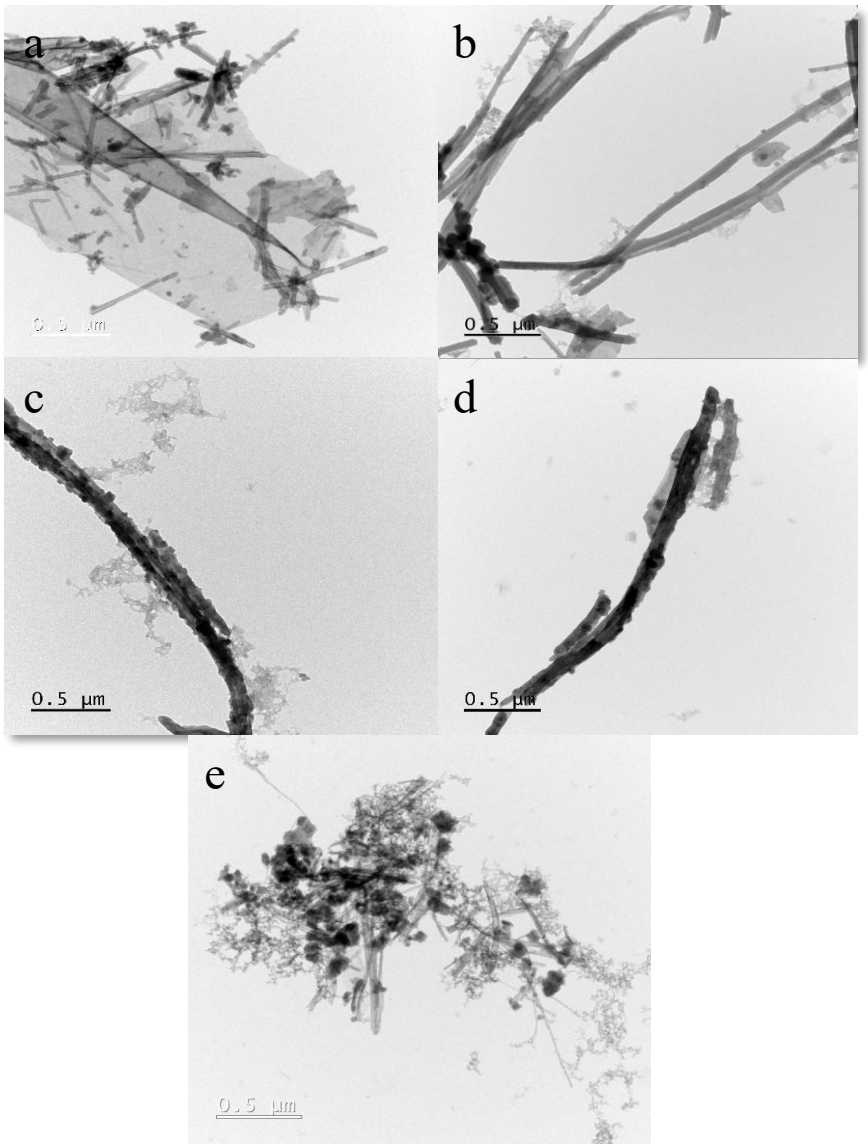


Figure 4.9: TEM micrographs showing the morphological growth across the developed GO-SbSI binary composite series at a uniform 0.5 µm scale: (a) GO-SbSI 70/30, (b) GO-SbSI 60/40, (c) GO-SbSI 50/50, (d) GO-SbSI 40/60, and (e) GO-SbSI 30/70.

4.2.4 TEM of GSM 1:20:80 and GSM 1:80:20

The morphology and crystal structure of the GSM composite with a ratio of 1:20:80 were investigated by HRTEM (Figure 4.10). In this composite, MnO_2 is the main component, SbSI is present in a smaller amount, and GO is only a minor additive. The primary magnification view (Figure 4.10a) shows long, straight, rod-like and ribbon-like 1D nanostructures with lengths extending across several micrometers. Because both the main MnO_2 phase and the secondary SbSI component naturally crystallize into high-aspect-ratio wire shapes, they form a co-existing, extensively interwoven nanowire matrix. These nanowires differ in thickness and cross or overlap each other. Their surfaces show dark segments and small dark spots, which correspond to local thickness variations or to fine

particles deposited on the wires. Small, irregular, and angular particles and thin flakes belonging to the GO sheets are scattered between the nanowires and attached to their sides, especially near bundle junctions.

The HRTEM image (Figure 4.10b) shows continuous, parallel, and regularly spaced lattice fringes over the whole imaged area, with no visible amorphous layer at the edge of the nanowire. This indicates high crystallinity of the nanowire core. In the magnified profile (Figure 4.10c), the interplanar spacing was determined to be d = 0.634(24) nm. The experimental d-spacing of 0.634 nm recorded for the GSM 1:80:20 ternary composite represents a transitional value situated between the SbSI lattice distance of 0.6517 nm [160] and the MnO_2 d-spacing of 0.619 nm [161]. This intermediate spacing is attributed to interfacial lattice distortions occurring at the heterojunction. The anchoring role of the GO support induces collaborative tensile strain in the MnO_2 matrix and compressive strain in the SbSI structure, yielding a balanced hybrid interface that facilitates enhanced charge transport across the composite network.

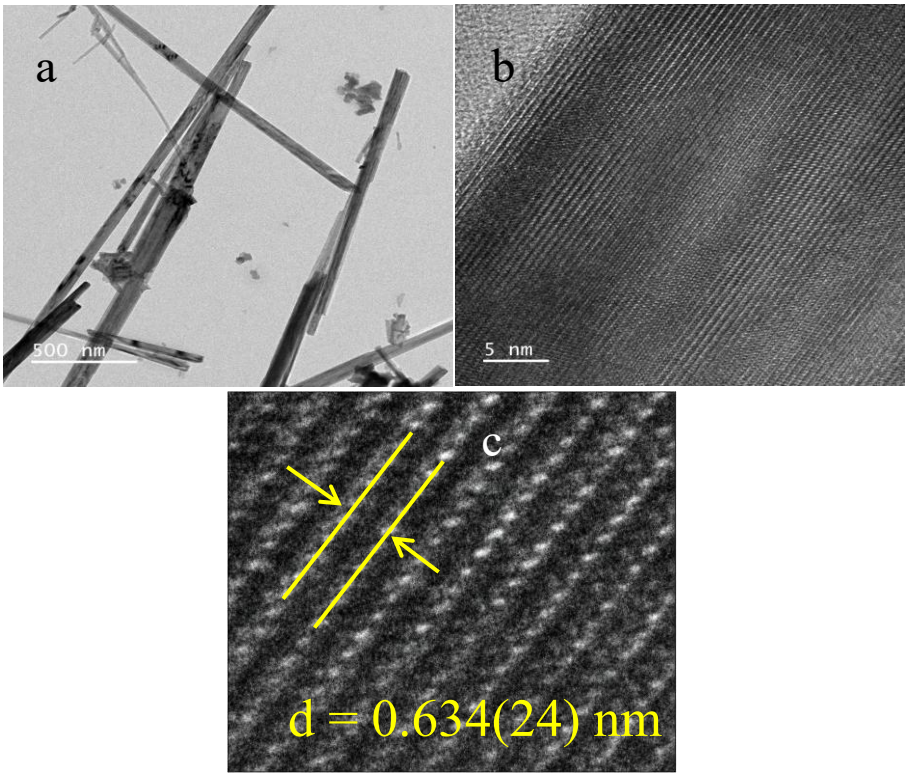


Figure 4.10: TEM and HRTEM micrographs of the GSM composite with a ratio of 1:20:80: (a) TEM image of the composite, (b) HRTEM image of the crystal lattice of a nanowire, and (c) magnified lattice fringes with the measured interplanar spacing d = 0.634(24) nm.

The morphology of the GSM 1:80:20 composite was investigated by HRTEM (Figure 4.11). In this composite, SbSI is the main component, MnO_2 is present in a smaller amount, and GO is a

minor additive. The low-magnification image (Figure 4.11a) shows that the sample consists of densely packed, irregular objects of different shapes and sizes. Two types of structures can be distinguished. The first are short, rod-like and prismatic crystals with well-defined edges, with lengths of several hundred nanometres and widths on the order of 100 nm. The second are irregular, angular particles and thin plate-like fragments. These smaller objects are attached to the rods and fill the spaces between them, which leads to dense, dark agglomerates, especially on the right side of the image. Compared with the MnO_2-rich sample (1:20:80), long, continuous nanowires are not observed. The SbSI phase is present mainly as short crystals embedded in an agglomerated mixture with the other components.

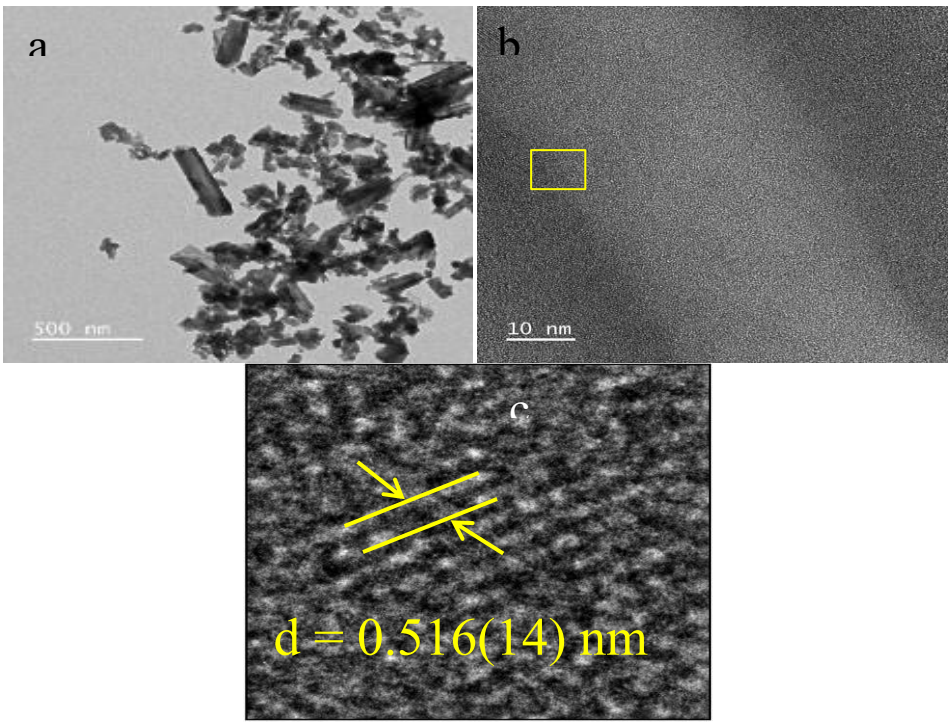


Figure 4.11: TEM and HRTEM micrographs of the GSM 1:80:20 composite: (a) TEM image of the composite, (b) HRTEM image of the selected area, and (c) magnified region marked in yellow box with the measured interplanar spacing d=0.516(14) nm.

The HRTEM image (Figure 4.11b) shows a granular, low-contrast structure in which continuous lattice fringes are not clearly resolved over large areas. The yellow square marks the region magnified in Figure 4.13c. The formation of nanowires possessing a nanorod-like morphology. Increasing the SbSI concentration to its highest ratio triggers a structural transition, resulting in a lattice spacing of 0.516(14) nm. While this value numerically deviates from the 0.619 nm spacing reported for standalone MnO_2 nanostructure [161], both samples share a highly similar morphological feature: the formation of short nanowire fragments. In standalone systems, the nanowires grow unhindered to expose the characteristic 0.619 nm plane. However, in this composite, the high concentration of SbSI alters the local surface energies and creates a spatially confined environment. This chemical

environment forces the emerging 1D nanostructure to undergo facet switching, growing along a different crystallographic orientation that exposes a more compressed, stable plane at 0.516(14) nm.

In summary, HRTEM observations show that the relative mass ratios of SbSI to MnO_2 alter the visible morphology and crystallinity of the GSM composites. In the sample with a 1:20:80 ratio (Figure 4.10), long, straight nanowires with a lattice spacing of 0.378 nm are observed, interwoven with a small number of MnO_2 and GO fragments. When the SbSI content is increased to the 1:80:20 ratio (Figure 4.11), the morphology shifts toward shorter rods and irregular particles forming dense agglomerates, accompanied by less clearly resolved lattice fringes. These variations demonstrate a distinct structural transformation across the composition range, as visually mapped by the progressive modification of the active phase distributions.

4.3 X-ray Diffractometry

XRD is one of the most commonly used techniques for analyzing the structural properties of crystalline materials. It is widely applied to identify different phases, determine crystal structure, calculate interplanar spacing, evaluate crystallinity, etc. It provides useful information about structural changes after synthesis or interfacial coupling processes. The obtained diffraction pattern is generally compared with standard reference data available in the Joint Committee on Powder Diffraction Standards (JCPDS) [162] database to confirm the crystal phase and purity of the prepared material.

During the experiment, a monochromatic X-ray beam is directed onto the sample surface, where it is scattered by different crystal planes. Constructive interference occurs only when a specific geometric condition is satisfied, described by Bragg's law, formulated by Sir William Henry Bragg in 1913 [163]. According to this law, diffraction occurs when the path difference between two reflected X-ray waves equals an integer multiple of the wavelength, as given by the Bragg equation [163, 164].

$$n\lambda = 2dsin\theta \qquad (4\text{-}1)$$

where n is the diffraction order, λ is the wavelength of the X-ray, d is the spacing between adjacent crystal planes, and θ is the angle of diffraction. The detector scans through a range of diffraction angles and records the intensity of the reflected beam, which is plotted as an XRD pattern; each crystalline phase produces a characteristic set of peaks that can be compared with standard reference data for phase identification.

The diffraction peaks correspond to specific crystallographic planes, indexed using Miller indices (hkl), and their positions and relative intensities are related to the reciprocal lattice of the crystal. This information allows the crystal structure, lattice parameters, and phase composition of the material to be determined.

In this work, the structural characterization of the prepared samples was performed using a Bruker D8 Advance X-ray diffractometer. The instrument was employed to obtain diffraction patterns,

identify the crystalline phases, examine structural purity, and evaluate the crystal structure of the synthesized materials. The measured diffraction data were further compared with standard reference patterns to confirm the successful formation of the desired phase and to investigate any structural changes introduced during material preparation.

4.3.1 XRD of GO

The crystalline structure and phase purity of the synthesized materials were investigated using X-ray Diffraction (XRD), performed on a Bruker D8 Advance diffractometer, with the permission of the University of Silesia, Faculty of Science and Technology, Institute of Material Science, Chorzów, Poland, for GO, SbSI, and GO-SbSI composites. The measurements were carried out at room temperature over a 2θ range of 10°-60°, using Cu-Kα radiation (λ=1.5406 Å), to identify the crystalline phases present and estimate the average crystallite size of the synthesized samples.

The XRD spectrum of GO is shown in Figure 4.12. The XRD spectrum of the sample was performed using a D8 Bruker, with Cu Kα (1.5406Å). The XRD spectra were performed in the range of 10-80°. In the XRD spectrum of GO, two main diffraction peaks are observed at 12.58° and 25.10°. A sharp and intense diffraction peak is observed at 2θ. The dominant peak at 12.58° corresponds to the characteristic (001) reflection of GO [165], arising from the interlayer spacing created by the introduction of oxygen-containing functional groups (such as hydroxyl, epoxide, and carboxyl groups) between the graphene sheets during oxidation. The second peak at 25.10° is attributed to the (002) plane, indicating the presence of residual, non-exfoliated graphite or disordered stacking of partially reduced graphitic layers within the GO framework [166].

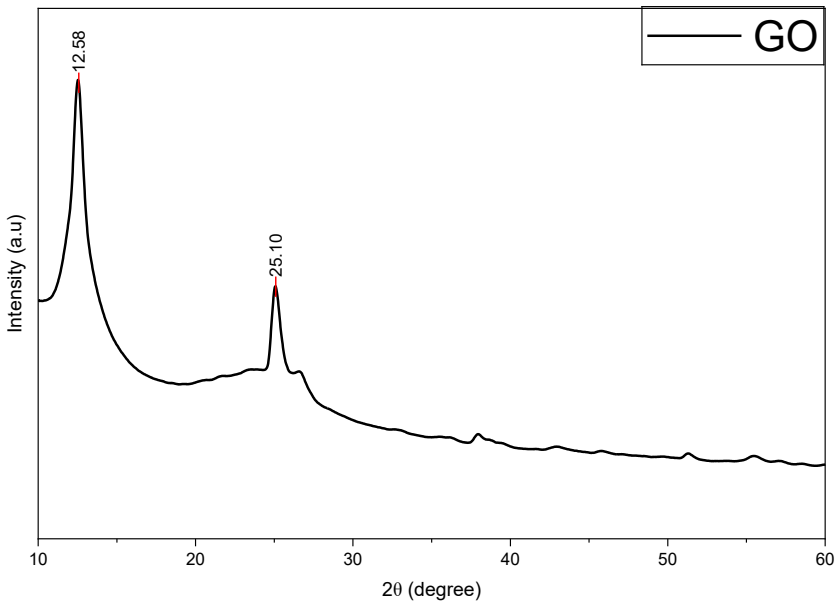


Figure 4.12: XRD pattern of GO in the range of 10-60°.

4.3.2 XRD of SbSI

In Figure 4.13, the XRD spectrum of SbSI (10-60°) is shown. The peaks are detected at 13.84°, 17.48°, 20.78°, 21.05o, 22.85°, 24.01°, 25.20°, 27.61°, 28.96°, 30.18°, 31.72°, 32.99°, 33.68°, 34.64°, 35.71°, 36.36°, 40.39°, 42.23°, 43.50°, 44.42°, 46.26°, 47.38°, 48.26°, 49.14°, 51.83°, 53.51°, 55.13°, 56.16°, and 59.65° corrospond to (110), (020), (120), (200), (210), (111), (220), (130), (121), (201), (211), (310), (230), (031), (040), (131), (311), (141), (002), (150), (241), (411), (250), (151), (341), (510), (350) and (142). The same spectra of SbSI are observed in the literature, which confirms the formation of SbSI. These peaks are well matched with JCPDS 88-0988 [147].

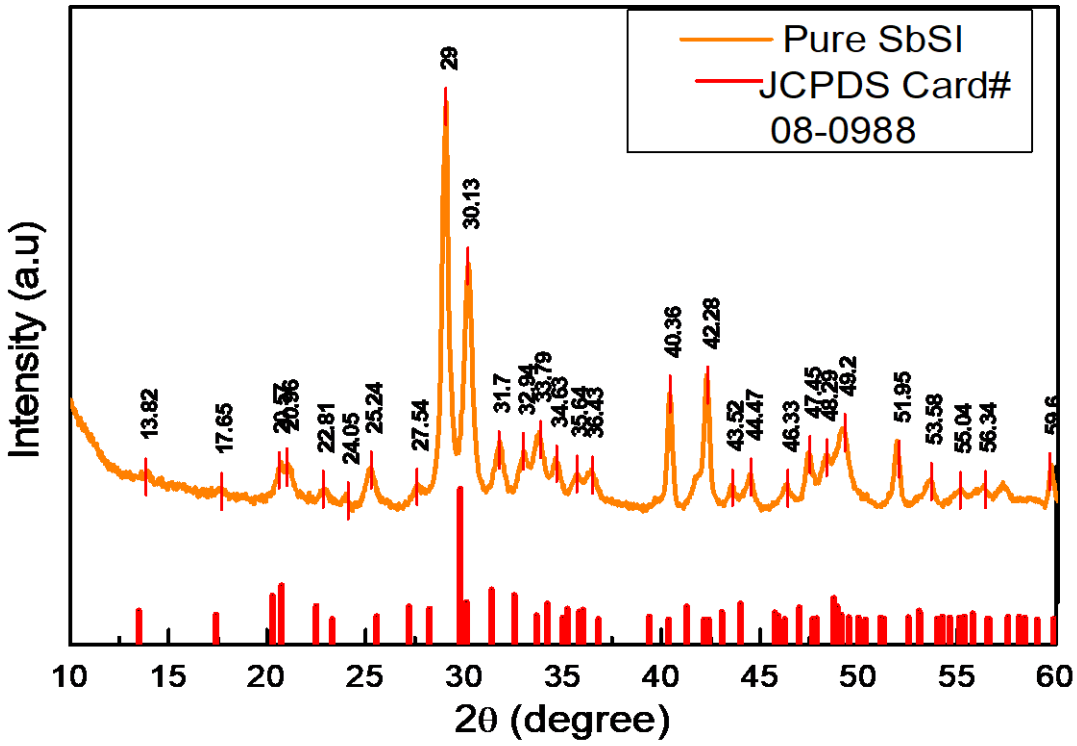


Figure 4.13: XRD Spectra of SbSI with JCPDS card # 88-0988.

4.3.3 XRD of GO-SbSI Composites

The XRD patterns of GO-SbSI composites with different compositions of GO and SbSI, along with GO and SbSI, are exhibited in Figure 4.14. The composite spectra clearly display the characteristic peaks of both GO and SbSI, which are labeled accordingly. In this XRD spectrum, the peaks of SbSI are well-matched with the JCPDS card no. 88-0988 [167]. The major peaks of SbSI are noticed at 13.61, 17.49, 20.54, 20.96, 22.85, 27.5, 28.21, 29.3, 30.19, 30.83, 31.65, 32.67, 33.84, 34.67, 35.59, 36.42, 37.33, 39.43, 40.43, 41.66, 42.23, 43.5, 44.43, 46.08, 47.49, 48.27, 49.11, 50.45, and 51.96

(degree) with crystal planes (110), (020), (120), (200), (130), (121), (201), (211), (310), (230), (031), (040), (131), (320), (311), (330), (141), (002), (150), (420), (241), (340), (401), (411), (250), (051), and (151) of JCPDS card# 88-0988. Also, several minor peaks are observed in the spectra, and these peaks are well matched with the JCPDS card no. 88-0988. When SbSI experiences interfacial coupling with GO, GO shares its 002-crystal plane peak with SbSI and is observed at 27.45, 27.66, 27.98, 27.87, and 27.45°, in all GO-SbSI composites, respectively. It is marked with * in Figure 4.3. Additionally, the relative intensity of minor peaks decreases due to the scaling of the pattern; only the major peaks remain clearly visible.

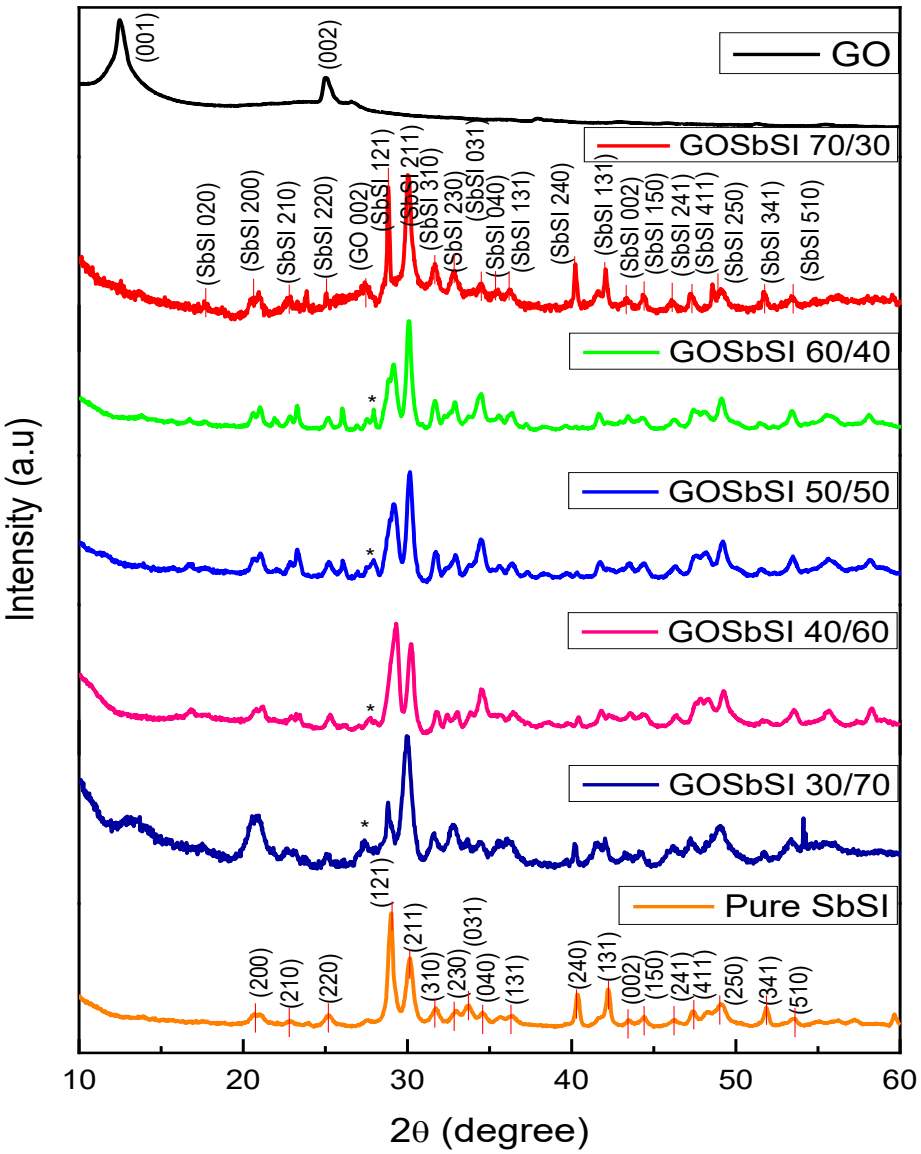


Figure 4.14: XRD spectra of the GO, SbSI, and GO-SbSI composites.

GO exhibits the characteristic (001) and (002) reflections. In the composite XRD patterns, the distinct GO (001) reflection at approximately 12° is strongly suppressed. This suppression may indicate disruption of the regular stacking of GO sheets following the incorporation of SbSI nanowires. However, the reduced GO content, its relatively low crystallinity, and the dominant diffraction intensity of crystalline SbSI may also contribute to the weak GO signal.

GO exhibited a weak diffraction feature near 26.48°, which can be associated with residual or restacked graphitic (002) domains. In the GO-SbSI composites, the carbon-related contribution in the 24-27° region could not be resolved independently from the adjacent SbSI reflections because of its weak and broad character [168].

The remaining reflections of the composites can predominantly be indexed to the orthorhombic SbSI phase. No additional distinct reflections attributable to a secondary crystalline phase are observed, indicating that the main SbSI crystal structure is retained after its incorporation with GO. Nevertheless, the relative intensities of the SbSI reflections vary with the GO/SbSI ratio. In particular, the reflection near 30.3° becomes relatively more prominent in the GO-SbSI 60/40 and GO-SbSI 50/50 samples, whereas some of the other SbSI reflections become less intense. With increasing SbSI content, the overall diffraction pattern increasingly resembles that of SbSI. These intensity variations can primarily be associated with changes in phase fraction and may also be influenced by preferred orientation, crystallite size, and the distribution of SbSI nanowires on the GO sheets.

The measured positions of the two principal SbSI reflections indexed to the (121) and (211) planes were 28.70° and 30.40° for GO-SbSI 70/30, 29.25° and 30.30° for GO-SbSI 60/40, 29.30° and 30.33° for GO-SbSI 50/50, 29.30° and 30.30° for GO-SbSI 40/60, and 28.60° and 29.90° for GO-SbSI 30/70, respectively are presented in Figure 4.15. These changes are not monotonic with composition. Such variations may arise from lattice strain, structural defects, crystallite-size effects, or sample displacement and instrumental uncertainties. Interfacial interactions between GO and SbSI may contribute to these changes.

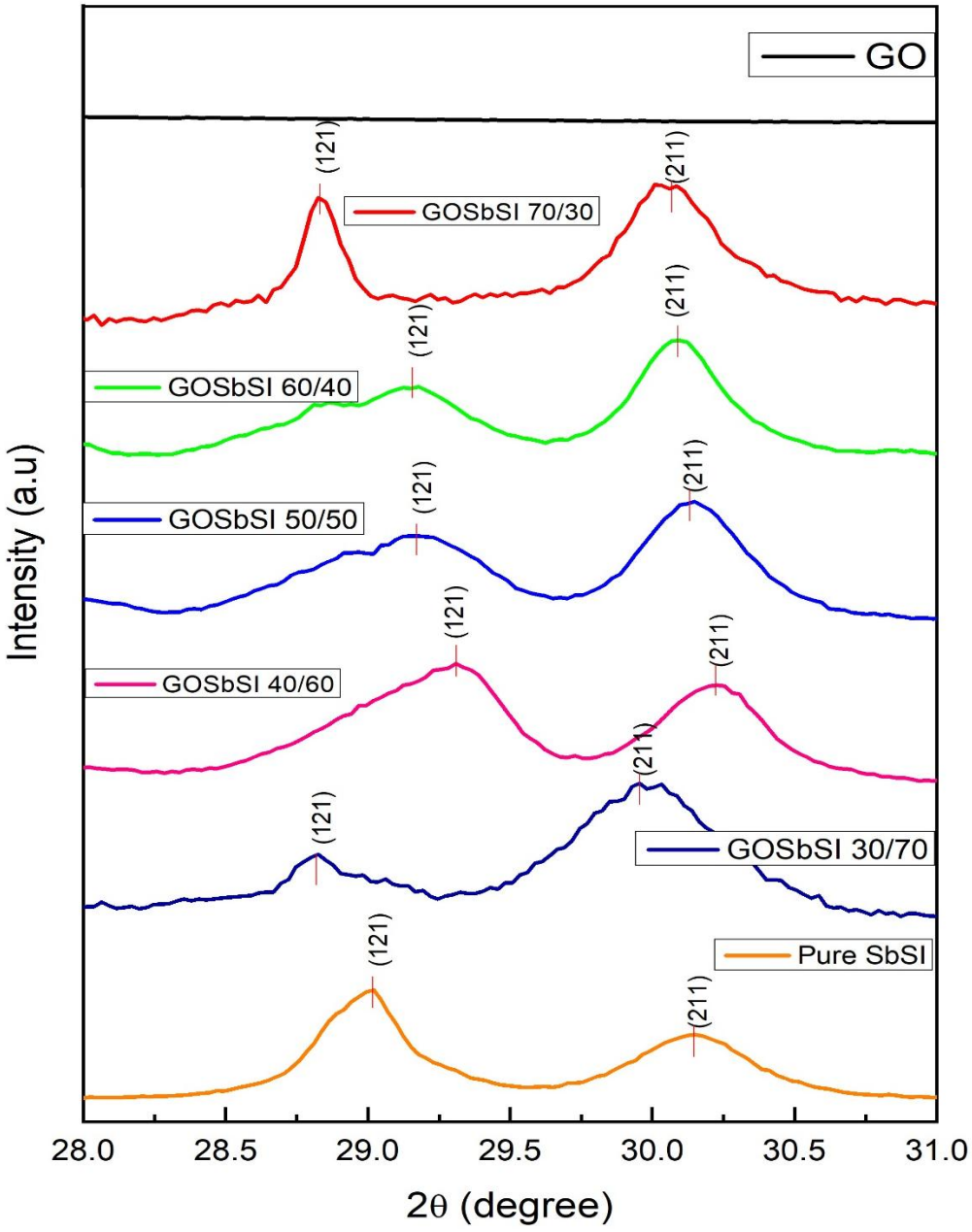


Figure 4.15: XRD peak variations due to interfacial coupling in GO, SbSI, and GO-SbSI composites.

4.3.4 XRD of GSM Composites

The crystalline structure and phase purity of the synthesized materials were investigated using X-ray Diffraction (XRD), performed on a Bruker D8 Advance diffractometer, with permission from the School of Materials and Mineral Resources Engineering, Universiti Sains Malaysia. The measurements were carried out at room temperature over a 2θ range of 10°-60°, using Cu-Kα radiation (λ=1.5406 Å), to identify the crystalline phases present and estimate the average crystallite size of the synthesized samples.

In this work, the XRD spectra of GSM samples labeled as GSM 1:20:80 to GSM 1: 80:20 are presented in Figure 4.16. The XRD peaks of SbSI are denoted as ●, and the α-MnO_2 are presented with *, and GO peaks are presented with +. Several peaks are observed in the XRD spectra of all samples. The major peaks of α-MnO_2 are observed at 12.6º, 17.8º, 28.4º, 37.2º, 41.5º, 42.7º, 49.4º, 55.6º, 64.8º, 68.9º, and 72.3º, which correspond to crystal planes (110), (200), (310), (211), (420), (301), (411), (600), (002), (514), and (312) respectively. These peaks are well matched with the JCPDS card no. 44-0141 [169]. The other peaks are observed at angles 19.3º, 23.4º, 24.3º, 30.6º, 31.6º, 32.9º, 52.2º, 55.6º, 59.5º, and 63.0º, at crystal planes (120), (130), (201), (031), (040), (141), (510), (260), (530), and (332) these peaks belong to SbSI crystal structure and matched with the JCPDS card #88-0988 [167], While the GO appearance can be noticed through a broad signal around 26° due to partial graphitization [170].

The intense overlapping reflection near 28.4°, highlighted in Figure 4.16, is retained within the 28-29º region in all GSM composites. The extreme positions available for this reflection range approximately from 28.25º to 28.69º. These variations are non-monotonic and therefore do not demonstrate a systematic shift with the GO/SbSI/MnO- ratio. The exact positions of the 28.4° reflection in each composite should be determined independently from the original XRD data using an identical peak-fitting procedure.

The overlapping feature near 17.8º exhibits a lower relative intensity in GSM 1:30:70, GSM 1:40:60 and GSM 1:50:50 compared with the other composites. Its peak position also varies among the samples. Because this feature may contain contributions from the α-MnO_2 (200) and SbSI (020) reflections, changes in its profile and apparent position may arise from variations in the relative contributions of these phases rather than from displacement of a single crystallographic reflection. The SbSI-related reflection near 23.5º becomes less pronounced in the intermediate composites but is more clearly resolved in GSM 1:70:30 and GSM 1:80:20. This behavior is consistent with the higher SbSI fraction in these samples.

The shared peak near 37.2º was observed at 37.18º, 37.23º, 37.16º, 37.66º, 37.19º, 37.23º and 37.50º for GSM 1:20:80, GSM 1:30:70, GSM 1:40:60, GSM 1:50:50, GSM 1:60:40, GSM 1:70:30 and GSM 1:80:20, respectively. These values vary non-monotonically over a range of approximately 0.50º. The apparent differences may result from changes in the relative contributions of the combined SbSI and α-MnO2 reflections, lattice strain, structural disorder, or peak-fitting uncertainty.

Overall, the diffraction patterns are consistent with the coexistence of crystalline SbSI and α-MnO_2 in the GSM composites, together with a comparatively weak contribution from the GO component. Changes in the relative peak intensities primarily reflect variations in the proportions of the constituent phases. Although small differences in the apparent peak positions are observed, their structural significance cannot be established without considering instrumental uncertainty, sample-displacement effects, peak-fitting errors, and replicate measurements. Therefore, the present results

suggest possible composition-dependent structural variations but do not confirm systematic lattice distortion or concentration-dependent peak shifting.

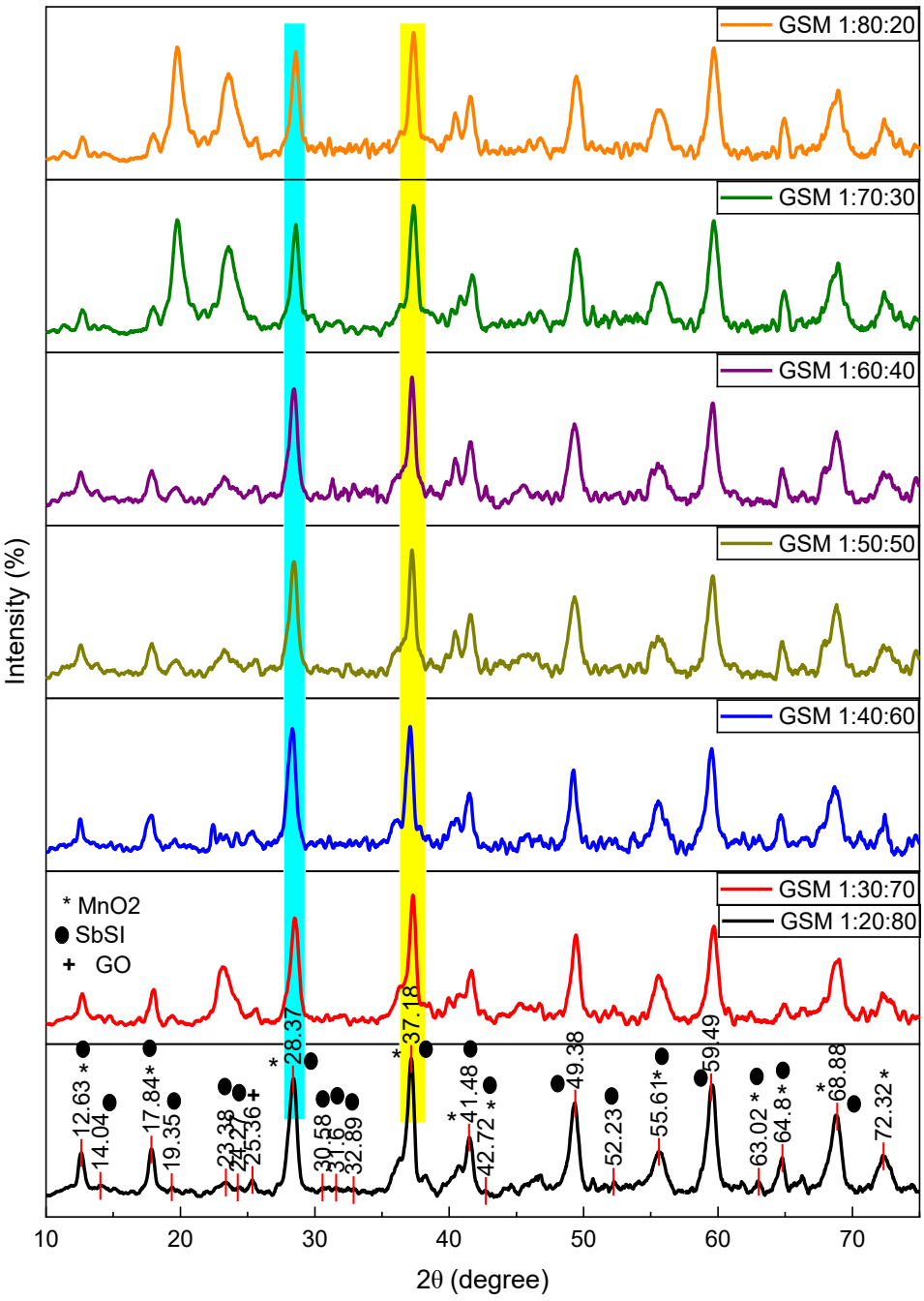


Figure 4.16: XRD patterns of GMS composites (1:20:80 -1:80:20). Peaks correspond to α-MnO_2, SbSI, and GO phases in composites.

4.4 X-ray Photoelectron Spectroscopy

X-ray photoelectron spectroscopy (XPS) is a surface-sensitive analytical technique used to investigate the elemental composition, chemical states, and electronic structure of materials. The technique is based on the photoelectric effect, whereby photoelectrons are emitted from a material upon irradiation with monochromatic X-rays. By measuring the kinetic energy and intensity of the emitted electrons, the corresponding binding energies can be determined. Since each element and its chemical state possess characteristic binding energies, XPS provides valuable information regarding elemental identification, oxidation states, surface chemical bonding, and electronic configurations. Owing to its shallow sampling depth of only a few nanometers, XPS is particularly effective for the surface characterization of organic, inorganic, polymeric, and nanostructured materials.

In the present work, XPS was employed to analyze the elemental composition, oxidation states, and interfacial chemical interactions within the GO-SbSI nanocomposites. The measurements were carried out using an ultra-high vacuum (UHV) system with a base pressure of 8.5×10^{-9} Pa, equipped with a PREVAC EA15 hemispherical electron energy analyzer fitted with a two-dimensional microchannel plate (2D-MCP) detector. Sample irradiation was performed using a monochromatized X-ray source consisting of a PREVAC dual-anode XR-40B source and an RMC50 monochromator, operating with the Al Kα radiation line (1486.60 eV)**.** Survey spectra were acquired with a pass energy of 200 eV and a scanning step size of 0.8 eV**,** whereas high-resolution spectra for selected energy regions were recorded using a pass energy of 100 eV and a scanning step size of 0.06 eV. To achieve maximum energy resolution, all measurements were conducted at a normal photoelectron take-off angle using a curved analyzer exit slit with dimensions of 0.8 × 25 mm**.** The binding energy scale of the analyzer was calibrated using the Au $4f_{7/2}$ peak at 84.0 eV obtained from a gold-coated reference sample positioned on the same sample holder [171].To minimize possible charging effects and ensure accurate energy calibration, the binding energy scale was additionally referenced to the adventitious C 1s peak following the procedure proposed by Greczynski and Hultman [172]**.** The acquired spectra were processed using CASA XPS software (version 2.3.25**)**. Peak deconvolution was performed using mixed Gaussian-Lorentzian line shapes consisting of 30% Gaussian and 70% Lorentzian contributions, unless otherwise specified. Background subtraction was carried out using the Shirley method**,** enabling reliable quantitative analysis and identification of the chemical states present in the GO SbSI nanocomposites.

4.4.1 GO-SbSI composites

The XPS survey spectrum (Figure 4.17a) exhibits characteristic photoelectron signals corresponding to C, O, S, Sb, and I, demonstrating the expected elemental composition of the SbSI/GO nanocomposite and indicating the successful integration of SbSI crystallites within the oxygen-

functionalized GO matrix. The high-resolution C1s spectrum (Figure 4.17b) was deconvoluted into three prominent components centered at 284.6, 285.8, 287.3, and 288.6 eV, which are assigned to C-C/C=C, C-O, O=C-C, and O=C-O bonds, respectively [173]. These features are characteristic of graphene oxide and indicate the presence of abundant oxygen-containing functional groups on the GO surface. In addition, the peak observed at 283.7 eV may be attributed to an interaction between the metal and carbon, suggesting the possible formation of a C-Sb bond between carbon and antimony [174].

The high-resolution Sb3d spectrum (Figure 4.17c) requires careful interpretation because the Sb $3d_{5/2}$ photoelectron peak significantly overlaps with the O 1s signal in the 530-532 eV binding energy region. Consequently, the peak centered at approximately 530.3 eV originates from the combined contributions of Sb $3d_{5/2}$ and O 1s rather than representing a single chemical state. To distinguish the antimony contribution, peak deconvolution was performed and supported by analysis of the well-resolved Sb $3d_{3/2}$ component located at approximately 539.7 eV [175, 176]. The obtained binding energy values are consistent with Sb^{3+} species incorporated within the SbSI lattice. The O 1s contribution is mainly associated with oxygen-containing functional groups of GO, together with a minor contribution from surface-adsorbed oxygen species. The observed overlap between Sb $3d_{5/2}$ and O 1s is a well-known characteristic of Sb-containing oxide and composite systems and therefore must be considered when evaluating the chemical state of antimony.

The S 2p spectrum (Figure 4.17d) exhibits characteristic doublet peaks within the 160-163 eV range, confirming the presence of sulfur species coordinated within the SbSI crystal framework. The I 3d spectrum (Figure 4.17e) displays two distinct peaks at 619.1 and 630.7 eV, corresponding to the I $3d_{5/2}$ and I $3d_{3/2}$ spin-orbit components, respectively, which are characteristic of iodide ions bonded to antimony in the SbSI structure [176, 177]. Small shoulder features observed in both the Sb 3d/O 1s and S 2p regions suggest slight variations in the local chemical environment, which may arise from surface defects, lattice distortions, or the presence of a minor amount of Sb-rich surface species. These additional fitted components further indicate a degree of surface electronic heterogeneity relative to the bulk crystal structure. The XPS results provide strong evidence for the successful formation of the SbSI/GO nanocomposite while highlighting the importance of accounting for the Sb $3d_{5/2}$-O 1s overlap when interpreting the surface chemical states of antimony.

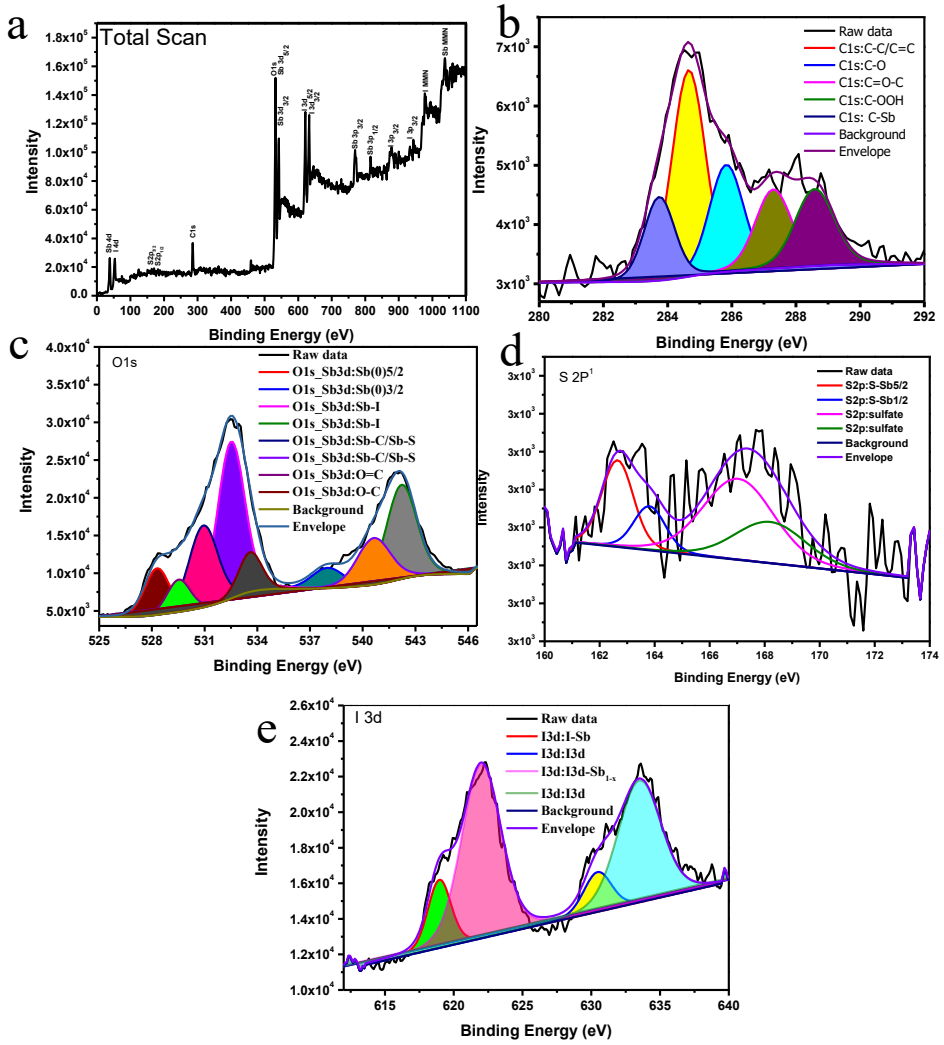


Figure 4.17: XPS spectra of GO-SbSI 70/30: (a) survey scan and elemental peaks of (b) C 1s, (c) O 1s- Sb 3d, (d) S 2p, and (e) I 3d.

The XPS survey spectrum (Figure 4.18a) displays distinct signals corresponding to C, O, S, Sb, and I, indicating the successful formation of the SbSI/GO nanocomposite with a high SbSI loading of 80 wt.%. Compared with the composites containing lower amounts of SbSI, the intensities of the Sb and I peaks are considerably higher, reflecting the increased contribution of the SbSI phase to the surface composition of the material. The high-resolution C 1s spectrum (Figure 4.18b) can be resolved into several components associated with C-C/C=C, C-O, O=C-C, and O=C-O bond functionalities, similar to the previous one, demonstrating that the graphene oxide framework maintains its oxygen-containing surface groups after composite formation [173]. A particularly interesting observation is the significant increase in the intensity of the peak at 283.7 eV, which is attributed to the formation of a C-Sb bond between carbon and antimony. This enhancement suggests that the higher loading of SbSI was successfully incorporated into the GO matrix [174].

The high-resolution Sb 3d spectrum (Figure 4.18c) is dominated by intense antimony-related signals. However, the interpretation of the Sb $3d_{5/2}$ component is complicated by its overlap with the O 1s peak in the 529-532 eV binding energy region. As a result, the peak centered at approximately 529.2 eV represents the combined contribution of Sb $3d_{5/2}$ and O 1s species. To reliably identify the antimony chemical state, peak deconvolution was performed together with analysis of the clearly resolved Sb $3d_{3/2}$component located at approximately 538.6 eV. The obtained binding energies are characteristic of Sb^{3+} species and are in good agreement with reported values for crystalline SbSI. [176] The relatively narrow and intense spectral features indicate a well-ordered chemical environment around antimony atoms, suggesting the formation of a highly crystalline SbSI phase. The O 1s spectrum (Figure 4.18c) exhibits multiple components associated with different oxygen environments, including oxygen bonded to carbon-containing functional groups and adsorbed surface species [175]. The increased contribution of these oxygen-related components reflects the complex surface chemistry arising from the interaction between SbSI particles and the GO support.

The high-resolution S2p spectrum (Figure 4.18d) shows characteristic spin-orbit doublets in the range of 160-163 eV attributable to sulfur incorporated within the SbSI crystal lattice. In addition, the I 3d spectrum (Figure 4.18e) presents two well-defined peaks at 619.3 eV and 630.8 eV, corresponding to the I $3d_{5/2}$ and I $3d_{3/2}$ states, respectively. These binding energies are characteristic of iodide ions coordinated within the SbSI structure and confirm the retention of the expected chemical composition of the composite [177].

The shoulder features in the O 1s and S 2p regions, as previously mentioned, indicate minor variations in the local chemical environment. The significantly enhanced Sb and I signals, together with the sharp and well-resolved spectral features, provide evidence for the dominance of the SbSI phase and its high degree of crystallinity. The abundance of electrochemically active Sb^{3+} and I^{1-} species is expected to promote faradaic charge-storage processes and facilitate charge transport during electrochemical operation. These characteristics are consistent with the improved capacitive performance and cycling stability observed in the CV and GCD measurements.

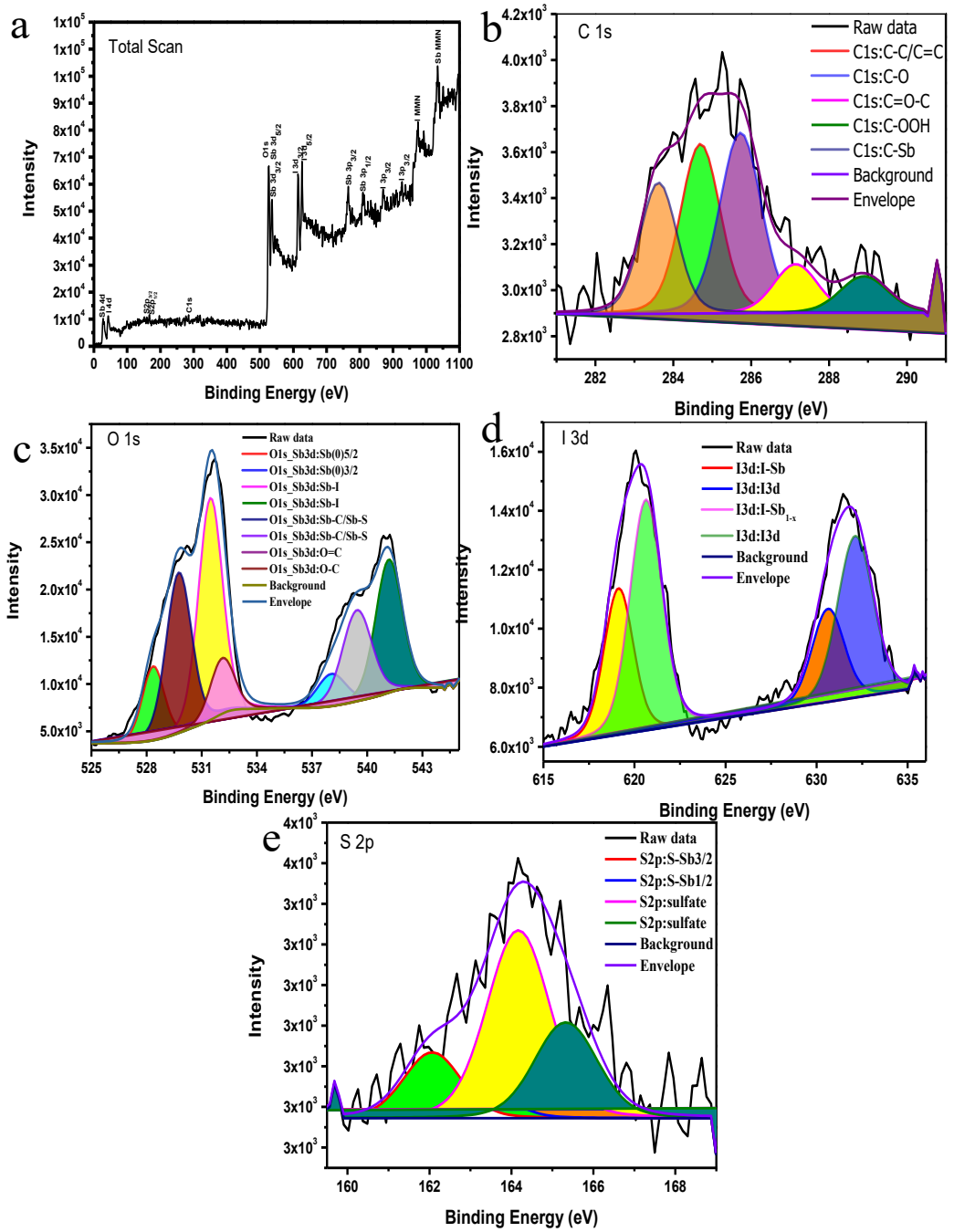


Figure 4.18: XPS spectra of GO-SbSI 30:70: (a) survey scan and elemental peaks of (b) C 1s, (c) O 1s- Sb 3d, (d) S 2p, and (e) I 3d.

4.4.2 GSM composites

The XPS spectra of GSM 1:20:80 (Figure 4.19(a-g)) demonstrate the presence of Mn, O, C, S, Sb, and I, confirming the successful incorporation of both MnO_2 and SbSI within the GO matrix. The relative intensities of the detected elements reflect the compositional ratio of the composite, with Mn

and O signals being predominant due to the high MnO_2 content (80 wt.%) and comparatively lower SbSI loading. The survey spectrum (Figure 4.19a) clearly demonstrates the coexistence of all constituent elements, indicating the formation of a multicomponent hybrid structure.

The high-resolution Mn 2p spectrum (Figure 4.19b) exhibits two pronounced peaks centered at approximately 642.1 eV (peak 1) and 653.8 eV (peak 2), corresponding to Mn $2p_{3/2}$ and Mn $2p_{1/2}$, respectively, with a spin-orbit splitting of about 11.7 eV. These binding energies are characteristic of Mn^{4+} species present in α-MnO_2 [178]. A weak shoulder observed at slightly lower binding energy may be attributed to a small fraction of Mn^{3+} species arising from oxygen vacancies or partial surface reduction, which are commonly observed in MnO_2-based materials. Such defects can generate additional electrochemically active sites and influence charge-transfer behavior [179].

The O 1s spectrum (Figure 4.19c) is dominated by a lattice oxygen component located at approximately 529.7 eV, confirming the presence of Mn-O bonds within the MnO_2 framework. Additional contributions observed in the 531-532 eV regions are associated with surface hydroxyl groups, oxygen-containing functional groups, and adsorbed water molecules [180]. The coexistence of these oxygen species suggests a chemically active surface that can improve electrolyte accessibility during electrochemical processes.

Figure 4.19d shows the high-resolution XPS spectrum of C 1s, deconvoluted into five peaks centered at approximately 284.8, 286.0, 287.0, 288.5, and 290.0 eV. The peaks at 284.8, 286.0, 287.0, and 288.5 eV are assigned to C–C/C=C, C–O, C=O, and O–C=O functional groups, respectively, confirming the oxygenated carbon structure of GO [173]. The peak at 290.0 eV is attributed to the interaction between Mn species and carbonate (CO_3^{2-}) groups, indicating the formation of a Mn-CO_3 surface complex [181]. The presence of these oxygen-containing functionalities and Mn-associated carbonate species confirms the successful incorporation of MnO_2 onto the GO surface. These features are characteristic of graphene oxide and indicate the retention of oxygen-containing functional groups following composite synthesis. The persistence of these functionalities is important for anchoring MnO_2 and SbSI particles onto the GO sheets and promoting interfacial interactions between the individual components.

The Sb 3d spectrum (Figure 4.19e) exhibits characteristic antimony-related features associated with the incorporated SbSI phase. However, the assignment of the Sb $3d_{5/2}$ component requires careful consideration due to its overlap with the O 1s signal in the 530-532 eV binding energy region. Consequently, the peak centered near 530.3 eV originates from the combined contributions of Sb $3d_{5/2}$ and O 1s species rather than representing a single chemical state. The corresponding Sb $3d_{3/2}$ peak appears at approximately 539.7 eV and, together with peak deconvolution of the overlapping region,

confirms the presence of Sb^{3+}species within the SbSI lattice [176, 177]. The relatively weak Sb intensity is consistent with the lower SbSI content in GSM 1:20:80.

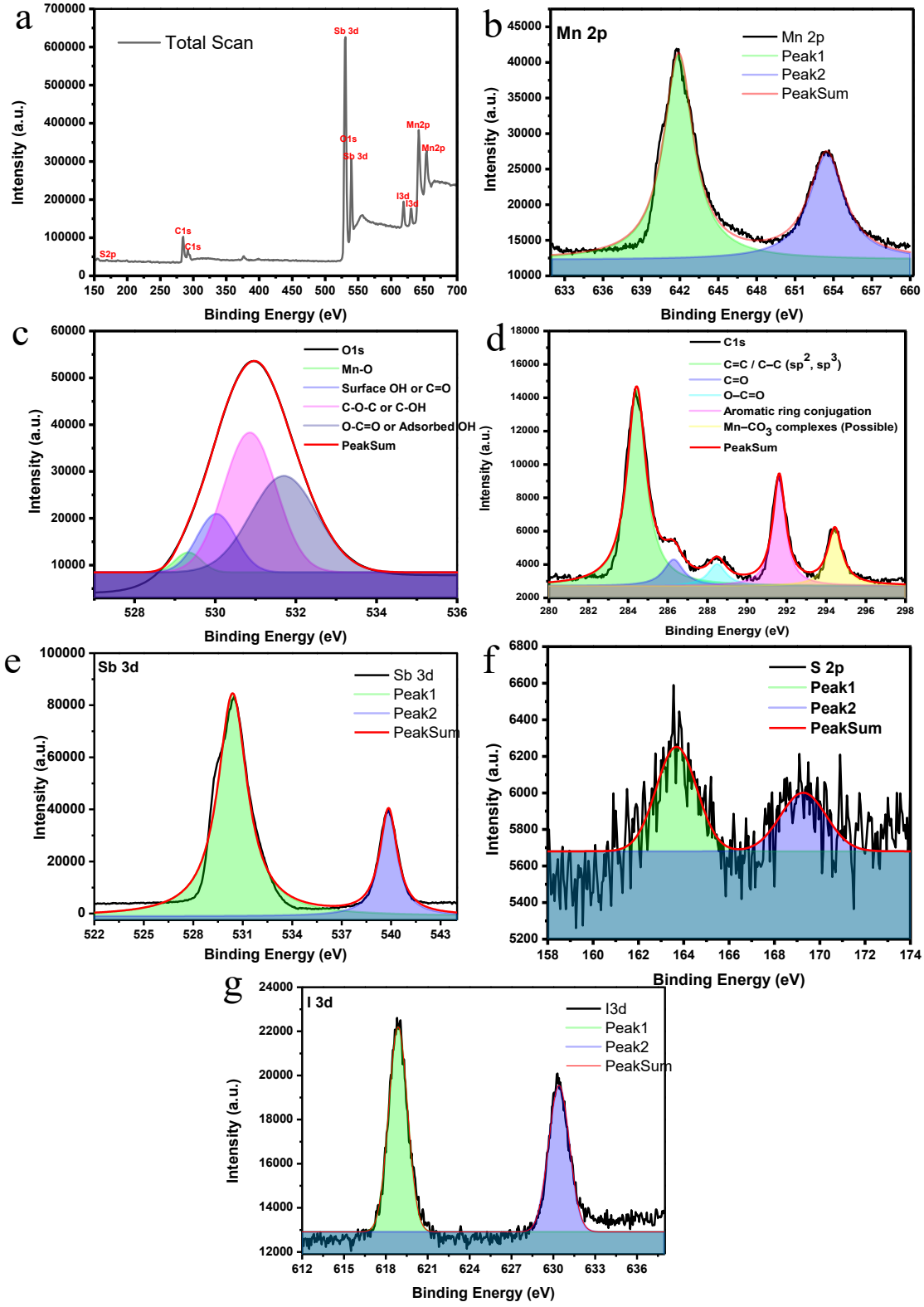


Figure 4.19: High-resolution XPS spectra of GSM 1:20:80: (a) survey spectrum, (b) Mn 2p, (c) O 1s, (d) C 1s, (e) Sb 3d, (f) S 2p, and (g) I 3d.

The S 2p spectrum (Figure 4.19f) displays characteristic spin-orbit doublets in the 160-163 eV region, indicating sulfur ions coordinated within the SbSI crystalline framework [176, 177]. The I 3d spectrum (Figure 4.19g) contains two well-defined peaks at 619.1 eV and 630.7 eV, corresponding to the I $3d_{5/2}$ and I $3d_{3/2}$ states, respectively. These binding energies are characteristic of iodide ions bonded to Sb^{3+} within the SbSI structure [176, 177].

Overall, the XPS analysis demonstrates that the surface chemistry of GSM 1:20:80 is primarily governed by MnO_2, while the presence of SbSI introduces additional Sb-, S-, and I-related active sites. The coexistence of Mn^{4+}/Mn^{3+} redox centers from MnO_2 and the incorporated SbSI phase is expected to contribute synergistically to the electrochemical behavior of the composite through enhanced charge storage and improved electron transport pathways.

The XPS spectra of GSM 1:80:20 are presented in Figure 4.20, including the corresponding survey spectrum (Figure 4.20a), the high-resolution spectra of Mn 2p (Figure 4.20b), O 1s (Figure 4.24c), C 1s (Figure 4.20d), Sb 3d (Figure 4.20e), and I 3d (Figure 4.20f-g). The survey spectrum (Figure 4.20a) reveals the presence of Mn, O, C, Sb, and I, confirming the successful formation of the GSM 1:80:20 composite. Compared with GSM 1:20:80, the intensities of the Sb and I signals are substantially enhanced, reflecting the higher SbSI content (80 wt.%) and the reduced proportion of MnO_2 within the composite. The strong Sb- and I-related signals indicate that the surface chemistry of GSM 1:80:20 is predominantly governed by the SbSI phase.

The high-resolution Mn 2p spectrum (Figure 4.20b) also exhibits peaks centered at approximately 642.1 and 653.8 eV, corresponding to the Mn $2p_{3/2}$ and Mn $2p_{1/2}$ states, respectively [178]. Although the peak intensities are considerably weaker than those observed for GSM 1:20:80, they retain the characteristic features of Mn^{4+} species associated with α-MnO_2 together with a minor contribution from Mn^{3+} species. This observation confirms that MnO_2 remains present as a secondary phase despite its lower concentration in the composite.

The O 1s spectrum (Figure 4.20c) can be deconvoluted into several components associated with lattice oxygen, surface hydroxyl groups, and adsorbed oxygen-containing species, as in the case of GSM 1:20:80. Compared with GSM 1:20:80, the contribution of lattice oxygen is reduced, which is consistent with the lower MnO_2 content. Simultaneously, the relative intensity of surface-related oxygen species becomes more pronounced, reflecting the more complex surface chemistry arising from the increased SbSI fraction and its interaction with the GO support.

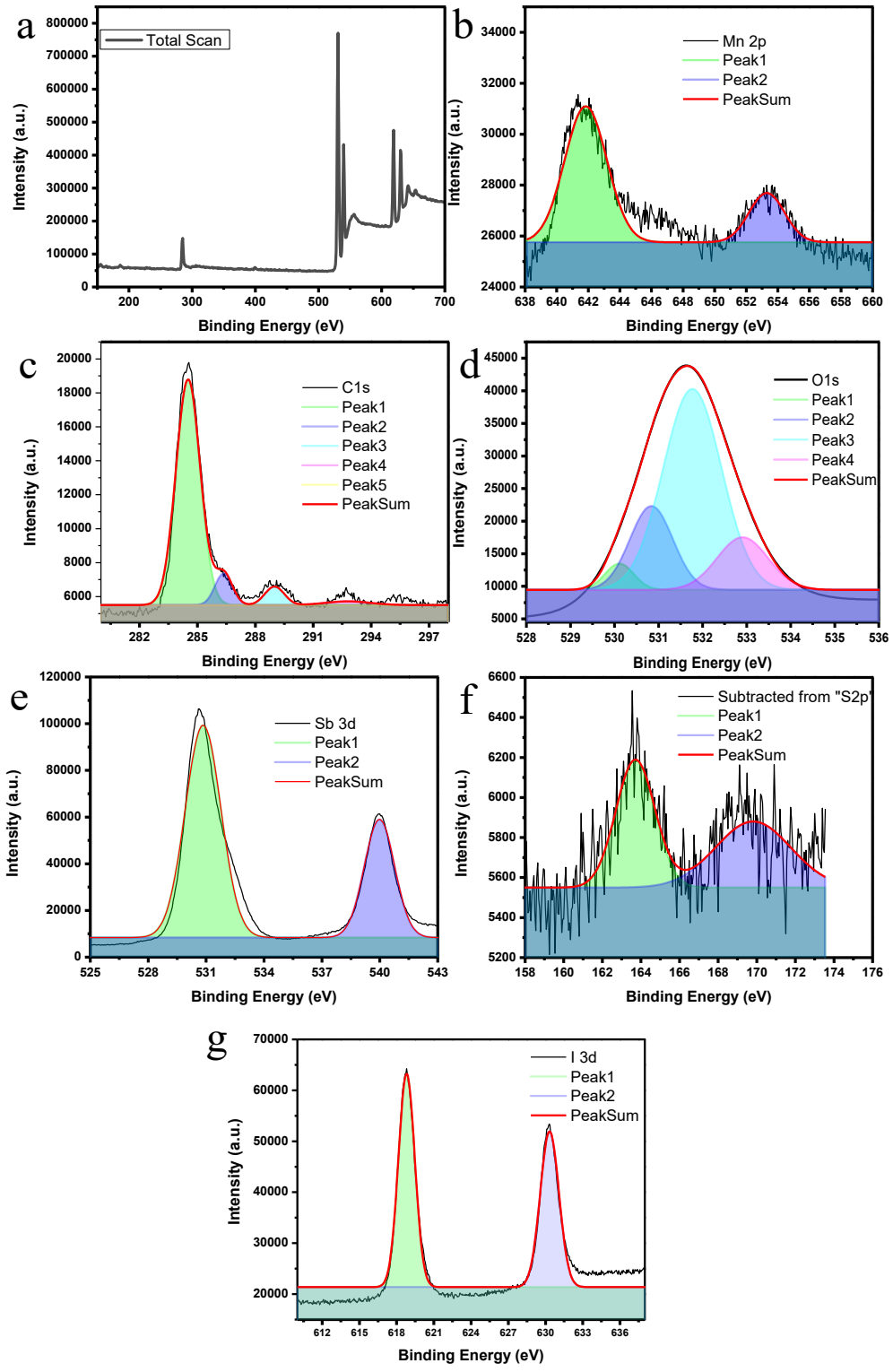


Figure 4.20: High-resolution XPS spectra of GSM 1:80:20: (a) survey spectrum, (b) Mn 2p, (c) O 1s, (d) C 1s, (e) Sb 3d, (f) I 3d$_{5/2}$, and (g) S 2p[1].

The C 1s spectrum (Figure 4.20d) displays similar characteristic peaks corresponding to C–C/C=C, C–O, C=O, O–C=O, and Mn–CO_3 bonds, like GSM 1:20:80 nanocomposites, indicating the continued presence of graphene oxide functional groups within the composite and its interaction with MnO_2 [173, 181].

The Sb 3d spectrum (Figure 4.20e) is characterized by strong antimony-related features associated with the dominant SbSI phase. Similar to the previous samples, interpretation of the Sb $3d_{5/2}$ component is complicated by its overlap with the O 1s signal in the 529-532 eV regions. Therefore, the intense feature centered at approximately 529.2 eV is attributed to the combined contributions of Sb $3d_{5/2}$ and O 1s species. The corresponding Sb $3d_{3/2}$ peak is observed at approximately 538.6 eV, and together with the deconvolution of the overlapping envelope, confirms the presence of Sb^{3+} species within the SbSI structure [176, 177]. The sharp and symmetric nature of the Sb peaks suggests a relatively homogeneous chemical environment surrounding the antimony atoms and indicates the formation of a highly crystalline SbSI phase.

The I 3d and S spectra (Figure 4.20 f-g) exhibit two well-defined peaks located at approximately 619.3 eV and 630.8 eV, corresponding to the I $3d_{5/2}$ and I $3d_{3/2}$ states, respectively. These binding energies are characteristic of iodide ions coordinated within the SbSI crystal lattice and demonstrate the preservation of the expected chemical composition of the antimony sulfoiodide phase. The strong intensity and narrow peak widths further support the high crystallinity of the SbSI component [176, 177].

The XPS analysis demonstrates that GSM 1:80:20 possesses a surface chemistry dominated by the SbSI phase, as evidenced by the significantly enhanced Sb and I signals. The coexistence of residual MnO_2 with highly crystalline SbSI creates a composite containing multiple electrochemically active species. The abundance of Sb^{3+} and I^- centers, together with the conductive GO framework, is expected to facilitate charge transfer and faradaic reactions, contributing to the superior electrochemical performance observed in the corresponding CV and GCD measurements.

The differences in surface composition and chemical states between GSM 1:20:80 and GSM 1:80:20 play a significant role in determining their electrochemical performance. In GSM 1:20:80, the surface chemistry is predominantly governed by MnO_2, where Mn^{4+} species act as the primary electrochemically active centers. The presence of a small amount of Mn^{3+} and oxygen-defect sites, evidenced by the O 1s spectrum, may facilitate electrolyte ion diffusion and provide additional charge-storage sites. However, the relatively low SbSI content limits the contribution of Sb- and I-related species to faradaic charge-storage processes. In contrast, GSM 1:80:20 exhibits substantially enhanced Sb and I signals, indicating the dominance of the SbSI phase and the presence of abundant Sb^{3+} and I^- species on the material surface. The coexistence of residual Mn redox centers with the highly

crystalline SbSI phase increases the number of electrochemically active sites available for reversible charge-transfer reactions. Moreover, the well-defined Sb and I spectral features suggest a stable and ordered chemical environment that favors efficient electron transport and structural integrity during repeated cycling. The synergistic interaction between SbSI, MnO_2, and the GO framework is therefore expected to enhance charge-transfer kinetics, improve active-site utilization, and promote stable electrochemical behavior. These characteristics are consistent with the superior capacitive performance and improved charge-storage capability observed for GSM 1:80:20 in the CV and GCD measurements. This can be further confirmed through other characterization, such as UV-Vis spectroscopy and FTIR.

Chapter 5

OPTICAL STUDY

UV-visible spectroscopy (UV-Vis) is an analytical technique that is used to study the optical properties of materials. Provides information on electronic transitions and their corresponding energy levels. The technique can be applied to solid, liquid, and gaseous samples. It is widely used to investigate the absorption, transmission, and reflection behavior of materials over the ultraviolet and visible regions of the electromagnetic spectrum.

The UV-Vis region is generally divided into two wavelength ranges. The ultraviolet region extends from approximately 200 to 400 nm [182], and the visible region from 400 to 800 nm [182]. Different materials interact differently with radiation in these regions; therefore, their optical spectra provide useful information about their electronic structure, transitions, and corresponding energy levels.

The basic principle of UV-Vis spectroscopy is based on the absorption of electromagnetic radiation by a material. When a beam of light falls on the sample, photons having suitable energy are absorbed by the electrons present in the material. As a result, electrons are excited from lower energy levels to higher energy levels. This process is known as an electronic transition. Concurrently, a portion of the incident light is reflected and scattered at the material interfaces, while the remaining transmitted light reaches the detector, where its intensity is measured.

The amount of radiation absorbed depends on the nature and concentration of the material. The optical response of a sample can be expressed in terms of absorbance, transmittance, and reflectance. The relationship between the intensity of the incident and transmitted light is explained by the Beer-Lambert law [183]. This law is strictly applicable under specific boundary conditions, including the use of monochromatic incident light, a completely homogeneous medium, and low concentration ranges where particle-particle interactions and scattering effects are negligible.

$$T = \frac{I}{I_o} = 10^{-kcl} \tag{5-1}$$

$$Abs = \log(\frac{1}{T}) = \log(\frac{I_o}{I}) = -kcl \tag{5-2}$$

where *Abs* is the absorbance, T is transmittance, I_0 is the intensity of incident light, I is the transmitted light, *k* is the molar absorption coefficient, c is the concentration of the absorbing species, and l is the optical path length. This equation shows that the absorbance of a material is directly proportional to its concentration and the path length of light that passes through the sample. Physically, a higher concentration introduces a greater number of absorbing molecules or particles into the optical pathway,

which increases the probability of photon-electron interactions. Similarly, a longer path length extends the distance the light must travel through the material, ensuring the incident beam encounters more active absorbing centers and resulting in a linear decrease in the transmitted light intensity.

The optical properties of the prepared GO nanowires, the SbSI nanowires, and their binary and ternary nanocomposites were investigated to determine their absorption behavior. The optical measurements were performed using the Cary 50 Conc UV-vis spectrometer. The data were collected by recording the absorption spectrum in the 190-1000nm wavelength range to evaluate the changes in electronic transitions and electronic structures after the formation of a composite.

5.1.1 UV-Vis of GO

The optical absorption properties of GO were examined using UV-Vis spectroscopy in the wavelength range of 200-1000 nm (Figure 5.1).

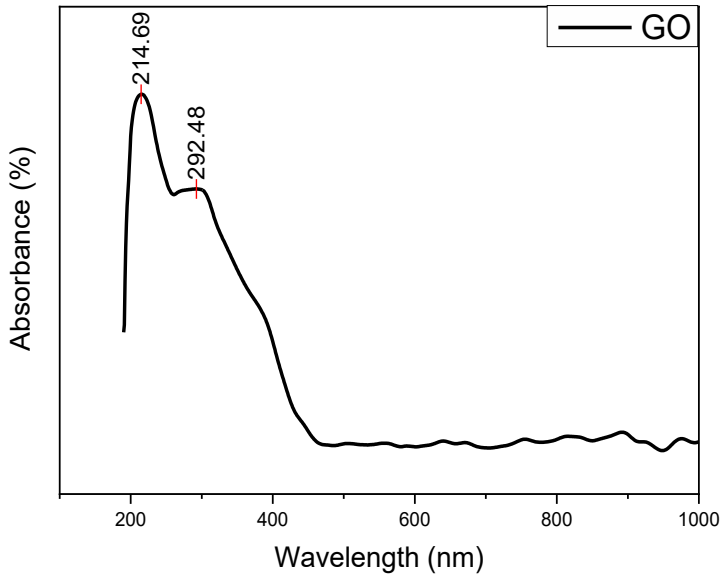


Figure 5.1: UV-Vis absorption spectrum of the GO showing characteristic electronic transitions in the ultraviolet and visible wavelength regions.

For pure GO, the UV-Vis spectrum shows (Figure 5.1) two characteristic absorption peaks at approximately 214.69 nm and 292.48 nm. The strong peak around 214.69 nm is attributed to π to π* transitions in the aromatic C=C bonds within the graphitic domains [184]. This feature reflects the presence of delocalized π-electrons typical of graphene-based structures. The second, weaker peak near 292.48 nm corresponds to n to π* transitions associated with oxygen-containing functional groups such as hydroxyl, epoxy, carbonyl, and carboxyl groups [185]. These functional groups are introduced during the oxidation of graphite, confirming the successful formation of graphene oxide [165, 170].

5.1.2 UV-Vis of SbSI

The SbSI nanowires' response to UV-Vis spectroscopy is illustrated in Figure 5.2. Their UV-Vis spectrum reveals a broad and intense absorption band centered around 605 nm, extending well across the visible region [186-188]. This strong absorption arises from electronic transitions between the valence and conduction bands and is consistent with the relatively narrow band gap of SbSI. Such behavior confirms its semiconducting nature and highlights its ability to efficiently utilize visible light, making it suitable for photoactive applications [188].

Also, around 198 nm and 225 nm, two peaks are observed, which suggests that these peaks are due to the presence of sulfur (S) [189] and iodine (I) [190]. These deep-ultraviolet features correspond to high-energy electronic transitions associated with the constituent sulfur and iodine species within the synthesized matrix.

Nanowires can enhance light absorption through multiple scattering effects and increased photon interaction paths. The observed absorption profile aligns well with previously reported results, although standard reference spectra for SbSI typically cover a narrower wavelength range focused primarily on the visible region. The detection of these well-defined bands maps the characteristic high-energy profiles of the integrated elements within the framework, confirming the successful synthesis of the intended material [186, 188].

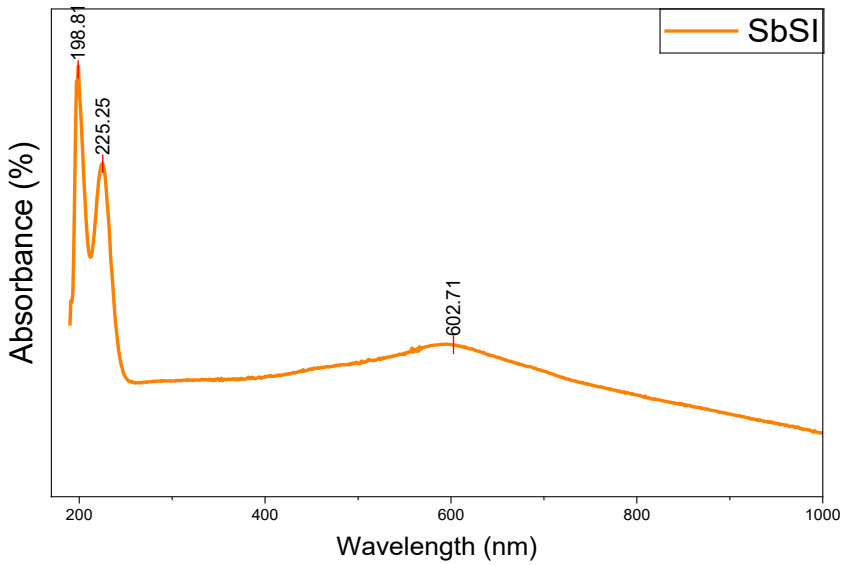


Figure 5.2: UV-Vis absorption spectrum of the SbSI showing characteristic electronic transitions in the ultraviolet and visible wavelength regions.

5.1.3 UV-Vis of GO-SbSI Composite

The UV-Vis absorption spectrum of pure GO, pure SbSI, and its associated binary composite is shown in Figure 5.3(a,b), and Figure 5.3a focuses on the ultraviolet (200-400 nm) and 5.3b shows the visible spectrum (300-1000 nm) responses. As shown in Figure 5.3a, the pure GO shows a transition π to π* peak of 214.3 nm along the large shoulder near 302.25 nm (n to π*), while the pure SbSI illustrates a high-energy band of 198.92 nm and 225.42 nm. All GO-SbSI samples exhibit wide absorption bands of about 450-700 nm, clearly dominated by the contribution of pure SbSI phases, with an extreme absorption peak of 605.12 nm. Compared to pure GO, composites show significant improvements in visible light absorption, reflecting the optical integration of the two phases and the co-absorption behavior of the GO-SbSI binary matrix.

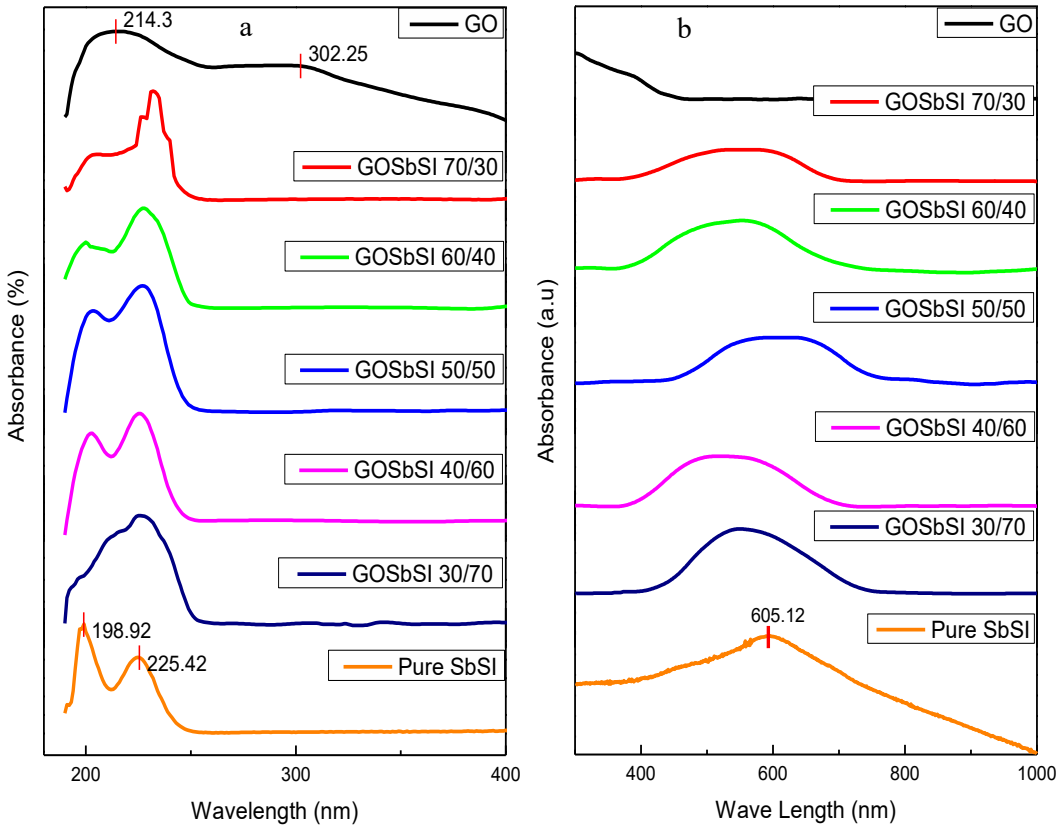


Figure 5.3 (a,b): (a) The UV region spectra of GO, various ratios of GO-SbSI 70/30, - 30/70, and SbSI against absorbance. (b) The visible region spectra of GO, various ratios of GO-SbSI 70/30, - 30/70, and SbSI against absorbance.

Among the composites, GO-SbSI 70/30 shows the lowest relative absorption feature in the visible region, displaying a peak at around 601 nm. Although the characteristic SbSI absorption band is present, its moderate profile definition suggests a relatively low concentration of SbSI nanowires.

Its absorption is still higher than that of pure GO, demonstrating that even a small amount of SbSI can alter the light-harvesting capability. A small change is observed at 197.5 nm and 227.52 nm.

In GO-SbSI 60/40, the absorption profile becomes broader and more pronounced; around 602 nm, the peak is observed. This indicates that more SbSI nanowires are actively contributing to light absorption. Additionally, increased interfacial contact between GO and SbSI enhances the optical profile development. A small change is observed at 196.4 nm and 226.42 nm.

The absorption band becomes slightly broader, and nearly 608 nm a peak is observed. The changing profile suggests a higher density of active sites and a more effective structural combination between the two components. GO provides a conductive pathway for electron transport, while SbSI remains responsible for photon absorption, leading to a synergistic change in optical behavior. Also, peak shifting is observed in π to π* and n to π*peaks and is observed, at 200.2 nm and 225.52 nm.

A similar enhancement is observed in GO-SbSI 40/60; the peak is observed around 590 nm. The increased SbSI loading enhances the likelihood of photon absorption, while GO helps suppress recombination of photo-generated charge carriers by acting as an electron acceptor. This dual role contributes to both improved absorption characteristics and better charge dynamics. Due to the concentration changes, the peaks are observed at 199.55 nm and 224.32 nm.

In GO-SbSI 30/70, which shows the most intense absorption profile among all samples, the broad peak is observed near 598 nm. This can be attributed to the high concentration of SbSI nanowires, providing abundant active sites for electronic transitions. A small change is observed at 198.2 and 223.62 nm.

Overall, the gradual development of the visible-light absorption profiles from GO-SbSI 70/30 to GO-SbSI 30/70 demonstrates the crucial role of SbSI content in determining the optical properties of the composites. The combination of these two materials creates a synergistic effect that alters performance compared to the individual components, as evidenced by the systematic growth of the 605 nm peak heights across the entire investigated concentration series.

5.1.4 UV-Vis of GSM Composites

The UV-Vis spectra of GSM 1:20:80 to GSM 1:80:20 are depicted in Figure 5.4. In the UV region, two prominent peaks are observed in the 190-200 nm and 240-250 nm ranges in all samples. In the visible region, around the 510-520 nm range, a broad peak is observed. The peak at 196.65 nm is observed due to sp^2 hybridization, which can be produced due to carbon skeletal vibration in GO [191]. This vibration relates to π to π* transitions. The shoulder peak at 242.01 nm is observed due to sp^3 hybridization and the Mn^{3+}/Mn^{4+} combination, which causes n to π* transitions inside the composite [192]. It is also suggested that this combination is observed because of charge transfer from O 2p to Mn 3d orbitals, which are associated with α-MnO_2, a common feature of transition metal oxides

with a d_0 electronic configuration [193, 194]. Characteristically, the optical spectrum of pristine a-MnO2 displays a high-energy UV absorption band between 200 and 350 nm due to interband transitions from O 2p valence bands to Mn 3d conduction bands. Additionally, it features a broad, continuous absorption envelope extending across the visible range (400-700 nm), which arises from d-d crystal field transitions within the MnO_6 octahedra. When integrated into the ternary matrix, these overlapping electronic states of MnO_2 help broaden the composite's overall light absorption spectrum. These transitions are typically indirect and can occur due to high energies, which are connected with band gaps and localized electronic structure. Further, a third broad combined peak is noticed at 514.51 nm, which is attributed to SbSI transition ion transfer [186-188] and Mn-O charge transfer [193, 194].

As the relative SbSI fraction is systematically varied across the ternary concentration series, a distinct blue/red shift is observed in the characteristic absorption positions of the nanocomposites. For the GSM 30/70 sample, the prominent optical features are resolved at 196.45 nm, 241.99 nm, and 509.56 nm. This displacement toward shorter wavelengths indicates an alteration of the electronic transition states, where the systematic shift of the absorption edges reflects a modification of the optical energy band gap rather than changes in absolute absorbance intensity. These variations depend directly on the relative concentration adjustments, which modulate the interfacial charge-transfer pathways between the overlapping Mn, Sb, I, and O coordination spheres. Specifically, varying the component mass ratios modifies the electronic contributions of the low-energy Sb 5s/6s and I 5p valence states [195, 196], thereby shifting the overall interband transition energies. Furthermore, the intrinsic polar structure of the ferroelectric SbSI phase generates localized internal dipole fields at the heterointerface. These spontaneous polarization vectors induce strong local electrostatic interactions that shift the localized energy bands, causing the characteristic absorption profiles to migrate systematically across the spectrum as a function of material composition.

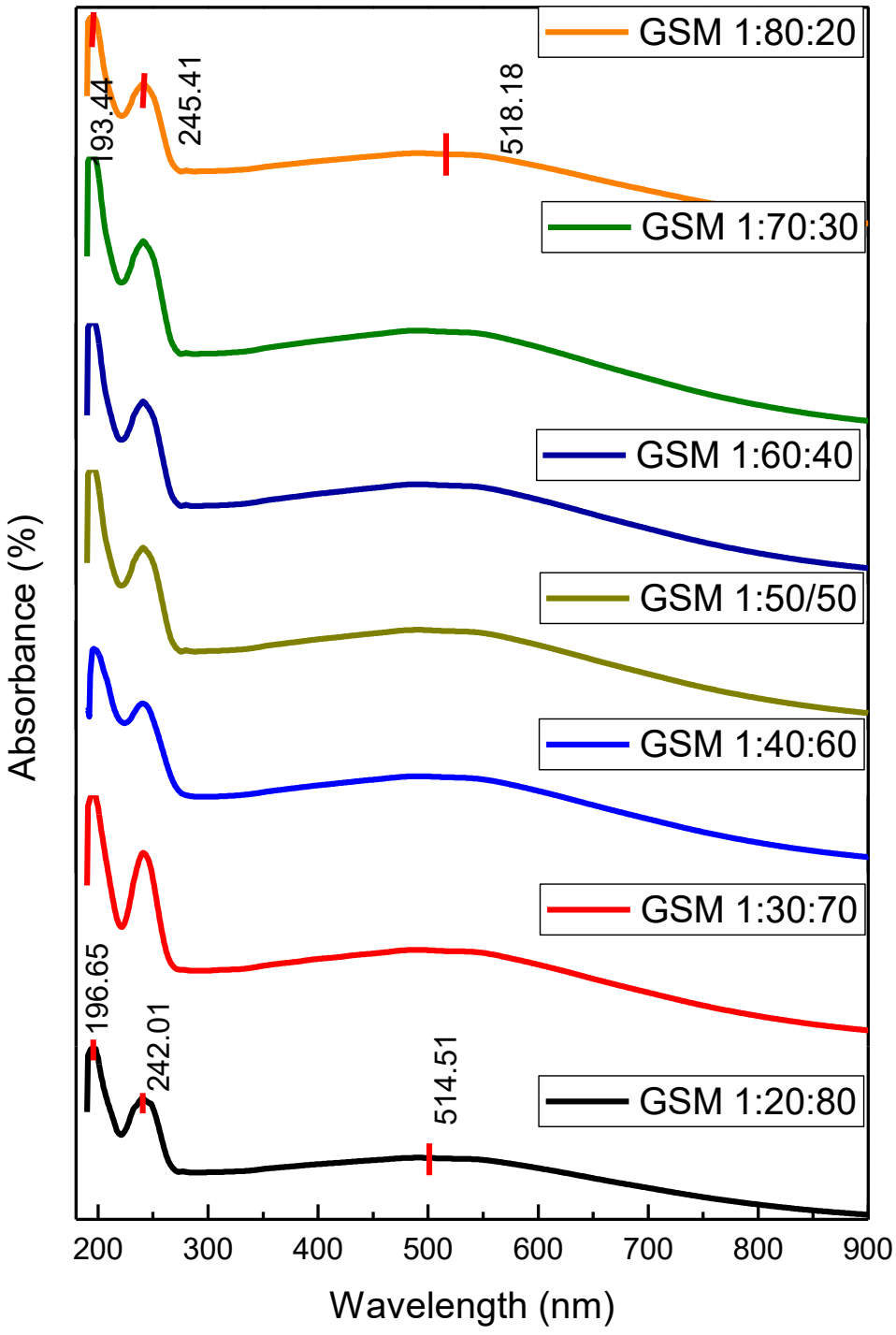


Figure 5.4: Optical absorption spectra demonstrating the high-energy ultraviolet absorption features alongside a distinct visible-region shoulder, highlighting the electronic band structure modifications of the material (GSM composites).

The UV-Vis absorption spectrum clearly shows the correlation between the composition of the synthesized sample and its optical response. As the concentration of SbSI increases, the absorption band gradually shifts to a longer wavelength (red shift). The specific GSM 80/20 composites resolve the different absorption peaks at 193.44nm, 245.41nm, and 516.12nm, representing the most severe redshift and the narrowest optical band gap throughout the sample series.

These characteristics are not considered absolute certainty, but similar absorption peaks of related multi-component frameworks are usually assigned based on previous literature. In the case of GO, the characteristic UV absorption peaks are usually observed at about 214 nm and 302 nm, respectively, corresponding to the local electronic transition of the carbon network-particularly the local electronic transition of high energy and the aromatic C=C bond function from π to π* [184]. After the incorporation and IC of transition metal oxide hosts MnO_2 and chalcohalide materials, significant electronic changes occur through chemical interaction and charge transfer across heterojunctions [165]. This changes the UV peaks of these carbon networks slightly, ranging from 214 nm to 196 nm. At the same time, a new, unique absorption peak appeared in the visible region at about 516 nm. The peak in this visible range is strongly consistent with the characteristic band-band transition of the chalcohalide nanostructure, which demonstrates dynamic interactions with transition metal oxide frameworks and expands the spectrum of optical absorption [197, 198], confirming successful composite formation.

The shift of the observed peaks is categorized in Table 5.1:

Table 5-1: An overview of the UV-Vis peak position for all GSM sample composites and the proposed optical transition mechanisms.

Sample	**Peak 1**	**Peak 2**	**Peak 3**	**Shifting of Peaks**
GSM 1:20:80	196.65 (π to π*)	242.01 (GO-TMO interaction) [199]	514.51(Carbo-MnO_2/ Carbon-SbSI) [86, 200]	As Reference
GSM 1:30:70	193.46 (π to π*)	241.12 (GO-TMO interaction) [199]	516.91(Carbo-MnO_2/ Carbon-SbSI) [86, 200]	Blue, Blue, Red
GSM 1:40:60	194.84 (π to π*)	239.99 (GO-TMO interaction) [199]	514.22 (Carbo-MnO_2/ Carbon-SbSI) [86, 200]	Blue, Blue, Blue
GSM 1:50:50	192.14 (π to π*)	241.10 (GO-TMO interaction) [199]	510.16 (Carbo-MnO_2/ Carbon-SbSI) [86, 200]	Blue, Blue, Blue
GSM 1:60:40	193.24 (π to π*)	242.00 (GO-TMO interaction) [199]	515.16 (Carbo-MnO_2/ Carbon-SbSI) [86, 200]	Blue, Blue, Red
GSM 1:70:30	194.84 (π to π*)	240.60 (GO-TMO interaction) [199]	514.31 (Carbo-MnO_2/ Carbon-SbSI) [86, 200]	Blue, Blue, Blue
GSM 1:80:20	193.44 (π to π*)	245.41 (GO-TMO interaction) [199]	518.18 (Carbo-MnO_2/ Carbon-SbSI) [86, 200]	Blue, Red, Red

5.2 Fourier Transform Infrared Spectroscopy (FTIR)

FTIR is an analytical technique that is used to study the chemical structure of materials. It is useful to identify the different functional groups, chemical bonds, and lattice vibration modes present in a sample. FTIR can be used for the analysis of solid, liquid, and gaseous materials. It provides highly resolved infrared spectra by measuring the absorption of infrared radiation at different wavelengths. In the present work, FTIR was used to investigate the chemical bonding and functional groups of GO, SbSI nanowires, GO-SbSI composites, and MnO_2 nanocomposites.

The structural characteristics and functional groups of the synthesized nanocomposites GO, SbSI, and MnO_2 were evaluated with FTIR spectroscopy. The spectrum was recorded using a PerkinElmer Spectrum One FTIR spectrometer at the Energy Materials Research Group (EMRG), School of Materials and Mineral Resources Engineering, Universiti Sains Malaysia.

To analyze solid materials, the samples were prepared using the KBr pellet method. The composite samples and dry potassium bromide (KBr) were thoroughly mixed at a 1:10 weight ratio and ground to ensure a highly uniform distribution. The uniform powder mixture was then transferred to a steel pellet die, compressed under hydraulic pressure, and produced transparent and mechanically stable pellets.

The pellets manufactured were immediately transferred to the spectrometer's sample holder. Under ambient conditions, spectral data were collected over a range of 400-4000 cm^{-1} wavenumbers. The results of the experiments were used to confirm the success of target matrix formation and to investigate the interfacial interaction between the GO, SbSI, and MnO_2 phases.

5.2.1 FTIR of GO

The bonding structure of the GO was analyzed through FTIR spectroscopy (Figure 5.5). The testing was done through the FTIR KBr pellet method. FTIR spectrum of the synthesized GO displays all characteristic vibrational modes typical of highly oxidized carbon frameworks, are observed at 3699.56 cm^{-1}, 3426.91 cm^{-1}, 2925.59 cm^{-1}, 1720.67 cm^{-1}, 1620.99 cm^{-1}, 1396.18 cm^{-1}, and 1034.65 cm^{-1}, due to the presence of water bonds (O-H), alkoxy (C-O), epoxy bond (O-H), C=O deformation and stretching of O-H respectively and cited in the literature [201, 202]. The peaks at 1034.65 cm^{-1} and 1720.67 cm^{-1} are attributed to the epoxy and carboxylic functional groups. Graphite contributes to a skeleton vibration of carbon atoms, which produces a peak at 1620.99 cm^{-1}. The peaks of O-H are observed at 2925.59 cm^{-1}, 3426.91 cm^{-1}, and 3699.56 cm^{-1} [201, 202]. The presence of these prominent oxygen-containing functional groups indicates a standard, well-functionalized GO matrix that aligns with established literature baselines.

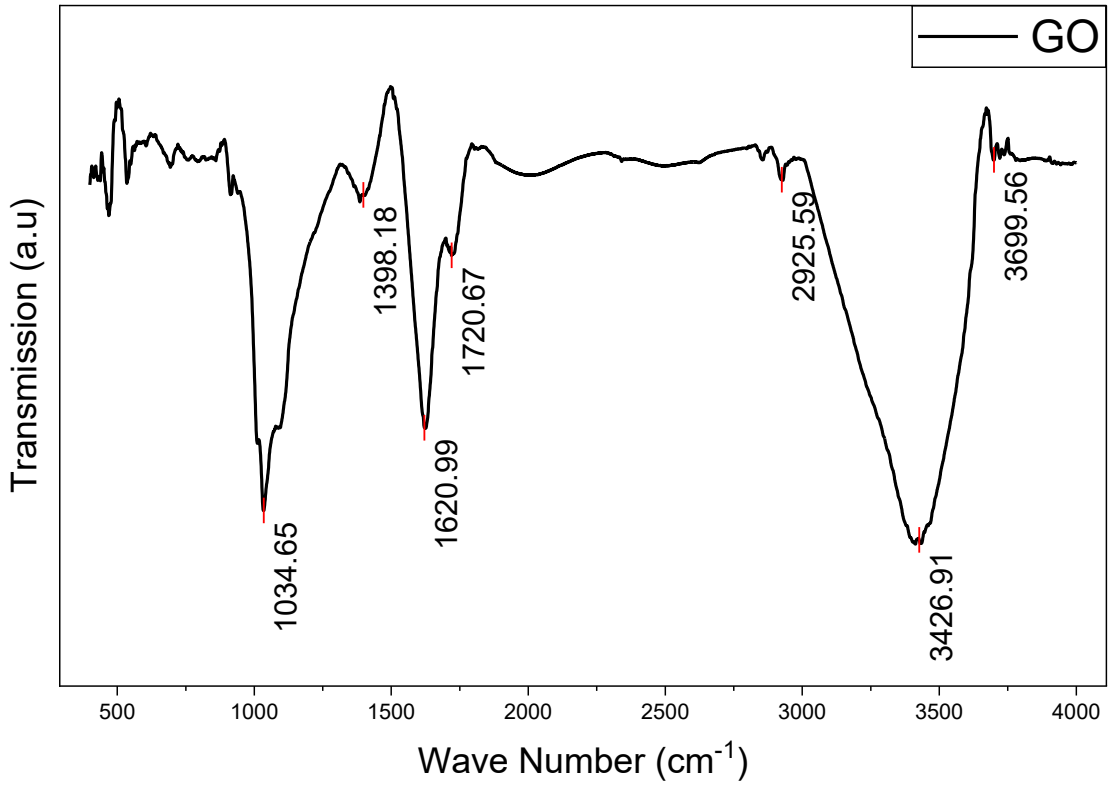


Figure 5.5: FTIR spectrum of GO.

5.2.2 FTIR of SbSI

SbSI FTIR spectrum is presented in Figure 5.6. According to the data reported on the SbSI nanowires synthesized by sonochemistry, the bulk crystal SbSI does not have an intrinsic infrared active vibration band within the 400-4000 cm^{-1} range. Consequently, the spectral peaks observed in this region correspond to the surface-absorbed species and residual components of the synthesis gel matrix [203]. Metal-sulfur bonds were detected at 633.79 cm^{-1} [204]. The C=O and the H_2O group with OH absorption bonding peaks are exhibited at 1628.27 cm^{-1} [205] and 3441.37 cm^{-1} [205], respectively. These features are associated with the structural deformations and stretching modes of adsorbed moisture layers and surface-bound hydroxyl networks [203]. The peak of C-O is observed at 834.12 cm^{-1} [206]. The stretching of $-CH_3$ in ethanol gel is observed at 1042.15 cm^{-1} [207]. Another peak of O-H in ethanol is located at 1335.76 cm^{-1}. These localized bands correspond to organic coordinates originating from molecularly adsorbed ethanol and stable ethoxide species formed dissociatively during sonolysis, which passivate the high-surface-area nanowire coordinates [203]. The related SbSI FTIR spectra are presented in the literature [208].

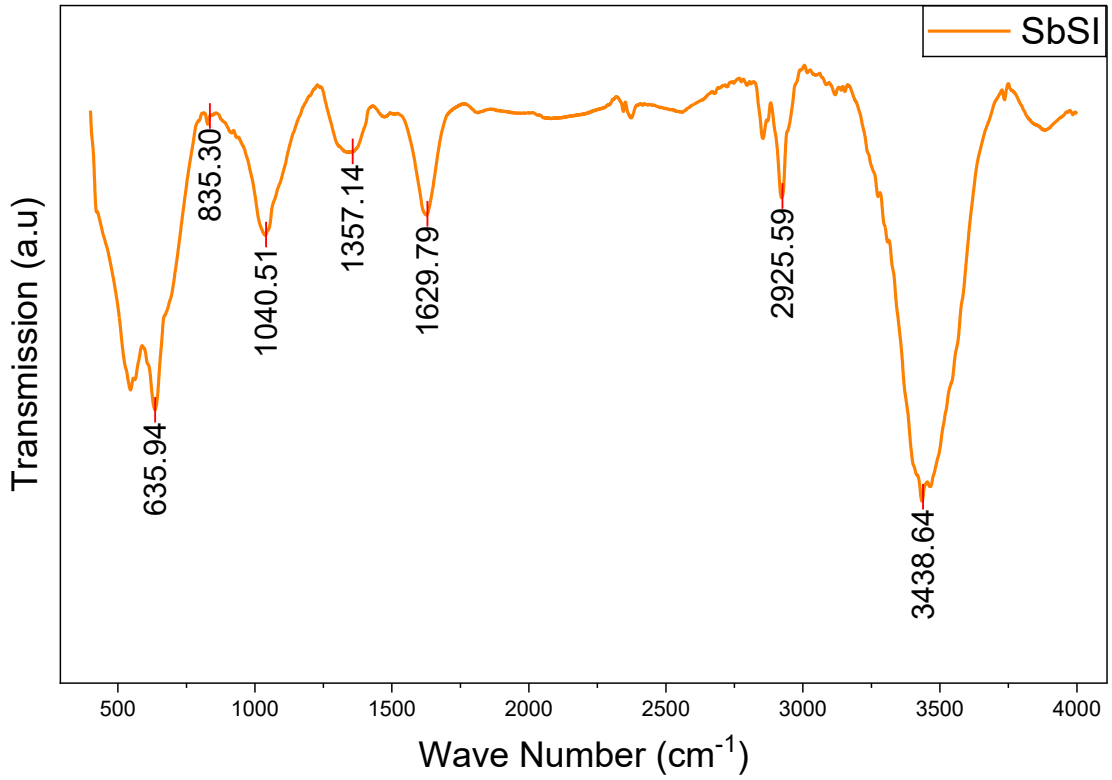


Figure 5.6: FTIR spectrum of SbSI.

5.2.3 FTIR of GO-SbSI Composites

Figure 5.7 shows the FTIR spectra of pure and concentration-based prepared materials. Upon combining these components to form the GO-SbSI nanocomposite series, the simultaneous coexistence of core fingerprints from both parent materials verifies a successful interfacial hybrid assembly across all compositional ratios. The baseline Sb-S lattice modes near 633.79 cm^{-1} and the principal hydroxyl bands near 3441.37 cm^{-1} are structurally preserved across all five composites; however, their gradual broadening and marginal shifting signify active interfacial hydrogen-bonding configurations bridging the oxide networks with the chalcohalide material.

The graphitic skeleton vibrations (C=C at 1620.35 cm^{-1} from GO) smoothly overlap with the localized SbSI transitions at 1628.27 cm^{-1}, ensuring mechanical and structural continuity without disrupting the carbon matrix backbone. Furthermore, tracking across the composite series from GO-SbSI 70/30 to GO-SbSI 30/70 reveals a controlled attenuation and progressive reduction in the relative intensity of oxygenated peaks, most notably the sharp carbonyl C=O mode at 1720.72 cm^{-1}. This systematic modification confirms that adjusting the component ratios successfully alters the local electronic density and induces beneficial structural defect states, promoting enhanced charge-carrier delocalization essential for optimized electrochemical performance in supercapacitor applications.

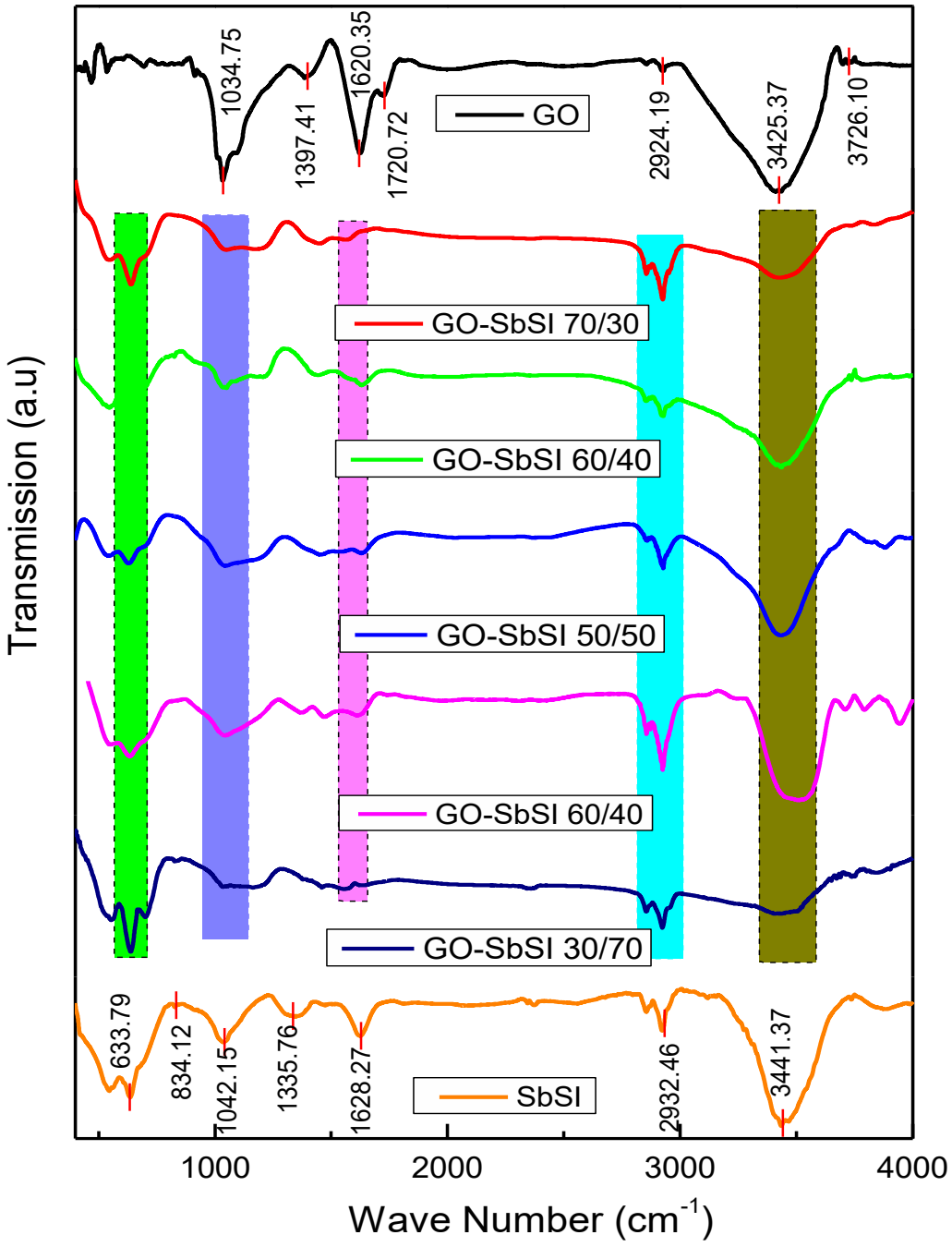


Figure 5.7: FTIR transmission spectra of GO, SbSI nanowires, and their corresponding GO-SbSI composites (70/30, 60/40, 50/50, 40/60, and 30/70). The highlighted vertical bars indicate characteristic functional groups and vibrational modes tracking interfacial coupling.

Table 5-2: The peaks of GO-SbSI 70/30, GO-SbSI 60/40, GO-SbSI 50/50, GO-SbSI 40/60, and GO-SbSI 30/70 are presented in the table with their bonding group ranges.

Wave Numbers:	Functional Groups/Bonding:	Related Material:	References
3200–3600 cm^{-1}	O–H	GO, SbSI	[170, 203, 209, 210]
2850–2925 cm^{-1}	C–H	GO	[170, 209, 210]
1715–1730 cm^{-1}	C=O	GO	[170, 209, 210]
~ 1620–1630 cm^{-1}	C=O and C=C	SbSI, GO	[170, 203, 209, 210]
~1220–1270 cm^{-1}	OH and C–O–C	SbSI, GO	[170, 203, 209-211]
~1040–1100 cm^{-1}	C–O	GO	[165, 170, 209, 210]
~800–900 cm^{-1}	$-CH_3$	SbSI	[203]

5.2.4 FTIR of GSM Composites

The FTIR spectrum of the composite series from the GSM (1:20:80) to the GSM (1:80:20) samples is shown in Figure 5.8. The recorded spectra show a wide absorption band of 3400-3300 cm^{-1}, a weak peak of around 2920 cm^{-1}, and a prominent band of around 1630 cm^{-1}. In addition, lower-intensity peaks can be seen in the mid-infrared region between 1400-1380 cm^{-1} and 1100-1000 cm^{-1}. Based on the FTIR spectra (Figure 5) for samples GSM (1:20:80) to GSM (1:80:20), the observed functional groups and bonding structures are interpreted as follows.

A broad absorption band between ~3400-3300 cm^{-1} appears across all samples, indicative of O-H stretching vibrations characteristic of hydroxyl groups from water molecules or -OH functionalities in GO [212]. It can be clearly pointed out that this peak in this specific range in all tested samples originates from a dual structural source that combines the native oxygen functions of the GO framework with the surface-adsorbent environmental humidity layers of high surface-area SbSI nanostructures. This band is strongest in GSM 1:20:80 and progressively weakens toward GSM 1:80:20, suggesting a reduction in oxygen-containing groups as MnO_2 and SbSI proportions increase.

The weak peak around ~2920 cm^{-1} is attributed to C-H stretching vibrations of aliphatic $-CH_2$ or $-CH_3$ groups, possibly from residual organic components or unoxidized carbon frameworks in GO [212, 213]. The persistence of this band points to a higher degree of GO presence or less integration with MnO_2-SbSI phases in these samples.

A strong, broad band near ~1630 cm^{-1} is consistently present and assigned to C=C stretching from carbonyl group vibrations [214]. This peak narrows and diminishes in intensity in GSM 1:70:30 and GSM 1:80:20, consistent with improved deoxygenation and hybrid phase formation due to SbSI and MnO_2 incorporation.

Peaks around ~1400-1380 cm^{-1} correspond to COO^- bending or symmetric stretching of carboxylates [170], prominent in GO-rich composites such as GSM 1:20:80-GSM 1:40:60. The reduction in intensity across GSM 1:50:50-GSM 1:80:20 confirms effective interaction or reduction of GO, potentially driven by MnO_2-induced redox processes or structural bonding with SbSI.

The absorption region between 1100-1000 cm^{-1} encompasses C-O-C stretching modes in epoxide groups [170]. This band becomes weaker and more diffuse in GSM 1:60:40 to GSM 1:80:20, further validating the consumption or chemical transformation of GO oxygen functionalities.

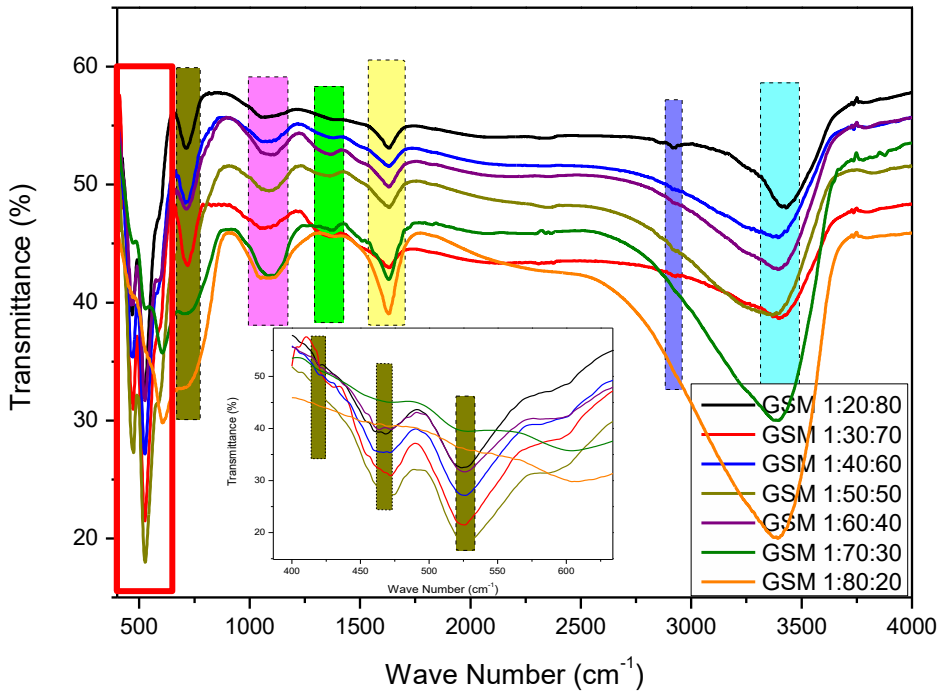


Figure 5.8: FTIR spectra of GSM 1:20:80 to GSM 1:80:20. Characteristic Mn-O, Sb-S, Sb-I, and GO functional groups are observed, with intensity changes reflecting compositional tuning.

Below 800 cm^{-1}, multiple sharp bands emerge. Notably, peaks at 720 cm^{-1} and 540-500 cm^{-1} are assigned to Sb-S and Sb-O bond vibrations, confirming successful incorporation and rising concentration of the SbSI phase [204]. These features are characteristic of orthorhombic SbSI and correlate with the XRD findings.

A strong band near 510-470 cm^{-1}, most intense in GSM 1:20:80 to GSM 1:60:20, corresponds to Mn-O vibrations from MnO_2 octahedra [215, 216]. Its gradual disappearance toward GSM 1:80:20 reflects declining MnO_2 content and an increasing SbSI ratio, supporting the structural evolution observed in XRD.

The transformation in bonding character from GSM 1:20:80 to GSM 1:80:20 indicates structural reorganization. This compositional evolution and the corresponding shifts in characteristic functional environments are systematically summarized in Table 5.3, which highlights the structural and bonding extremes among the synthesized materials.

Table 5-3:Summary of the peak positions of FTIR, the allocation of functional groups, and the origin of the underlying materials in the GSM composite series.

Wavenumber Region	Functional Group	Material Origin	Reference
~ 3200-3400 cm^{-1}	O-H	SbSI, GO, MnO_2	[203, 213, 217]
~ 2850-2950 cm^{-1}	C-H	GO, SbSI	[203, 213]
~ 1620-1630 cm^{-1}	C=C or C=O	SbSI, GO, MnO_2	[203, 213, 215]
~ 1380-1480 cm^{-1}	COO^- symmteric	GO, SbSI	[203, 213]
~ 1000-1100 cm^{-1}	C-O-C	GO, SbSI	[203, 213]
~ 470-550 cm^{-1}	Mn-O	MnO_2	[215]

FTIR confirms phase evolution and functional interaction across the GSM series. The reduced -OH and C-O signatures with increasing MnO_2 and SbSI reflect improved structural order and hybridization. Based on subsequent electrochemical measurements, including CV, GCD, and EIS, which demonstrate a reduction in charge transfer resistance, this structural restructuring has been directly correlated with enhanced supercapacitor performance through synergistic charge storage, improved conductivity, and stable bonding in optimized samples such as GSM 1:70:30 and GSM 1:80:20.

Chapter 6

IMPEDANCE SPECTROSCOPY

Impedance spectroscopy is employed to investigate the electrical response of the prepared materials over the selected frequency range. This technique provides insight into the effects of interfacial interactions between the constituent phases on charge-transport behavior, polarization phenomena, and relaxation processes.

The measurements were performed using compressed pellets. The measurements were conducted over a frequency range of 42 Hz to 5 MHz using an AC amplitude of 0.01 V at room temperature with a Hioki 3532-50 LCR HI tester.

6.1 GO, SbSI and GO-SbSI Composites

6.1.1 Complex Impedance and Nyquist Plot Analysis

Analysis of the real component of complex impedance, Z ', is employed to evaluate the resistive (in-phase, energy-dissipating) response of a material and to distinguish the resistive contributions originating from the bulk grains, grain boundaries, and electrode/sample interfaces under an alternating electric field. Figure 6.1 illustrates the variation in Z' as a function of frequency (from 42 Hz to 5 MHz for GO, SbSI, and the GO-SbSI binary composites with varying compositional ratios (70/30, 60/40, 50/50, 40/60, and 30/70). Across the measured range, the spectra display two primary operational regimes: a static, frequency-independent plateau region in the lower-frequency domain, followed by frequency-dependent dispersion in the intermediate-to-high frequency window.

Across the measured range, the spectra display two distinct operational regimes: a static, frequency-independent plateau in the lower-frequency domain, followed by a frequency-dependent dispersion window at intermediate-to-high frequencies. The low-frequency plateau corresponds to the near-DC bulk resistance of the samples. Mechanistically, this region is governed by the accumulation of space charges and Maxwell-Wagner interfacial polarization at internal boundaries-a behavior characteristic of high-impedance semiconducting chalcohalides. As the frequency exceeds 10^3 Hz, the curves undergo a continuous roll-off and converge toward a common low-impedance window 10^1-10^2 above 1 MHz. This high-frequency convergence signifies the release of trapped space charges and the onset of relaxation dynamics once the alternating field outpaces the relaxation time of the charge carriers.

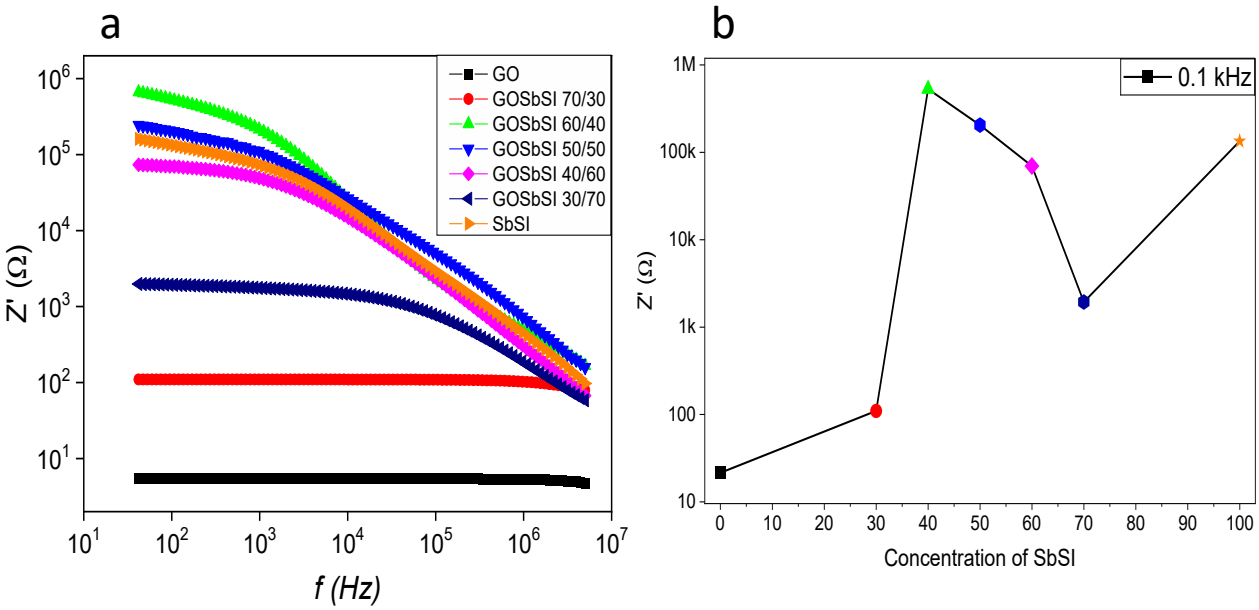


Figure 6.1: (a) Frequency dependence of the real part of complex impedance Z' for GO, SbSI, and the GO-SbSI binary composites with varying compositional ratios; (b) Dependence of Z' on the SbSI content for a frequency of 100 Hz.

The magnitude of the impedance varies significantly with composition. GO exhibits the lowest overall impedance, maintaining a flat profile across the entire frequency spectrum at approximately 5-6 Ω, consistent with its high intrinsic electrical conductivity and established literature models [218]. The GO-rich composite (70/30) exhibits a similarly flat response up to high frequencies, plateauing at roughly 102 Ω. In contrast, SbSI and the higher-impedance composites (60/40 and 50/50) demonstrate elevated low-frequency plateaus on the order of 10^5-10^6 ohm. The 30/70 composite tracks an intermediate trajectory, plateauing around 2×10^3 ohm before converging with the other spectra at elevated frequencies.

To isolate the composition-dependent conduction pathways, the Z' at 0.1 kHz is plotted against SbSI concentration (Figure 6.1b). This low-frequency limit effectively isolates the DC-like resistive pathway available for charge transport; the applied AC field varies slowly enough that capacitive reactance ($X_C = 1/2\pi fC$) becomes very large, making capacitive contributions negligible and allowing carriers ample time to traverse grain boundaries and interfaces before the field reverses [219]. As demonstrated in Figure 6.1b, the variation of Z' at 0.1 kHz follows a distinctly non-monotonic trend, confirming that the composite's electrical network is governed by evolving microstructural connectivity rather than a simple linear combination of the two phases. At 0% SbSI (GO), the low-frequency Z' is highly conductive at 20 Ω, owing to facile charge hopping through its partially reduced, Sp^2-conjugated network. Incorporating 30% SbSI yields only a marginal increase to 100 Ω, indicating that the highly conducting GO framework remains largely continuous and dominant. However, between 30% and 40% SbSI, a sharp percolation-type threshold is crossed, causing Z' to surge by

nearly four orders of magnitude to its maximum value (105 Ω). This abrupt transformation indicates that the semiconducting SbSI phase fragments the continuous GO pathways, compelling charge carriers to navigate highly resistive GO-SbSI interfaces and grain boundaries. Beyond this threshold, increasing the SbSI concentration introduces a localized resistive minimum near 70% SbSI (10^3 Ω) before tracking up to the SbSI value of 1.5×10^5 Ω, demonstrating the complex structural changes within the binary network. The subsequent roll-off of Z' and convergence across the curves at elevated frequencies signifies the release of these trapped space charges, the onset of relaxation dynamics, and a corresponding enhancement of AC conductivity once the frequency of the alternating field outpaces the relaxation time of the trapped carriers [220, 221].

Figure 6.2 presents the frequency dependence of the imaginary part of the impedance (Z″) for GO, SbSI, and the GO-SbSI composites with ratios of 70/30, 60/40, 50/50, 40/60, and 30/70. The measurements cover the range from approximately 42 Hz to 5 MHz. Z″ varies over roughly six orders of magnitude across the series. The samples are divided into three groups according to the shape of their Z″ spectra. In the first group, GO and the GO-SbSI 70/30 composite have by far the lowest Z″ values, which consist of a conductive, GO-dominated network. Their Z″ increases steadily with frequency and shows no resolved maximum within the measured window. In the second group, the GO-SbSI 60/40, GO-SbSI 50/50, and SbSI samples have the highest Z″ values, in the range of 10^4-10^5 Ω. Their spectra are nearly flat at low frequencies and decrease above roughly 10^3-10^4 Hz, and the curves converge at high frequencies (10^6-10^7 Hz). In the third group, the GO-SbSI 40/60 and 30/70 composites show well-defined, broad maxima. For the 40/60 sample, Z″ starts at about 6×10^3 Ω and peaks near 10^3 Hz. The 30/70 sample has an intermediate magnitude (about 4-5×10^2 Ω) and a peak near 10^5 Hz. The change in Z″ with composition is not monotonic, which suggests that percolation of the GO network and interfacial (Maxwell-Wagner-Sillars) polarization at the GO-SbSI boundaries strongly influence the response. The peaks are also broader than a single Debye process would produce [222], which indicates a distribution of relaxation times. The peak frequencies and corresponding relaxation times were determined from the experimental data using [223].

$$\boldsymbol{\tau = \frac{1}{2\pi f_{max}}} \qquad \textbf{(6-1)}$$

Where f_{max} is the peak frequency, the calculated relaxation times systematically decrease across this composition range.

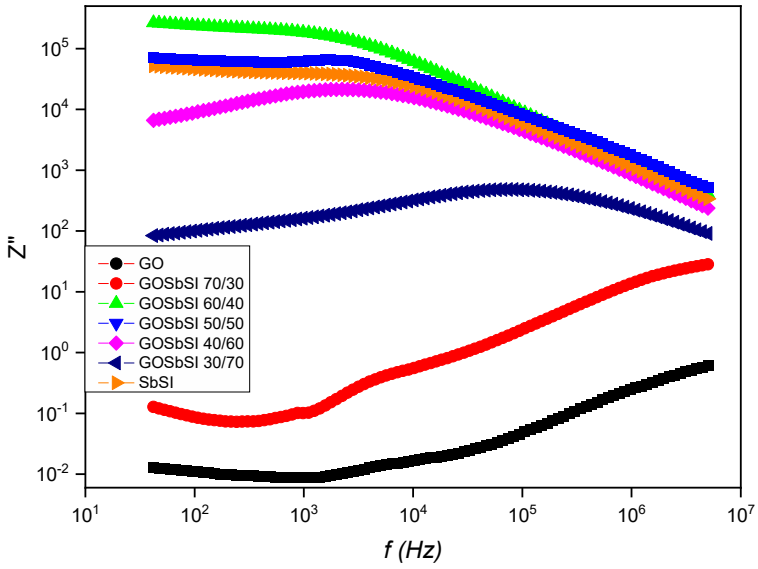


Figure 6.2: Imaginary part of impedance as a function of frequency for GO, SbSI and GO-SbSI composites (70/30, 60/40, 50/50, 40/60, and 30/70).

The peak frequency increases from the hundreds of Hz region for 60/40 to 1.573 kHz for 50/50, 2.234 kHz for 40/60, and reaches a maximum of 74.424 kHz for the 30/70 sample (Table 6.1). For the remaining samples-including GO, 70/30, 60/40, and SbSI-the relaxation peaks remain unresolved within the experimental frequency boundaries. It is suggested that this behavior might be related to the physical nature of the compressed powder specimens. Because the measurements were conducted on pelletized compacts, the calculated Z″ quantities reflect effective composite parameters that incorporate the influence of air-filled pores and internal microscopic voids rather than the pure intrinsic impedance of the isolated materials. Such structural porosity could potentially alter the local electric field lines or modify the underlying charge-transport paths, which might explain why the relaxation processes are either shifted or broadened completely beyond the examined experimental window.

Table 6-1: Extracted f_{max} and τ values of GO, SbSI and GO-SbSI composites under varying weight percentage compositions.

Composition	f_{max} (Hz)	τ (µs)
GO	Unresolved	0.0318 At 5 MHz
GO-SbSI 70/30	Unresolved	0.0318 At 5 MHz
GO-SbSI 60/40	Unresolved	--
GO-SbSI 50/50	1,572.98	101.18
GO-SbSI 40/60	2,233.54	71.26
GO-SbSI 30/70	74,423.60	2.14
SbSI	Unresolved	-

Figure 6.3 shows the Nyquist plots (Z″ versus Z′) of GO, SbSI, and the GO-SbSI composites with compositional ratios of 70/30, 60/40, 50/50, 40/60, and 30/70, measured over the frequency range of about 42 Hz to 5 MHz. The spectra differ greatly in magnitude. Z′ reaches about 6.7×105 Ω for the 60/40 composite, whereas GO and the GO-rich composites remain within a few hundred ohms, so on the scale of the figure they appear as points near the origin. The impedance response therefore depends on the GO/SbSI ratio, and the samples fall into three groups.

The first group consists of GO and GO-SbSI 70/30. GO shows no resolvable arc, and its Z′ and Z″ values are only a few ohms at most. This indicates an almost purely resistive, highly conductive response in the measured frequency window. The 70/30 composite behaves similarly. Its data points lie at Z′ (70-110 Ω) with Z″ below about 10 Ω, which is the onset of a very small arc. Its resistance is therefore of the order of 100 Ω, which is consistent with a continuous conduction path through the GO network.

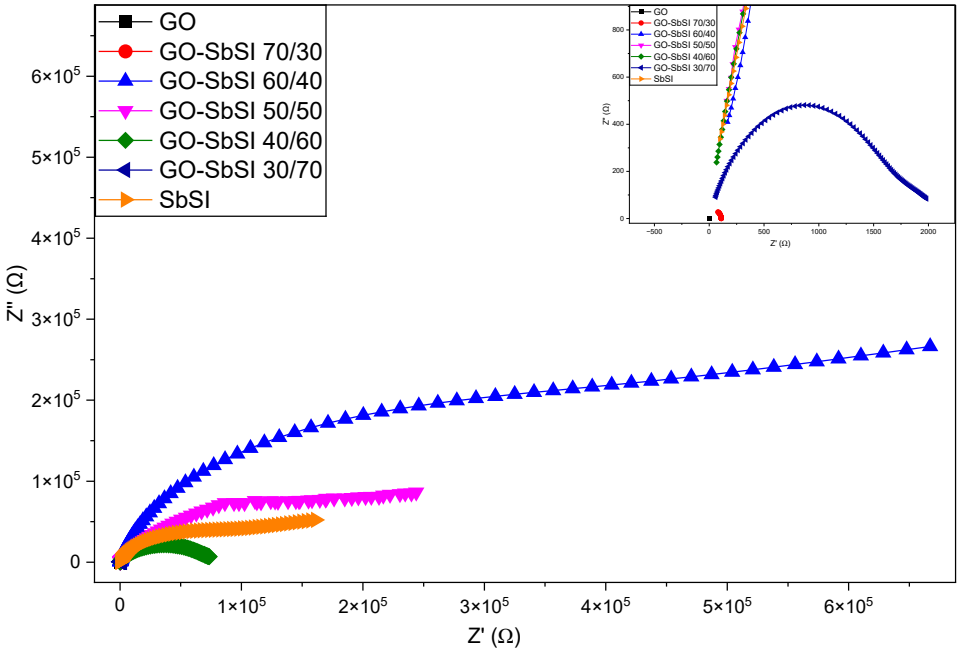


Figure 6.3: Nyquist plots (Z' vs. Z") for GO, SbSI, and GO-SbSI composites as (70/30, 60/40, 50/50, 40/60, and 30/70).

The second group contains the samples with the largest impedance: GO-SbSI 60/40, GO-SbSI 50/50, SbSI, and GO-SbSI 40/60. All four show depressed arcs whose centres lie below the real axis. This is typical of non-Debye relaxation with a distribution of relaxation times [222], and it agrees with the broad Z″ maxima discussed previously. The 60/40 composite gives by far the largest response. Its curve rises steeply to Z″ around 1.5×10^5 Ω at Z′ around 1×10^5 Ω and then continues as a gently rising, nearly linear tail up to Z′ ≈ 6.7×10^5 Ω and Z″ ≈ 2.7×10^5 Ω. The arc is not closed within the measured

range, so the total resistance is at least of the order of 106 Ω. The 50/50 composite follows a similar path on a smaller scale, with $Z'' \approx 7\times10^4$ Ω at $Z' \approx 8\times10^4$ Ω and a shallow tail extending to $Z' \approx 2.4\times10^5$ Ω. SbSI has a flatter arc with $Z'' \approx 4\times10^4$ Ω and a tail ending at $Z' \approx 1.6\times10^5$ Ω. The 40/60 composite is the only member of this group that forms an almost complete semicircle. Its maximum lies at $Z' \approx 3.5\times10^4$ Ω and $Z'' \approx 2\times10^4$ Ω, and the arc returns towards the real axis at $Z' \approx 7\text{-}8\times10^4$ Ω, which gives a resistance of about 8×10^4 Ω. All four samples have small high-frequency intercepts of roughly 65-150 Ω, followed by a steep rise of Z'' that develops into the arcs described above. The low-frequency tails of the 60/40, 50/50 and SbSI samples may originate from a second, overlapping relaxation, such as a grain-boundary or interfacial process, or from electrode polarization. Because the measurements stop at about 40 Hz, these arcs are incomplete, and the resistances quoted for them should be regarded as lower-bound estimates.

The third group contains only GO-SbSI 30/70, whose behavior lies between the two extremes. Although it is barely visible at the scale of the figure, its response is a well-defined, depressed semicircular arc, with a high-frequency intercept of about 50 Ω, a maximum at $Z' \approx 900$ Ω and Z'' of a few hundred ohms, and a slightly asymmetric descent towards the real axis at about 2000 Ω. The arc diameter corresponds to a resistance of roughly 2-3 kΩ. This value is approximate because the arc is not completely closed. Its resistance is about two orders of magnitude lower than that of the other SbSI-rich samples, so this composition supports a much more effective conduction pathway.

Overall, the arc size demonstrates that this composition facilitates a substantially more efficient conduction pathway. In terms of resistive behavior, the arc size-and thus the bulk resistance-was highest for GO-SbSI 60/40, progressively lower for 50/50, SbSI, and 40/60, exhibited a marked decline in 30/70, and further decreased through 70/30, so the dependence on composition is clearly non-monotonic. The GO-rich samples are highly conductive, which suggests a percolating GO network. When the SbSI content increases to the 60/40 and 50/50 composites, the resistance rises above that of SbSI. This suggests that the GO phase becomes partly isolated by SbSI, so that the continuous conduction path is lost and the many GO/SbSI interfaces act as barriers. This would enhance interfacial (Maxwell-Wagner-Sillars) polarization. At higher SbSI contents (40/60 and 30/70), the resistance decreases again, which may indicate the formation of a different conduction pathway, although the present data cannot identify its nature. This trend is consistent with the Z'' spectra, in which the same samples show the largest low-frequency values.

6.1.2 Real and Imaginary Permittivity, Tangent Losses, and AC Conductivity

The real permittivity describes the ability of a material to store electrical energy through polarization when subjected to an external AC field. It explains the behavior of dipolar, ionic, electronic, and interfacial (space-charge) polarization mechanisms as they respond to the changing

field frequency. The ε' for the prepared pellets was calculated using the standard capacitive geometric relationship [224].

$$\varepsilon' = \frac{C_I d}{A\varepsilon_0} \qquad (6\text{-}2)$$

where C' is the real part of the complex capacitance of the sample, A is the surface area of the electrode contact, d is the compact thickness, and ε_0 is the vacuum permittivity. The frequency dependence of the calculated room-temperature permittivity across the binary series is plotted in Figure 6.4a. Because these electrical measurements were performed on specimens fabricated in the form of compressed pellets from raw synthesized powders, the calculated parameters represent the so-called effective permittivity of the porous compact-which explicitly includes the contributions of internal air-filled voids-rather than reflecting the actual intrinsic permittivity of the fully dense solid materials themselves. The presence of these internal microscopic pores naturally introduces a low-permittivity boundary phase that affects the overall capacitance response. Consequently, this evaluation avoids commenting on absolute numerical thresholds and focuses exclusively on a relative comparison of the permittivity behaviors observed between the distinct samples across the series.

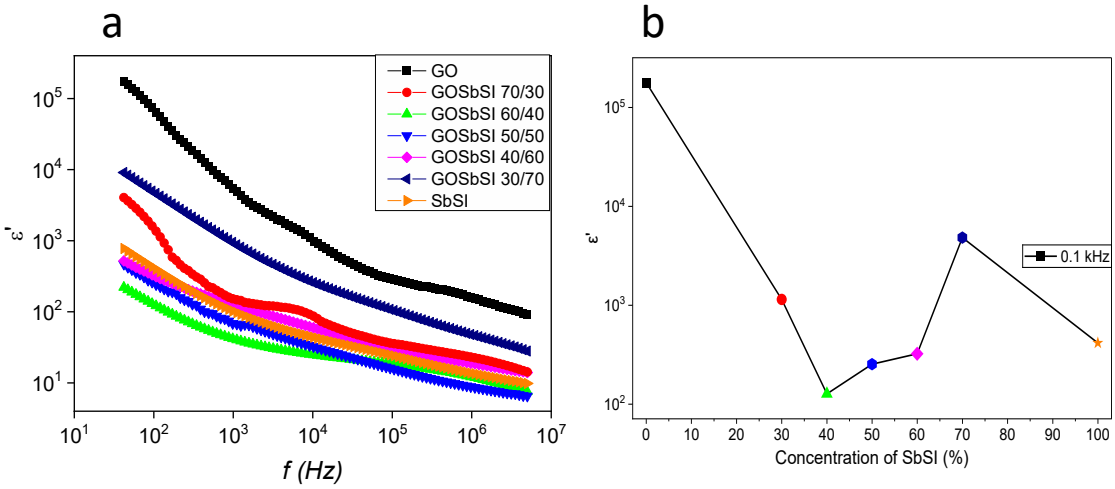


Figure 6.4: (a) Frequency dependence of the real part of permittivity ε' as a function of frequency for GO, SbSI, and various GO/SbSI composites as (70/30, 60/40, 50/50, 40/60, and 30/70) composites; (b) Dependence of ε' on the SbSI content for a frequency of 100 Hz.

As illustrated by the permittivity spectra, all curves exhibit a continuous, monotonic decrease as the field frequency increments from 42 Hz to 5 MHz. However, the magnitude of this capacitive response changes non-monotonically with the composition of the composite. GO displays the highest effective permittivity profile across the entire monitored frequency range and is well matched with literature [218], followed immediately by the highest concentration of the SbSI 30/70 mixture and the GO concentration 70/30 sample. In contrast, the remaining intermediate balances (40/60 and 50/50) alongside SbSI cluster tightly together at a significantly lower baseline, while the 60/40 ratio maintains

the absolute lowest effective permittivity profile overall. As the alternating current frequency scales up toward higher limits, the curves systematically converge due to standard permittivity dispersion, where the rapid field oscillation outpaces the localized relaxation times of the space charge accumulated at internal phase boundaries.

GO exhibits by far the highest ε′, starting near 2×10^5 at 42 Hz and decreasing steadily to about ~10^2 at 5 MHz, a classic large-magnitude permittivity dispersion typical of a highly defective, interface-rich carbon material. This rapid dispersion at lower frequencies stems from the combined contributions of multiple polarization mechanisms, including ionic, electronic, and orientational processes, which are strongly dominated by robust space-charge and Maxwell-Wagner-Sillars interfacial polarization phenomena [225, 226]. However, as the applied frequency increases, these heavier charge carriers can no longer rapidly alternate or synchronize with the high-frequency external electric field, resulting in a significant relaxation drop where the curves approach a high-frequency plateau governed strictly by swift electronic displacements. The 30/70 composite follows next, starting near 10^4 and falling to ~30. The 70/30 composite shows an unusual non-monotonic feature: after an initial fall from ~10^3, it displays a broad hump/shoulder in the 10^3-10^4 Hz region before resuming its decline - suggestive of an additional, superimposed relaxation process specific to this composition. The remaining composites (60/40, 50/50, 40/60) and SbSI cluster together at intermediate-to-low ε′ values (a few hundred down to below 10), showing the conventional monotonic decrease with frequency expected from interfacial and dipolar polarization mechanisms losing their ability to track the field.

Figure 6.4b shows the variation of the real part of the permittivity (ε′) with SbSI concentration in GO-SbSI composites at 0.1 kHz. GO (0% SbSI) exhibits an extremely high ε′ (~10^6), indicating that its low-frequency response is governed by conductive rather than polarizable behavior. With the introduction of SbSI, ε′ decreases sharply by two orders of magnitude, reaching ~10^3 at 30% SbSI due to strong interfacial (Maxwell-Wagner-Sillars) polarization in the GO-SbSI composites. Between 40% and 60% SbSI, ε′ drops to its lowest values (~10^2), suggesting a more homogeneous SbSI-rich microstructure with reduced interfacial charge accumulation. A second, more pronounced maximum (~10^3) appears at 70% SbSI, where a well-percolated SbSI network combined with residual conductive GO produces a synergistic enhancement of both interfacial and intrinsic ferroelectric polarization. Beyond this point, ε′ decreases for pure SbSI (~10^2), as the absence of GO removes the conductive bridging required to sustain enhanced polarization.

The ε′ composition trend is non-monotonic and correlates inversely with the impedance behavior of the same series, confirming that the 70/30 composite offers the optimum balance of percolating SbSI conduction and interfacial GO bridging, yielding maximum permittivity response and minimum resistive loss among the studied composite samples.

The imaginary permittivity ε″ quantifies the energy dissipated as heat during the polarization process-i.e., the fraction of stored electrical energy lost due to the finite response time (relaxation) of dipoles and charge carriers, together with any DC conduction loss. It explains the behavior of loss mechanisms arising from ionic/electronic hopping conduction and from dipolar relaxation.

The imaginary part of permittivity ε″ and tangent losses *tan δ* were extracted from formulas [227, 228]; both values were used as:

$$\varepsilon'' = \frac{C''d}{A\varepsilon_0} \qquad (6\text{-}3)$$

and

$$\tan\delta = \frac{C''}{C'} \qquad (6\text{-}4)$$

Where C″ is the imaginary part of the complex capacitance.

From Figures 6.5 and 6.6, it can be noticed that both imaginary permittivity and tangent losses follow the real permittivity pattern. The value of ε″ is high at lower frequencies because the charge carriers can retain their orientation at lower frequencies [229, 230]. The figure shows ε″ decreasing monotonically and smoothly with increasing frequency for every sample, over a very wide magnitude range (from ~10^8 down to below 1). GO again shows the highest loss throughout the spectrum, falling from ~10^8 to 10^3, followed closely by the 70/30 composite. The 30:70 composite forms a clearly separated intermediate band (105 down to ~10), while the 60/40, 50/50, 40/60 composites and SbSI form a tightly grouped lower band, with SbSI showing the lowest loss of all (falling below 1 at high frequency).

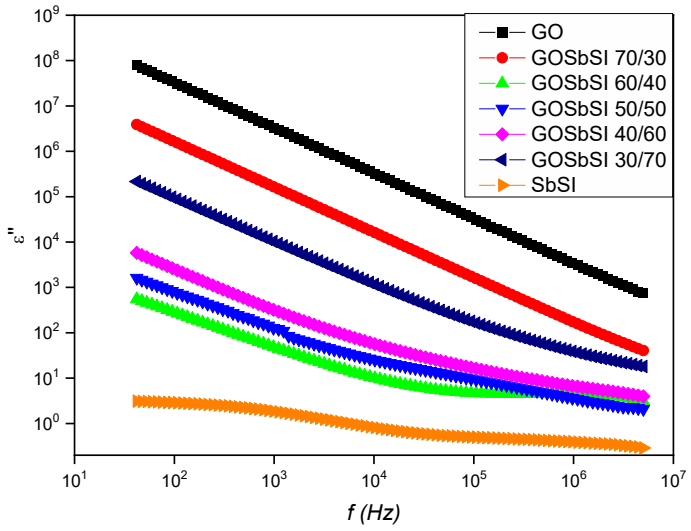


Figure 6.5: Variations of the imaginary part of permittivity versus frequency for GO, SbSI, and GO-SbSI composites (70/30, 60/40, 50/50, 40/60, and 30/70).

Across all composites, ε″ decreases with increasing frequency, consistent with the suppression of interfacial and dipolar contributions at high frequencies. However, the magnitude and slope of this decline vary significantly with SbSI content, revealing how the incorporation of the ferroelectric semiconductor modifies the permittivity response of the GO matrix. Composites with low SbSI fractions display relatively modest ε″ values, indicating limited dipolar mobility and a dominant GO-controlled permittivity behavior. As the SbSI concentration increases, the ε″ curves shift upward, demonstrating enhanced permittivity losses associated with stronger dipolar polarization, increased charge-carrier participation, and more active relaxation processes.

At higher SbSI loadings, particularly in the 60/40, 70/30, and SbSI samples, the permittivity loss becomes substantially larger across the entire frequency range. This behavior suggests the formation of continuous or near-continuous SbSI domains capable of supporting pronounced polarization under an alternating electric field. The steep decline in ε″ with frequency for these composites reflects the transition from low-frequency interfacial polarization to high-frequency dipolar relaxation typical of ferroelectric semiconductors. In contrast, the GO-rich samples (0 and 30/70) exhibit weaker dispersion, indicating restricted dipole dynamics and limited charge transport. Overall, the comparison suggests that SbSI concentration is the primary factor governing permittivity loss behavior in GO-SbSI composites, driving the system from a low-loss, GO-dominated regime toward a highly polarizable, SbSI-controlled permittivity response as the ferroelectric phase becomes increasingly integrated.

The *tan δ*, also termed the dissipation factor, evaluates the ratio of electrical energy dissipated as heat to the electrical energy stored per AC cycle, serving as a measure of energy losses caused by electrical conduction and dipole relaxation under an alternating electric field. Figure 6.6 illustrates the frequency dependence of tan δ over the frequency range from 42 Hz to 5 MHz for GO, SbSI, and the GO-SbSI binary composites (70/30, 60/40, 50/50, 40/60, and 30/70). Across the entire series, the loss tangent values vary by nearly four orders of magnitude and display distinctive relaxation peaks and roll-offs across the low-to-high frequency spectrum. Each exhibits a broad maximum: the GO peak around 10^3 Hz, while the 70/30 composite peaks at a slightly lower frequency (~10^2-10^3 Hz), before both decay toward the high-frequency end. The other samples (SbSI, 60/40, 50/50, 40/60, and 30/70) show much lower tan δ that decreases gradually with frequency. This phenomenon highlights the sample's dispersion behavior in response to varying frequencies. Graphene boasts an extensive surface area and contains nanosheets characterized by substantial grain boundaries. As a result, the electrical properties are considerably impacted by both grains and grain boundaries, underscoring the remarkable potential of graphene for advanced applications in electronics and materials science.

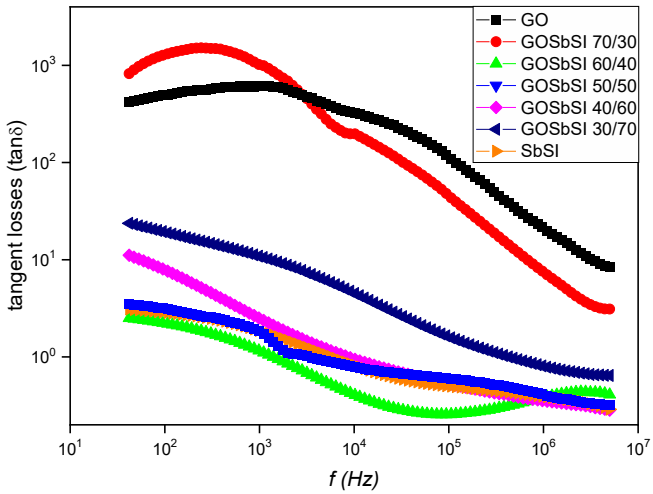


Figure 6.6: Frequency dependence of the tangent loss (*tan δ*) for GO, SbSI, and their various GO-SbSI composites.

AC conductivity describes the frequency-dependent ability of the material to transport charge under the applied field, with a frequency-dependent AC contribution (from hopping/localized charge motion). The frequency dependence of the σ for GO, SbSI, and the GO-SbSI composites at room temperature is shown in Figure 6.7. As illustrated by the logarithmic conductivity spectra, the electrical response across all samples demonstrates a characteristic frequency-dependent behavior. The AC conductivity is dependent on temperature and frequency [147, 231]. The AC conductivity value $\boldsymbol{\sigma_{ac}}$ was calculated through the formula.

$$\boldsymbol{\sigma_{ac} = \omega\, \varepsilon_0 \varepsilon''} \quad \textbf{(6-5)}$$

In this formula $\omega = 2\pi f$ where f is the frequency of the applied voltage. ε_0 represents the free-space permittivity, and ε'' represents the imaginary part of the permittivity constant.

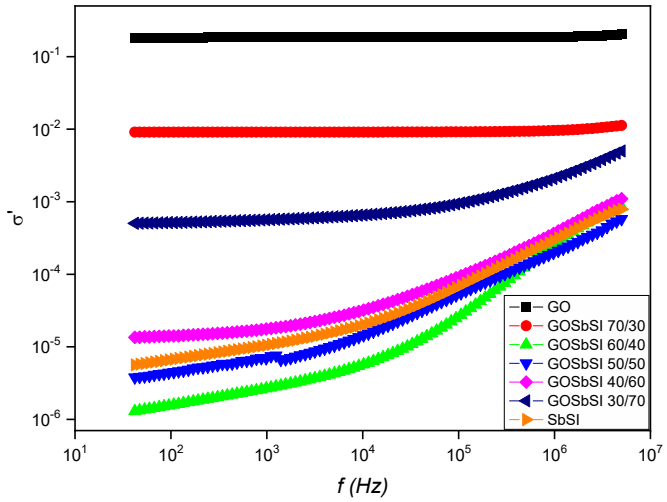


Figure 6.7: Frequency dependence of AC electrical conductivity of GO, SbSI, GO-SbSI 70/30, GO-SbSI 60/40, GO-SbSI 50/50, GO-SbSI 40/60, and GO-SbSI 30/70.

GO displays the highest electrical conductivity, maintaining a frequency-independent value of 0.0206 S/m across the entire window, and the same phenomenon is observed in the literature [218], followed by the 70/30 composite with a stable plateau at ~ 10^{-2} S/m. In contrast, pristine SbSI and the remaining composite ratios exhibit lower low-frequency baseline conductivities, followed by a pronounced upward dispersion. This trend follows power-law scaling rather than direct linear proportionality, signaling charge carrier hopping between localized states in a disordered structure, consistent with recent carbon-based systems [232]. The 70/30 composite shows a similar but lower plateau near 10^{-2} S/m, with a slight upturn only at the highest frequencies. The 30/70 composite sits roughly an order of magnitude below that, with a gentle upward slope beginning around 10^{4}-10^{5} Hz. The remaining composites (60/40, 50/50, 40/60) and SbSI form a lower-conductivity group (starting near 10^{-6} S/m) that rises steadily and almost linearly with frequency. The non-monotonic variations highlight alterations in structural homogeneity, phase distribution, and filler agglomeration [233] within the network of GO-SbSI composites.

6.2 GSM composites

6.2.1 Complex Impedance and Nyquist Plot Analysis

Figure 6.8 presents the frequency dependence of Z' for the GSM composites. All samples showed higher Z' values in the low-frequency region, followed by a continuous decrease with increasing frequency. The differences among the composites were more noticeable at lower frequencies, while the curves became closer at higher frequencies. The magnitude of Z' changed non-monotonically with the SbSI:MnO_2 ratio. GSM 1:70:30 exhibited the highest Z' over the measured frequency range. GSM 1:60:40 and GSM 1:40:60 also showed relatively high values, whereas GSM 1:30:70 and GSM 1:50:50 displayed intermediate impedance responses. Comparatively lower values were observed for GSM 1:20:80 and GSM 1:80:20. The order of the curves therefore did not follow a continuous increase or decrease with either the GO or SbSI content. This indicates that the composition influenced Z', although the contribution of each component cannot be separated from these curves alone.

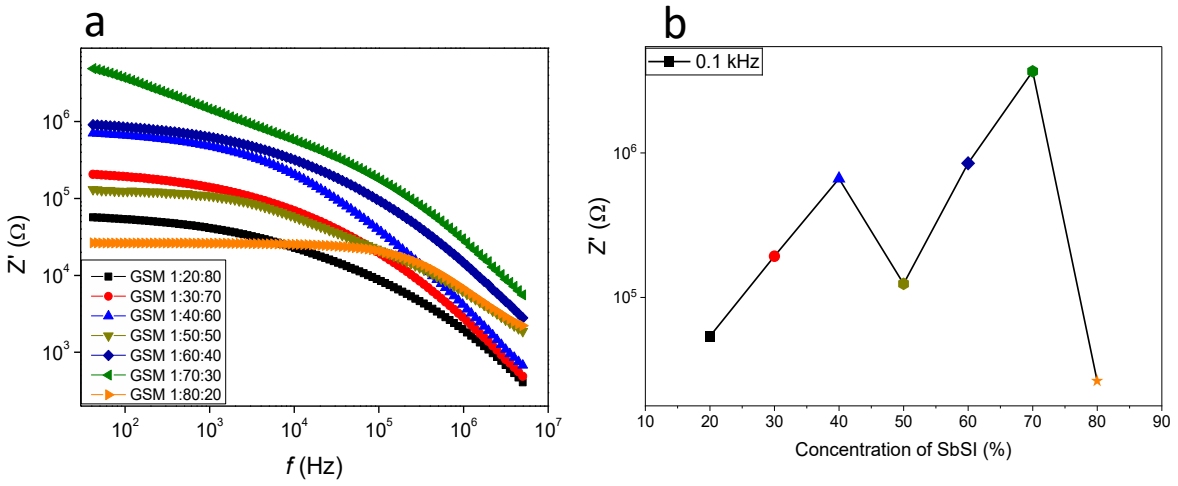


Figure 6.8: Frequency dependence of the real part of impedance Z' as a function of frequency for GSM composites with various component ratios (1:20:80, 1:30:70, 1:40:60, 1:50:50, 1:60:40, 1:70:30, and 1:80:20); (b) Variation of real part of impedance (Z') with concentration of SbSI in GSM ternary composites at 0.1 kHz.

The effect of MnO_2 was evaluated by comparison with the MnO_2-free GO-SbSI composites having corresponding GO-SbSI ratios. GSM 1:70:30, GSM 1:40:60 and GSM 1:30:70 exhibited higher Z' than GO-SbSI 70/30, GO-SbSI 40/60 and GO-SbSI 30/70, respectively. GSM 1:60:40 and GO-SbSI 60/40 remained within a similar impedance range, whereas GSM 1:50:50 showed lower Z' than GO-SbSI 50/50. Therefore, the addition of MnO_2 did not produce the same change at every GO-SbSI ratio.

The Z' behavior of the GSM composites did not show a continuous increase or decrease with increasing SbSI concentration. Instead, the values increased at some composites and decreased at

others. This non-monotonic variation shows that the real impedance was not controlled by the concentration of SbSI alone. The distribution of SbSI nanowires, arrangement of GO sheets [233], presence of MnO_2 [234, 235], number of interfaces [236], grain boundaries [236], and structural defects [236] can all affect the movement of charge carriers. Therefore, the increase and decrease in (Z') values across the GSM composites can be connected with the combined effects of material distribution, interfacial contact, grain boundaries, defects, and charge-carrier movement [230, 233, 236-238].

Figure 6.8b presents the variation of the Z′ with SbSI concentration in the ternary composite system, at 0.1 kHz. Unlike the binary GO-SbSI system discussed earlier, the present composite exhibits a more complex, multi-step non-monotonic trend, reflecting the additional interfacial and grain-boundary contributions introduced by the MnO_2 phase. Starting from 20% SbSI, Z′ is relatively low (~5×10^4 Ω) and increases progressively with SbSI content up to 40% (~6×10^5 Ω), indicating a gradual disruption of the conductive GO-MnO_2 network as increasing amounts of resistive SbSI are incorporated. Interestingly, a sharp dip is observed at 50% SbSI, where Z′ drops to ~1.3×10^5 Ω, before rising again through 60% and reaching a pronounced maximum at 70% SbSI (~3×10^6 Ω), the highest impedance value in the entire series. This alternating rise-fall-rise pattern suggests a delicate, composition-sensitive competition between the percolating conductive pathways of GO/MnO_2. Beyond the 70% maximum, Z′ falls sharply to its lowest value (~2×10^4 Ω) at 80% SbSI, implying that at high SbSI loading, a new well-connected conduction pathway, possibly through direct SbSI-MnO_2 contact or grain amalgamation, becomes dominant, substantially enhancing charge transport.

The Z′ composition behavior of the GSM composite is markedly more complex than that of the binary GO-SbSI system, exhibiting two resistive maxima (at 40% and 70% SbSI) separated by a conductive dip (at 50%), followed by a sharp drop at 80% SbSI. This behavior confirms that the introduction of MnO_2 significantly modifies the percolation and interfacial polarization landscape of the composite, with impedance being governed by a dynamic competition between GO/MnO_2-mediated conduction and SbSI-induced resistive blocking. The pronounced impedance minimum at 80% SbSI identifies this composition as favorable for enhanced charge transport in the GSM ternary system, making it a promising candidate for applications requiring low resistive loss.

Figure 6.9 presents the frequency dependence of the imaginary part of complex impedance Z″ for the GSM ternary composite series across varying compositions. All samples exhibit a characteristic decrease in Z″ with increasing frequency, indicating the gradual suppression of interfacial polarization and space-charge effects as dipoles become unable to follow the rapidly oscillating electric field. However, the magnitude of Z″ and the steepness of its decline vary distinctly with composition, revealing how the balance between SbSI and MnO_2 governs the permittivity relaxation behavior. The experimental curves reveal a well-defined relaxation peak for every evaluated sample within the monitored frequency window, with the exact peak parameters compiled in Table 6.2. The magnitude and frequency position f_{max} of these peaks display a highly distinct, non-monotonic distribution that

depends strongly on the component ratios. The GSM 1:70:30 composite demonstrates the highest overall Z″ peak magnitude, which is situated at the lowest extreme frequency boundary. Conversely, the GSM 1:80:20 sample exhibits its relaxation maximum at the highest frequency extreme with the lowest low-frequency amplitude. The remaining composites (GSM 1:20:80, 1:30:70, 1:40:60, 1:50:50, and 1:60:40) form a closely clustered intermediate group, displaying highly overlapping curves with peak maxima located in the narrow kilohertz range. The peak frequency f_{max} represents the characteristic relaxation frequency, and the corresponding relaxation time was calculated using Eq. 6.1 [223].

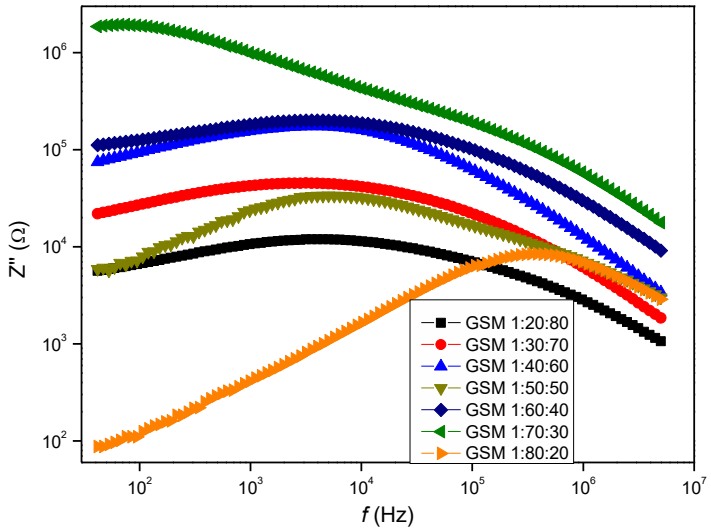


Figure 6.9: Imaginary part of impedance as a function of frequency for GSM composites (1:20:80, 1:30:70, 1:40:60, 1:50:50, 1:60:40, 1:70:30, and 1:80:20).

When evaluating the trends calculated in Table 6.2, the electrical relaxation time changes non-monotonically as the chalcohalide loading varies. For the highest MnO_2 ratio to intermediate concentrations spanning from GSM 1:20:80 up to GSM 1:60:40, the relaxation times remain highly stable within a narrow corridor ranging between 31.44 and 50.18 µs. This plateau is interrupted by a pronounced, multi-order-of-magnitude increase for the GSM 1:70:30 composite, which tracks the longest relaxation time of 2374.33 µs. Conversely, a sharp, dramatic drop is recorded when shifting to the GSM 1:80:20 ratio, which yields the shortest relaxation time of 0.416 µs.

It is suggested that this non-monotonic relaxation behavior physically represents localized charge trapping and polarization occurring at the internal phase boundaries between the coexisting 1D SbSI nanowires, 1D α-MnO_2 networks, and 2D GO templates. Because these electrical measurements were performed on pelletized powder compacts, the calculated parameters act as effective composite relaxation signatures that incorporate the structural influence of air-filled microscopic voids and

localized variations in sample homogeneity. The extreme increase in relaxation time for the GSM 1:70:30 sample indicates a highly unique interfacial arrangement where charge carriers become heavily trapped along high-resistance phase boundaries, demanding a longer timescale to respond to the external field.

To sum up, the lack of a continuous, linear composition-dependent relaxation trend demonstrates that the permittivity relaxation dynamics within these ternary systems are not dictated by the volumetric concentration of a single component alone. Instead, the final relaxation rates are governed by the specific spatial connectivity and structural distribution of the integrated phases, which directly regulate the charge transport velocity and local polarization decay paths across the multi-component junctions.

Table 6-2: Observed Z'' peak frequencies and corresponding impedance relaxation times of the GSM composite with different compositional ratios.

GSM ratio	Observed f_{max} (Hz)	τ (μs)
GSM 1:20:80	4,006.64	39.72
GSM 1:30:70	3,171.51	50.18
GSM 1:40:60	3,564.70	44.65
GSM 1:50:50	5,061.68	31.44
GSM 1:60:40	3,564.70	44.65
GSM 1:70:30	67.03	2,374.33
GSM 1:80:20	382,218.00	0.416

.

Figure 6.10 shows the Nyquist plots (Z″ versus Z′) of the GSM samples with ratios of 1:20:80, 1:30:70, 1:40:60, 1:50:50, 1:60:40, 1:70:30 and 1:80:20. The main panel covers Z′ up to about 5×10^6 Ω, and the inset magnifies the low-impedance region (Z′ up to about 3.3×10^5 Ω), where most curves lie close to the origin. The impedance changes by more than two orders of magnitude across the series, from about 3×10^4 Ω to more than 10^7 Ω, so the electrical response depends on composition. Every spectrum is an arc with its centre below the real axis, i.e., a depressed semicircle.

In the main panel, GSM 1:70:30 dominates the plot. Its curve rises almost linearly at low Z′, with a slope of roughly 35-40°, and then bends into a broad arc with a maximum at $Z' \approx 4\times10^6$ Ω and $Z'' \approx 1.9\times10^6$ Ω. It only begins to descend at the end of the measured range ($Z' \approx 4.9\times10^6$ Ω), so the arc is not closed. The resistance is therefore at least 5×10^6 Ω and probably of the order of 10^6 Ω. The nearly linear onset suggests that a second, overlapping relaxation contributes at high frequencies and makes the arc more depressed. GSM 1:60:40 has the next largest response. Its arc reaches a maximum Z″ of about 2×10^5 Ω at $Z' \approx 4$ to 5×10^5 Ω and ends at $Z' \approx 9\times10^5$ Ω with $Z'' \approx 1\times10^5$ Ω. This arc is also incomplete, and its resistance is of the order of 106 Ω or higher. The remaining samples are small at this scale and appear only as features close to the origin.

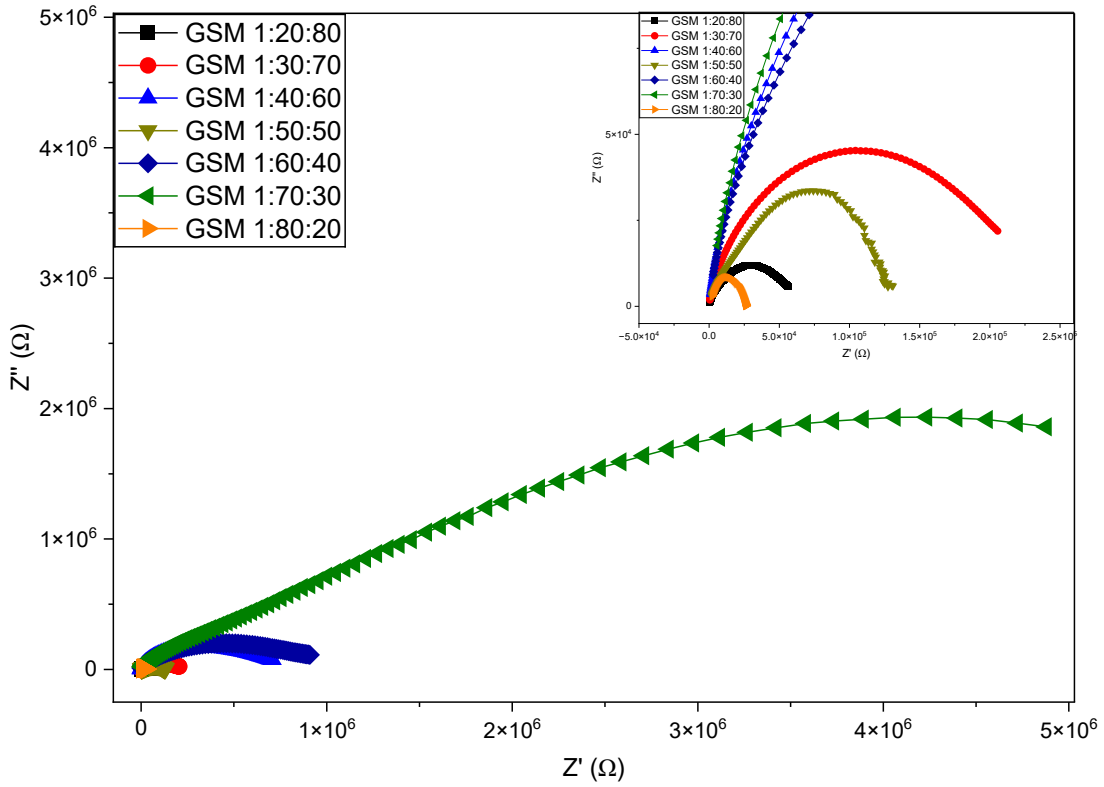


Figure 6.10: Nyquist plots (Z' vs. Z") for GSM composites as (1:20:80, 1:30:70, 1:40:60, 1:50:50, 1:60:40, 1:70:30, and 1:80:20).

The inset resolves these smaller arcs. GSM 1:30:70 gives a clearly flattened, depressed arc with a maximum Z″ of about 4.5×10^4 Ω at Z′ ≈ 1.1×10^5 Ω, ending at Z′ ≈ 2×10^5 Ω, which corresponds to a resistance of about 2-2.5×10^5 Ω. GSM 1:50:50 forms an almost complete arc with a maximum Z″ of about 3.5×10^4 Ω at Z′ ≈ 6-7×10^4 Ω, and it returns to the real axis at Z′ ≈ 1.3×10^5 Ω. GSM 1:20:80 has a maximum Z″ of about 1.2×10^4 Ω at Z′ ≈ 4×10^4 Ω and ends at about 6×104 Ω. GSM 1:80:20 has the smallest response, with a maximum Z″ of about 8×10^3 Ω, and its arc closes at Z′ ≈ 2.5-3×10^4 Ω. This is also the most nearly semicircular arc of the series. All the arcs start close to the origin, so the resistance is dominated by the arcs themselves rather than by a high-frequency series resistance. The arcs of 1:70:30, 1:60:40 and 1:40:60 are incomplete or only just closed, so their resistances are lower-bound estimates.

The resistance does not vary monotonically with composition. Reading the series from 1:20:80 to 1:70:30, the resistance increases overall, from about 6×10^4 Ω to more than 5×10^6 Ω. The increase is interrupted by a dip at 1:50:50 (about 1.3×10^5 Ω), which is lower than that of both 1:40:60 and 1:60:40. The resistance then falls sharply at 1:80:20, to about 3×10^4 Ω, which is the lowest value of the series and roughly two orders of magnitude below 1:70:30. The maximum at 1:70:30 and the abrupt fall at

1:80:20 point to a sudden change in the conduction pathway between these two compositions. Such behavior is typical of percolation, where the connectivity of the conducting phase and the number and quality of interfaces between the phases control the transport.

6.2.2 Real and Imaginary Permittivity, Tangent Losses, and AC Conductivity

Figure 6.11 presents the frequency dependence of the real part of the permittivity ε' plotted across a broad frequency spectrum from 42 Hz to 5 MHz for the GSM ternary composite series across varying compositions. The experimental curves reveal that while ε' systematically decreases as the alternating current frequency increases for every single composition, the absolute magnitude of this response changes non-monotonically with the component ratios. The GSM 1:20:80 composite exhibits the highest overall effective permittivity profile across the full frequency spectrum, decreasing from approximately 10^{-6} at 42 Hz down to near 10^{-11} at 5 MHz. The intermediate GSM 1:30:70 and GSM 1:50:50 ratios follow in closely matching upper aligned curves. Conversely, the GSM 1:40:60, GSM 1:60:40, and the chalcohalide-rich GSM 1:80:20 configurations cluster within a parallel lower capacitive band. The absolute lowest real permittivity profile across the entire operational spectrum is tracked by the GSM 1:70:30 sample, which sits nearly two orders of magnitude below the peak profile at the upper frequency limit.

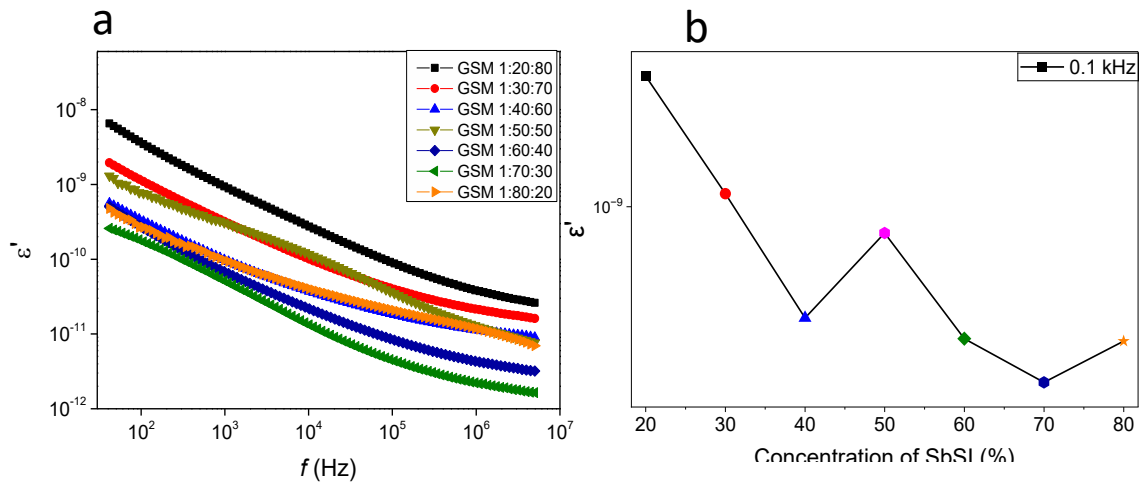


Figure 6.11: Frequency dependence of the real part of permittivity e as a function of frequency for GSM ternary composites (1:20:80, 1:30:70, 1:40:60, 1:50:50, 1:60:40, 1:70:30, and 1:80:20); (b) Variation of the real part of permittivity (ε') with concentration of SbSI in GSM ternary composites at 0.1 kHz.

When correlating these permittivity curves with the microstructural layouts established in Chapter 4, the observed trends can be interpreted through the localized phase arrangements and interfacial boundaries. The graphene oxide template possesses a large surface area, which provides

dense attachment networks for the synthesized SbSI and α-MnO_2 nanowires. Because both active components exhibit prominent high-aspect-ratio one-dimensional geometries, their multi-step assembly generates a high density of grain boundaries and phase interfaces that exert a large impact on the bulk electrical properties. Due to the targeted interfacial coupling of the MnO_2 and SbSI phases onto the GO sheets, the change in the active surface area of the grains and grain boundaries alters the local spatial constraints, leading to a visible reduction in the movable charge carriers depending on the composition.

The observed relative behavior of the experimental curves is well aligned with Koop's theory [239], and it explains the Maxwell-Wagner model of uniform double structure [238]. This model describes a heterogeneous medium composed of highly conductive grains separated by highly resistive grain boundaries. The conductive grains are represented by the extensive networks of interconnected MnO_2 and SbSI nanowires, while the resistive boundaries are established by the localized phase interfaces and the internal air-filled pores of the pressed compact. When an alternating electric field is applied at low frequencies, charge carriers readily migrate through the conductive grains but accumulate at these resistive grain boundary interfaces. This space-charge accumulation induces strong interfacial (Maxwell-Wagner-Sillars) polarization alongside contributing ionic and atomic mechanisms, resulting in the high relative ε' values recorded at the lower frequency limit. As the applied frequency increases, the charge carriers fail to follow the rapid reversals of the applied field, effectively suppressing the space-charge relaxation process. Consequently, these slower polarization mechanisms are sequentially filtered out, leaving the fast charge transformations of electronic and dipolar polarizabilities to dominate the high-frequency regime. This frequency-dependent suppression drives a sharp decremental behavior in permittivity, ultimately causing ε' to approach a stabilized, flat baseline at the higher frequency range [239, 240].

Figure 6.11b shows the variation of the real part of permittivity (ε′) with SbSI concentration in the GSM ternary composite, at 0.1 kHz, on a scale of the order of 10^{-9}. At 20% SbSI, ε′ exhibits its highest value in the series, after which it decreases sharply to a minimum at 40% SbSI, indicating a reduction in interfacial polarizability as the conductive GO/MnO_2 network becomes increasingly interrupted by the resistive SbSI phase. A recovery is observed at 50% SbSI, where ε′ rises again, suggesting a transient enhancement of interfacial charge accumulation consistent with the corresponding conductive drop seen in the Z′ plot at the same composition. Beyond 50%, ε′ decreases progressively through 60% SbSI, reaching a pronounced minimum at 70% SbSI, before showing a slight recovery at 80% SbSI.

The ε′ composition trend is found to vary inversely with the corresponding Z′ composition behavior of the GSM system: the permittivity minimum at 70% SbSI coincides with the impedance maximum at the same composition, while the permittivity rise at 80% SbSI mirrors the sharp impedance drop observed there. This inverse correlation confirms that the dominant polarization

mechanism in the GSM composite is closely tied to charge-carrier mobility and interfacial connectivity between the GO/MnO_2 conductive phases and the resistive SbSI domains; compositions favoring higher conductivity (lower Z′) correspondingly support greater charge accumulation and polarization (higher ε′), and vice versa. The permittivity response of the GSM ternary composite is strongly composition-dependent and inversely correlated with its impedance behavior, with 80% SbSI emerging as the composition offering both minimum resistive loss and enhanced permittivity polarizability, reinforcing it as the electrically optimum formulation within the studied GSM series.

Figure 6.12 presents the frequency dependence of the imaginary part of the permittivity ε″ plotted across a broad frequency spectrum from 42 Hz to 5 MHz for the GSM ternary composite series across varying compositions. The experimental curves reveal that ε″ decreases continuously and monotonically across the entire measured window for every single sample, spanning a very wide magnitude range of nearly seven orders of magnitude. The absolute magnitude of this dissipation response shows a highly non-monotonic distribution that depends strongly on the component ratios. Across the lower frequency regime, the GSM 1:80:20 composite exhibits the highest overall permittivity loss profile, starting near 2×10^{-7} at 42 Hz. The 1:20:80 composite and the intermediate GSM 1:50:50 and GSM 1:30:70 follow closely within an upper overlapping corridor. Conversely, the GSM 1:40:60 and GSM 1:60:40 configurations form a parallel intermediate band. The absolute lowest imaginary permittivity profile across the entire operational spectrum is tracked by the GSM 1:70:30 sample, which sits nearly two orders of magnitude below the peak profile at approximately 8×10^{-10} at 42 Hz and decays to the absolute baseline at the higher frequency limit.

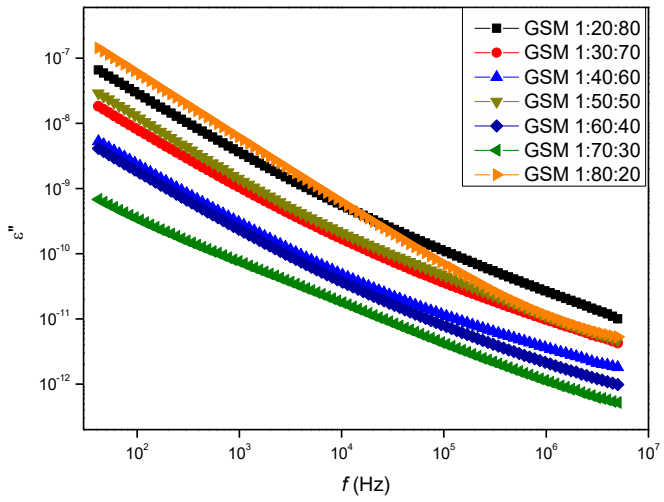


Figure 6.12: Variations of the imaginary part of permittivity (ε'') versus frequency for GSM ternary composites (1:20:80, 1:30:70, 1:40:60, 1:50:50, 1:60:40, 1:70:30, and 1:80:20).

The ε″ spectra of the GSM composites (Figure 6.12) show a consistent decrease with increasing frequency for all composites, reflecting the typical attenuation of interfacial and dipolar polarization as the applied field oscillation becomes too rapid for charge carriers and dipoles to respond. Although the overall trend is similar across the series, the magnitude of ε″ varies systematically with composition, revealing how the balance between SbSI and MnO_2 governs permittivity loss behavior.

Samples with low SbSI content (20:80 and 30:70) exhibit the lowest ε″ values, indicating weak dipolar activity and limited polarization processes. This behavior is characteristic of MnO_2-rich composites, where the permittivity response is dominated by the oxide's lower polarizability and the restricted charge-carrier mobility within the GO matrix. As SbSI concentration increases (40:60 to 80:20), the ε″ curves shift upward, demonstrating progressively stronger permittivity losses. SbSI's ferroelectric and semiconducting nature enhances dipolar polarization and space-charge contributions, resulting in higher ε″ values at low frequencies and more pronounced dispersion. The highest-SbSI compositions show the strongest permittivity loss, confirming that SbSI plays the dominant role in amplifying polarization mechanisms, while MnO_2 acts as a suppressing phase.

Overall, the comparison shows a clear composition-controlled transition: MnO_2-rich samples exhibit low permittivity loss and weak dispersion, whereas SbSI-rich samples display high permittivity loss and strong frequency dependence, highlighting SbSI as the key contributor to enhanced permittivity relaxation in the GSM composite system.

As shown in Figure 6.13, *tan* δ decreases with increasing frequency for most GSM composites, converging from a dispersed low-frequency state to a narrow baseline of ~0.20-0.77 at 5 MHz; the 1:70:30 composite is a partial exception, showing a shallow plateau with a slight non-monotonic dip in the mid-frequency range (~10^3-10^4 Hz) before resuming its decline. At low frequency (~10^1-10^2 Hz), the response varies non-monotonically with matrix composition rather than scaling linearly with constituent mass fraction: GSM 1:80:20 exhibits the highest *tan* δ, GSM 1:70:30 the lowest, and the remaining composites (1:20:80, 1:30:70, 1:40:60, 1:50:50, 1:60:40) fall in an intermediate, overlapping band. The enhanced low-frequency loss is generally attributed to the combined effects of electrical conduction, electrode polarization, and charge accumulation at internal phase boundaries; at higher frequencies, these slower polarization mechanisms can no longer follow the applied field and drop out of the measured response. While the literature often analyzes such heterogeneous permittivity behavior through space-charge transport and distributed relaxation-time models rather than a strict two-layer (KOOPS' theory) [221, 223, 241] treatment, the present single-temperature, ambient-condition results do not allow individual mechanisms to be isolated.

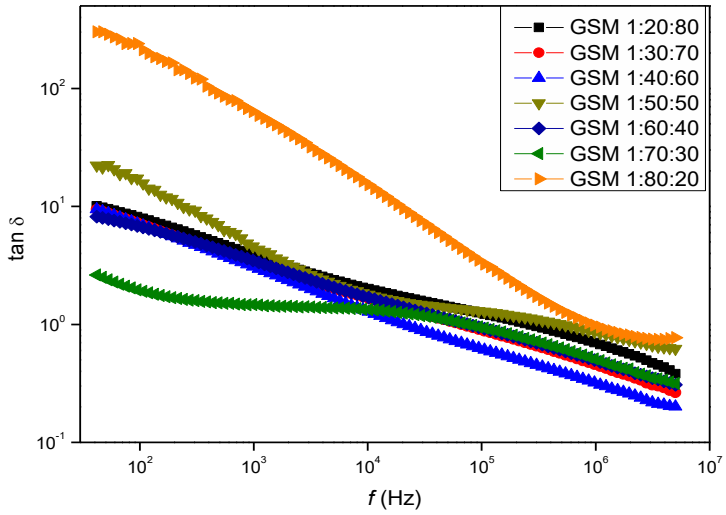


Figure 6.13: Frequency dependence of the tangent loss (tan δ) for GSM ternary composites (1:20:80, 1:30:70, 1:40:60, 1:50:50, 1:60:40, 1:70:30, and 1:80:20).

The AC conductivity explains how much charge can easily pass through the material. The AC conductivity of all samples of GSM is depicted in Figure 6.14. The AC conductivity of the materials was measured through the permittivity study and calculated using Eq. 6.5 [231]:

Due to the IC of SbSI NWs into GO sheets with MnO_2 NWs, a new mode of transportation is created. Because of this, at lower frequencies, the charge transport is enhanced. In Figure 6.20, GSM 1:20:80 and GSM 1:80:20 both display a near-flat, weakly frequency-dependent conductivity plateau at low-to-mid frequency (approximately 2-4 × 10^{-5} S/cm) before rising at higher frequencies-behavior consistent with a dominant, in line with a percolating (or near-percolating) conductive network through the composite. GSM 1:50:50 shows a similar but slightly lower plateau. In contrast, GSM 1:30:70, 1:40:60, 1:60:40, and 1:70:30 show conductivity rising almost linearly across the entire measured range with no low-frequency plateau, the classic dispersive/hopping-conduction signature in which charge carriers move via successive localized hops rather than through a continuous conductive path. Notably, GSM 1:70:30 shows the lowest conductivity of all composites across most of the spectrum, mirroring its position as the composition with the lowest ε′ and ε″ (Figures 12-13) and the highest, most sharply falling Z′ and Z″ (Figures 8-9)-collectively indicating that this particular ratio produces the most resistive, least interconnected microstructure among the GSM series.

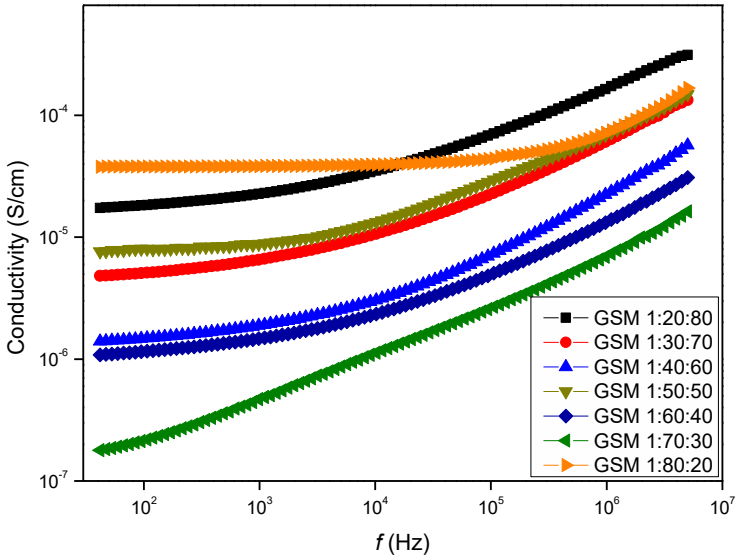


Figure 6.14: Frequency dependence of AC electrical conductivity of GSM ternary composites (1:20:80, 1:30:70, 1:40:60, 1:50:50, 1:60:40, 1:70:30, and 1:80:20).

Together, the impedance, modulus, real permittivity, imaginary permittivity, and conductivity results describe the frequency-dependent electrical response of the GSM composites. Their direct relationship with electrochemical energy storage performance is examined comprehensively in the following chapter; however, a linear correlation between permittivity properties and electrochemical behavior should not be assumed without explicit electrochemical evidence. The evaluation of the material's electrical response across varying frequency regimes outlines its intrinsic charge transport and polarization characteristics. These fundamental bulk and boundary properties directly influence how efficiently charge carriers accumulate and migrate under an external stimulus. To understand how these dynamic electrical traits translate into functional, macroscale energy storage capacity, the system is systematically investigated using electrochemical techniques in Chapter 7.

Chapter 7

ELECTROCHEMICAL STUDY

Electrochemical measurements were performed to investigate the charge-storage behavior of the prepared electrode materials. CV, GCD, electrochemical impedance spectroscopy (EIS), and cycling-stability measurements were performed. All electrochemical measurements were carried out using Autolab PGSTAT AUT40037 (With the permission of the School of Materials and Mineral Resources Engineering, Universiti Sains Malaysia, Penang, Malaysia) and AUT84500 (With the permission of the Department of Physical Chemistry and Polymer Technology, Silesian University of Technology, Gliwice, Poland) potentiostats/galvanostats connected to a computer for data acquisition and analysis. Cyclic voltammetry was performed at scan rates of 5, 10, 20, 40, 60, 80, and 100 mV/s. GCD measurements were performed at current densities of 0.5, 1.0, 1.5, 2.0, and 2.5 A/g. EIS was further used to study the internal resistance, charge-transfer process, and ion-diffusion behavior in the frequency range of 1- 100 kHz, at an amplitude of 0.005 V. The three-electrode configuration used for the electrochemical measurements is shown in Figure 7.1. This system consists of a working electrode, a reference electrode, a counter electrode, an electrolyte, and an electrochemical cell. In Figure 7.1, the yellow wire is connected to the Hg/HgO reference electrode, which provides a stable potential against which the potential of the working electrode is measured. The red wire is connected to the platinum-wire counter electrode, which completes the electrical circuit and carries the current required by the working-electrode reaction. The white wire is connected to the working electrode prepared from the synthesized material. The electrochemical response of this electrode is the principal parameter investigated during the measurements. Potassium hydroxide (KOH) was used as the electrolyte because it provides exceptionally high ionic conductivity and exceptionally low internal resistance.



Figure 7.1: Experimental setup of the electrochemical cell employed for electrochemical characterization testing, comprising an Hg/HgO reference electrode (yellow), a platinum-wire counter electrode (red), and a working electrode (white).

7.1 GO, SbSI, and GO-SbSI composites

7.1.1 Cyclic voltammetry of GO

The CV testing was performed multiple times, and a suitable working window was chosen for the overall testing. The CV performance of the GO electrode at scan rates ranging from 5 to 100 mV/s within a potential window of 1 V (-0.7 V to +0.3V) is shown in Figure 7.2. Typical quasi-rectangular CV curves were observed at lower scan rates, indicating a predominantly surface-controlled charge-storage response. They maintain the shape throughout the higher scan rates. Similar CV curves of GO are reported in the literature [242]. This response may include electrical double-layer charging and surface redox contributions from the oxygen-containing functional groups of GO. The specific capacitance (Eq. 1.1), P_D, and E_D (Eq. 1.2) values calculated from the CV curves at different scan rates are presented in Table 7.1. The highest specific capacitance of 57.60 F/g was obtained at 5 mV/s. Lower values of GO C_S 43.5 F/g and 19.5 F/g are observed in the literature [243, 244]. The specific capacitance generally decreased with increasing scan rate, although an increase from 26.10 to 37.33 F/g was observed between 80 and 100 mV/s.

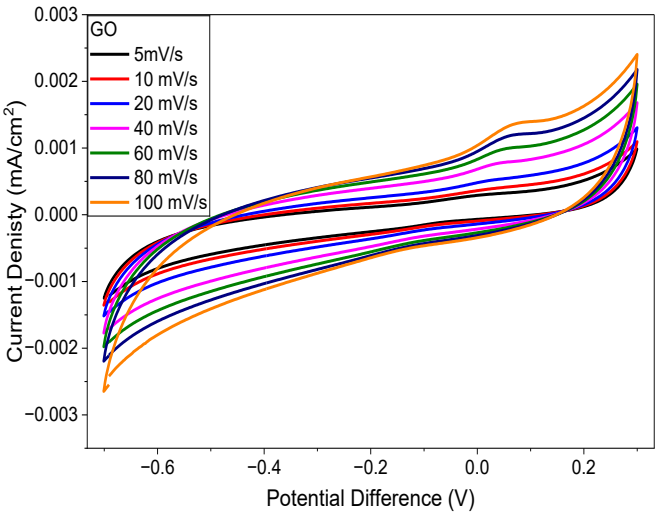


Figure 7.2: CV curves of the GO electrode recorded at scan rates ranging from 5 to 100 mV/s.

As the scan rate increases, the shorter experimental time limits ion access to less accessible electrochemical sites, resulting in a lower specific capacitance. GO contains oxygen-containing functional groups, including carboxyl, epoxy, and hydroxyl groups, which improve electrolyte wettability and may contribute to the charge-storage response [245, 246]. However, these functional groups disrupt the sp^2 carbon network, reducing the electrical conductivity of GO, which may limit its charge-storage response at higher scan rates [247]. Previous studies [246] have similarly reported that surface ion adsorption contributes substantially to the charge-storage behavior of GO.

7.1.2 Cyclic voltammetry of SbSI

The CV curves of the SbSI electrode recorded at scan rates ranging from 5 to 100 mV/s within a potential window of 1 V (-0.7V + 0.3V) are shown in Figure 7.3. All the curves exhibit a non-rectangular loop shape superimposed with a pair of redox humps, indicating that the charge storage mechanism in SbSI is governed by a combination of capacitive and pseudocapacitive (faradaic) processes, rather than purely non-faradaic behavior. At all scan rates, a prominent anodic peak is observed in the potential range of approximately 0.2 V-0.3 V, corresponding to the oxidation reaction occurring at the electrode-electrolyte interface, while a broader cathodic hump appears in the range of 0.2 to -0.05 V during the reverse scan, attributed to the corresponding reduction process. The redox-related features indicate a faradaic contribution to the charge-storage response of SbSI. The electrochemical parameters calculated from the CV curves are presented in Table 7.1. The highest specific capacitance of 52.82 F/g was obtained at 5 mV/s. Although mass plays a critical role in the calculation, a small change in the mass can affect the calculated parameters.

Manoharan et al. investigated the capacitive behavior of SbSI through a coin cell and attributed its redox-related features to a reversible change in the oxidation state of antimony between Sb^{3+} and Sb^{4+} by using $TEABF_4$ electrolyte [84].

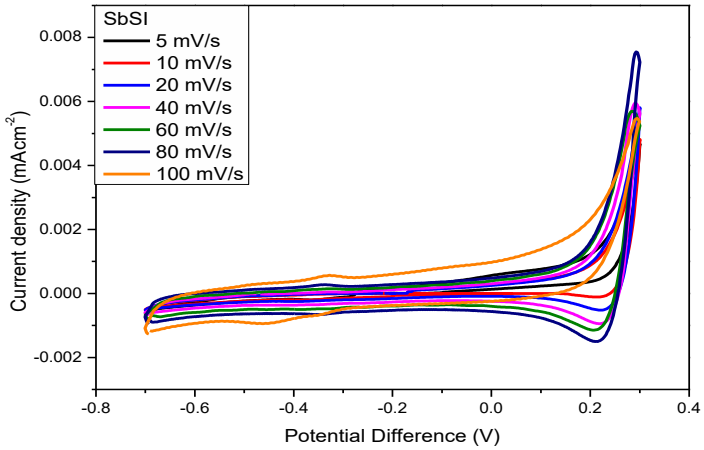


Figure 7.3: CV curves of the SbSI electrode recorded at scan rates ranging from 5 to 100 mV/s.

7.1.3 Cyclic voltammetry of GO-SbSI composites

The CV curves of the GO-SbSI composite electrodes with different GO:SbSI ratios recorded at different scan rates are shown in Figure 7.4(a-f). The CV curves exhibit two distinct shapes depending on the composite ratio. GO-SbSI 70/30 and GO-SbSI 30/70 exhibit broad, leaf-like CV profiles with weak redox-related features, indicating a faradaic contribution in addition to surface-controlled charge storage. At lower scan rates, the redox peak observation is very small around +0.1 V to -0.4 for GO-SbSI 70/30 and around +0.07 V and -0.5 V for GO-SbSI 30/70. By increasing the scan

rates, the peaks are more pronounced in both samples. In contrast, GO-SbSI 60/40, GO-SbSI 50/50, and GO-SbSI 40/60 (Figures 7.4 b,c,d) show more distinct redox-related features, indicating a stronger faradaic contribution to the charge-storage response. These redox peaks are clearly visible at lower and higher scan rates, which shows the stable behavior of CV curves of all composites.

Figure 7.4f compares the CV curves of GO, SbSI, and GO-SbSI composites recorded at a scan rate of 100 mV/s over a potential window of approximately -0.7 V to 0.3 V. GO exhibits the quasi-rectangular shape of surface-controlled charge storage. SbSI shows a non-rectangular loop with a redox peak around 0.2- 0.3 V, consistent with a weak capacitive response. As GO is incorporated into SbSI, the CV response changes markedly: the GO-SbSI 30/70 and 30/70 composites display broadened, leaf-shaped loops with small redox peaks.

Notably, the GO-SbSI 60/40 and 40/60 composites exhibit the most pronounced electrochemical activity and a well-defined broad anodic hump centered around -0.3 V, while the 40/60 sample shows a similar but slightly less intense redox feature at around -0.25 V. GO-SbSI 50/50 shows a hump (-0.3 V) at the same potential as GO-SbSI 40/60, but its intensity in comparison is low with respect to GO-SbSI 40/60. Overall, this comparison indicates that the GO-SbSI composite ratio strongly governs the electrochemical performance, with the 60/40 and 40/60 ratios representing the most electrochemically active composites among those studied, likely due to a suitable balance between conductive GO matrix and electroactive SbSI content.

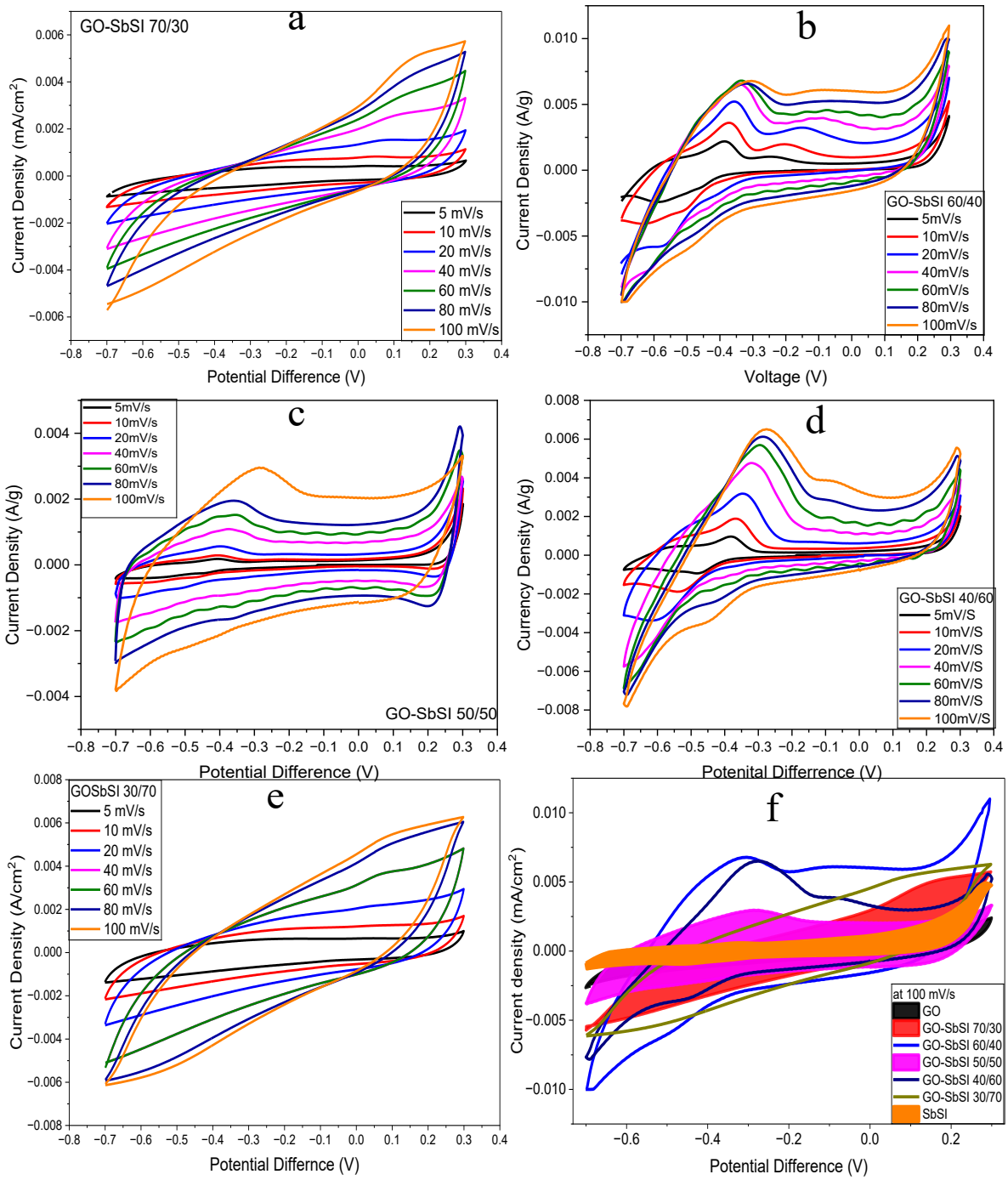


Figure 7.4(a-e): Cyclic voltammetry curves of GO-SbSI composites with varying weight ratios. Comparative CV profiles recorded at different scan rates for (a) GO-SbSI 70:30, (b) GO-SbSI 60:40, (c) GO-SbSI 50:50, (d) GO-SbSI 40:60, and (e) GO-SbSI 30:70. (f) CV curves comparison at 100 mV/s among GO, SbSI, and GO-SbSI composites.

The electrochemical parameters calculated from the CV measurements are summarized in Table 7.1. GO-SbSI 50/50 showed a moderate specific capacitance among the investigated composites, whereas GO-SbSI 40/60 produced a higher CV response. GO-SbSI 30/70 produced the highest overall CV response.

Table 7-1: Electrode mass, scan rate, integrated CV area, specific capacitance, energy density, and power density of GO, SbSI, and GO-SbSI composite electrodes.

Material	Mass (g)	Scan Rate (mV/s)	Area under CV (A·V)	C_S (F/g)	ED (Wh/kg)	PD (W/kg)
GO	0.0015	5	0.000432	57.6	8	144
	0.0015	10	0.000661	44.07	6.12	220.33
	0.0015	20	0.001	33.33	4.63	333.33
	0.0015	40	0.00179	29.83	4.14	596.67
	0.0015	60	0.00248	27.56	3.83	826.67
	0.0015	80	0.003132	26.1	3.62	1044
	0.0015	100	0.0056	37.33	5.19	1866.67
GO-SbSI 70/30	0.0018	5	0.000562	62.44	8.67	156.11
	0.0018	10	0.000925	51.39	7.14	256.94
	0.0018	20	0.0014	38.89	5.4	388.89
	0.0018	40	0.002	27.78	3.86	555.56
	0.0018	60	0.0024	22.22	3.09	666.67
	0.0018	80	0.0027	18.75	2.6	750
	0.0018	100	0.0028	15.56	2.16	777.78
GO-SbSI 60/40	0.0022	5	0.0012	109.09	15.15	272.73
	0.0022	10	0.0022	100	13.89	500
	0.0022	20	0.0033	75	10.42	750
	0.0022	40	0.0045	51.14	7.1	1022.73
	0.0022	60	0.0054	40.91	5.68	1227.27
	0.0022	80	0.0061	34.66	4.81	1386.36
	0.0022	100	0.007	31.82	4.42	1590.91
GO-SbSI 50/50	0.0019	5	0.000778	83.21	11.56	208.02
	0.0019	10	0.00099	52.94	7.35	264.71
	0.0019	20	0.00092	24.6	3.42	245.99
	0.0019	40	0.00144	19.25	2.67	385.03
	0.0019	60	0.0021	18.72	2.6	561.5
	0.0019	80	0.0027	18.05	2.51	721.93
	0.0019	100	0.0032	17.11	2.38	855.61
GO-SbSI 40/60	0.0015	5	0.001023	136.4	18.94	341
	0.0015	10	0.00102	68	9.44	340
	0.0015	20	0.00177	59	8.19	590
	0.0015	40	0.0025	41.67	5.79	833.33
	0.0015	60	0.0031	34.44	4.78	1033.33
	0.0015	80	0.0036	30	4.17	1200
	0.0015	100	0.0044	29.33	4.07	1466.67
	0.0015	5	0.0024	320	44.00	800

GO-SbSI 30/70	0.0015	10	0.0038	253.33	35.19	1266.67
	0.0015	20	0.0038	126.67	17.59	1266.67
	0.0015	40	0.0054	90	12.5	1800
	0.0015	60	0.0059	65.56	9.1	1966.67
	0.0015	80	0.006	50	6.94	2000
	0.0015	100	0.0065	43.33	6.02	2166.67
SbSI	0.0013	5	0.000343	52.82	7.34	132.04
	0.0013	10	0.000344	26.44	3.67	132.19
	0.0013	20	0.000465	17.9	2.49	179
	0.0013	40	0.000707	13.6	1.89	271.92
	0.0013	60	0.00094	12.05	1.67	361.38
	0.0013	80	0.0012	11.54	1.6	461.54
	0.0013	100	0.0011	8.46	1.18	423.08

Figure 7.5 compares the CV-derived specific capacitance of GO, SbSI, and the GO-SbSI composite electrodes at 5 mV/s. Typically, the lowest scan rate shows a high specific capacitance, which decreases with an increase in scan rate. The specific capacitance did not change uniformly with increasing SbSI concentration. At 5 mV/s, the specific capacitance increased from 57.60 F/g for GO to 62.44 F/g for GO-SbSI 70/30 and 109.09 F/g for GO-SbSI 60/40. A lower value of 83.21 F/g was obtained for GO-SbSI 50/50, followed by an increase to 136.40 F/g for GO-SbSI 40/60. GO-SbSI 30/70 showed the highest specific capacitance of 320.00 F/g and maintained the highest value among the composites investigated at every applied scan rate. The corresponding theoretical specific energy calculated from its CV-derived capacitance reached 44.44 Wh/kg at 5 mV/s. These results show that the electrochemical response depended on the relative GO and SbSI contents rather than increasing uniformly with SbSI content. Among the investigated composites, GO-SbSI 30/70 provided the highest CV-derived charge-storage response.

When compared with the literature, materials such as GO and SbSI exhibit significantly smaller values for C_S and P_D when tested alone or with other materials [86, 243, 244]. The severe performance limitations of these isolated or single-component materials are effectively overcome through the formation of the multi-component composite. By establishing a synergistic network between GO and SbSI, the composite yields substantially higher electrochemical metrics, demonstrating the clear performance advantages of this integrated material architecture over its individual constituents.

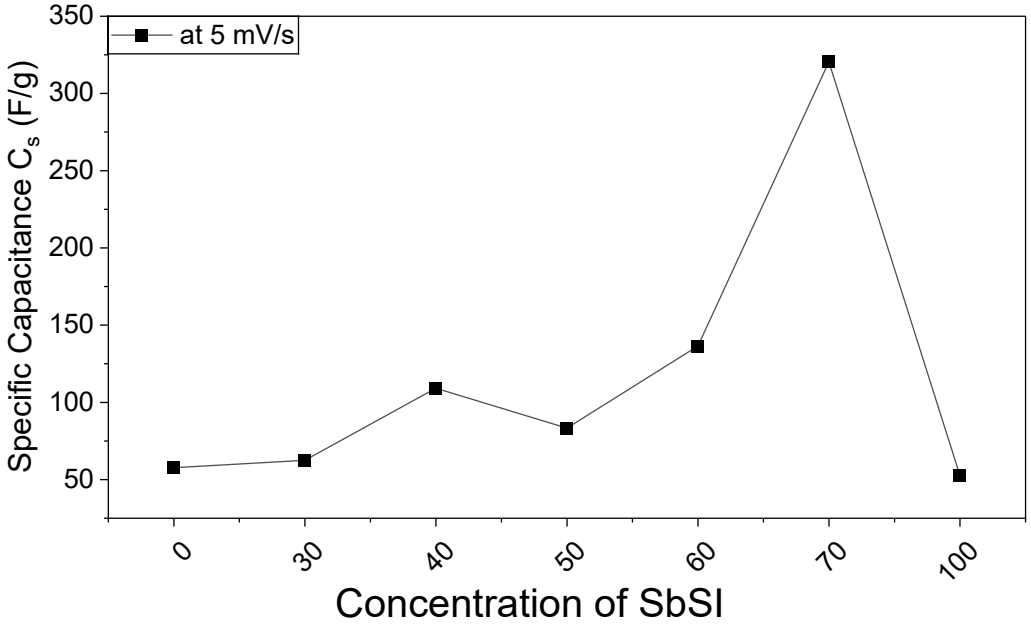


Figure 7.5: Dependence of specific capacitance on SbSI concentration at a scan rate of 5 mV/s.

7.1.4 GCD testing of GO

The GCD curves of the GO electrode recorded at different current densities within a 1 V potential window (-0.7 to +0.3V) are shown in Figure 7.6. The electrode was tested at current densities of 0.5, 1.0, 1.5, 2.0, and 2.5 A/g. The GCD curves exhibited asymmetric and non-linear profiles rather than ideal triangular shapes. The shapes of the GCD curves are influenced by electrostatic surface ion adsorption, active-site accessibility, ion-transport limitations, and the internal resistance of the electrode [245]. Consequently, the GO electrode exhibits a predominantly surface-controlled response involving electrical double-layer charging and possible surface-faradaic contributions from oxygen-containing functional groups. Similar non-linear GCD profiles have been reported for GO-based electrodes [248]. The deviation from an ideal triangular profile may arise from internal resistance, ion-transport limitations, and surface redox reactions associated with oxygen-containing functional groups. A faster rate of charge transfer accelerates ion depletion and magnifies the internal ohmic voltage drop (IR drop), causing the electrode to reach its cutoff voltage limits more rapidly. The curve recorded at 0.5 A/g showed the longest discharge time (90 s), whereas that recorded at 2.5 A/g showed the shortest discharge time (10 s). The discharge time, P_D (Eq. 1.2), and E_D values calculated from the GCD curves at different current densities are presented in Table 7.2.

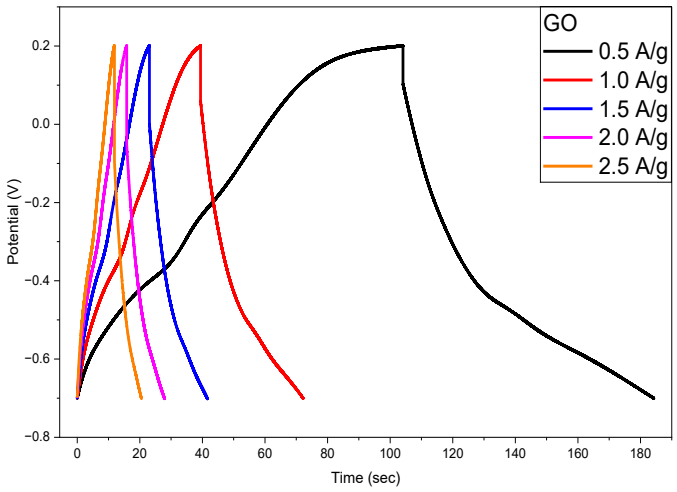


Figure 7.6: GCD curves of the GO electrode recorded at current densities ranging from 0.5 to 2.5 A/g.

7.1.5 GCD testing of SbSI

The GCD curves of the SbSI electrode recorded at different current densities within a 1 V potential window (-0.7 V to 0.3V) are shown in Figure 7.7. The curves exhibit asymmetric and non-linear profiles with a plateau-like region near the upper potential limit during charging and discharging. These non-linear profiles and plateau-like regions indicate a substantial faradaic contribution rather than a purely electrical double-layer response. A previous study of SbSI nanorods also reported non-linear GCD curves with plateau-like regions and attributed this behavior to faradaic charge storage [84]. The discharge time, P_D, and E_D values calculated from the GCD curves at different current densities are presented in Table 7.2.

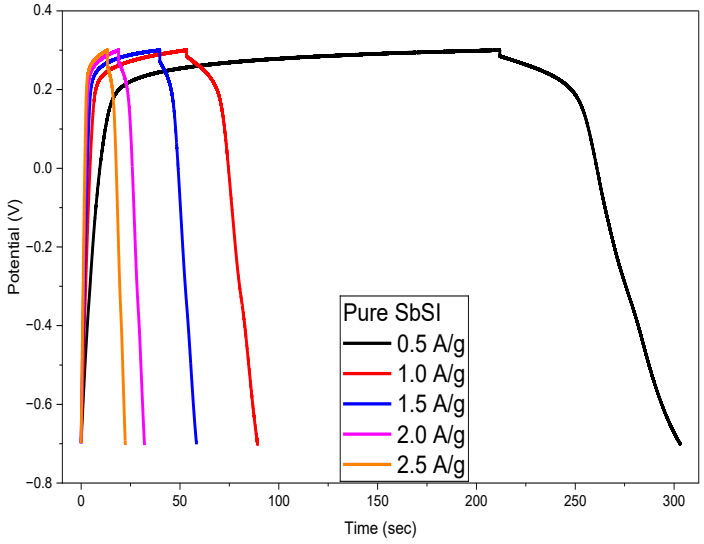


Figure 7.7: GCD curves of the SbSI electrode recorded at current densities ranging from 0.5 to 2.5 A/g.

7.1.6 GCD testing of GO-SbSI Composites

Figure 7.8(a-e) presents the GCD curves of the GO-SbSI composite electrodes recorded at different current densities. The operating window was 1V (-07 V to +0.3 V) for all measurements. The shapes of the GCD curves vary considerably with the GO-SbSI ratio. The GO-SbSI 70/30 (Figure 7.8a) and GO-SbSI 30/70 (Figure 7.8e) exhibit asymmetric, quasi-triangular profiles with continuous, sloping voltage changes. In contrast, GO-SbSI 60/40 (Figure 7.8b) and GO-SbSI 40/60 (Figure 7.8d exhibit more strongly distorted profiles with plateau-like regions. These curves show EDLC behavior with a faradaic-controlled process. GO-SbSI 50/50 (Figure 7.8c) shows an asymmetric, quasi-triangular geometry with continuous, non-linear sloping voltage variations, confirming a combination of EDLC and pseudocapacitive faradaic processes. A minor IR drop is observed in all samples, which may include resistance from the electrode, electrolyte, current collector, and electrical contacts.

The GCD testing curves comparing results of charging and discharging behavior at a current density of 2.5 A/g are shown in Figure 7.8f. They reveal a clear compositional dependence of the electrochemical performance, with discharge time increasing progressively as the SbSI content rises relative to GO. GO and GO-rich composites (70/30, 60/40, 50/50) exhibit narrow, near-symmetric loops with short discharge durations (7-15 s), indicative of limited charge storage capacity dominated by electrical double-layer behavior. In contrast, the GO-SbSI 40/60 composite displays a markedly broader curve with the longest discharge time (40 s) and a distinctly non-linear, sloped profile, suggesting enhanced pseudocapacitive (faradaic) contributions, but due to the high mass loading on the electrode, its power density and energy density are lower than GO-SbSI 30/70. The 30/70 ratio shows a discharge time of 25 s, but due to the lower mass loading, it shows higher values of calculated power density and energy density. The discharge time, P_D, and E_D values calculated from the GCD curves at different current densities are presented in Table 7.2.

These profiles complement the CV results and indicate that charge storage does not occur exclusively through an electrical double-layer mechanism. Surface ion adsorption on GO is accompanied by a faradaic contribution from the SbSI-containing phase [84, 249]. However, these electrochemical signatures alone are insufficient to assign the observed processes to the direct conversion of Sb-S or Sb-I bonds.

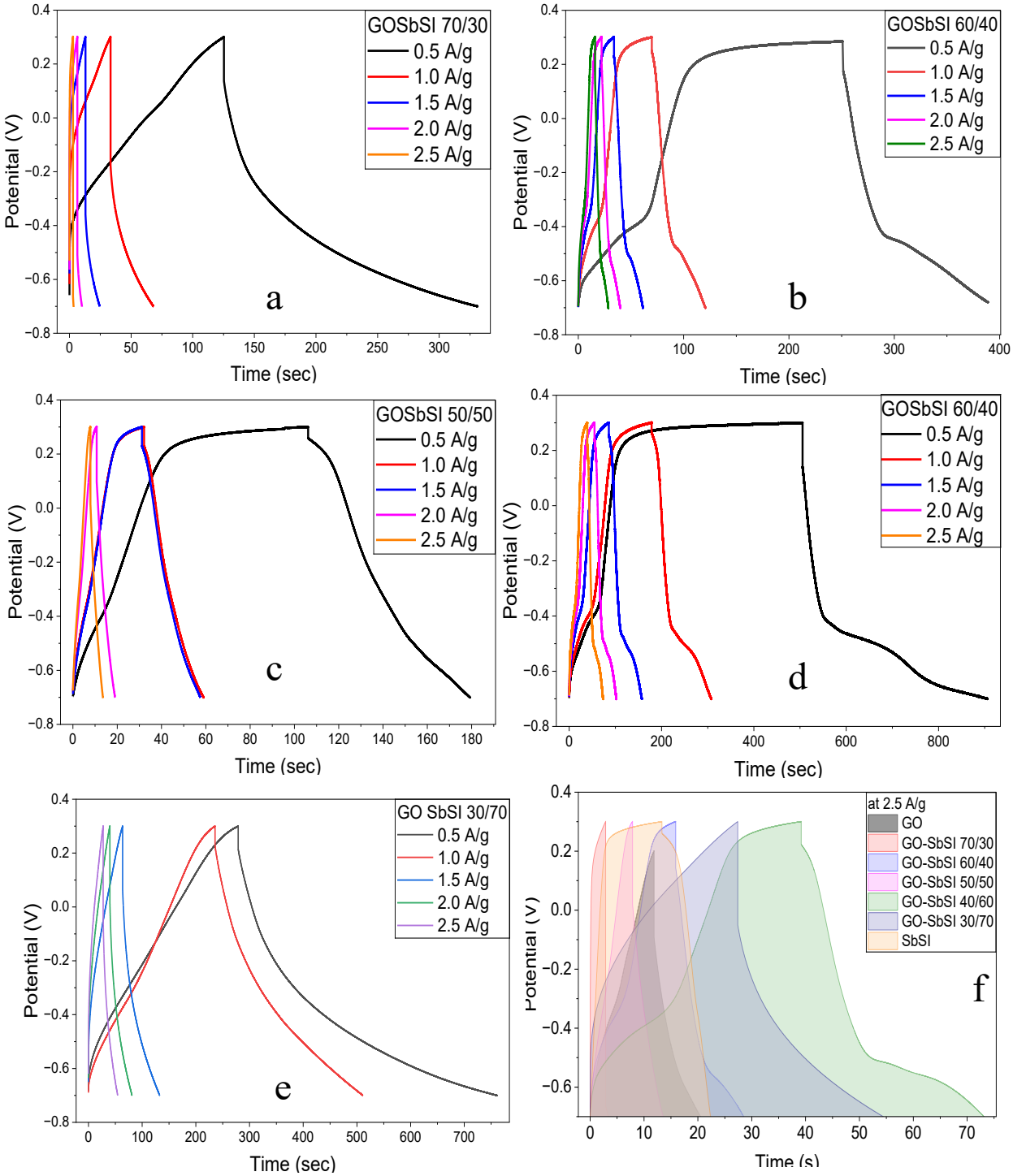


Figure 7.8: GCD curves of (a) GO-SbSI 70/30, (b) GO-SbSI 60/40, (c) GO-SbSI 50/50, (d) GO-SbSI 40/60, and (e) GO-SbSI 30/70 recorded at current densities ranging from 0.5 to 2.5 A/g.

Table 7-2: Specific capacitance, energy density, and power density of GO, SbSI, and GO-SbSI composite electrodes calculated from GCD measurements at different current densities.

Material	Current Density (A/g)	Discharge Time (s)	C_S (F/g)	E_D (Wh/kg)	P_D (W/kg)
GO	0.5	90	30	4.17	166.67
	1	40	26.67	3.7	333.33
	1.5	20	20	2.78	500
	2	15	20	2.78	666.67
	2.5	10	16.67	2.31	833.33
GO-SbSI 70/30	0.5	180	50	6.94	138.89
	1	40	22.22	3.09	277.78
	1.5	25	20.83	2.89	416.67
	2	14	15.56	2.16	555.56
	2.5	9	12.5	1.74	694.44
GO-SbSI 40/60	0.5	135	30.68	4.26	113.64
	1	65	29.55	4.1	227.27
	1.5	35	23.86	3.31	340.91
	2	18	16.36	2.27	454.55
	2.5	12	13.64	1.89	568.18
GO-SbSI 50/50	0.5	70	18.72	2.6	133.69
	1	26	13.9	1.93	267.38
	1.5	15	12.03	1.67	401.07
	2	10	10.7	1.49	534.76
	2.5	8	10.7	1.49	668.45
GO-SbSI 60/40	0.5	425	141.67	19.68	166.67
	1	110	73.33	10.19	333.33
	1.5	85	85	11.81	500
	2	55	73.33	10.19	666.67
	2.5	40	66.67	9.26	833.33
GO-SbSI 30/70	0.5	450	150	20.83	166.67
	1	210	140	19.44	333.33
	1.5	65	65	9.03	500
	2	45	60	8.33	666.67
	2.5	25	48.08	6.68	961.54
SbSI	0.5	100	38.46	5.34	192.31
	1	40	30.77	4.27	384.62
	1.5	25	28.85	4.01	576.92
	2	18	27.69	3.85	769.23
	2.5	15	28.85	4.01	961.54

The specific capacitance, energy density, and power density calculated from the GCD curves are summarized in Table 7.2. The calculated P_D generally increased with increasing current density because the discharge time decreased.

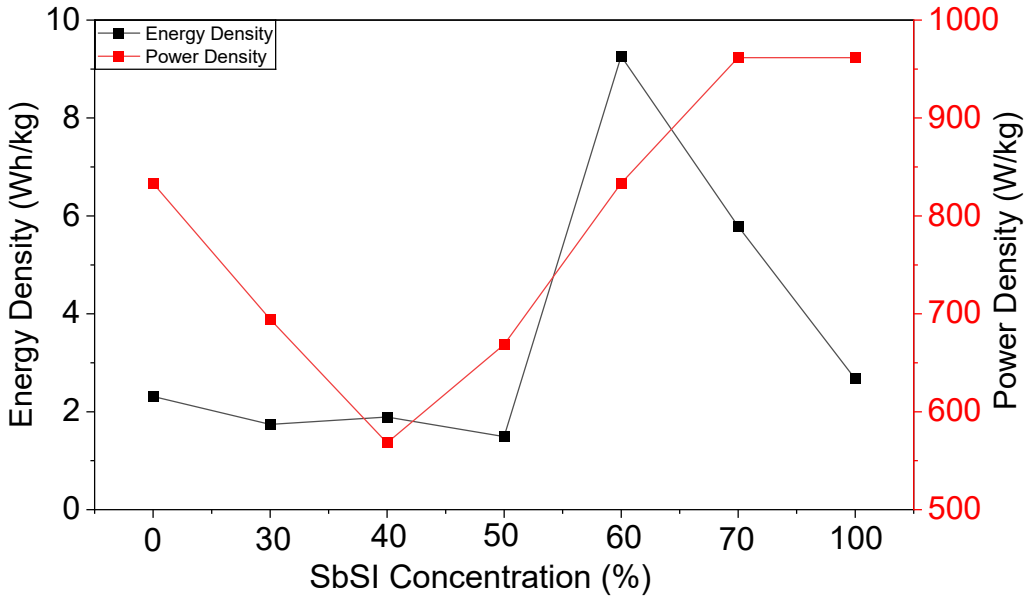


Figure 7.9: Energy density and power density of GO, SbSI, and GO-SbSI electrodes at 2.5 A/g.

Figure 7.9 compares the energy density and power density of GO, SbSI, and the GO–SbSI composite electrodes at a current density of 2.5 A/g. It can be observed that the energy density remains relatively stable and low across the GO (0%), 30%, 40%, and 50% SbSI concentrations, fluctuating between 1.5 and 2.3 Wh/kg. However, it dramatically increases to a peak value of approximately 9.3 Wh/kg at a 60% SbSI concentration, before declining at 70% and 100%. These changes are attributed to the optimized synergistic interaction between GO and SbSI at specific concentration ratios.

Regarding the power density, the value begins at approximately 833 W/kg for GO (0%), decreases to a minimum of 568.18 W/kg at 40%, and then steadily increases with higher SbSI concentrations. At 2.5 A/g, both the 70% ratio and pure SbSI (100%) show the same maximum calculated power density of approximately 961.54 W/kg. However, the 70% ratio exhibits a higher energy density (6.68 Wh/kg) than pure SbSI (4.01 Wh/kg), indicating a longer discharge time and superior electrochemical performance due to the incorporation of GO.

Among all the prepared samples, the GO-SbSI 30/70 composite was selected for cyclic stability testing due to its superior power density and specific capacitance, which are critical metrics for supercapacitor performance. Figure 7.10 presents the capacitance retention of the GO-SbSI composite over 3000 galvanostatic charge-discharge (GCD) cycles. The electrode exhibits high

durability, maintaining a capacitance retention value of approximately 92.5% during the initial cycles. With continuous cycling, the capacitance retention decreases gradually. Ultimately, after completing the full 3000-cycle stability test, the system maintains a stable capacitance retention of approximately 78.5%.

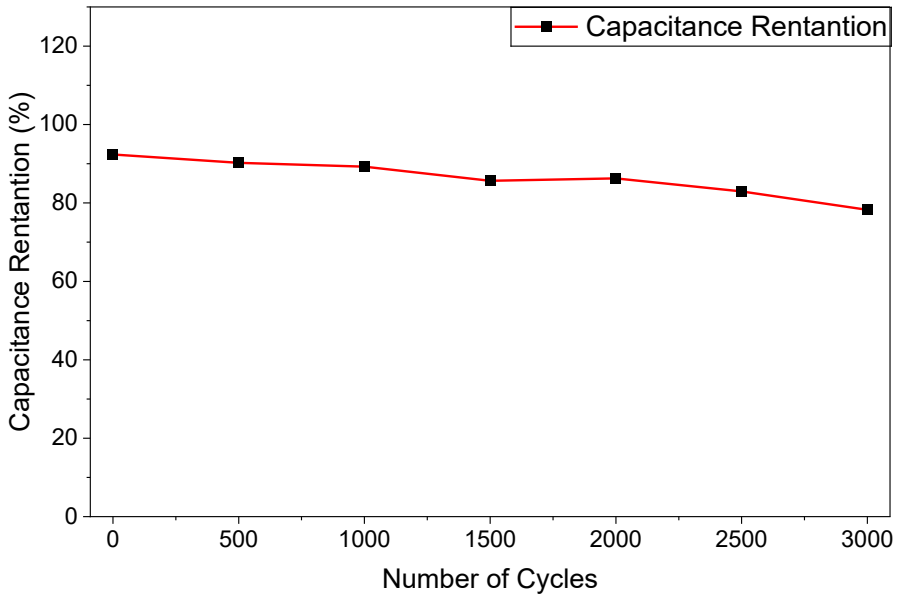


Figure 7.10:Capacitance retention of the GO-SbSI 70/30 electrode over 3000 GCD cycles.

7.1.7 Electrochemical Impedance Spectroscopy

The EIS responses of GO, SbSI, and the GO-SbSI composite electrodes are presented as Nyquist plots of Z'' versus Z' in Figure 7.11. Within the measured frequency range (1-100 kHz), all profiles exhibit a remarkably linear and uninterrupted inclined behavior, completely lacking any discernible high-frequency semicircular arcs. This seamless linear response indicates highly rapid charge-transfer kinetics and an exceptionally low charge-transfer resistance (R_{ct}) at the electrode/electrolyte interface. The steep, straight lines approach an inclination angle near 45°, which corresponds to a dominant Warburg impedance contribution and confirms a highly efficient, diffusion-controlled ion transport mechanism within the porous electrode matrix [250]. The smooth continuity of these plots from high to low frequencies highlights the highly accessible surface morphology of the composite architectures, showcasing that uniform diffusion-related processes effectively govern the impedance response to facilitate stable capacitive performance.

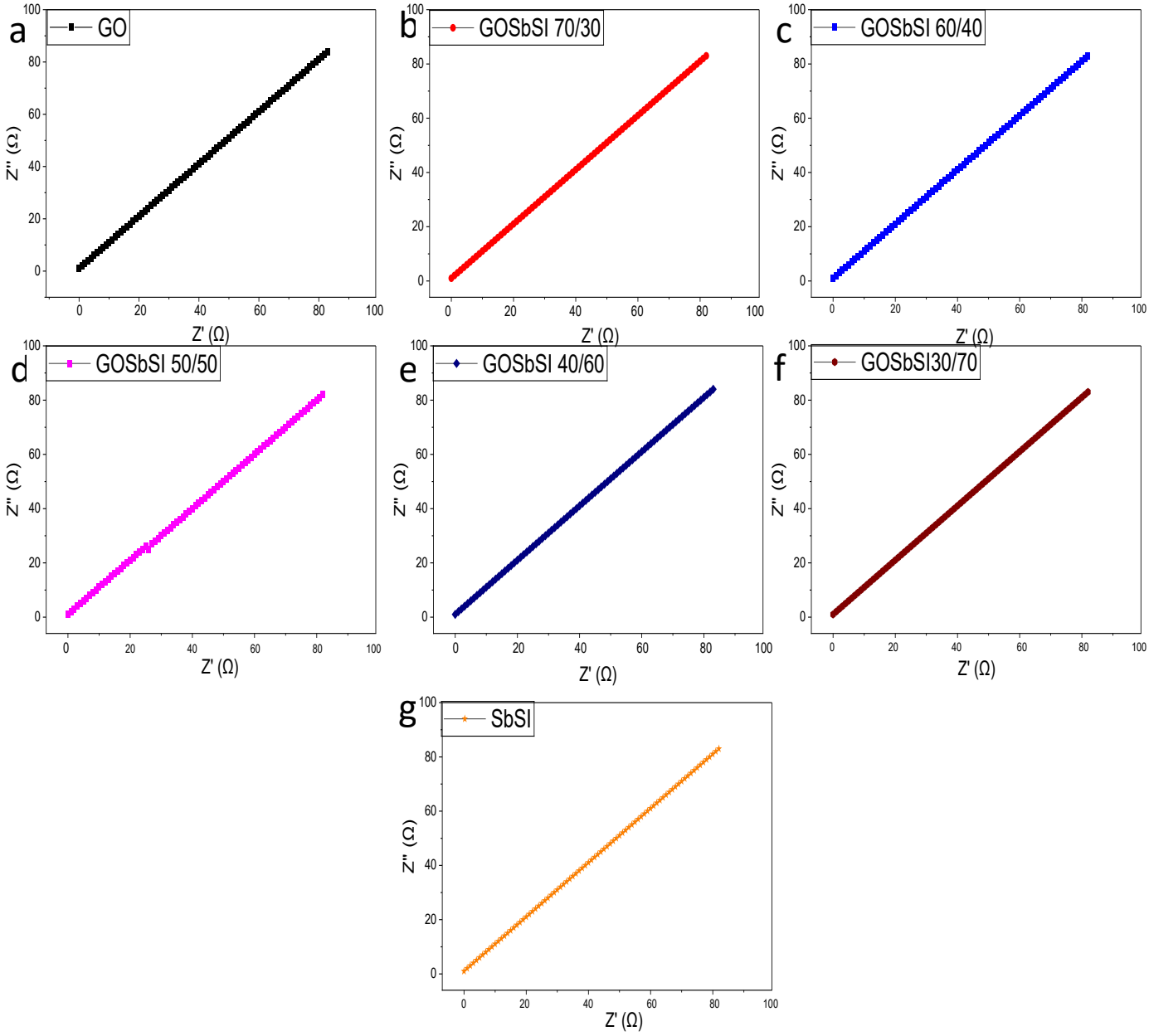


Figure 7.11: Nyquist plots of (a) GO, (b) SbSI, (c) GO-SbSI 70/30, (d) GO-SbSI 60/40, (e) GO-SbSI 50/50, (f) GO-SbSI 40/60, and (g) GO-SbSI 30/70 electrodes.

7.1.8 Charge-storage kinetics

Charge storage kinetics were performed for GO-SbSI composites based on the Dunn method [251]. This analytical approach distinguishes between different charge-storage mechanisms by decoupling surface-confined processes from bulk diffusion behaviors. In this study, the method was used to quantify the surface-controlled capacitive contributions (associated with fast surface adsorption) and the diffusion-controlled contributions (connected to Faradaic redox reactions) relative to the total current measured via cyclic voltammetry. This analysis was performed using CV curves

recorded at different scan rates. At a fixed potential, the measured current can be expressed as the combination of these two contributions:

$$\boldsymbol{i(V) = k_1 v + k_2 v^{0.5}} \quad \boldsymbol{i\,(V)/V^{0.5} = k_1 v + k_2} \quad \textit{(7-1)}$$

where i(V) is the current at a selected potential, v is the scan rate, and k_1 and k_2 are constants. The term $k_1 v$ represents the surface-controlled current, which may include electrical double-layer charge storage and fast surface redox reactions. The term $k_2 v^{1/2}$ represents the diffusion-controlled contribution associated with slower ion movement towards electrochemically accessible regions of the electrode.

To determine k_1 and k_2, the equation can be rearranged as:

$$\boldsymbol{i\,(V)/V^{0.5} = k_1 v + k_2} \textit{ (7-2)}$$

A linear plot of i(V)/$V^{0.5}$ against $V^{1/2}$ provides k_1 from the slope and k_2 from the intercept. These values can then be used to calculate the estimated percentages of surface-controlled and diffusion-controlled current at each scan rate.

Using the power-law equation $I = a v^b$ [252], it is possible to determine the main contribution of charge storage behavior. If a b-value approaches 0.5, it indicates a predominantly diffusion-controlled response, whereas if it approaches 1.0, it indicates a predominantly surface-controlled response.

Figure 7.12 presents the power-law and Dunn analyses performed for the GO-SbSI 30/70 electrode, the power-law and Dunn analyses used to evaluate the charge-storage kinetics of the GO-SbSI 30/70 electrode. The calculated b-value of 0.732 indicates that the electrochemical response of GO-SbSI 30/70 involved both surface-controlled and diffusion-controlled contributions.

The *log(i)-log(v)* fit produced an R^2 value of approximately 0.92. This indicates moderate agreement with the power-law relationship but also shows that the current response does not follow a single idealized mechanism over the investigated scan-rate range. The relative contributions estimated using the Dunn method changed with scan rate, with the surface-controlled contribution becoming more prominent as the scan rate increased. The surface-controlled contribution increased with scan rate because the shorter experimental time restricted ion access to diffusion-limited electrochemical regions.

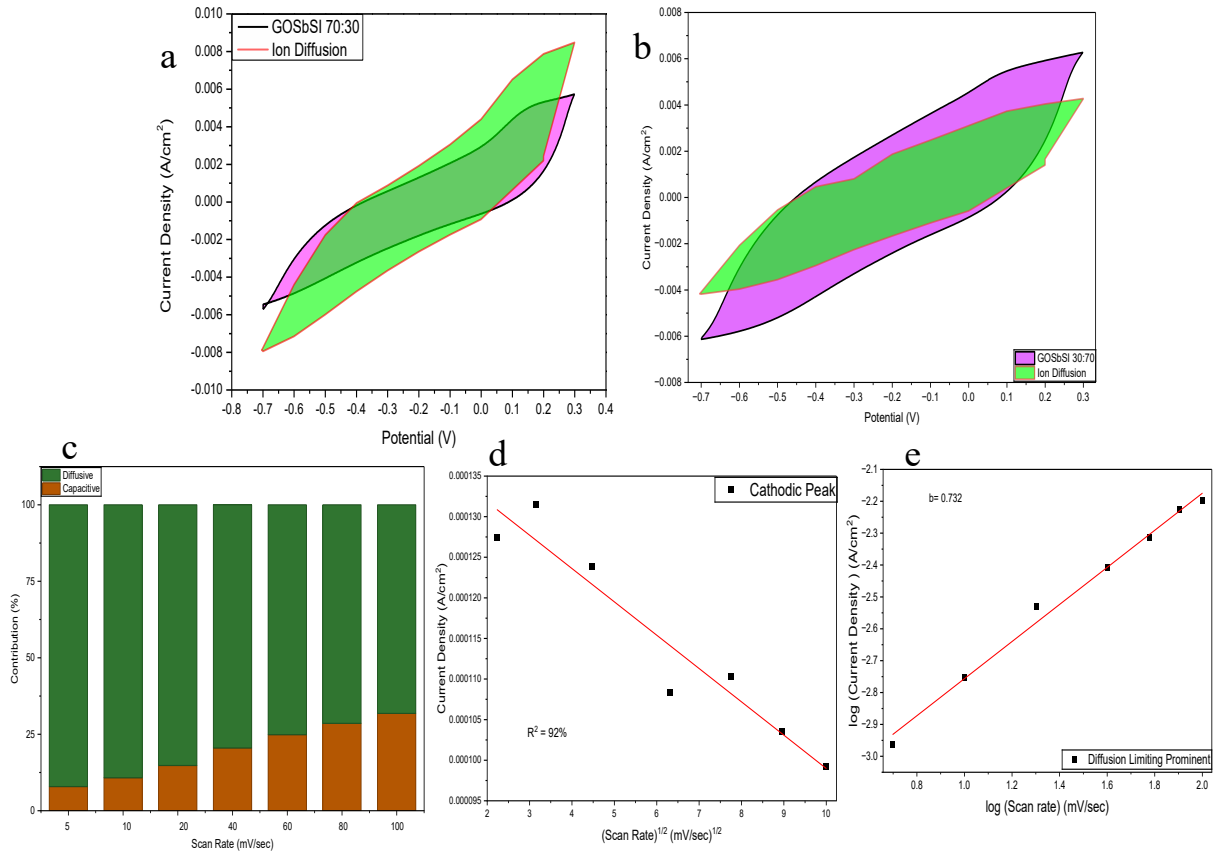


Figure 7.12: Charge-storage kinetic analysis of the GO-SbSI composite electrodes. Dunn-method separation of surface-controlled and diffusion-controlled current contributions for (a) measured and calculated CV curve of GO-SbSI 70/30; (b) measured and calculated CV curve of GO-SbSI 30/70; (c) Estimated surface-controlled and diffusion-controlled contributions at different scan rates; (d) Cathodic peak-current density plotted against ($v^{1/2}$), for V= 0.1V; the line represents the best linear fitting; (e)log (i)-log (v) plot used to determine a b-value of 0.732.

Among the investigated GO-SbSI composites, GO-SbSI 30/70 showed the highest CV-derived specific capacitance. Its comparatively high current response and the presence of redox features indicate that the SbSI-containing composite exhibited a considerable faradaic contribution in addition to surface-controlled charge storage. Nevertheless, the present kinetic analysis does not directly establish continuous electron-transport pathways, ion intercalation, suppression of GO restacking, or a specific interfacial mechanism between GO and SbSI.

This method provides a comparative evaluation of charge-storage kinetics but does not independently identify the exact electrochemical reactions or ion-transport pathways occurring within the electrode material [253].

7.2 GSM Composites

7.2.1 Cyclic voltammetry

Figure 7.13(a-f) presents the CV curves of GSM composites (GSM 1:20:80, GSM 1:30:70, GSM 12:40:60, GSM 1:50:50, GSM 1:60:40 and GSM 1:70:30) recorded at scan rates ranging from 5 to 100 mV/s within a potential window of 1V (-0.7 V to +0.3V). Figure 7.13(a) (GSM 1:20:80) exhibits a narrow, near-rectangular CV shape with minimal hysteresis and a faint, poorly resolved redox hump near 0.2-0.3 V. Figure 7.13(b) (GSM 1:30:70) shows a moderately widened quasi-rectangular loop with a more discernible redox bump around 0.2-0.3 V. Figure 7.13(c) (GSM 1:40:60) displays a broader, leaf-like CV profile with a distinct shoulder near 0.0-0.2 V. Figure 13(d) (GSM 1:50:50) reveals a further widened and asymmetric loop with a pronounced redox hump around 0.1-0.3 V. Figure 13(e) (GSM 1:60:40) presents the large and elongated leaf-shaped CV curve with a sharp, well-defined redox peak near 0.2-0.3 V. Figure 13(f) (GSM 1:70:30) exhibits a highly elongated, diagonally skewed CV shape with a small redox hump, with pronounced overlapping, indicating increased resistive distortion. It has been observed that the CV curves of all samples show the same curve shape at lower and higher scan rates with increasing surface area.

The CV area and current density increase progressively from GSM 1:20:80 to GSM 1:70:30, reflecting enhanced capacitive and pseudocapacitive contributions with increasing GSM ratio; however, the diminished rectangularity and absence of well-defined redox features in GSM 1:70:30 suggest that excessive GSM loading compromises electrochemical reversibility.

These changes in curve shape provide information about the charge-storage behavior of the GSM electrodes. The comparatively small CV area of GSM 1:20:80 indicates limited charge storage under the applied conditions. Its high MnO_2 content may contribute to this response because MnO_2 has relatively low intrinsic electrical conductivity. For the other composites, the broader redox-related features indicate a faradaic contribution in addition to surface-controlled charge storage. The low intrinsic electrical conductivity and faradaic behavior of MnO_2 have been previously reported [254].

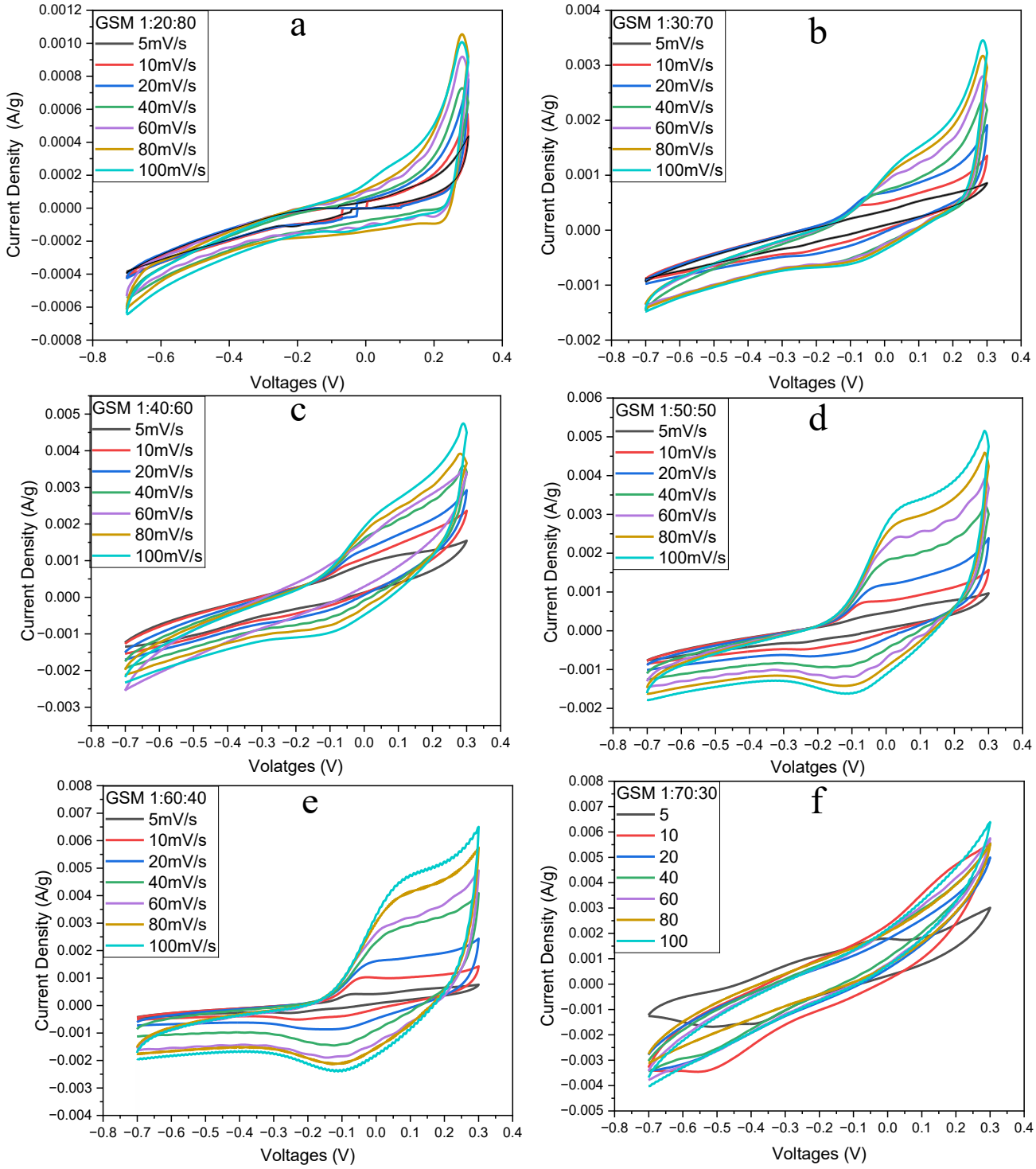


Figure 7.13: CV curves of (a) GSM 1:20:80, (b) GSM 1:30:70, (c) GSM 1:40:60, (d) GSM 1:50:50, (e) GSM 1:60:40, and (f) GSM 1:70:30 recorded at scan rates ranging from 5 to 100 mV/s.

As shown in Figure 7.14, GSM 1:80:20 produced the largest enclosed CV area and exhibited broad redox-related features near 0.01 and -0.27 V versus Hg/HgO. These features indicate a faradaic contribution; however, CV alone cannot assign them to specific Sb, I, or Mn redox reactions.

Among the investigated GSM composites, GSM 1:80:20 produced the largest CV current response and enclosed area. This result shows that the relative contents of GO, SbSI, and MnO_2 strongly influenced the measured charge-storage response.

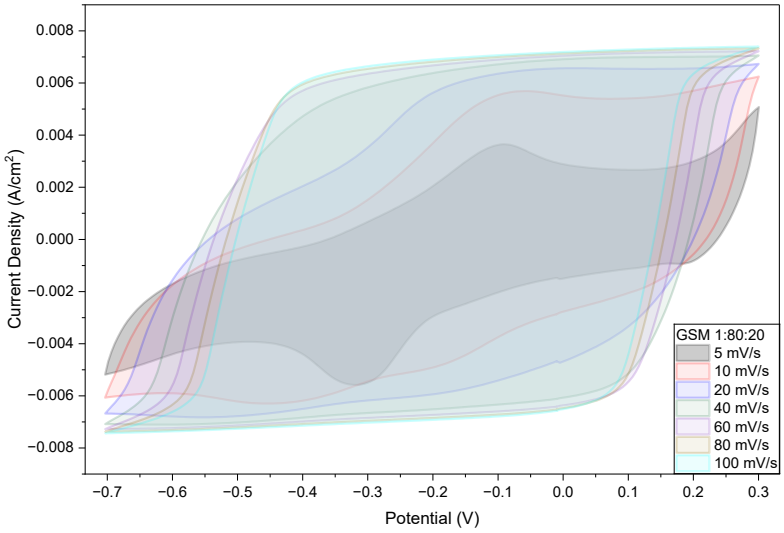


Figure 7.14: CV curves of GSM 1:80:20 recorded at scan rates ranging from 5 to 100 mV/s.

The specific capacitance, energy density, and power density calculated from the CV measurements are summarized in Table 7.3. Typically, C_S generally decreased with increasing scan rate, although the magnitude of the decrease varied among the GSM composites.

Table 7-3: Electrode mass, scan rate, integrated CV area, specific capacitance, energy density, and power density of the GSM electrodes.

Material	Mass (g)	Scan Rate (mV/s)	Area under CV (A·V)	C_S (F/g)	E_D (Wh/kg)	P_D (W/kg)
GSM 1:20:80	0.0016	5	0.000988	123.5	17.15	308.75
	0.0016	10	0.00105	65.62	9.11	328.12
	0.0016	20	0.00107	33.44	4.64	334.37
	0.0016	40	0.0014	21.87	3.04	437.5
	0.0016	60	0.0015	15.62	2.17	468.75
	0.0016	80	0.0017	13.28	1.84	531.25
	0.0016	100	0.0018	11.25	1.56	562.5
GSM 1:30:70	0.002	5	0.0027	270	37.5	675
	0.002	10	0.0031	155	21.53	775
	0.002	20	0.0035	87.5	12.15	875
	0.002	40	0.00488	61	8.47	1220
	0.002	60	0.0051	42.5	5.9	1275
	0.002	80	0.0054	33.75	4.69	1350
	0.002	100	0.0056	28	3.89	1400
	0.0019	5	0.00455	478.95	66.52	1197.37

GSM 1:40:60	0.0019	10	0.0054	284.21	39.47	1421.05
	0.0019	20	0.0062	163.16	22.66	1631.58
	0.0019	40	0.0072	94.74	13.16	1894.74
	0.0019	60	0.0082	71.93	9.99	2157.89
	0.0019	80	0.00921	60.59	8.42	2423.68
	0.0019	100	0.0084	44.21	6.14	2210.53
GSM 1:50:50	0.0022	5	0.0027	245.45	34.09	613.64
	0.0022	10	0.0035	159.09	22.1	795.45
	0.0022	20	0.0046	104.55	14.52	1045.45
	0.0022	40	0.0062	70.45	9.79	1409.09
	0.0022	60	0.0075	56.82	7.89	1704.55
	0.0022	80	0.0086	48.86	6.79	1954.55
	0.0022	100	0.0096	43.64	6.06	2181.82
GSM 1:60:40	0.002	5	0.0021	210	29.17	525
	0.002	10	0.0031	155	21.53	775
	0.002	20	0.0047	117.5	16.32	1175
	0.002	40	0.0074	92.5	12.85	1850
	0.002	60	0.0099	82.5	11.46	2475
	0.002	80	0.011	68.75	9.55	2750
	0.002	100	0.013	65	9.03	3250
GSM 1:70:30	0.002	5	0.009	900	125	2250
	0.002	10	0.0134	670	93.06	3350
	0.002	20	0.0113	282.5	39.24	2825
	0.002	40	0.0123	153.75	21.35	3075
	0.002	60	0.013	108.33	15.05	3250
	0.002	80	0.011	68.75	9.55	2750
	0.002	100	0.014	70	9.72	3500
GSM 1:80:20	0.0015	5	0.009	1200	166.67	3000
	0.0015	10	0.017	1133.33	157.41	5666.67
	0.0015	20	0.021	700	97.22	7000
	0.0015	40	0.023	383.33	53.24	7666.67
	0.0015	60	0.024	266.67	37.04	8000
	0.0015	80	0.026	216.67	30.09	8666.67
	0.0015	100	0.0292	194.67	27.04	9733.33

At 5 mV/s, the specific capacitance increased from 123.50 F/g for GSM 1:20:80 to 270.00 F/g for GSM 1:30:70 and 478.95 F/g for GSM 1:40:60. Lower values of 245.45 and 210.00 F/g were obtained for GSM 1:50:50 and GSM 1:60:40, respectively. A further increase was observed for GSM 1:70:30 and GSM 1:80:20, which delivered 900.00 and 1200.00 F/g, respectively.

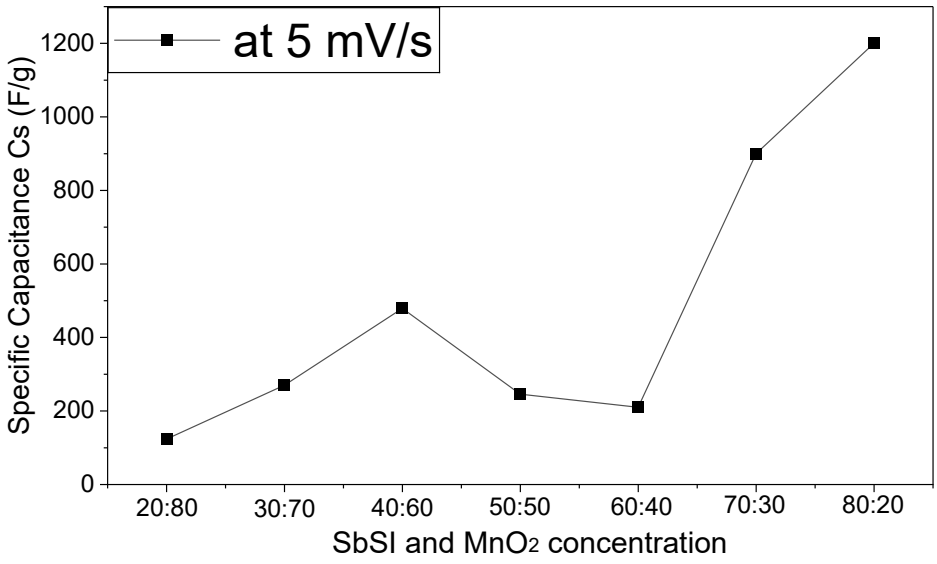


Figure 7.15: CV-derived specific capacitance of the GSM electrodes at mV/s.

Figure 7.15 shows the variation of specific capacitance as a function of SbSI:MnO_2 concentration ratio (GO ratio is fixed) at a scan rate of 5 mV/s. The specific capacitance initially increases from 123.5 F/g at 20:80 to a maximum of 478.95 F/g at 40:60, followed by a decline to 245-210 F/g at the 50:50 and 60:40 ratios. Than it rise sharply to 900 F/g at 70:30 and reaching a maximum of 1200 F/g at 80:20. This non-monotonic trend indicates that capacitance is not simply proportional to increasing SbSI content but is instead governed by a competing interplay between the two components at lower SbSI:MnO_2 ratios, MnO_2's pseudocapacitive contribution dominates but is limited by its poor intrinsic conductivity, while the dip at intermediate ratios (50:50, 60:40) suggests a less favorable structural or interfacial synergy between SbSI and MnO_2. The pronounced capacitance enhancement at higher SbSI content (70:30, 80:20) indicates that SbSI increasingly dominates the charge storage behavior, likely due to its superior electroactivity and improved ion-accessible surface area at these ratios, with the 80:20 composite yielding the highest overall specific capacitance among the tested formulations.

When compared with the literature, pristine materials such as GO, SbSI, and MnO_2 exhibit significantly smaller values for C_S and P_D when tested alone or within standard binary matrices [67, 76, 84-86, 243, 244, 255, 256]. These severe performance limitations are effectively overcome through the formation of the multi-component architecture. By establishing this highly effective synergistic network, the integration of the three components systematically enhances the overall electrochemical performance, demonstrating clear advantages over both individual constituents and related literature composites.

7.2.2 GCD testing

Figure 7.16(a-f) presents the galvanostatic charge-discharge (GCD) curves of the GSM composites at varying current densities (0.5-2.5 A/g), showing the effect of composition ratio on charge storage duration. Figure 7.16a (GSM 1:20:80) shows short, near-symmetric triangular charge-discharge profiles with the longest charge-discharge time of 18 s occurring only at 0.5 A/g, while higher current densities collapse into narrow loops (<5 s).

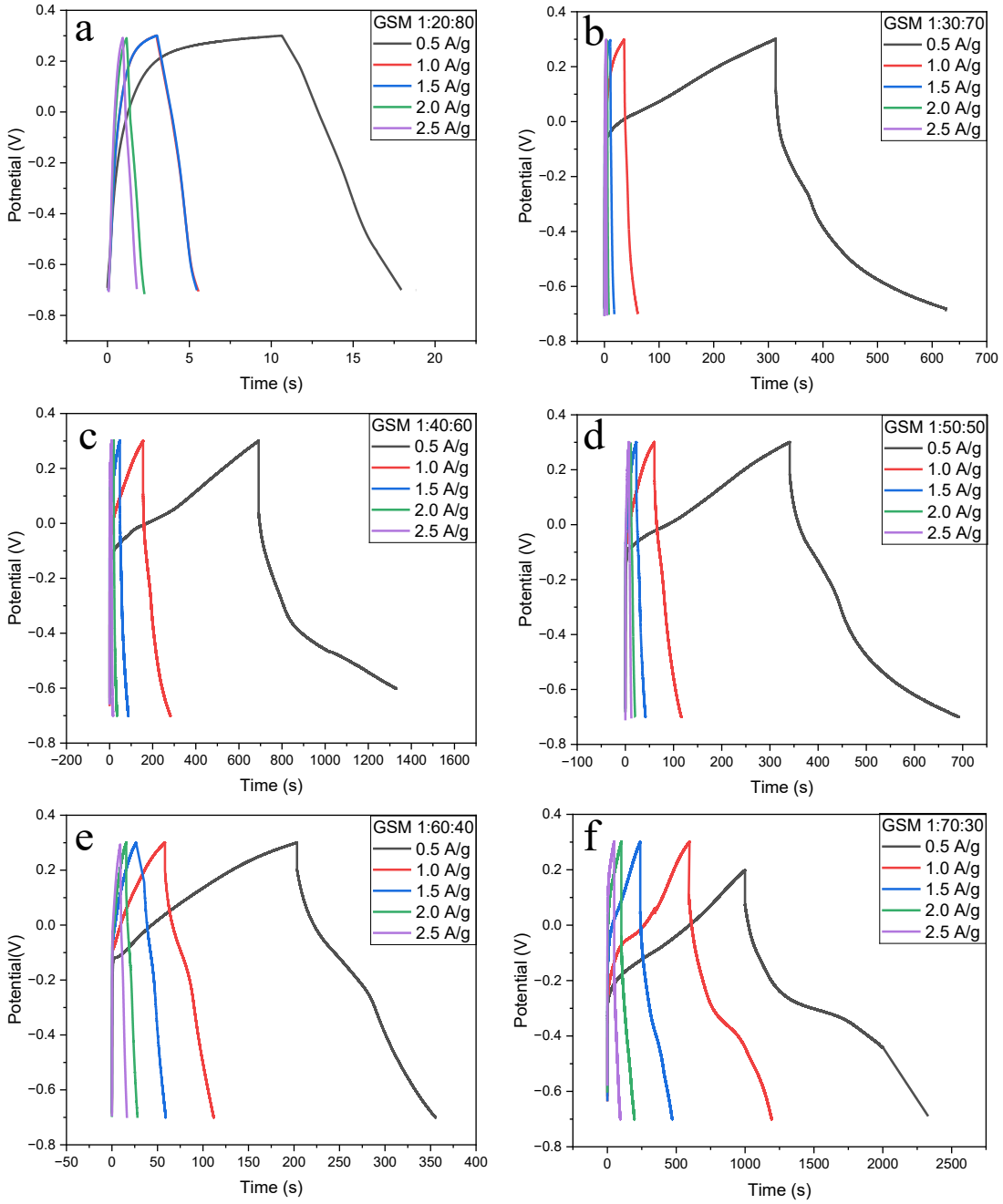


Figure 7.16: GCD curves of GSM composites (a) GSM 1:20:80, (b) GSM 1:30:70, (c) GSM 1:40:60, (d) GSM 1:50:50, (e) GSM 1:60:40, and (f) GSM 1:70:30 recorded at current densities ranging from 0.5 to 2.5 A/g.

Figure 7.16b (GSM 1:30:70) displays a longer charge-discharge duration (640 s at 0.5 A/g) with a distinctly curved, non-linear discharge slope indicating pseudocapacitive behavior, while higher current densities remain compressed near the origin. Figure 7.16c (GSM 1:40:60) exhibits an even longer charge-discharge time (1380 s at 0.5 A/g) with a pronounced plateau/shoulder in the discharge curve, reflecting strong faradaic contribution. Figure 7.16d (GSM 1:50:50) shows a shorter charge-discharge time (700 s at 0.5 A/g) with a smoother, less-plateaued curve compared to GSM 1:40:60. Figure 7.16e (GSM 1:60:40) presents a further reduced charge-discharge duration (370 s at 0.5 A/g) with tightly clustered curves at higher current densities. Figure 7.16f (GSM 1:70:30) shows a long and complex charge-discharge profile (2380 s at 0.5 A/g) compared to GSM1:20:80 to GSM 1:60:40, featuring a distinct two-stage slope with a plateau around 0.0-0.2 V, indicating the strongest pseudocapacitive/battery-like behavior. The deviation from ideal triangular profiles indicates that charge storage did not arise solely from electrical double-layer formation and included a faradaic contribution.

Figure 7.17 shows the GCD curves of the GSM 1:80:20 composite at current densities of 0.5-2.5 A/g, presented as overlaid shaded charge-discharge profiles. At 0.5 A/g, the electrode exhibits the longest charge-discharge time (3480 s) with a broad, multi-stage discharge curve featuring a clear plateau around -0.2 to +0.3 V followed by a steep final drop, indicative of strong pseudocapacitive/faradaic charge storage. As current density increases (1.0-2.5 A/g), the discharge time decreases, becoming narrower and more symmetric. This behavior confirms that GSM 1:80:20 delivers the highest charge storage capacity at low current density, consistent with its highest specific capacitance value (1200 F/g) observed in Figure 7.15, while the pronounced rate-dependent narrowing indicates diffusion-limited charge storage kinetics at higher current densities.

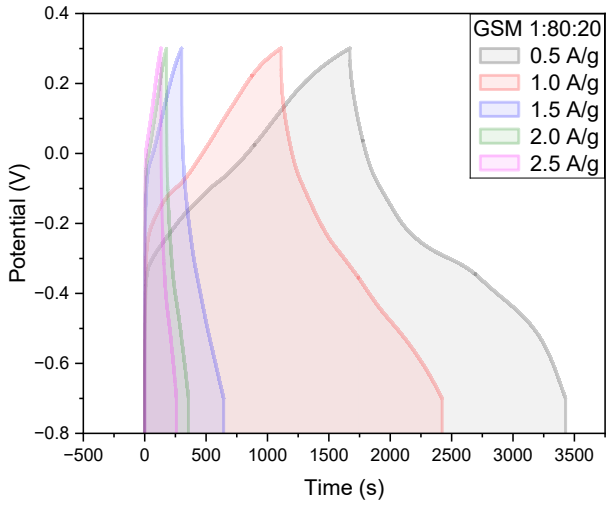


Figure 7.17: GCD curves of GSM 1:80:20 recorded at current densities ranging from 0.5 to 2.5 A/g.

Table 7-4: Electrode mass, current density, discharge time, specific capacitance, energy density, and power density of the GSM electrodes calculated from GCD measurements.

Material	Mass (g)	Current Density (A/g)	Discharge Time (s)	C_S (F/g)	E_D (Wh/kg)	P_D (W/kg)
GSM 1:20:80	0.0016	0.5	9	2.81	0.39	156.25
	0.0016	1	2.5	1.56	0.22	312.5
	0.0016	1.5	2.5	2.34	0.33	468.75
	0.0016	2	1.5	1.88	0.26	625
	0.0016	2.5	1.5	2.34	0.33	781.25
GSM 1:30:70	0.002	0.5	300	75	10.42	125
	0.002	1	40	20	2.78	250
	0.002	1.5	20	15	2.08	375
	0.002	2	15	15	2.08	500
	0.002	2.5	10	12.5	1.74	625
GSM 1:40:60	0.0019	0.5	675	177.63	24.67	131.58
	0.0019	1	150	78.95	10.96	263.16
	0.0019	1.5	75	59.21	8.22	394.74
	0.0019	2	50	52.63	7.31	526.32
	0.0019	2.5	35	46.05	6.4	657.89
GSM 1:50:50	0.0022	0.5	350	79.55	11.05	113.64
	0.0022	1	60	27.27	3.79	227.27
	0.0022	1.5	25	17.05	2.37	340.91
	0.0022	2	18	16.36	2.27	454.55
	0.0022	2.5	12	13.64	1.89	568.18
GSM 1:60:40	0.002	0.5	170	42.5	5.9	125
	0.002	1	55	27.5	3.82	250
	0.002	1.5	27	20.25	2.81	375
	0.002	2	14	14	1.94	500
	0.002	2.5	10	12.5	1.74	625
GSM 1:70:30	0.002	0.5	1250	347.22	39.06	112.5
	0.002	1	650	325	45.14	250
	0.002	1.5	250	187.5	26.04	375
	0.002	2	200	200	27.78	500
	0.002	2.5	125	156.25	21.7	625
GSM 1:80:20	0.0015	0.5	1875	625	86.81	166.67
	0.0015	1	1150	766	106	333
	0.0015	1.5	350	350	48	500
	0.0015	2	200	266.67	37.04	666.67
	0.0015	2.5	125	208.33	28.94	833.33

Table 7.4 summarizes the discharge time, specific capacitance, energy density, and power density of all GSM composites across current densities of 0.5-2.5 A/g, confirming the expected inverse

relationship between energy density and power density with increasing current, and identifying GSM 1:80:20 and GSM 1:70:30 as the top-performing composites in terms of overall energy storage capability.

Figure 7.18 compares the E_D and P_D of all GSM composites at a fixed current density of 2.5 A/g, highlighting the compositional dependence of the energy-power trade-off. Energy density shows a non-linear trend, increasing from 0.33 Wh/kg (GSM 1:20:80) to a minimum of 1.74 Wh/kg in the 1:50:50 to 1:60:40 range. Then rised sharply to 21.7 Wh/kg (1:70:30) and peaking at 28.94 Wh/kg (1:80:20). Power density follows a broadly inverse pattern, starting high at 781.25 W/kg for GSM 1:20:80, dipping to its lowest value (568 W/kg) at 1:50:50, and then recovering to its maximum of 833.33 W/kg at GSM 1:80:20. Notably, GSM 1:80:20 achieves simultaneous maxima in both energy density and power density, indicating that this composite offers the most favorable overall electrochemical performance even under high-rate (2.5 A/g) operating conditions.

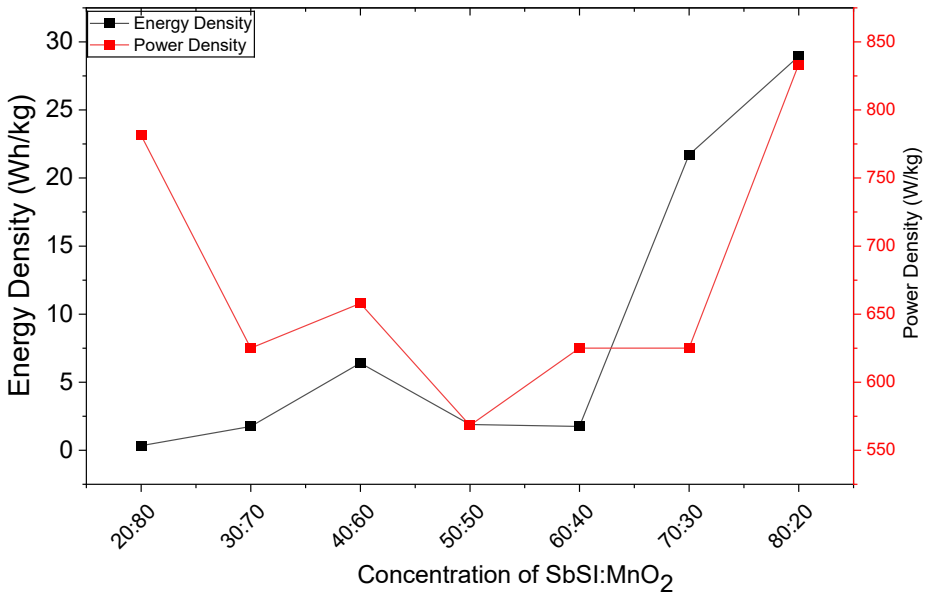


Figure 7.18: E_D and P_D of the GSM electrodes at 2.5 A/g.

Figure 7.19 presents the cyclic stability of the optimized GSM 1:80:20 composite, evaluated over 3000 charge-discharge cycles, selected for long-term testing based on its superior energy density and power density performance identified in Figure 7.18. The capacitance retention decreases gradually and near-linearly from approximately 95% at the initial cycle to 80% after 3000 cycles, corresponding to a total capacitance loss of approximately 15%. This steady, moderate decline-without any abrupt drop- indicates good structural and electrochemical stability of the GSM 1:80:20 electrode under repeated cycling, confirming its suitability for long-term supercapacitor applications alongside its high E_D and P_D characteristics.

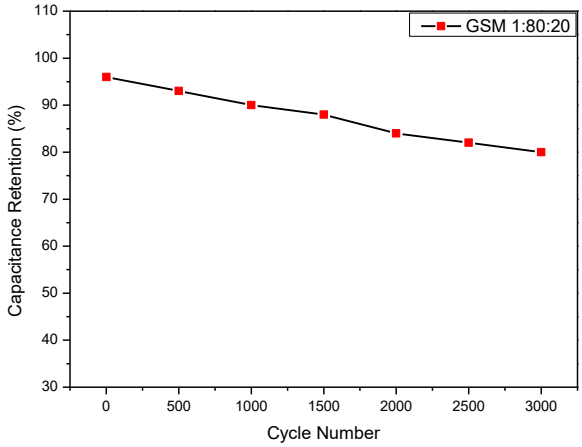


Figure 7.19: Capacitance retention of GSM 1:80:20 over 3000 GCD cycles.

7.2.3 Electrochemical Impedance Spectroscopy

Figure 7.20 shows the Nyquist plots (Z″ versus Z′) obtained from the electrochemical impedance spectroscopy measurements of the GSM electrodes with ratios of 1:20:80, 1:30:70, 1:40:60, 1:50:50, 1:60:40, 1:70:30 and 1:80:20. Z′ extends to about 700 Ω and Z″ to about 470 Ω. None of the electrodes shows a fully developed semicircle in the measured range. Each curve has a small high-frequency feature close to the origin, followed by an inclined, almost linear branch that rises towards higher Z′ and Z″. The high-frequency intercept with the real axis gives the equivalent series resistance (electrolyte, contact, and intrinsic electrode resistance). It is small for all samples, roughly 10-50 Ω, with the lowest value for GSM 1:20:80. The small arc at high frequency is associated with the charge-transfer process at the electrode/electrolyte interface. It is only a few tens of ohms wide for most samples, which points to fast interfacial charge transfer and good contact between the active material and the electrolyte.

The inclined branch at lower frequencies is characteristic of diffusion-controlled or capacitive behavior, as in a Warburg-type response. Its steepness shows how strongly the electrode behaves as an ion-diffusion or capacitive element, and the slope is the main feature distinguishing the samples. From the last measured points, the slope angle relative to the real axis is about 43° for GSM 1:40:60, 36° for 1:70:30, 29° for 1:30:70, 25° for 1:60:40, 24° for 1:50:50, 14° for 1:80:20 and only about 6° for 1:20:80. GSM 1:40:60 therefore has the steepest branch, close to the 45o expected for semi-infinite diffusion, and it reaches the highest Z″ of about 470 Ω at Z′ ≈ 690 Ω. GSM 1:70:30 follows with Z″ ≈ 400 Ω. GSM 1:30:70 and 1:60:40 reach about 310-320 Ω, and 1:50:50 reaches about 250 Ω. GSM 1:80:20 behaves differently from the rest. Its Z″ is the highest of the series in the range of 100-300 Ω, which indicates a better-developed high-frequency arc. Its curve then flattens and bends towards the real axis, reaching only about 220 Ω at Z′ ≈ 680 Ω, so the arc is not closed, and the charge-transfer resistance is

larger than in the other samples. GSM 1:20:80 is almost purely resistive in this window, with Z″ of only about 58 Ω at Z′ ≈ 690 Ω. It has the lowest series resistance, but its very low slope indicates a weak diffusion or capacitive response.

The behavior is not monotonic with composition. The slope of the diffusion branch, and hence the capacitive character, rises from 1:20:80 to a maximum at 1:40:60, decreases through 1:50:50 and 1:60:40, rises again at 1:70:30, and falls to the second-lowest value at 1:80:20. This suggests that the ion-transport pathways and the accessible electroactive surface depend on the balance between the components, with 1:40:60 as the optimum in this series.

All the GSM electrodes show low series and charge-transfer resistances, as expected for an electrode that supports fast interfacial charge transfer. The composition controls the diffusion or capacitive response, with the steepest low-frequency branch and the largest reactive impedance.

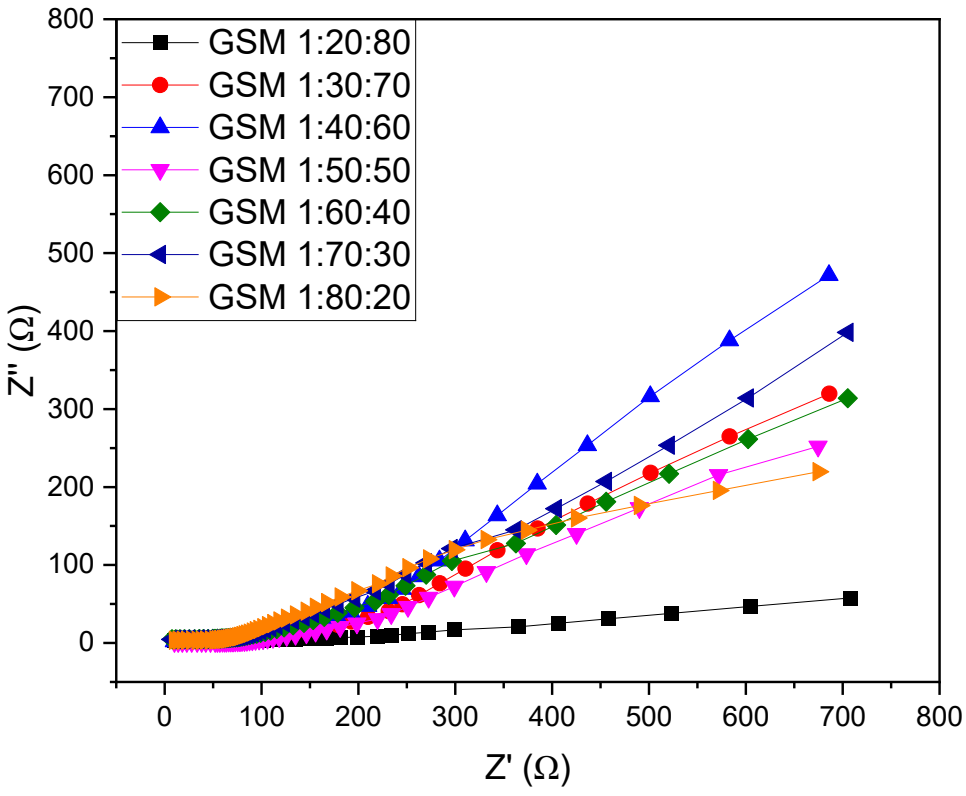


Figure 7.20: Nyquist plots of GSM 1:20:80, GSM 1:30:70, GSM 1:40:60, GSM 1:50:50, GSM 1:60:40, GSM 1:70:30, and GSM 1:80:20 electrodes.

7.2.4 Charge-storage Kinetics

The charge-storage kinetics of the GSM 1:80:20 electrode evaluated using the power-law and Dunn methods are presented in Figure 7.21. The relationship between the anodic peak current and scan rate was analyzed using the power-law relationship. The log (*i*)-log(*v*) analysis produced a b-value of 0.70 with an adjusted coefficient of determination of (R^2=0.99). The high R^2 value indicates good agreement between the anodic peak current and the applied power-law relationship [253]. The obtained b-value indicates mixed charge-storage kinetics involving both surface-controlled and diffusion-controlled processes.

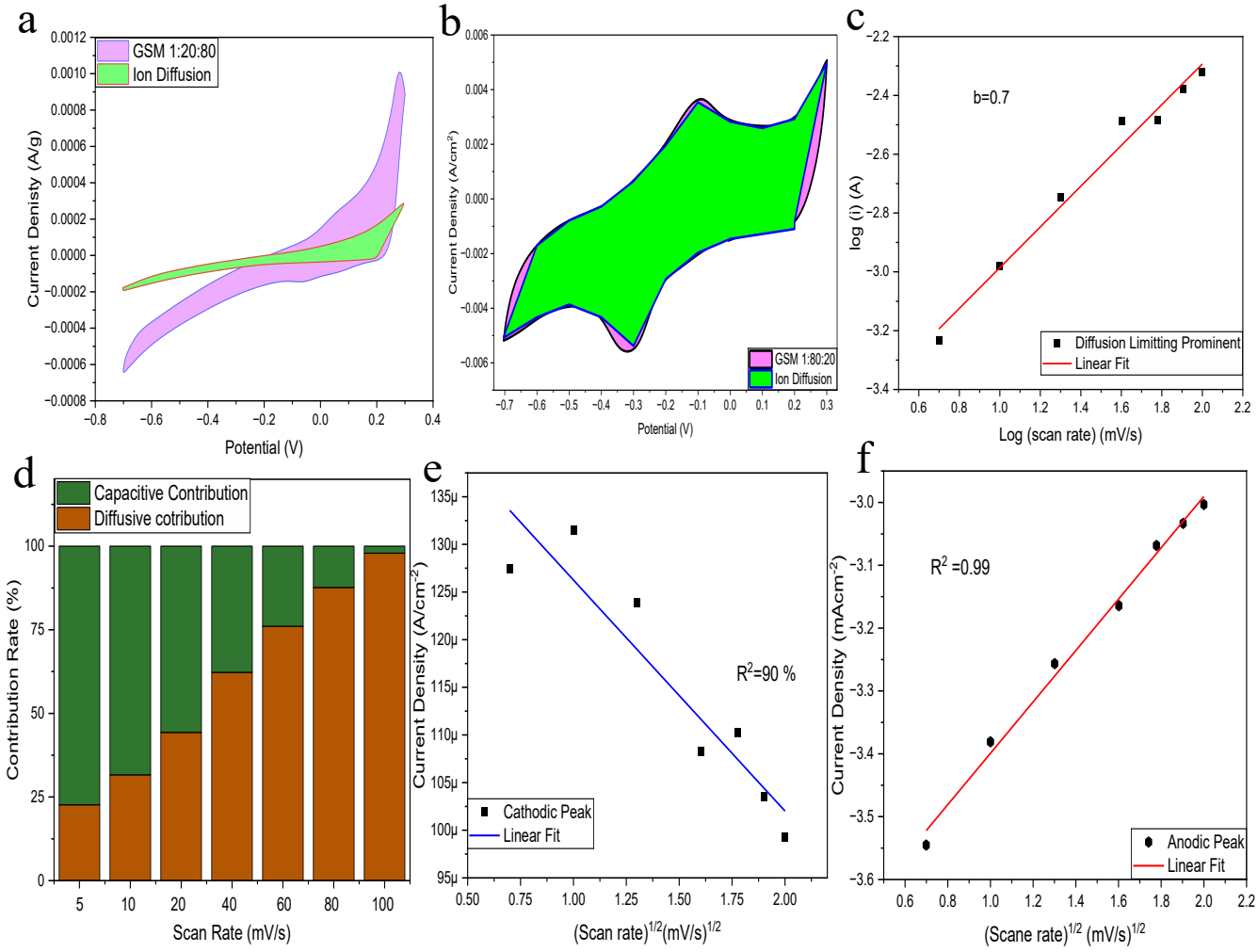


Figure 7.21: Charge-storage kinetic analysis of the GSM electrodes. Dunn-method separation of surface-controlled and diffusion-controlled current contributions for (a) GSM 1:20:80 and (b) GSM 1:80:20; (c) log(i)-log(v) plot for b-value determination (b=0.7). (d) Estimated surface-controlled and diffusion-controlled contributions at different scan rates. (e, f) Peak-current density plotted against $v^{1/2}$; for V = 0.1 V.

The non-linear CV response suggests the presence of a faradaic contribution. MnO_2 may contribute through manganese-related redox reactions, whereas the oxygen-containing functional groups of GO can improve electrolyte wettability and provide sites for surface ion adsorption. The redox-related features in the CV curves also suggest a contribution from electrochemically active sites associated with SbSI [84]. However, the individual contributions of GO, SbSI, and MnO_2 cannot be quantified from these curves alone.

The estimated surface-controlled contribution increased with scan rate because the shorter experimental time restricted ion access to diffusion-limited electrochemical regions [257]. The obtained b-value indicates mixed charge-storage kinetics involving both surface-controlled and diffusion-controlled processes [258]. However, these results do not independently establish ion-intercalation pathways, GO-mediated conductive networks, or a ferroelectric-field effect from SbSI.

The interaction of the active material with the KOH solution decomposed the electrodes. After testing the electrodes, it looks the same as before testing, which shows that the materials are firmly stuck on the electrode and show a lower rate of decomposition.

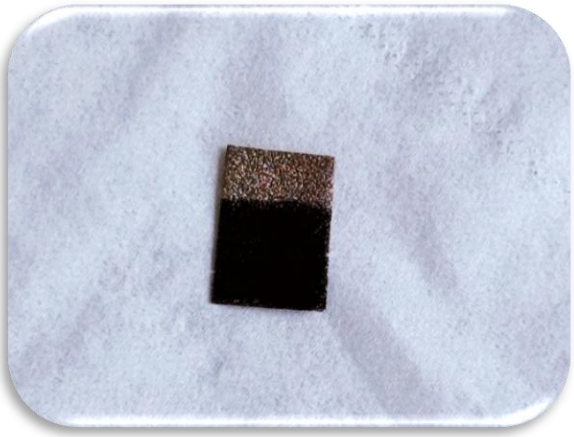


Figure 7.22: The degradation of the electrode tested after testing.

After three-electrode characterization, GSM 1:80:20 was assembled in a two-electrode coin-cell configuration for full-cell testing.

Chapter 8

DEVICE STUDY

Two-electrode coin cells are widely used to evaluate the device-level electrochemical performance of supercapacitors because they provide a more representative assessment than individual-electrode measurements [259, 260]. In this study, asymmetric coin cells were fabricated using the selected GO–SbSI 30/70 and GSM 1:80:20 based on the combined results of their three-electrode characterization, in which these composites exhibited the highest specific capacitance and power density among the samples tested, both of which are key performance indicators for supercapacitor applications. In this study, asymmetric coin cells were assembled using these composites as the positive electrode and a carbon-based material as the negative electrode. Figure 8.1 presents the exploded view of such a coin cell, consisting of a top cover, a wave spring, a spacer, the composite positive electrode, the separator, the carbon-based negative electrode, and a bottom case. A Grade 392 quantitative cellulose filter paper was placed between the positive and negative electrodes as the separator. The separator was soaked with electrolyte to prevent direct electrical contact between the electrodes while allowing ionic transport. This electrode-separator assembly was then placed between the top cover and bottom case, which acted as the positive and negative current collectors, respectively, providing electrical contact with the external electrochemical workstation. A wave spring and spacer were placed inside the assembly, between the top cover and the positive electrode, before mechanical crimping to ensure internal contact and uniform compression of the electrodes, separator, and metallic components [261]. During operation, the positive and negative electrodes participated simultaneously in the charge-storage process; therefore, the measured response represented the performance of the complete cell. Electrochemical measurements of the assembled asymmetric coin cells were performed using an Autolab AUT84500 potentiostat/galvanostat.



Figure 8.1: Exploded view of the coin cell consisting of a top cover (positive current collector), wave spring, spacer, composite positive electrode, Grade 392 quantitative cellulose filter-paper separator, carbon-based negative electrode, and bottom case (negative current collector).

Figure 8.2 presents the assembled coin cells used for electrochemical measurements. The cell components are held within insulating clamps and connected to external electrical leads for electrode characterization. The composite positive electrode was connected to the positive terminal of the electrochemical workstation, while the carbon-based negative electrode was connected to the negative terminal. CV, GCD, EIS, and cycling stability measurements were performed to evaluate the complete-cell response.

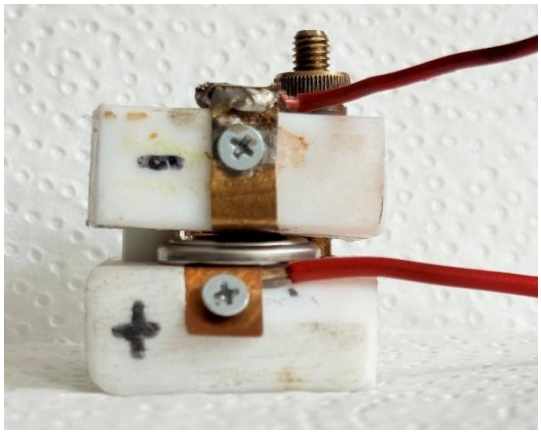


Figure 8.2: Photograph of the assembled coin cell.

8.1 Electrochemical testing of GO-SbSI coin cell

8.1.1 Cyclic Voltammetry

Figure 8.3 demonstrates the CV curves of the GO-SbSI 30/70 coin cell recorded at different scan rates ranging from 5 to 100 mV/s within a potential range of 0.0-1.1 V. This differs from the -0.7 to 0.3 V window used in the three-electrode setup because the coin cell has no reference electrode and instead measures the overall voltage between the positive (GO-SbSI 30/70) and negative (carbon-based) electrodes. The asymmetric design combines the complementary potential windows of both electrodes, extending the operating voltage beyond that of GO-SbSI 30/70 alone and enabling higher energy density. All curves exhibit a quasi-rectangular shape with a broad, superimposed redox hump rather than an ideal rectangular EDLC profile, indicating that charge storage arises from a combination of electric double-layer capacitance (from the carbon-based negative electrode) and pseudocapacitive faradaic reactions (from the GO-SbSI composite).

At low scan rates (5, 10, and 20 mV/s), a well-defined oxidation hump appears at approximately 0.3-0.4 V, accompanied by a corresponding reduction feature at lower potential. These distinct redox features arise because, at slow scan rates, there is sufficient time for ions to diffuse into and out of the electroactive sites [247] of the GO-SbSI structure, allowing the redox reaction to proceed near completion. As the scan rate increases (40, 60, 80, and 100 mV/s), the redox humps progressively broaden and become less resolved, merging into the overall quasi-rectangular envelope. This behavior reflects the limited time available for ion diffusion at higher scan rates: the faradaic reaction becomes kinetically limited, and IR drop becomes more pronounced, shifting the apparent oxidation and reduction features apart and suppressing their sharpness. Consequently, the response shifts from a diffusion-controlled regime toward a more surface-controlled, capacitive-like regime. The enclosed area of the CV loop increases systematically with scan rate, consistent with the expected linear relationship between current density and scan rate for capacitive systems.

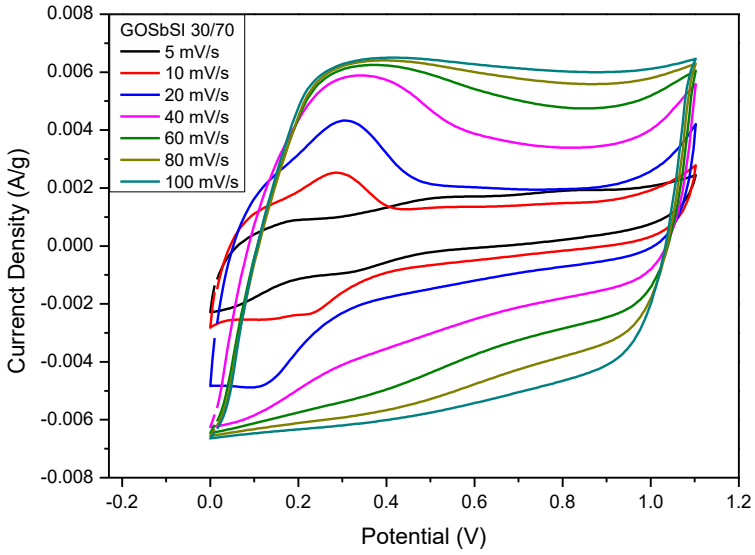


Figure 8.3: CV curves of the GO-SbSI 30/70 coin cell recorded at scan rates ranging from 5 to 100 mV/s.

The observed redox-related features are consistent with the previously reported electrochemical activity of SbSI-containing electrodes [84, 86].

The electrochemical parameters calculated from the CV curves of the GO-SbSI 30/70 coin cell are summarized in Table 8.1. At 100 mV/s, the cell retained approximately 29.4% of its initial CV-derived capacitance. The corresponding calculated energy density decreased from 31.25 to 9.20 Wh/kg. The cell retained approximately 29.4% of its initial CV-derived capacitance at 100 mV/s, corresponding to a capacitance loss of approximately 70.6%. Therefore, although the cell maintained measurable charge storage at 100 mV/s, its CV-derived capacitance retention over the investigated scan-rate range was limited.

Table 8-1: Scan rate, electrode mass, integrated CV area, specific capacitance, energy density, and power density of the GO-SbSI 30/70 coin cell.

Material	Scan Rate (mV/s)	Mass (g)	Area under CV curve (A·V)	C_S (F/g)	E_D (Wh/kg)	P_D (W/kg)
GO-SbSI 30/70	5	0.0016	0.0018	225	31.25	562.5
	10	0.0016	0.0026	162.5	22.57	812.5
	20	0.0016	0.0045	140.62	19.53	1406.25
	40	0.0016	0.0071	110.94	15.41	2218.75
	60	0.0016	0.0089	92.71	12.88	2781.25
	80	0.0016	0.0099	77.34	10.74	3093.75
	100	0.0016	0.0106	66.25	9.2	3312.5

8.1.2 GCD testing

Figure 8.4 presents the GCD profiles of the GO-SbSI 30/70-coin cell at current densities ranging from 1, 2, 5, 10, 15, and 20 A/g within a potential window of 0.0 to 1.1 V. All curves display a non-linear, non-triangular profile, particularly during the charging segment, which curves upward rather than rising as a straight line. This deviation from ideal triangular EDLC behavior confirms the pseudocapacitive contribution from the GO-SbSI composite, consistent with the redox features observed in the CV curves (Figure 8.3).

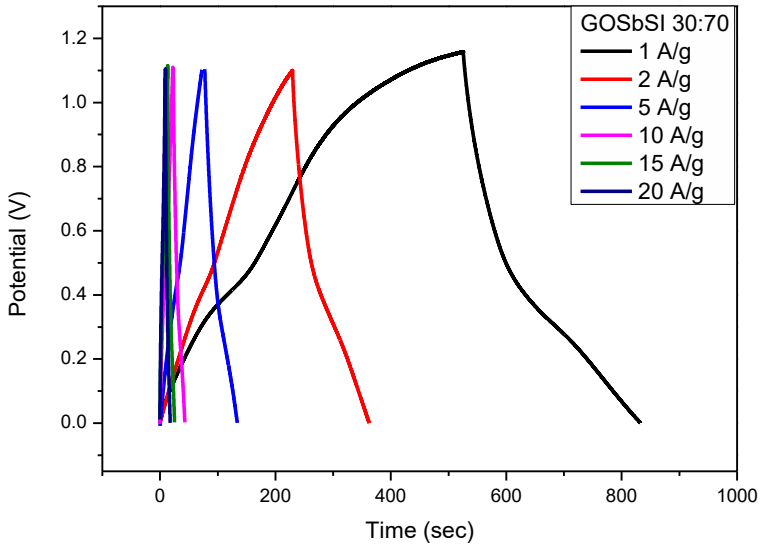


Figure 8.4: GCD curves of the GO-SbSI 30/70 coin cell recorded at applied currents ranging from 1 to 20 mA.

At the lowest current density (1 A/g), the charge and discharge times are the longest, extending to nearly 830 s. The charging segment shows a distinct sigmoidal (S-shaped) curvature with an inflection around 0.5-0.7 V, reflecting a redox process that has sufficient time to proceed at low current, similar to the diffusion-controlled behavior seen at low scan rates in the CV data. The discharge segment is correspondingly slow and gradual, indicating efficient utilization of the stored charge.

As the current density increases to 2 A/g and 5 A/g, the total charge-discharge time decreases sharply, and the curves become progressively steeper and more linear. This shortening of cycle time with increasing current density is typical, since a fixed amount of stored charge is delivered over a shorter period at higher current. The reduced curvature also indicates that at these higher rates, the redox reaction contributes less to completion within the available time, so the response shifts toward a more capacitive, less diffusion-limited profile.

At higher current densities (10, 15, and 20 A/g), the charge-discharge times become very short, with the curves compressed close to the time axis. This behavior is characteristic of diffusion limitations at high current: ions cannot penetrate the electroactive material fast enough to sustain the faradaic process, so an increasing fraction of the response is confined to the electrode surface, and much of the pseudocapacitive contribution is lost. A noticeable IR drop is also expected at the start of each discharge at these higher rates, consistent with increased internal resistance and ohmic losses at high current, though this is difficult to quantify precisely from the compressed curves and warrants closer inspection of the raw data at these rates [262].

The electrochemical parameters calculated from the GCD curves of the GO-SbSI 30/70 coin cell are presented in Table 8.2. The cell delivered a specific capacitance of 256.25 F/g at 1 A/g. At the highest applied current density of 20 A/g, based on 1.6 mg of active material, the specific capacitance decreased to 162.50 F/g, corresponding to a retention of approximately 63.4%. The calculated energy density decreased from 35.59 to 22.57 Wh/kg, whereas the power density increased from 312.50 to 6250.00 W/kg. Thus, the coin cell retained approximately 63.4% of its initial GCD-derived capacitance at the highest investigated applied current.

Table 8-2: Current density, discharge time, specific capacitance, energy density, and power density of the GO-SbSI 30/70 coin cell calculated from GCD measurements.

Material	Current Density (A/g)	Discharge Time (s)	C_S (F/g)	E_D (Wh/kg)	P_D (W/kg)
GO-SbSI 30/70	1	410	256.25	35.59	312.5
	2	180	225	31.25	625
	5	75	234.38	32.55	1562.5
	10	40	250	34.72	3125
	15	20	187.5	26.04	4687.5
	20	13	162.5	22.57	6250

The cyclic stability of the GO-SbSI 30/70 coin cell was monitored over 3000 charge-discharge cycles, as shown in Figure 8.5. The coulombic efficiency decreased from approximately 89% at the beginning of the plotted interval to approximately 84-85% after 3000 cycles. The comparatively small change indicates that the GCD performance exhibited excellent cyclic stability during the investigated cycling period.

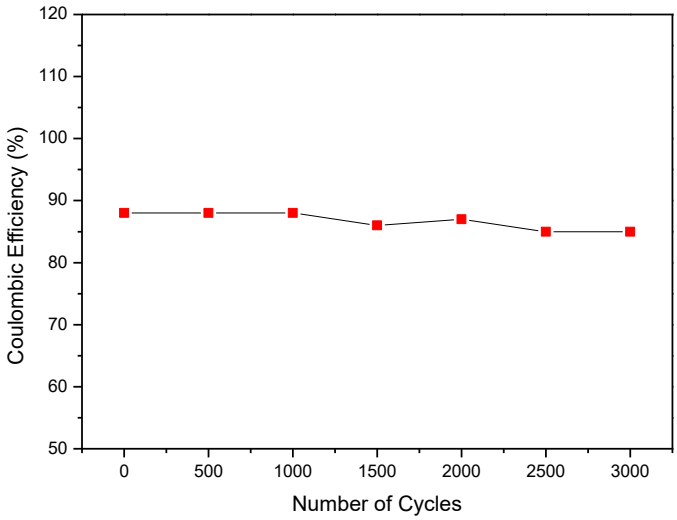


Figure 8.5: Coulombic efficiency of the GO-SbSI 30/70 coin cell over 3000 charge-discharge cycles.

8.1.3 Electrochemical Impedance Spectroscopy

Figure 8.6 presents the electrochemical impedance spectroscopy Nyquist plot of the GO-SbSI 30/70 electrode, showing the imaginary component of impedance (Z″) plotted against the real component of impedance (Z′), both expressed in ohms, over a range of approximately 0 to 100 Ω. The plot displays an almost linear profile extending diagonally across the entire frequency range, with a nearly 45° slope and negligible curvature, rather than the classical combination of a semicircle in the high-frequency region followed by a straight line in the low-frequency region. The absence of a distinct semicircular arc at high frequencies suggests a very low R_{ct} for this electrode, indicating fast interfacial charge-transfer kinetics between the electrode and the electrolyte. The near-linear, steeply rising trend throughout the low-to mid-frequency region reflects predominantly diffusion-controlled (Warburg-type) behavior; this indicates a diffusion-limited pseudocapacitive charge storage mechanism.

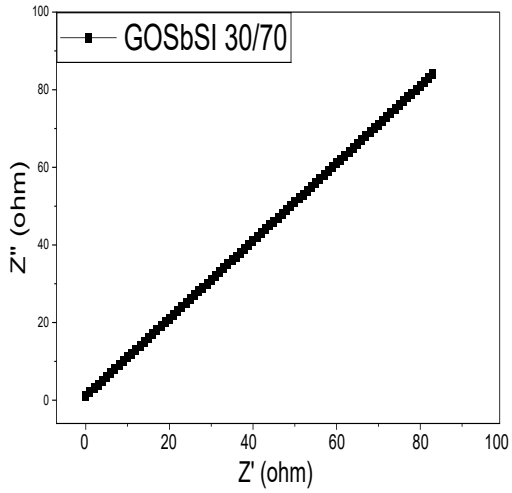


Figure 8.6: Nyquist plot of GO-SbSI 30/70 coin cell.

8.1.4 Charge-storage kinetics

Figure 8.6(a) presents the estimated surface-controlled (capacitive) and diffusion-controlled current contributions (measured value) of the GO-SbSI 30/70 coin cell at a scan rate of 100 mV/s, with the shaded orange region representing the ion-diffusion contribution to the total CV response. The diffusion-controlled contribution clearly dominates over the surface-controlled contribution, occupying the majority of the enclosed CV area. The power-law analysis in Figure 8.6(b) produced a b-value of 0.6, obtained from the linear fit of log(i) versus log(scan rate), confirming a diffusion-limiting response as indicated in the plot. The peak-current analysis in Figure 8.6(c) shows a strong linear relationship between cathodic peak current and (scan rate)$^{1/2}$, yielding an R^2 value of 95%, which further validates the diffusion-controlled nature of the charge-storage process. Because the b-value of 0.6 lies closer to 0.5 than to 1.0, it supports mixed charge-storage kinetics with a dominant diffusion-controlled contribution [263].

The estimated kinetic contributions across scan rates of 5-100 mV/s are summarized in Figure 8.6(d), where the diffusion-controlled contribution (olive) consistently exceeds 90% across the entire scan-rate range, while the surface-controlled/capacitive contribution (maroon) remains below 10% throughout. A slight increase in the capacitive contribution is observed with increasing scan rate, consistent with the restricted ion accessibility to diffusion-limited electrochemical regions at shorter experimental timescales, allowing relatively faster surface-adsorption processes to contribute marginally more to the overall current response.

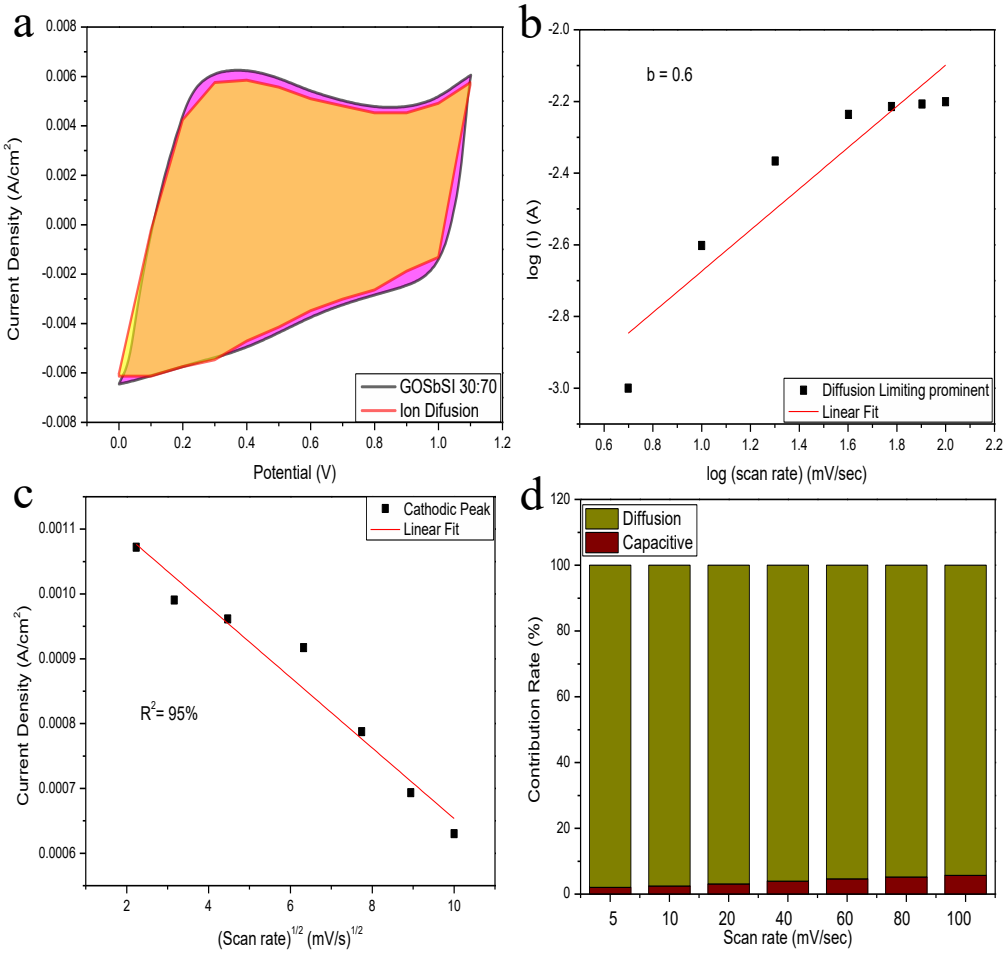


Figure 8.7(a-d): Charge-storage kinetic analysis of the GO-SbSI 30/70 coin cell: Dunn-method separation of surface-controlled and diffusion-controlled current contributions for (a) measured and calculated CV curve of GO-SbSI 70/30 coin cell, (b)log(i)-log(v) plot used to determine the b-value of 0.6 (c) peak-current dependence on $v^{1/2}$ with the corresponding linear fits, and (d) estimated surface-controlled and diffusion-controlled contributions at different scan rates.

8.2 Electrochemical testing of GSM coin cell

8.2.1 Cyclic Voltammetry

Figure 8.7 presents the CV curves of the GSM 1:80:20 coin cell at scan rates ranging from 5 to 100 mV/s, over a potential window of 0.0-1.1 V. At the lowest scan rate (5 mV/s), the CV curve displays a well-resolved, broad redox hump centered around 0.4-0.6 V on the anodic sweep, along with a corresponding cathodic feature, reflecting distinct faradaic (pseudocapacitive) behavior with sufficient time for ion diffusion into the electrode. As the scan rate increases (10-100 mV/s), the current density rises substantially, and the redox humps progressively broaden and merge into the overall CV envelope, transitioning the curve shape toward a more quasi-rectangular profile. At higher scan rates (60-100 mV/s), the curves become nearly overlapped with one another, closely overlapping near the current density limits of approximately ±0.007 A/cm², indicating that the electrode reaches its

capacitive saturation and that charge storage becomes increasingly dominated by fast surface/near-surface processes rather than slower diffusion-limited redox reactions.

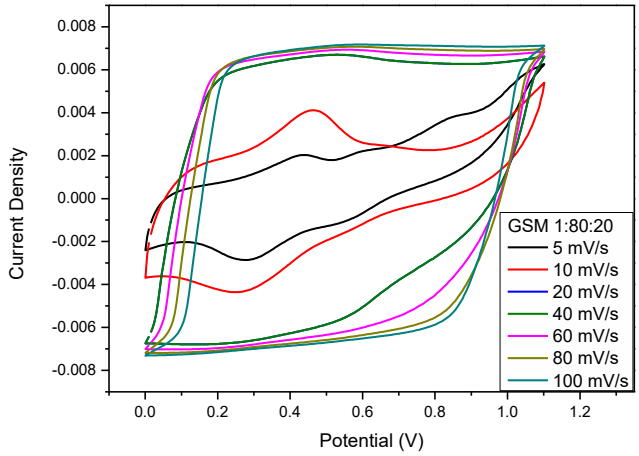


Figure 8.8: CV curves of the GSM 1:80:20 coin cell recorded at different scan rates.

The CV-derived electrochemical parameters of the GSM 1:80:20 coin cell are summarized in Table 8.3. The specific capacitance decreased progressively from 400.00 F/g at 5 mV/s to 77.86 F/g at 100 mV/s. The corresponding energy density decreased from 55.56 to 10.81 Wh/kg. At 100 mV/s, the cell retained approximately 19.5% of its initial CV-derived capacitance, indicating limited capacitance retention over the investigated scan-rate range.

Table 8-3: Scan rate, electrode mass, integrated CV area, specific capacitance, energy density, and power density of the GSM 1:80:20 coin cell.

Material	Scan Rate (mV/s)	Mass (g)	Area under CV curve (A·V)	Specific Capacitance (F/g)	Energy Density (Wh/kg)	Power Density (W/kg)
GSM 1:80:20	5	0.0014	0.0028	400	55.56	1000
	10	0.0014	0.0044	314.29	43.65	1571.43
	20	0.0014	0.0066	235.71	32.74	2357.14
	40	0.0014	0.0102	182.14	25.3	3642.86
	60	0.0014	0.011	130.95	18.19	3928.57
	80	0.0014	0.0109	87.5	12.15	3500
	100	0.0014	0.0028	77.86	10.81	3892.86

8.2.2 GCD testing

The GCD curves of the GSM 1:80:20 coin cell were recorded at different current densities (1, 2, 5, 10, 15, 20, and 25 A/g) within a potential window of 0 to 1.1 V, as shown in the figure. At the lowest current density (1 A/g), the electrode exhibits the longest charge-discharge duration

(approximately 1050 seconds), with a distinctly non-linear, S-shaped charging profile and a plateau-like region near 0.8-1.1 V, indicating a strong pseudocapacitive/battery-type contribution to the overall charge storage mechanism rather than pure double-layer capacitance. As the current density increases from 2 to 25 A/g, the charge-discharge time decreases gradually, and the curve shapes become more asymmetric and quasi-triangular, though slight deviations from linearity and small voltage plateaus persist across the curves, further supporting the presence of faradaic redox reactions superimposed on the capacitive behavior. Similar non-linear GCD profiles with plateau-like regions have been reported for battery-type hybrid supercapacitors [264].

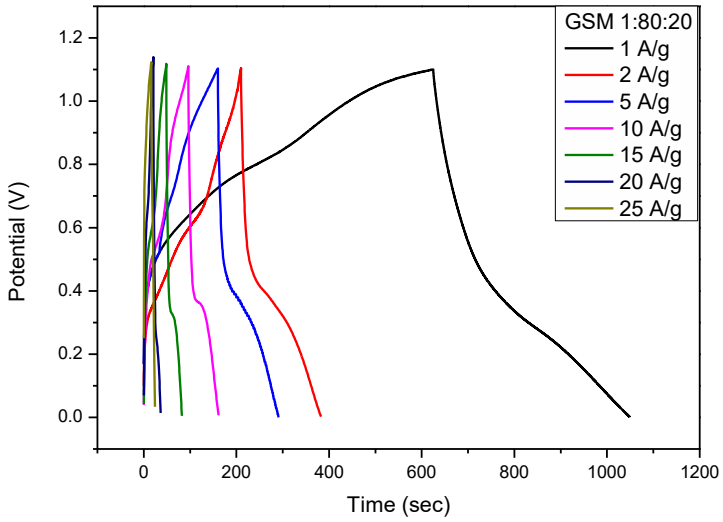


Figure 8.9: GCD curves of the GSM 1:80:20 coin cell recorded at applied current densities ranging from 1 to 25 A/g.

The table presents the CS, ED and PD values of the GSM (1:80:20) electrode calculated from the GCD curves at various current densities ranging from 1 to 25 A/g, within a voltage window of 0-1.1 V. a simple monotonic decline, the specific capacitance exhibits a non-linear trend with increasing current density; increasing from 49.6 Wh/kg at 1 A/g to a peak of 89.29 Wh/kg at 10 A/g, then decreasing to 66.96, 59.52, and 52.08 Wh/kg at 15, 20, and 25 A/g, respectively, since energy density is directly proportional to capacitance. In contrast, typically power density increases consistently and substantially across the entire current density range, from 357.14 W/kg at 1 A/g to a maximum of 8928.57 W/kg at 25 A/g, reflecting the expected inverse relationship between power density and discharge time.

Table 8-4: Current density, discharge time, specific capacitance, energy density, and power density of the GSM 1:80:20 coin cell calculated from GCD measurements.

Material	Current Density (A/g)	Discharge Tiem (s)	Specific Capacitance (F/g)	Energy Density (Wh/kg)	Power Density (W/kg)
GSM 1:80:20	1	500	357.14	49.6	357.14
	2	200	285.71	39.68	714.29
	5	125	446.43	62	1785.71
	10	90	642.86	89.29	3571.43
	15	45	482.14	66.96	5357.14
	20	30	428.57	59.52	7142.86
	25	21	375.0	52.08	8928.57

Figure 8.9 presents the coulombic efficiency of the GSM 1:80:20 coin cell as a function of cyclic number evaluated over 3000 charge-discharge cycles. The coulombic efficiency remains remarkably stable throughout cycling, starting at approximately 91% and fluctuating only slightly between approximately 89% and 91% up to 2500 cycles. At 3000 cycles, a decline is observed to around 84%. This overall stability, with a small drop toward the end of cycling, indicates good reversibility of the charge-discharge process and confirms the electrochemical stability of the GSM 1:80:20 coin cell over extended cycling.

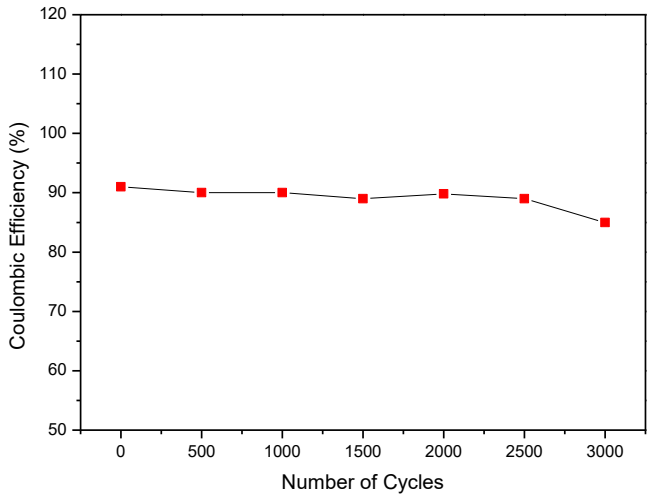


Figure 8.10: Coulombic efficiency of the GSM 1:80:20 coin cell over 3000 charge-discharge cycles.

8.2.3 Electrochemical Impedance Spectroscopy

Figure 8.11 presents the Nyquist plot of the GSM (1:80:20) electrode, showing the imaginary impedance (Z″) as a function of the real impedance (Z′), over a comparable range of approximately 0 to 100 ohms. The plot exhibits a nearly linear trace with a steep slope significantly greater than 45°, extending upward through the mid- and low-frequency regions without any clearly resolved semicircle

in the high-frequency range [265]. The absence of a high-frequency semicircular arc indicates minimal charge-transfer resistance and excellent electrical conductivity within the GSM 1:80:20 composite matrix. Furthermore, the steeply rising, nearly vertical linear trend in the low-frequency region demonstrates dominant capacitive behavior with rapid, unhindered ion transport at the electrode-electrolyte interface.

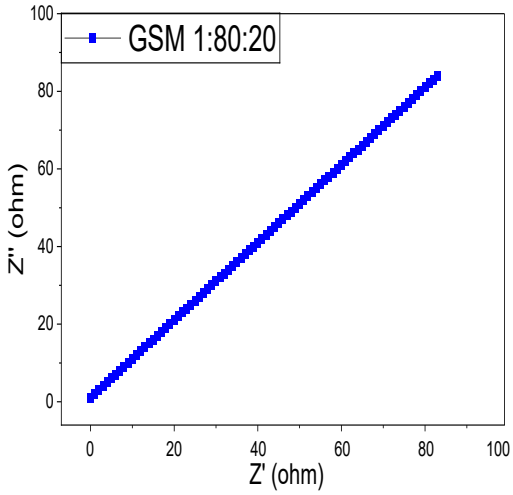


Figure 8.11(a,b): Nyquist plots Z'' versus Z' of (a) the GO-SbSI 30/70 coin cell and (b) the GSM 1:80:20 coin cell.

8.2.4 Charge-storage kinetics

Figure 8.12 presents the estimated surface-controlled (capacitive) and diffusion-controlled (measured) current contributions of the GSM 1:80:20 coin cell using the power-law and Dunn methods. Figure 8.12a shows the separated CV response at 5 mV/s, where the orange shaded region represents the diffusion-controlled (ion-diffusion) contribution and the green shaded region represents the surface-controlled (capacitive) contribution to the total CV envelope; the diffusion-controlled area visibly dominates over the capacitive contribution. The power-law analysis in Figure 8.12b yields a b-value of 0.49, obtained from the linear fit of log(i) versus log(v), indicating a predominantly diffusion-controlled charge-storage response, since the b-value lies very close to 0.5 [263]. The peak-current analysis in Figure 8.12c shows a linear relationship between cathodic peak current and v1/2, with an R2 value of 79%, further supporting the diffusion-limited nature of the process.

The estimated kinetic contributions across scan rates of 5-100 mV/s are summarized in Figure 8.12d. At low scan rates (5-10 mV/s), the diffusion-controlled contribution (orange) dominates strongly, accounting for approximately 85-90% of the total current, while the capacitive contribution (green) is minimal (around 10-15%). As the scan rate increases, the capacitive contribution progressively increases, reaching approximately 45% at 100 mV/s, while the diffusion-controlled

contribution correspondingly decreases to around 55%. This clear scan-rate-dependent shift toward surface-controlled behavior at higher scan rates is consistent with the restricted ion diffusion into less accessible electrochemical regions during shorter experimental timescales, allowing faster surface-adsorption processes to increasingly dominate the charge-storage mechanism.

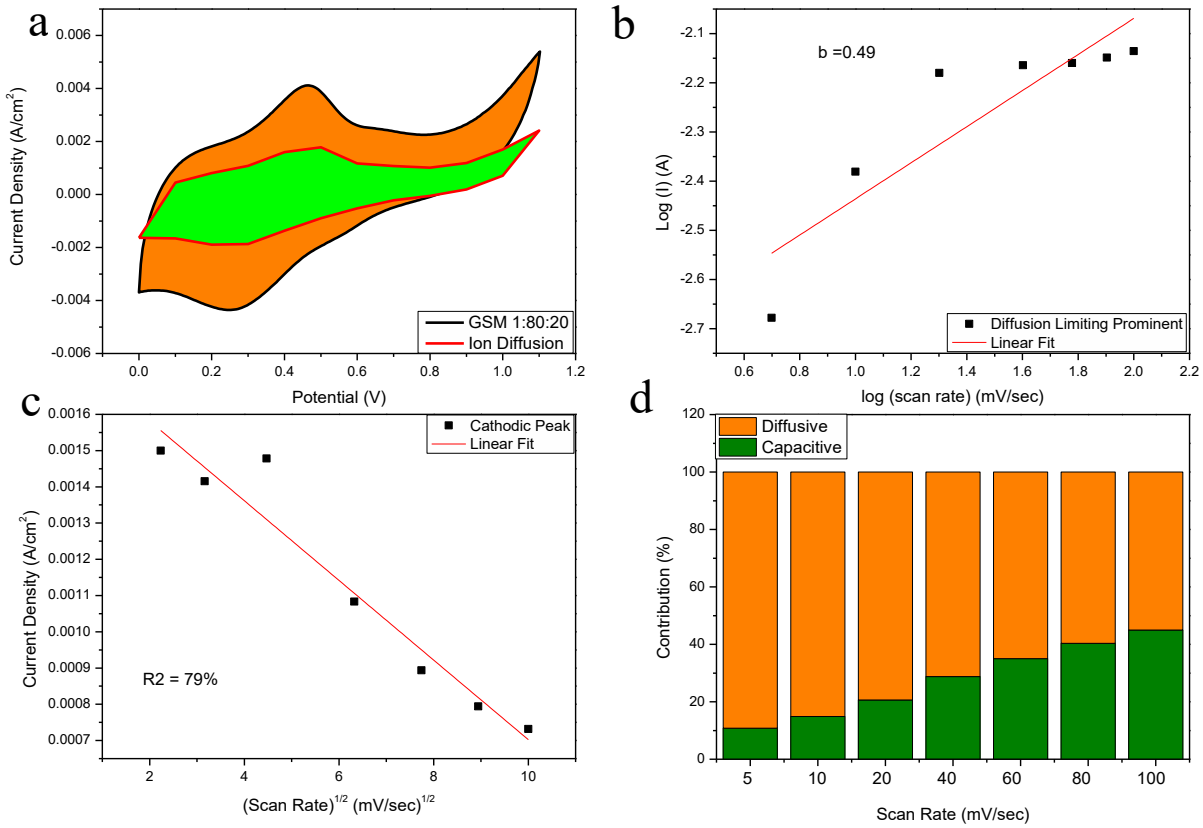


Figure 8.12(a-d). Charge-storage kinetic analysis of the GSM 1:80:20 coin cell: (a) estimated surface-controlled and diffusion-controlled current contributions at a selected scan rate; (b) log (i)-log(v) plot used to determine b-value of 0.49; (c) cathodic peak-current dependence on $v^{1/2}$ with the corresponding linear fit; and (d) estimated surface-controlled and diffusion-controlled contributions at different scan rates.

Chapter 9

CONCLUSION

The incorporation of SbSI into GO was investigated as an approach to modify the structural, electrical, and electrochemical properties of the resulting composite materials. MnO_2 was subsequently introduced to form a ternary GO-SbSI-MnO_2 system and further modify the charge-storage characteristics. Accordingly, the main purpose of this thesis was to prepare and investigate GO-SbSI binary and GO-SbSI-MnO2 ternary nanomaterials for their possible application as supercapacitor electrodes. Instead of examining a single formulation, individual samples were prepared at selected GO:SbSI and GO:SbSI:MnO2 ratios so that their measured structural, morphological, optical, permittivity, and electrochemical properties could be compared. The results therefore show clear differences among the investigated composites; however, because only one sample was prepared for each composition, these differences cannot be considered statistically established concentration-dependent trends. The selected binary and ternary materials were also examined in two-electrode coin-cell configurations to determine whether the electrochemical response obtained during electrode testing could also be observed in an assembled device.

All three starting components used in the composite systems were prepared within this work. GO was synthesized from graphite by chemical oxidation, MnO_2 nanostructures were prepared by the hydrothermal method, and SbSI nanowires were synthesized by a sonochemical route. In addition, the preparation procedure used to combine these materials into GO-SbSI binary and GO-SbSI-MnO_2 ternary composites was developed during the experimental work. The final procedure was established after systematic adjustment of the reaction conditions and was then used to prepare the complete composition series. This synthesis stage was therefore an important part of the thesis, because it provided both the individual nanomaterials and a defined route for preparing the investigated composite systems.

The XRD results distinguished the two composite systems clearly. In the GO-SbSI series, the diffraction patterns were dominated by reflections assigned to orthorhombic SbSI, while the GO-related contribution was comparatively weak and partly overlapped with the SbSI reflections in the carbon-related region. In the GSM ternary series, reflections assigned to both SbSI and alpha-MnO_2 were observed, together with a weak contribution from GO. The positions, intensities, and widths of the measured reflections differed among the prepared samples, but the changes were not monotonic across the full series. The values calculated by the Scherrer equation represent apparent coherent diffraction-domain sizes rather than the physical length of the nanowires. For the selected GSM reflection, the endpoint values changed from approximately 18.6 nm for GSM 1:20:80 to 15.6 nm for GSM 1:80:20, corresponding to a difference of about 16.1%. Because this reflection contains

overlapping contributions from SbSI and α-MnO_2, these values cannot be assigned exclusively to one phase.

FTIR analysis identified the oxygen-containing functional groups of GO and the characteristic vibration regions associated with SbSI and MnO_2. Differences in band position and intensity were observed among the investigated samples, but FTIR alone was not used as proof of composite formation. XPS analysis of selected endpoint composites provided more direct information about surface elemental composition and chemical states. The GO-SbSI samples contained C, O, Sb, S, and I signals, whereas the selected GSM samples additionally contained Mn. The stronger Sb- and I-related signals in the SbSI-rich materials and the stronger Mn- and O-related signals in the MnO_2-rich material were consistent with the prepared formulations. Taken together with XRD, EDX, and microscopy, these measurements support the coexistence of the intended components in the binary and ternary materials without requiring unmeasured reaction mechanisms to be assumed.

The microscopy results showed distinct structural features in the prepared materials. GO exhibited sheet-like structures, whereas SbSI showed elongated one-dimensional nanowires. The GO-SbSI samples contained both GO-related sheet features and SbSI-related elongated structures, with the relative prominence of these features differing among the investigated ratios. The GSM samples also showed mixed nanowire and rod-like morphologies associated with the SbSI- and MnO_2-containing system. FESEM, TEM, and EDX confirmed the presence of the expected elements within the examined regions and showed clear morphological differences between the selected composites. These observations describe the sampled areas of the materials; they do not establish perfectly uniform distribution throughout the complete electrode or a simple monotonic morphological trend with composition.

The optical and electrical measurements also differed among the prepared composites, although no simple relationship with composition was established across all samples. The impedance, ε′, ε″, and frequency-dependent conductivity likewise varied among GO, SbSI, and the binary and ternary materials. The largest differences were generally observed in the lower-frequency region, while the responses became comparatively more stable as frequency increased. These results show measurable differences among the investigated materials under the applied conditions, but the data do not support a single monotonic dielectric or optical trend across the complete composite series.

The electrochemical measurements provided the clearest distinction among the GO-SbSI binary electrodes. At 5 mV/s, the CV-derived specific capacitance was 57.60 F/g for GO and 52.82 F/g for SbSI. The GO-SbSI composites produced 62.44 F/g for 70/30, 109.09 F/g for 60/40, 83.21 F/g for 50/50, 136.40 F/g for 40/60 and 320.00 F/g for 30/70. The values therefore did not follow a continuous increase with the amount of either individual component. GO-SbSI 30/70 produced the highest CV-derived capacitance within the binary series and remained the highest-performing binary composite over the investigated scan-rate range, reaching 43.33 F/g at 100 mV/s. The GCD results showed a different ranking, demonstrating that the composition giving the highest CV-derived response was not

necessarily the composition giving the highest GCD-derived energy response under every applied condition. This difference is important because it shows that the electrochemical performance of the binary materials depended on the measurement mode as well as on the selected GO:SbSI ratio.

GO-SbSI 30/70 was subsequently examined in an assembled two-electrode coin cell. The CV-derived specific capacitance decreased from 225.00 F/g at 5 mV/s to 66.25 F/g at 100 mV/s, corresponding to retention of approximately 29.4% over the investigated scan-rate range. In the GCD measurements, the cell delivered 256.25 F/g at 1 A/g and 162.50 F/g at 20 A/g, corresponding to approximately 63.4% retention between these current densities. During 3000 charge-discharge cycles, the measured coulombic efficiency decreased from approximately 89% to about 84-85%. The power-law analysis gave a b-value of approximately 0.60, indicating that diffusion-related processes made a substantial contribution to the measured response. These device-level results confirm that the selected binary material remained electrochemically active after assembly into a complete cell, while its response decreased as the scan rate or applied current was increased.

The GSM ternary electrodes showed a wider range of electrochemical responses than the binary materials. At 5 mV/s, the CV-derived specific capacitance values were 123.50 F/g for GSM 1:20:80, 270.00 F/g for GSM 1:30:70, 478.95 F/g for GSM 1:40:60, 245.45 F/g for GSM 1:50:50, 210.00 F/g for GSM 1:60:40, 900.00 F/g for GSM 1:70:30 and 1200.00 F/g for GSM 1:80:20. The sequence was therefore non-monotonic, with a decrease at the intermediate composites followed by a substantial increase for the two SbSI-rich samples. GSM 1:80:20 remained the highest-capacitance ternary electrode at the higher scan rates and retained 194.67 F/g at 100 mV/s. Its GCD curves also showed the longest discharge duration within the ternary series at low current density, and the electrode retained approximately 80% of its initial capacitance after 3000 GCD cycles. The kinetic analysis produced a b-value of approximately 0.70, which is consistent with mixed surface-controlled and diffusion-influenced charge storage. In the Nyquist comparison, GSM 1:80:20 occupied a comparatively low-impedance region and showed a smaller high-to-mid-frequency arc than GSM 1:40:60 and GSM 1:60:40; however, exact series and charge-transfer resistance values were not assigned from visual inspection alone.

The GSM 1:80:20 composite was also evaluated in a two-electrode coin-cell configuration. Its CV-derived specific capacitance decreased from 400.00 F/g at 5 mV/s to 77.86 F/g at 100 mV/s. The practical GCD measurements showed a current-density-dependent and non-monotonic response: the calculated specific capacitance was 357.14 F/g at 1 A/g, 285.71 F/g at 2 A/g, 446.43 F/g at 5 A/g, 642.86 F/g at 10 A/g, 482.14 F/g at 15 A/g, 428.57 F/g at 20 A/g and 375.00 F/g at 25 A/g. These values are reported as the measured response of the assembled device under the applied conditions. The coulombic efficiency remained at approximately 89-91% during most of the 3000-cycle test and decreased to about 86% at the end. The power-law analysis gave a b-value of approximately 0.49, indicating a predominantly diffusion-controlled contribution in the assembled ternary device. The Nyquist plots of both coin cells showed strongly inclined responses without a clearly resolved high-

frequency semicircle, supporting a substantial diffusion-related impedance contribution in the measured frequency range.

Direct comparison of the two coin cells shows that the ternary GSM 1:80:20 device produced the larger CV-derived capacitance at 5 mV/s, 400.00 F/g compared with 225.00 F/g for GO-SbSI 30/70. At 1 A/g, the GCD-derived values were 357.14 F/g for GSM 1:80:20 and 256.25 F/g for GO-SbSI 30/70. The two devices also showed comparable coulombic efficiencies after prolonged cycling, with final values of about 86% for GSM 1:80:20 and 84-85% for GO-SbSI 30/70. The comparison therefore indicates that introducing the MnO_2-containing ternary configuration changed the device response and increased the measured capacitance for the selected pair of composites, but the present data do not establish that MnO_2 alone was responsible for the improvement because the binary and ternary systems differ in more than one compositional variable.

The electrochemical performance obtained in this thesis can also be placed in the context of the representative materials summarized in Chapter 1. Table 1.2 lists reported specific capacitances of approximately 259 F/g for SbSI, 211 F/g for GO-MnO_2, about 617 F/g for a MOF/GO composite, 860 F/g for Ni/Co-MOF-rGO and 1017 F/g for Ni-MOF/GO, while a higher value of 2221.2 F/g was reported for Ce-MOF/GO. Against this background, the 1200 F/g obtained for GSM 1:80:20 at 5 mV/s is higher than several representative carbon-, metal-oxide-, and MOF-based systems included in the literature review and falls within the range reported for advanced composite electrodes. This comparison is indicative rather than absolute because the literature values were obtained using different electrolytes, potential windows, electrode masses, test configurations, and calculation methods. Nevertheless, it shows that the measured performance of the highest-performing investigated ternary composition is not outside the range of established high-capacitance electrode materials.

Overall, the thesis achieved its main objective of preparing GO-SbSI and GO-SbSI-MnO_2 nanomaterials, characterizing their structural and physicochemical properties, comparing their electrochemical responses at selected composites, and evaluating the most suitable materials in complete two-electrode cells. GO-SbSI 30/70 provided the highest CV-derived specific capacitance within the binary series, whereas GSM 1:80:20 provided the highest overall capacitance within the ternary series and maintained measurable performance after device assembly. The substantial differences observed among neighboring GSM composites indicate that the relative proportions of SbSI and MnO_2 are an important experimental variable for the measured charge-storage response, even though the present single-sample series does not establish a statistically defined concentration law. The results therefore identify the SbSI-rich GSM region as a promising direction for further composition optimization. A finer adjustment of the GO:SbSI:MnO_2 ratio around this region may allow the charge-storage performance and cycling behavior to be balanced more effectively and could produce composites that are competitive with established supercapacitor electrode materials.

References

1. Bae, J., et al., *Fiber supercapacitors made of nanowire-fiber hybrid structures for wearable/flexible energy storage.* Angewandte Chemie International Edition, 2011. **50**(7): p. 1683-1687.
2. Castiglia, V., et al., *Modeling, simulation, and characterization of a supercapacitor in automotive applications.* IEEE Transactions on Industry Applications, 2022. **58**(2): p. 2421-2429.
3. Kim, J., et al., *Design and optimization of supercapacitor hybrid architecture for power supply-connected batteries lifetime enhancement.* Electronics, 2019. **8**(1): p. 41.
4. Kim, J., et al. *Aging mitigation of power supply-connected batteries*. in *Proceedings of the 2014 international symposium on Low power electronics and design*. 2014.
5. Wang, S., T. Wei, and Z. Qi. *Supercapacitor energy storage technology and its application in renewable energy power generation system*. in *Proceedings of ISES World Congress 2007 (Vol. I–Vol. V) Solar Energy and Human Settlement*. 2008. Springer.
6. Qu, L. and W. Qiao, *Constant power control of DFIG wind turbines with supercapacitor energy storage.* IEEE Transactions on Industry Applications, 2010. **47**(1): p. 359-367.
7. Huenges, E. and P. Ledru, *Geothermal energy systems: exploration, development, and utilization*. 2011: John Wiley & Sons.
8. Khan, M.A.H., et al., *Investigation of biofuel as a potential renewable energy source.* Atmosphere, 2021. **12**(10): p. 1289.
9. Wagner, H.-J. and J. Mathur, *Introduction to hydro energy systems: basics, technology and operation*. 2011: Springer Science & Business Media.
10. Panchenko, V., et al., *Photovoltaic solar modules of different types and designs for energy supply*, in *Research Anthology on Clean Energy Management and Solutions*. 2021, IGI Global. p. 731-752.
11. Rahman, A., et al., *Recent progress in electrical generators for oceanic wave energy conversion.* IEEE Access, 2020. **8**: p. 138595-138615.
12. Haas, O. and E.J. Cairns, *Electrochemical energy storage.* Annual Reports Section" C"(Physical Chemistry), 1999. **95**: p. 163-198.
13. Revankar, S.T., *Chemical energy storage*, in *Storage and Hybridization of Nuclear Energy*. 2019, Elsevier. p. 177-227.
14. Alami, A.H., *Mechanical energy storage for renewable and sustainable energy resources*. 2020: Springer.
15. Komarnicki, P., P. Lombardi, and Z. Styczynski, *Electric energy storage system*, in *Electric Energy Storage Systems: Flexibility Options for Smart Grids*. 2017, Springer. p. 37-95.
16. Christen, T. and M.W. Carlen, *Theory of Ragone plots.* Journal of power sources, 2000. **91**(2): p. 210-216.
17. Saxena, S., G. Sanchez, and M. Pecht, *Batteries in portable electronic devices: A user's perspective.* IEEE Industrial Electronics Magazine, 2017. **11**(2): p. 35-44.
18. Rawat, S., et al., *Advancements and current developments in integrated system architectures of Lithium-Ion batteries for electric mobility.* World Electric Vehicle Journal, 2024. **15**(9): p. 394.
19. Burke, A., Z. Liu, and H. Zhao. *Present and future applications of supercapacitors in electric and hybrid vehicles*. in *2014 IEEE international electric vehicle conference (IEVC)*. 2014. IEEE.
20. Abraham, K., *Prospects and limits of energy storage in batteries.* The journal of physical chemistry letters, 2015. **6**(5): p. 830-844.
21. Turcheniuk, K., et al., *Battery materials for low-cost electric transportation.* Materials Today, 2021. **42**: p. 57-72.
22. Emadi, A. and S. Williamson. *Fuel cell vehicles: opportunities and challenges*. in *IEEE Power Engineering Society General Meeting, 2004.* 2004. IEEE.
23. Nordin, N. *Limitations of commercializing fuel cell technologies*. in *AIP Conference Proceedings*. 2010. American Institute of Physics.

24. Akinwolemiwa, B., C. Peng, and G.Z. Chen, *Redox electrolytes in supercapacitors.* Journal of the electrochemical society, 2015. **162**(5): p. A5054-A5059.
25. Satpathy, S., et al. *New characterization of electrode of supercapacitor with its application as a backup power supply*. in *Proceedings of the International Conference on Computational Intelligence and Sustainable Technologies: ICoCIST 2021*. 2022. Springer.
26. Phoosomma, P., N. Kasayapanand, and N. Mungkung, *Combination of supercapacitor and AC power source in storing and supplying energy for computer backup power.* Journal of Electrical Engineering & Technology, 2019. **14**(2): p. 993-1000.
27. Guo, W., et al., *Toward commercial-level mass-loading electrodes for supercapacitors: opportunities, challenges and perspectives.* Energy & Environmental Science, 2021. **14**(2): p. 576-601.
28. Partridge, J. and D.I. Abouelamaimen, *The role of supercapacitors in regenerative braking systems.* Energies, 2019. **12**(14): p. 2683.
29. Teasdale, A., et al., *A study on an energy-regenerative braking model using supercapacitors and DC motors.* World Electric Vehicle Journal, 2024. **15**(7): p. 326.
30. Wang, R., M. Yao, and Z. Niu, *Smart supercapacitors from materials to devices.* InfoMat, 2020. **2**(1): p. 113-125.
31. Huang, S., et al., *Challenges and opportunities for supercapacitors.* APL materials, 2019. **7**(10).
32. Mwambeleko, J.J. and T. Kulworawanichpong, *Supercapacitor and accelerating contact lines hybrid tram system.* Journal of Energy Storage, 2021. **44**: p. 103277.
33. Elsevier, *https://www.scopus.com/pages/search/publications?searchId=fe6d1069-d0a5-4cc6-810a-d42701f7121d*. 2025.
34. Becker, H.I., *Low voltage electrolytic capacitor*. 1957, Google Patents.
35. Rightmire, R.A., *Electrical energy storage apparatus*. 1966, Google Patents.
36. Boos, D.L. and J.E. Metcalfe, *Electrolytic capacitor employing paste electrodes*. 1972, Google Patents.
37. MURPHY, T. *Proceedings of The Fourth International Seminar on Double Layer Capacitor and Similar Energy Storage Devies*. in *Florida Educational Seminars, December, 1994.*
38. Wu, Z.S., et al., *Graphene-based in-plane micro-supercapacitors with high power and energy densities.* Nature communications, 2013. **4**(1): p. 2487.
39. Wang, F., et al., *Electrode materials for aqueous asymmetric supercapacitors.* Rsc Advances, 2013. **3**(32): p. 13059-13084.
40. Endo, M., et al., *High power electric double layer capacitor (EDLC's); from operating principle to pore size control in advanced activated carbons.* Carbon letters, 2001. **1**(3): p. 117-128.
41. Yadav, N. and S. Hashmi, *Hierarchical porous carbon derived from eucalyptus-bark as a sustainable electrode for high-performance solid-state supercapacitors.* Sustainable Energy & Fuels, 2020. **4**(4): p. 1730-1746.
42. Zhou, L., et al., *Metal oxides in supercapacitors*, in *Metal Oxides in Energy Technologies*. 2018, Elsevier. p. 169-203.
43. Han, Y. and L. Dai, *Conducting polymers for flexible supercapacitors.* Macromolecular chemistry and physics, 2019. **220**(3): p. 1800355.
44. Snook, G.A., P. Kao, and A.S. Best, *Conducting-polymer-based supercapacitor devices and electrodes.* Journal of power sources, 2011. **196**(1): p. 1-12.
45. Gautam, S., et al., *MOF/graphene oxide based composites in smart supercapacitors: a comprehensive review on the electrochemical evaluation and material development for advanced energy storage devices.* RSC advances, 2024. **14**(20): p. 14311-14339.
46. Wu, S., et al., *Making supercapacitors higher in energy density: wisdoms on electrolytes and device architecture.* The Chemical Record, 2026. **26**(6): p. e70126.
47. Pathak, M., et al., *High energy density supercapacitors: an overview of efficient electrode materials, electrolytes, design, and fabrication.* The Chemical Record, 2024. **24**(1): p. e202300236.
48. Okonye, L.U. and J. Ren, *A comprehensive review of PETW recycling for supercapacitor applications.* Heliyon, 2024. **10**(15).

49. Liu, N., J. Shen, and D. Liu, *Activated high specific surface area carbon aerogels for EDLCs.* Microporous and mesoporous materials, 2013. **167**: p. 176-181.
50. Wen, S., et al., *EDLC characteristics with high specific capacitance of the CNT electrodes grown on nanoporous alumina templates.* Current Applied Physics, 2006. **6**(6): p. 1012-1015.
51. Mitani, S., et al., *Contrast structure and EDLC performances of activated spherical carbons with medium and large surface areas.* Electrochimica Acta, 2006. **51**(25): p. 5487-5493.
52. Ullah, K., et al., *Preparation of highly expanded graphene with large surface area and its additional conductive effect for EDLC performance.* Journal of Materials Science: Materials in Electronics, 2015. **26**(9): p. 6945-6953.
53. Ivanov, V.D., *The Helmholtz model.* Journal of Solid State Electrochemistry, 2024. **28**(8): p. 2487-2493.
54. Helmholtz, H.v., *Ueber einige Gesetze der Vertheilung elektrischer Ströme in körperlichen Leitern, mit Anwendung auf die thierisch-elektrischen Versuche (Schluss.).* Annalen der Physik, 1853. **165**(7): p. 353-377.
55. Doblhoff-Dier, K. and M.T. Koper, *Modeling the Gouy–Chapman diffuse capacitance with attractive ion–surface interaction.* The Journal of Physical Chemistry C, 2021. **125**(30): p. 16664-16673.
56. Oldham, K.B., *A Gouy–Chapman–Stern model of the double layer at a (metal)/(ionic liquid) interface.* Journal of Electroanalytical Chemistry, 2008. **613**(2): p. 131-138.
57. Stern, O., *Zur theorie der elektrolytischen doppelschicht.* Zeitschrift für Elektrochemie und angewandte physikalische Chemie, 1924. **30**(21-22): p. 508-516.
58. Herrero, E., L.J. Buller, and H.D. Abruña, *Underpotential deposition at single crystal surfaces of Au, Pt, Ag and other materials.* Chemical Reviews, 2001. **101**(7): p. 1897-1930.
59. Sarno, M., *Nanotechnology in energy storage: the supercapacitors*, in *Studies in surface science and catalysis*. 2020, Elsevier. p. 431-458.
60. Feiner, A.-S. and A. McEvoy, *The nernst equation.* Journal of chemical education, 1994. **71**(6): p. 493.
61. Singh, N., et al., *A comprehensive review on supercapacitors: Basics to recent advancements.* Journal of Energy Storage, 2025. **121**: p. 116498.
62. Qu, Q., et al., *Electrochemical performance of MnO2 nanorods in neutral aqueous electrolytes as a cathode for asymmetric supercapacitors.* The Journal of Physical Chemistry C, 2009. **113**(31): p. 14020-14027.
63. Zhang, J. and X. Zhao, *On the configuration of supercapacitors for maximizing electrochemical performance.* ChemSusChem, 2012. **5**(5): p. 818-841.
64. Forouzandeh, P., V. Kumaravel, and S.C. Pillai, *Electrode materials for supercapacitors: a review of recent advances.* Catalysts, 2020. **10**(9): p. 969.
65. Hao, L., X. Li, and L. Zhi, *Carbonaceous electrode materials for supercapacitors*. 2013, Wiley Online Library.
66. Mendoza, R., J. Oliva, and V. Rodriguez-Gonzalez, *Effect of the micro-, meso-and macropores on the electrochemical performance of supercapacitors: A review.* International Journal of Energy Research, 2022. **46**(6): p. 6989-7020.
67. Reddy, R.N. and R.G. Reddy, *Sol–gel MnO2 as an electrode material for electrochemical capacitors.* Journal of Power Sources, 2003. **124**(1): p. 330-337.
68. Subramanian, V., et al., *Mesoporous anhydrous RuO2 as a supercapacitor electrode material.* Solid State Ionics, 2004. **175**(1-4): p. 511-515.
69. Kulal, P.M., et al., *Chemical synthesis of Fe2O3 thin films for supercapacitor application.* Journal of Alloys and Compounds, 2011. **509**(5): p. 2567-2571.
70. Acerce, M., D. Voiry, and M. Chhowalla, *Metallic 1T phase MoS2 nanosheets as supercapacitor electrode materials.* Nature nanotechnology, 2015. **10**(4): p. 313-318.
71. Eftekhari, A., L. Li, and Y. Yang, *Polyaniline supercapacitors.* Journal of power sources, 2017. **347**: p. 86-107.
72. Huang, Y., et al., *Nanostructured polypyrrole as a flexible electrode material of supercapacitor.* Nano Energy, 2016. **22**: p. 422-438.
73. Laforgue, A., et al., *Polythiophene-based supercapacitors.* Journal of power sources, 1999. **80**(1-2): p. 142-148.

74. Liu, Q., et al., *Ultrathin MoS2 nanosheets hybridizing with reduced graphene oxide for high-performance pseudocapacitors.* FlatChem, 2021. **26**: p. 100212.
75. Tamilselvi, R., et al., *Graphene oxide–Based supercapacitors from agricultural wastes: A step to mass production of highly efficient electrodes for electrical transportation systems.* Renewable Energy, 2020. **151**: p. 731-739.
76. Siyahjani, S., et al., *Enhanced capacitive behaviour of graphene based electrochemical double layer capacitors by etheric substitution on ionic liquids.* Journal of Power Sources, 2020. **467**: p. 228353.
77. Macherla, N., et al., *Heat assisted facile synthesis of nanostructured polyaniline/reduced crumbled graphene oxide as a high-performance flexible electrode material for supercapacitors.* Colloids and Surfaces A: Physicochemical and Engineering Aspects, 2021. **612**: p. 125982.
78. Wang, J., et al., *To increase electrochemical performance of electrode material by attaching activated carbon particles on reduced graphene oxide sheets for supercapacitor.* Journal of Power Sources, 2020. **450**: p. 227611.
79. Cao, X., et al., *Reduced graphene oxide-wrapped MoO3 composites prepared by using metal–organic frameworks as precursor for all-solid-state flexible supercapacitors.* Advanced Materials, 2015. **27**(32): p. 4695-4701.
80. Xin, L., et al., *Hierarchical metal-organic framework derived nitrogen-doped porous carbon/graphene composite for high performance supercapacitors.* Electrochimica Acta, 2017. **248**: p. 215-224.
81. Xu, X., et al., *Facile fabrication of three-dimensional graphene and metal–organic framework composites and their derivatives for flexible all-solid-state supercapacitors.* Chemistry of Materials, 2017. **29**(14): p. 6058-6065.
82. Rahmanifar, M.S., et al., *A dual Ni/Co-MOF-reduced graphene oxide nanocomposite as a high performance supercapacitor electrode material.* Electrochimica Acta, 2018. **275**: p. 76-86.
83. **Ali, M.D., et al., *Exploration of sp-sp2 carbon networks: advances in graphyne research and its role in next-generation technologies.* International Journal of Molecular Sciences, 2025. 26(11): p. 5140.**
84. Manoharan, S., et al., *Ultrasound irradiation mediated preparation of antimony sulfoiodide (SbSI) nanorods as a high-capacity electrode for electrochemical supercapacitors.* Materials Chemistry Frontiers, 2021. **5**(5): p. 2303-2312.
85. Chen, S., et al., *Graphene oxide− MnO2 nanocomposites for supercapacitors.* ACS nano, 2010. **4**(5): p. 2822-2830.
86. Justinabraham, R., et al., *Synthesis and characterization of SbSI modified g-C3N4 composite for photocatalytic and energy storage applications.* Journal of Alloys and Compounds, 2023. **935**: p. 168115.
87. Rawool, C.R., S.P. Karna, and A.K. Srivastava, *Enhancing the supercapacitive performance of Nickel based metal organic framework-carbon nanofibers composite by changing the ligands.* Electrochimica Acta, 2019. **294**: p. 345-356.
88. Banerjee, P.C., et al., *Electrochemical capacitance of Ni-doped metal organic framework and reduced graphene oxide composites: more than the sum of its parts.* ACS applied materials & interfaces, 2015. **7**(6): p. 3655-3664.
89. Azadfalah, M., A. Sedghi, and H. Hosseini, *Synthesis of Nano-Flower Metal–Organic Framework/Graphene Composites As a High-Performance Electrode Material for Supercapacitors: Azadfalah, Sedghi, and Hosseini.* Journal of Electronic Materials, 2019. **48**(11): p. 7011-7024.
90. Azadfalah, M., A. Sedghi, and H. Hosseini, *Synergistic effect of Ni-based metal organic framework with graphene for enhanced electrochemical performance of supercapacitors.* Journal of Materials Science: Materials in Electronics, 2019. **30**(13): p. 12351-12363.
91. He, F., et al., *Hydrothermal synthesis of Ni-based metal organic frameworks/graphene oxide composites as supercapacitor electrode materials.* Journal of Materials Research, 2020. **35**(11): p. 1439-1450.

92. Azadfalah, M., et al., *Cobalt based metal organic framework/graphene nanocomposite as high performance battery-type electrode materials for asymmetric supercapacitors.* Journal of Energy Storage, 2021. **33**: p. 101925.
93. Thi, Q.V., et al., *Electrochemical performance of zinc-based metal-organic framework with reduced graphene oxide nanocomposite electrodes for supercapacitors.* Synthetic Metals, 2022. **290**: p. 117155.
94. Wang, L., et al., *ZIF-8 nanocrystals derived N-doped carbon decorated graphene sheets for symmetric supercapacitors.* Electrochimica Acta, 2018. **289**: p. 494-502.
95. Ramachandran, R., et al., *Enhanced electrochemical properties of cerium metal–organic framework based composite electrodes for high-performance supercapacitor application.* RSC advances, 2018. **8**(7): p. 3462-3469.
96. Singh, M.K., et al., *A new hierarchically porous Cu-MOF composited with rGO as an efficient hybrid supercapacitor electrode material.* Journal of Energy Storage, 2021. **43**: p. 103301.
97. Choi, S., et al., *Large-scale synthesis of graphene and other 2D materials towards industrialization. Nat Commun 13: 1484*. 2022.
98. He, L., et al., *Copper metal–organic framework-derived CuOx-coated three-dimensional reduced graphene oxide and polyaniline composite: Excellent candidate free-standing electrodes for high-performance supercapacitors.* Electrochimica Acta, 2018. **275**: p. 133-144.
99. Pal, B., et al., *Electrolyte selection for supercapacitive devices: a critical review.* Nanoscale advances, 2019. **1**(10): p. 3807-3835.
100. Mendhe, A. and H. Panda, *A review on electrolytes for supercapacitor device.* Discover Materials, 2023. **3**(1): p. 29.
101. Prasad, K.R. and N. Miura, *Electrochemical synthesis and characterization of nanostructured tin oxide for electrochemical redox supercapacitors.* Electrochemistry communications, 2004. **6**(8): p. 849-852.
102. Khan, M.Z., et al., *Massive dielectric properties enhancement of MWCNTs/CoFe2O4 nanohybrid for super capacitor applications.* Journal of Magnetism and Magnetic Materials, 2017. **424**: p. 382-387.
103. Gittins, J.W., et al., *Understanding electrolyte ion size effects on the performance of conducting metal–organic framework supercapacitors.* journal of the American Chemical society, 2024. **146**(18): p. 12473-12484.
104. Bahaa, A., et al., *Ionic liquid electrolyte selection for high voltage supercapacitors in high-temperature applications.* Frontiers in Chemistry, 2024. **12**: p. 1349864.
105. Zhou, S., *How ion size influences energy storage in cylindrical nanoporous supercapacitors.* The Journal of Physical Chemistry C, 2019. **123**(49): p. 29638-29646.
106. Nguyen, H.V.T., et al., *Size effect of electrolyte ions on the electric double-layer structure and supercapacitive behavior.* ACS Applied Energy Materials, 2023. **6**(5): p. 3155-3166.
107. Kovalska, E. and C. Kocabas, *Organic electrolytes for graphene-based supercapacitor: Liquid, gel or solid.* Materials Today Communications, 2016. **7**: p. 155-160.
108. Yu, L. and G.Z. Chen, *Ionic liquid-based electrolytes for supercapacitor and supercapattery.* Frontiers in chemistry, 2019. **7**: p. 432729.
109. Pang, L. and H. Wang, *Inorganic aqueous anionic redox liquid electrolyte for supercapacitors.* Advanced Materials Technologies, 2022. **7**(4): p. 2100501.
110. Amaral, M.M., et al., *Recent advances on quasi-solid-state electrolytes for supercapacitors.* Journal of Energy Chemistry, 2022. **67**: p. 697-717.
111. Feng, G., et al., *Structure and dynamics of electrical double layers in organic electrolytes.* Physical Chemistry Chemical Physics, 2010. **12**(20): p. 5468-5479.
112. Goldfarb, D.L., M.P. Longinotti, and H.R. Corti, *Electrical conductances of tetrabutylammonium and decamethylferrocenium hexafluorophosphate in organic solvents.* Journal of solution chemistry, 2001. **30**(4): p. 307-322.
113. Rana, R., M.A. Sheikh, and D.K. Maity, *Fast lithium ion mobility in organic carbonates and acetonitrile: insights from ab initio and classical MD simulations.* Journal of Molecular Liquids, 2025. **431**: p. 127736.

114. Haskins, J.B., et al., *Computational and experimental investigation of Li-doped ionic liquid electrolytes:[pyr14][TFSI],[pyr13][FSI], and [EMIM][BF4].* The Journal of Physical Chemistry B, 2014. **118**(38): p. 11295-11309.
115. Wei, Y., et al., *A flexible, highly conductive, tough ionogel electrolyte containing LiTFSI salt and ionic liquid [EMIM][TFSI] based on PVDF-HFP for high-performance supercapacitors.* Polymer, 2023. **289**: p. 126501.
116. Dong, D., et al., *Aqueous electrolytes: from salt in water to water in salt and beyond.* Advanced Materials, 2025. **37**(46): p. 2418700.
117. Lee, H.Y. and J.B. Goodenough, *Supercapacitor behavior with KCl electrolyte.* Journal of Solid State Chemistry, 1999. **144**(1): p. 220-223.
118. Karaman, B. and A. Bozkurt, *Enhanced performance of supercapacitor based on boric acid doped PVA-H2SO4 gel polymer electrolyte system.* International Journal of Hydrogen Energy, 2018. **43**(12): p. 6229-6237.
119. Lobitz, P., et al., *Polymer solid electrolytes-PEO and alkali halides: A modified preparative technique.* Solid state ionics, 1992. **58**(1-2): p. 49-54.
120. Tatsumisago, M. and A. Hayashi, *Superionic glasses and glass–ceramics in the Li2S–P2S5 system for all-solid-state lithium secondary batteries.* Solid State Ionics, 2012. **225**: p. 342-345.
121. SUN, X.-Z., et al., *Effects of separator on the electrochemical performance of electrical double-layer capacitor and hybrid battery-supercapacitor.* Acta Physico-Chimica Sinica, 2014. **30**(3): p. 485-491.
122. Arora, P. and Z. Zhang, *Battery separators.* Chemical reviews, 2004. **104**(10): p. 4419-4462.
123. Zhu, J., et al., *Understanding glass fiber membrane used as a novel separator for lithium–sulfur batteries.* Journal of membrane science, 2016. **504**: p. 89-96.
124. Jangid, A., et al., *Separator material selection for supercapacitors*, in *Handbook of Nanocomposite Supercapacitor Materials III: Selection*. 2021, Springer. p. 201-232.
125. Zhang, X., et al., *High-performance aramid paper-based separator for supercapacitors.* ACS Applied Polymer Materials, 2024. **6**(21): p. 13319-13328.
126. Jabbarnia, A. and R. Asmatulu, *Synthesis and characterization of PVdF/PVP-based electrospun membranes as separators for supercapacitor applications.* Journal of Material Science and Technology Research, 2015. **2**(2): p. 43-51.
127. Godse, L.S., et al., *Process-based modeling of nylon separator supercapacitor.* Energy Storage, 2021. **3**(1): p. e204.
128. Khan, Y., et al., *Effect of salt concentration on poly (acrylic acid) hydrogel electrolytes and their applications in supercapacitor.* Journal of The Electrochemical Society, 2020. **167**(10): p. 100524.
129. Liu, W., et al., *Solid polymer electrolytes reinforced with porous polypropylene separators for all-solid-state supercapacitors.* RSC advances, 2023. **13**(49): p. 34652-34659.
130. Din, M.M.U. and R. Murugan, *Metal coated polypropylene separator with enhanced surface wettability for high capacity lithium metal batteries.* Scientific reports, 2019. **9**(1): p. 16795.
131. Szubzda, B., et al., *Polymer membranes as separators for supercapacitors.* Applied Physics A, 2014. **117**(4): p. 1801-1809.
132. Huang, Y., et al., *Hierarchically mesostructured aluminum current collector for enhancing the performance of supercapacitors.* ACS applied materials & interfaces, 2018. **10**(19): p. 16572-16580.
133. Mirzaee, M. and C. Dehghanian, *Synthesis of nanoporous copper foam-applied current collector electrode for supercapacitor.* Journal of the Iranian Chemical Society, 2019. **16**(2): p. 283-292.
134. Zhu, Z., et al., *Effects of various binders on supercapacitor performances.* International Journal of Electrochemical Science, 2016. **11**(10): p. 8270-8279.
135. Khatua, S., et al. *Comparative Study of Binders for Super-capacitor*. in *2019 IEEE Pune Section International Conference (PuneCon)*. 2019. IEEE.
136. Wang, G., et al., *Towards high-performance supercapacitor electrodes via achieving 3D cross-network and favorable surface chemistry.* ACS applied materials & interfaces, 2022. **14**(30): p. 34637-34648.

137. Liu, Y., et al., *Acetylene black enhancing the electrochemical performance of NiCo-MOF nanosheets for supercapacitor electrodes.* Applied Surface Science, 2019. **492**: p. 455-463.
138. Sudhakaran, S. and T. Bijoy, *A comprehensive review of current and emerging binder technologies for energy storage applications.* ACS Applied Energy Materials, 2023. **6**(23): p. 11773-11794.
139. Pazhamalai, P., et al., *Investigating composite electrode materials of metal oxides for advanced energy storage applications.* Nano Convergence, 2024. **11**(1): p. 30.
140. Kaur, N., et al., *Metal chalcogenide nanostructures: A promising class of materials for high-performance batteries and supercapacitors.* Journal of Power Sources, 2025. **656**: p. 238097.
141. Yang, H., et al., *High-Quality SbSI Nanowires via Chemical Vapor Transport for Anisotropic Polarized Photodetection.* Crystal Growth & Design, 2025. **25**(15): p. 6197-6203.
142. Gödel, K.C. and U. Steiner, *Thin film synthesis of SbSI micro-crystals for self-powered photodetectors with rapid time response.* Nanoscale, 2016. **8**(35): p. 15920-15925.
143. Phor, L., A. Kumar, and S. Chahal, *Electrode materials for supercapacitors: A comprehensive review of advancements and performance.* Journal of Energy Storage, 2024. **84**: p. 110698.
144. Palaniselvam, T. and J.-B. Baek, *Graphene based 2D-materials for supercapacitors.* 2D Materials, 2015. **2**(3): p. 032002.
145. Li, P., et al., *A general electrode design strategy for flexible fiber micro-pseudocapacitors combining ultrahigh energy and power delivery.* Advanced Science, 2017. **4**(8): p. 1700003.
146. Yan, J., et al., *Fast and reversible surface redox reaction of graphene–MnO2 composites as supercapacitor electrodes.* Carbon, 2010. **48**(13): p. 3825-3833.
147. **Ali, M.D., et al., *Doping-induced structural and electrical modifications in SbSI nanowires embedded in graphene oxide for enhanced optoelectronic applications.* Journal of Alloys and Compounds, 2025: p. 184183.**
148. Wang, N., et al., *Hydrothermal synthesis and electrochemical properties of MnO2 nanostructures.* Crystal Research and Technology: Journal of Experimental and Industrial Crystallography, 2009. **44**(11): p. 1230-1234.
149. Hummers Jr, W.S. and R.E. Offeman, *Preparation of graphitic oxide.* Journal of the american chemical society, 1958. **80**(6): p. 1339-1339.
150. Nowak, M., et al., *Sonochemical preparation of SbSI gel.* Ultrasonics sonochemistry, 2008. **15**(5): p. 709-716.
151. Wang, X. and Y. Li, *Selected-control hydrothermal synthesis of α-and β-MnO2 single crystal nanowires.* Journal of the American Chemical Society, 2002. **124**(12): p. 2880-2881.
152. Mroczkowska-Szerszeń, M., et al., *The organic matter type in the shale rock samples assessed by FTIR-ATR analyses.* Nafta-Gaz, 2015. **71**(6): p. 361-369.
153. Unnikrishnan, A., V. Megha, and L.K. Alexander, *Ascorbic acid sensing utilizing graphene oxide based on UV–Visible bathochromic shift.* Journal of Materials Science: Materials in Electronics, 2024. **35**(13): p. 904.
154. Esmaeili, Y., et al., *Graphene oxide and its derivatives as promising In-vitro bio-imaging platforms.* Scientific reports, 2020. **10**(1): p. 18052.
155. Chaudhary, K., et al., *In-depth understanding of a nano-bio interface between lysozyme and Au NP-immobilized N-doped reduced graphene oxide 2-D scaffolds.* Nanoscale Advances, 2020. **2**(5): p. 2146-2159.
156. Starczewska, A., et al., *Influence of humidity on impedance of SbSI gel.* Sensors and Actuators A: Physical, 2012. **183**: p. 34-42.
157. Starczewska, A., *New approach to well-known compounds: Fabrication and characterization of AVBVICVII nanomaterials.* Acta Phys. Pol. A, 2021. **139**(4): p. 394-400.
158. Mistewicz, K., et al., *SbSI nanosensors: from gel to single nanowire devices.* Nanoscale Research Letters, 2017. **12**(1): p. 97.
159. Mistewicz, K., et al., *Fast and efficient piezo/photocatalytic removal of methyl orange using SbSI nanowires.* Materials, 2020. **13**(21): p. 4803.
160. Starczewska, A., et al., *Interfacial polarization phenomena in compressed nanowires of SbSI.* Materials, 2022. **15**(4): p. 1543.

161. Kanha, P. and P. Saengkwamsawang, *Effect of stirring time on morphology and crystalline features of MnO2 nanoparticles synthesized by co-precipitation method.* Inorganic and Nano-Metal Chemistry, 2017. **47**(8): p. 1129-1133.
162. Jenkins, R., et al., *JCPDS—international centre for diffraction data sample preparation methods in X-Ray Powder Diffraction.* Powder Diffraction, 1986. **1**(2): p. 51-63.
163. Greenberg, B., *Bragg's law with refraction.* Foundations of Crystallography, 1989. **45**(3): p. 238-241.
164. Jauncey, G., *The scattering of x-rays and Bragg's law.* Proceedings of the national academy of sciences, 1924. **10**(2): p. 57-60.
165. **Ali, M.D., et al., *Dielectric and electrical properties of synthesized PBGO/Fe3O4 nanocomposite.* Ceramics International, 2021. 47(18): p. 26224-26232.**
166. Faiz, M.A., et al., *Low cost and green approach in the reduction of graphene oxide (GO) using palm oil leaves extract for potential in industrial applications.* Results in Physics, 2020. **16**: p. 102954.
167. Pathak, A.K., M.D. Prasad, and S.K. Batabyal, *One-dimensional SbSI crystals from Sb, S, and I mixtures in ethylene glycol for solar energy harvesting.* Applied Physics A, 2019. **125**(3): p. 213.
168. Park, A.R., et al., *Si–Mn/Reduced graphene oxide nanocomposite anodes with enhanced capacity and stability for lithium-ion batteries.* ACS applied materials & interfaces, 2014. **6**(3): p. 1702-1708.
169. Davoglio, R.A., et al., *Synthesis and characterization of α-MnO2 nanoneedles for electrochemical supercapacitors.* Electrochimica Acta, 2018. **261**: p. 428-435.
170. **Majid, F., et al., *Fe3O4/graphene oxide/Fe4 [Fe (CN) 6] 3 nanocomposite for high performance electromagnetic interference shielding.* Ceramics International, 2021. 47(8): p. 11587-11595.**
171. Lindau, I., et al., *Photoemission of gold in the energy range 30-300 eV using synchrotron radiation.* Physical Review B, 1976. **13**(2): p. 492.
172. Greczynski, G. and L. Hultman, *Reliable determination of chemical state in x-ray photoelectron spectroscopy based on sample-work-function referencing to adventitious carbon: resolving the myth of apparent constant binding energy of the C 1s peak.* Applied Surface Science, 2018. **451**: p. 99-103.
173. Al-Gaashani, R., et al., *XPS and structural studies of high quality graphene oxide and reduced graphene oxide prepared by different chemical oxidation methods.* Ceramics International, 2019. **45**(11): p. 14439-14448.
174. Jeon, I.-Y., et al., *Antimony-doped graphene nanoplatelets.* Nature communications, 2015. **6**(1): p. 7123.
175. Stobinski, L., et al., *Graphene oxide and reduced graphene oxide studied by the XRD, TEM and electron spectroscopy methods.* Journal of Electron Spectroscopy and Related Phenomena, 2014. **195**: p. 145-154.
176. Nowak, M., et al., *XPS analysis of sonochemically prepared SbSI ethanogel.* Applied surface science, 2009. **255**(17): p. 7689-7694.
177. Nowak, M., et al., *Fabrication and characterization of SbSI gel for humidity sensors.* Sensors and Actuators A: Physical, 2014. **210**: p. 119-130.
178. Yu, C., et al., *A simple template-free strategy to synthesize nanoporous manganese and nickel oxides with narrow pore size distribution, and their electrochemical properties.* Advanced Functional Materials, 2008. **18**(10): p. 1544-1554.
179. Biesinger, M.C., et al., *Resolving surface chemical states in XPS analysis of first row transition metals, oxides and hydroxides: Cr, Mn, Fe, Co and Ni.* Applied Surface Science, 2011. **257**(7): p. 2717-2730.
180. John, R.E., et al., *Surface-defect induced modifications in the optical properties of α-MnO2 nanorods.* Applied Surface Science, 2016. **367**: p. 43-51.
181. Eren, B. and A.R. Head, *Carbon monoxide adsorption on manganese oxide/cobalt: an ambient pressure X-ray photoelectron spectroscopy study.* The Journal of Physical Chemistry C, 2020. **124**(6): p. 3557-3563.

182. Vogt, C., C.S. Wondergem, and B.M. Weckhuysen, *Ultraviolet-visible (UV-Vis) spectroscopy*, in *Springer handbook of advanced catalyst characterization*. 2023, Springer. p. 237-264.
183. Mayerhöfer, T.G., A.V. Pipa, and J. Popp, *Beer's law-why integrated absorbance depends linearly on concentration.* ChemPhysChem, 2019. **20**(21): p. 2748-2753.
184. Pan, N., et al., *Removal of Th4+ ions from aqueous solutions by graphene oxide.* Journal of Radioanalytical and Nuclear Chemistry, 2013. **298**(3): p. 1999-2008.
185. Ebrahimi-Tazangi, F., S.H. Hekmatara, and J. Seyed-Yazdi, *Synthesis and remarkable microwave absorption properties of amine-functionalized magnetite/graphene oxide nanocomposites.* Journal of Alloys and Compounds, 2019. **809**: p. 151779.
186. Tasviri, M. and Z. Sajadi-Hezave, *SbSI nanowires and CNTs encapsulated with SbSI as photocatalysts with high visible-light driven photoactivity.* Molecular Catalysis, 2017. **436**: p. 174-181.
187. Wang, C., et al., *SbSI nanocrystals: An excellent visible light photocatalyst with efficient generation of singlet oxygen.* ACS Sustainable Chemistry & Engineering, 2018. **6**(9): p. 12166-12175.
188. Cho, I., et al., *One-dimensional single crystalline antimony sulfur iodide, SbSI.* Materials Letters, 2012. **86**: p. 132-135.
189. Lu, W., et al., *Shaping sulfur precursors to low dimensional (0D, 1D and 2D) sulfur nanomaterials: synthesis, characterization, mechanism, functionalization, and applications.* Small, 2023. **19**(28): p. 2301095.
190. Orellana, F., et al., *Spatial and temporal evaluation of iodine uptake and radiodensity in meniscus tissue using contrast-enhanced micro-CT.* Heliyon, 2024. **10**(24).
191. Manojkumar, P. and K. Koppole, *Surfactant-free facile synthesis of Ag/rGO nanohybrid for SERS-based detection of melamine.* Plasmonics, 2024. **19**(1): p. 471-480.
192. Mallakpour, S., A. Abdolmaleki, and H. Tabebordbar, *Facile synthetic route for the preparation of PVC/α-MnO2-PVA nanocomposites: morphology, thermal, mechanical and Cd (II) adsorption properties.* Polymer Bulletin, 2017. **74**(8): p. 2957-2973.
193. Sherman, D.M., *Electronic structures of iron (III) and manganese (IV)(hydr) oxide minerals: Thermodynamics of photochemical reductive dissolution in aquatic environments.* Geochimica et Cosmochimica Acta, 2005. **69**(13): p. 3249-3255.
194. Kwon, K.D., K. Refson, and G. Sposito, *On the role of Mn (IV) vacancies in the photoreductive dissolution of hexagonal birnessite.* Geochimica et Cosmochimica Acta, 2009. **73**(14): p. 4142-4150.
195. Ghorpade, U.V., et al., *Emerging chalcohalide materials for energy applications.* Chemical Reviews, 2022. **123**(1): p. 327-378.
196. Groom, R.A., et al., *Structural and optical properties of Sb-substituted BiSI grown from sulfur/iodine flux.* Inorganic Chemistry, 2017. **56**(20): p. 12362-12368.
197. Haque, F., et al., *Two-dimensional transition metal oxide and chalcogenide-based photocatalysts.* Nano-Micro Letters, 2018. **10**(2): p. 23.
198. Trifiletti, V., et al., *Quasi-zero dimensional halide perovskite derivates: Synthesis, status, and opportunity.* Frontiers in Electronics, 2021. **2**: p. 758603.
199. Shaheen, S., et al., *Effective disposal of methylene blue and bactericidal benefits of using GO-doped MnO2 Nanorods synthesized through one-pot synthesis.* ACS omega, 2021. **6**(38): p. 24866.
200. Khan, I., et al., *Manganese dioxide nanoparticles/activated carbon composite as efficient UV and visible-light photocatalyst.* Environmental Science and Pollution Research, 2019. **26**(5): p. 5140-5154.
201. Zhao, G., et al., *Few-layered graphene oxide nanosheets as superior sorbents for heavy metal ion pollution management.* Environmental science & technology, 2011. **45**(24): p. 10454-10462.
202. Farghali, M.A., M.M. Abo-Aly, and T.A. Salaheldin, *Modified mesoporous zeolite-A/reduced graphene oxide nanocomposite for dual removal of methylene blue and Pb2+ ions from wastewater.* Inorganic chemistry communications, 2021. **126**: p. 108487.
203. Starczewska, A., et al., *Infrared spectroscopy of ferroelectric nanowires of antimony sulfoiodide.* Infrared physics & technology, 2008. **51**(4): p. 307-315.

204. Li, L., et al. *The third-order nonlinear optical properties of Sb2S3/RGO nanocomposites*. in *Photonics*. 2022. MDPI.
205. He, H., et al., *Investigation of elemental sulfur speciation transformation mediated by Acidithiobacillus ferrooxidans.* Current microbiology, 2009. **58**(4): p. 300-307.
206. Ptak, S.H., et al., *Complementarity of Raman and Infrared spectroscopy for rapid characterization of fucoidan extracts.* Plant Methods, 2021. **17**(1): p. 130.
207. Shimanouchi, T., *Tables of molecular vibrational frequencies*. 1973: US Government Printing Office Washington, DC.
208. Guajardo, J.A.G., et al., *Synthesis of SbSI microspheres with urchin-like morphology via tartaric acid-assisted coprecipitation and evaluation of their photocatalytic activity.* Environmental Science and Pollution Research, 2026. **33**(8): p. 3339-3359.
209. Bera, M., P. Gupta, and P.K. Maji, *Facile one-pot synthesis of graphene oxide by sonication assisted mechanochemical approach and its surface chemistry.* Journal of nanoscience and nanotechnology, 2018. **18**(2): p. 902-912.
210. Ickecan, D., R. Zan, and S. Nezir. *Eco-friendly synthesis and characterization of reduced graphene oxide*. in *Journal of Physics: Conference Series*. 2017. IOP Publishing.
211. Emiru, T.F. and D.W. Ayele, *Controlled synthesis, characterization and reduction of graphene oxide: A convenient method for large scale production.* Egyptian Journal of Basic and Applied Sciences, 2017. **4**(1): p. 74-79.
212. Surekha, G., et al. *FTIR, Raman and XRD analysis of graphene oxide films prepared by modified Hummers method*. in *Journal of Physics: Conference Series*. 2020. IOP Publishing.
213. Shahriary, L. and A.A. Athawale, *Graphene oxide synthesized by using modified hummers approach.* Int. j. renew. energy environ. eng, 2014. **2**(01): p. 58-63.
214. Sudesh, et al., *Effect of graphene oxide doping on superconducting properties of bulk MgB2.* Superconductor Science and Technology, 2013. **26**(9): p. 095008.
215. Sannasi, V. and K. Subbian, *Influence of Moringa oleifera gum on two polymorphs synthesis of MnO2 and evaluation of the pseudo-capacitance activity.* Journal of Materials Science: Materials in Electronics, 2020. **31**(19): p. 17120-17132.
216. Ishaq, M., M. Jabeen, and W. Song, *Self-Assembly Synthesis and Electrochemical Performance of Partially Reduced Graphene Oxide Supported Hierarchical MnO2 Nanonocomposite for Supercapacitor.* Journal of the Chemical Society of Pakistan, 2019. **41**(4).
217. Yang, R. el al. Synthesis and characterization of single-crystalline nanorods of α-MnO2 and γ-MnOOH. Materials chemistry and physics, 93(1), 149-153.
218. Alfonso, M., et al., *Absence of giant dielectric permittivity in graphene oxide materials.* Journal of Physics: Materials, 2019. **2**(4): p. 045002.
219. Starczewska, A., et al., *Dielectric properties of SbSI in the temperature range of 292-475 K.* Acta Physica Polonica A, 2014. **126**(5): p. 1125-1127.
220. R Biswal, M., et al., *Dielectric and impedance spectroscopic studies of multiferroic BiFe1-xNixO3.* Advanced Materials Letters, 2014. **5**(9): p. 531-537.
221. Erol, İ., et al., *Dielectric properties of novel nanocomposites based on PVA incorporating CuO nanoparticles.* Journal of Materials Science: Materials in Electronics, 2025. **36**(16): p. 988.
222. Macdonald, J.R., *Impedance spectroscopy.* Annals of biomedical engineering, 1992. **20**(3): p. 289-305.
223. Barsoukov, E. and J.R. Macdonald, *Impedance spectroscopy: theory, experiment, and applications*. 2018: John Wiley & Sons.
224. **Majid, F., et al., *Cationic distribution of nickel doped NixCoX-1Fe2O4 nanparticles prepared by hydrothermal approach: Effect of doping on dielectric properties.* Materials Chemistry and Physics, 2021. 264: p. 124451.**
225. Wagner, K.W., *Zur theorie der unvollkommenen dielektrika.* Annalen der Physik, 1913. **345**(5): p. 817-855.
226. Maxwell, J.C., *A treatise on electricity and magnetism*. Vol. 1. 1873: Clarendon press.
227. **Anjum, S., et al., *Investigation of cationic distribution, Y–K angles, and optical and dielectric properties of as-synthesized cerium-doped cobalt nano-ferrites prepared by co-precipitation method.* Applied Physics A, 2022. 128(5): p. 383.**

228. **Majid, F., et al., *Cobalt doping of nickel ferrites via sol gel approach: effect of doping on the structural and dielectric properties.* Zeitschrift für Physikalische Chemie, 2021. 235(12): p. 1811-1829.**
229. Rodrigues, H., et al., *Study of the structural, dielectric and magnetic properties of Bi2O3 and PbO addition on BiFeO3 ceramic matrix.* Journal of Physics and Chemistry of Solids, 2010. **71**(9): p. 1329-1336.
230. De Loor, G.P., *Dielectric properties of heterogeneous mixtures with a polar constituent.* Applied Scientific Research, Section B, 1964. **11**(3): p. 310-320.
231. **Aslam, A., et al., *Electrical, dielectric, IV and antimicrobial behavior of cobalt incapacitated Prussian blue graphene ferrites composite.* Inorganic Chemistry Communications, 2022. 141: p. 109548.**
232. Nioua, Y., et al., *Analyzing the frequency and temperature dependences of the ac conductivity and dielectric analysis of reduced graphene oxide/epoxy polymer nanocomposites.* Journal of Materials Science, 2017. **52**(24): p. 13790-13798.
233. Wang, Y., J.W. Shan, and G.J. Weng, *Percolation threshold and electrical conductivity of graphene-based nanocomposites with filler agglomeration and interfacial tunneling.* Journal of Applied Physics, 2015. **118**(6).
234. Tan, F.K., et al., *Electrical conductivity and dielectric studies of MnO2 doped V2O5.* Results in physics, 2016. **6**: p. 420-427.
235. Han, M., et al., *Oxygen defects in β-MnO2 enabling high-performance rechargeable aqueous zinc/manganese dioxide battery.* Iscience, 2020. **23**(1).
236. Hona, R.K., G.S. Dhaliwal, and R. Thapa, *Investigation of grain, grain boundary, and interface contributions on the impedance of Ca2FeO5.* Applied Sciences, 2022. **12**(6): p. 2930.
237. Asami, K., *Characterization of heterogeneous systems by dielectric spectroscopy.* Progress in polymer science, 2002. **27**(8): p. 1617-1659.
238. Xia, X., Z. Zhong, and G.J. Weng, *Maxwell–Wagner–Sillars mechanism in the frequency dependence of electrical conductivity and dielectric permittivity of graphene-polymer nanocomposites.* Mechanics of Materials, 2017. **109**: p. 42-50.
239. Koops, C., *On the dispersion of resistivity and dielectric constant of some semiconductors at audiofrequencies.* Physical review, 1951. **83**(1): p. 121.
240. Patil, D., et al., *Studies on electrical and dielectric properties of Ba1− xSrxTiO3.* Materials chemistry and physics, 2007. **104**(2-3): p. 254-257.
241. Quader, R., L.K. Narayanan, and E.B. Caldona, *Dielectric characterization of fiber-and nanofiller-reinforced polymeric materials.* Journal of Applied Polymer Science, 2024. **141**(19): p. e55362.
242. Shao, Y., et al., *Fabrication of large-area and high-crystallinity photoreduced graphene oxide films via reconstructed two-dimensional multilayer structures.* NPG Asia Materials, 2014. **6**(8): p. e119-e119.
243. Gong, Y., et al., *Influence of graphene microstructures on electrochemical performance for supercapacitors.* Progress in Natural Science: Materials International, 2015. **25**(5): p. 379-385.
244. Khalil, K.A., et al., *A novel graphene oxide-based ceramic composite as an efficient electrode for capacitive deionization.* Scientific Reports, 2020. **10**(1): p. 9676.
245. Cao, H., et al., *Oxygen functional groups improve the energy storage performances of graphene electrochemical supercapacitors.* RSC advances, 2018. **8**(6): p. 2858-2865.
246. Jovanovic, Z., et al., *The role of surface chemistry in the charge storage properties of graphene oxide.* Electrochimica Acta, 2017. **258**: p. 1228-1243.
247. Le Fevre, L.W., et al., *Systematic comparison of graphene materials for supercapacitor electrodes.* ChemistryOpen, 2019. **8**(4): p. 418-428.
248. Saaid, F.I., et al., *The synergistic effect of iron cobaltite compare to its single oxides as cathode in supercapacitor.* Journal of Electroceramics, 2020. **44**(3): p. 183-194.
249. Manohar, A., et al., *Mechanistic insights into KOH-driven improvements in supercapacitor charge storage and stability.* Journal of Industrial and Engineering Chemistry, 2026.
250. Warburg, E., *Ueber das Verhalten sogenannter unpolarisirbarer Elektroden gegen Wechselstrom.* Annalen der Physik, 1899. **303**(3): p. 493-499.

251. Kannadasan, K., et al., *Enhanced lithium-ion/sodium-ion battery Performances using chrysanthemum flower-like NiO-CoO Anode: insights into Li+/Na+ charge storage mechanism.* Electrochimica Acta, 2025. **513**: p. 145574.
252. Naeini, M.J., et al., *Photoresponsive MoS2 Se PPy electrodes for flexible supercapacitors with self charging capability under light.* Scientific Reports, 2026.
253. Sakaray, M., S.C. Chidurala, and N. Kitchamsetti, *Enhanced charge transfer kinetics in supercapacitor electrodes: The synergistic effect of 2D Mo2Ti2C3 in PANI/MoO3 composite.* Inorganic Chemistry Communications, 2025. **173**: p. 113788.
254. Mahmudi, et al. *Electrolysis synthesis of MnO2 in acidic environment and its electrochemical performance for supercapacitor*. in *Journal of Physics: Conference Series*. 2018. IOP Publishing.
255. Gurunathan, K., et al., *Bifunctional Electrochemical Behavior of S-rGO@ GO/MnO2 for Advanced Supercapacitor and Lithium-Ion Hybrid Capacitor.* Batteries & Supercaps, 2026. **9**(3): p. e202500683.
256. Yugambica, S., A.C. Dhanemozhi, and S. Iswariya, *Synthesis and characterization of MnO2/rGO nanocomposite for supercapacitors.* Int. Res. J. Eng. Technol., 2017. **4**: p. 486-491.
257. Tian, Z., et al., *A high-performance asymmetric supercapacitor-based (CuCo) Se2/GA cathode and FeSe2/GA anode with enhanced kinetics matching.* Nanoscale, 2021. **13**(13): p. 6489-6498.
258. Van den Bogaert, R. and P. Joos, *Diffusion-controlled adsorption kinetics for a mixture of surface active agents at the solution-air interface.* The Journal of Physical Chemistry, 1980. **84**(2): p. 190-194.
259. Stoller, M.D. and R.S. Ruoff, *Best practice methods for determining an electrode material's performance for ultracapacitors.* Energy & Environmental Science, 2010. **3**(9): p. 1294-1301.
260. Gogotsi, Y. and P. Simon, *True performance metrics in electrochemical energy storage.* science, 2011. **334**(6058): p. 917-918.
261. Stoller, M.D., et al., *Using coin cells for ultracapacitor electrode material testing.* Journal of Applied Electrochemistry, 2011. **41**(6): p. 681-686.
262. Kisu, K., et al., *Internal resistance mapping preparation to optimize electrode thickness and density using symmetric cell for high-performance lithium-ion batteries and capacitors.* Journal of Power Sources, 2018. **396**: p. 207-212.
263. Wang, J., et al., *Pseudocapacitive contributions to electrochemical energy storage in TiO2 (anatase) nanoparticles.* The Journal of Physical Chemistry C, 2007. **111**(40): p. 14925-14931.
264. MP, H. and A. Chandra Bose, *Recent advances and future perspectives of VS4 and its nanostructure composites for supercapacitor applications: a review.* Energy & Fuels, 2023. **37**(15): p. 10799-10826.
265. Lasia, A., *Electrochemical impedance spectroscopy and its applications*, in *Modern aspects of electrochemistry*. 2002, Springer. p. 143-248.